UNIVERSIDAD NACIONAL AUTÓNOMA DE MEXICO

PROGRAMA DE MAESTRÍA Y DOCTORADO EN CIENCIAS QUÍMICAS

Implementación eficiente del método de matrices de la densidad reducida y su aplicación a sistemas fuertemente correlacionados

TESIS

PARA OPTAR POR EL GRADO DE

DOCTOR EN CIENCIAS

PRESENTA

M. en C. Juan Felipe Huan Lew Yee

Tutor Dr. Jorge Martín del Campo Ramírez
Departamento de Física y Química Teórica
Universidad Nacional Autónoma de México

Ciudad de México, noviembre, 2023

Implementación eficiente del método de matrices de la densidad reducida y su aplicación a sistemas fuertemente correlacionados

---

Juan Felipe Huan Lew Yee

Noviembre, 2023

Universidad Nacional Autónoma de México

Departamento de Física y Química Teórica
Facultad de Química

Comité Tutor

Tutor Principal Dr. Jorge Martín del Campo Ramírez
Departamento de Física y Química Teórica
Universidad Nacional Autónoma de México

Comité Tutor Dr. J. Jesus Hernández Trujillo
Departamento de Física y Química Teórica
Universidad Nacional Autónoma de México

Comité Tutor Dr. Marcelo Enrique Galván Espinosa
Departamento de Química
Universidad Autónoma Metropolitana

Sinodales

Presidente Dr. Luis Emilio Orgaz Baqué
Departamento de Física y Química Teórica
Universidad Nacional Autónoma de México

Vocal Dr. Marcelo Enrique Galván Espinosa
Departamento de Química
Universidad Autónoma Metropolitana

Vocal Dr. Tomás Rocha Rinza
Instituto de Química
Universidad Nacional Autónoma de México

Vocal Dr. José Eduardo Barrios Vargas
Departamento de Física y Química Teórica
Universidad Nacional Autónoma de México

Secretario Dra. Martha Magdalena Flores Leonar
Departamento de Física y Química Teórica
Universidad Nacional Autónoma de México

Juan Felipe Huan Lew Yee

Implementación eficiente del método de matrices de la densidad reducida y su aplicación a sistemas fuertemente correlacionados

Tesis, Noviembre, 2023

Comité Tutor: Dr. Jorge Martín del Campo Ramírez Dr. J. Jesus Hernández Trujillo y Dr. Marcelo Enrique Galván Espinosa

Sinodales: Dr. Luis Emilio Orgaz Baqué, Dr. Marcelo Galván Espinosa, Dr. Tomás Rocha Rinza, Dr. José Eduardo Barrios Vargas, Dra. Martha Magdalena Flores Leonar

Universidad Nacional Autónoma de México

Facultad de Química

Departamento de Física y Química Teórica

Av. Universidad 3000, Universidad Nacional Autónoma de México, C.U., Delegación Coyoacán, 04510, Ciudad de México

Resumen

La teoría de matrices de la densidad reducida, a través de los funcionales de orbitales naturales (en cuya base la 1RDM es diagonal), representa una opción atractiva para describir sistemas fuertemente correlacionados a un costo más accesible que los métodos basados en función de onda. Sin embargo, su desarrollo permanece activo, requiriendo una mayor eficiencia y análisis para competir contra el resto de métodos de estructura electrónica. En este trabajo se generó una implementación eficiente en lenguajes de programación modernos, dando lugar a PyNOF (Python), y DoNOF.jl (Julia). Ambos programas cuentan con soporte de aceleradores de cómputo a través de unidades de procesamiento gráfico, y se ha utilizado la aproximación de resolución de la identidad para reducir el escalamiento aritmético y de memoria a cuarto y tercer orden, respectivamente. Las implementaciones generadas permiten estudiar sistemas de interés químico con un tamaño mayor a lo previamente posible. Tales implementaciones fueron utilizadas para estudiar fenómenos como el comportamiento de los funcionales en el error de deslocalización de la carga y el orden relativo de estabilidad entre los estados triplete-quintuplete del sistema hierro-porfirina. Finalmente, se extendió la implementación para el estudio de estados excitados.

Producción

En relación con esta tesis, se publicaron los siguientes artículos:

- J.F.H. Lew-Yee, M. Piris, y J. M. del Campo, “Excited states by coupling Piris natural orbital functionals with the extended random phase approximation” (en revisión).

- L. Franco, J.F.H. Lew-Yee, y J. M. del Campo, “Correlation balance for describing carbenes: An NOF study,” AIP Adv. 13(6), (2023).

- J.F.H. Lew-Yee, J.M. del Campo, y M. Piris, “Electron Correlation in the Iron(II) Porphyrin by Natural Orbital Functional Approximations,” Journal of Chemical Theory and Computation 19(1), 211–220 (2023).

- J.F.H. Lew-Yee, M. Piris, y J.M. del Campo, “Outstanding improvement in removing the delocalization error by global natural orbital functional,” J. Chem. Phys. 158(8), 084110 (2023).

- J.F.H. Lew-Yee, y J. M. del Campo, “Charge delocalization error in Piris natural orbital functionals,” J. Chem. Phys. 157(10), 104113 (2022).

- J.F.H. Lew-Yee, M. Piris, y J. M. del Campo, “Resolution of the identity approximation applied to PNOF correlation calculations,” J. Chem. Phys. 154(6), 064102 (2021).

Se presentaron los siguientes trabajos en congresos:

- Benchmarking PNOFs for excitation energies, ACS Fall 2023, San Francisco, California, Estados Unidos.

- PNOF7 performance in the charge delocalization error, 12th Triennial Congress of the World Association of Theoretical and Computational Chemists 2022, Vancouver, Canadá.

- PNOF Correlation Calculations Performance in the Conformational Analysis of Glicine, ACS Fall 2021, Atlanta, Georgia, Estados Unidos.

- Análisis de Paralelización de DoNOF: MPI vs OpenMP, Coloquio de Supercómputo 2020, en línea, Ciudad de México, México.

- Resolution of the identity approximation applied to PNOF family of correlation calculations, APS March Meeting 2020, Denver, Colorado, Estados Unidos.

Además, se desarrollaron los siguientes programas de cómputo:

- PyNOF, desarrollado en Python.

- DoNOF.jl, desarrollado en Julia.

Agradecimientos Institucionales

Agradezco al Consejo Nacional de Ciencia y Tecnología (CONACyT) por la beca de doctorado brindada bajo el CVU 867718, así como por los recursos del proyecto CB-2016-282791. De igual forma, agradezco al Programa de Apoyo a Proyectos de Investigación e Innovación Tecnológica por los recursos otorgados a través del proyecto PAPIITIN201822, así como al Laboratorio Nacional de Cómputo de Alto Desempeño (LANCAD) por los recursos de cómputo proporcionados a través del proyecto LANCAD-UNAMDGTIC-270. Agradezco a los miembros de mi comité tutor, Dr. Jorge Martín del Campo Ramírez, Dr. Marcelo Enrique Galván Espinosa y Dr. J. Jesús Hernández Trujillo, quienes supervisaron y aportaron valiosos comentarios al trabajo contenido en este documento. De igual manera agradezco a mis sinodales, Dr. Emilio Orgaz Baqué, Dr. Marcelo Enrique Galván Espinosa, Dr. Tomás Rocha Rinza, Dr. José Eduardo Barrios Vargas y Dra. Martha Magdalena Flores Leonar, quienes revisaron este trabajo. Finalmente, agradezco a la Universidad Nacional Autónoma de México porque a través de la Facultad de Química y del Programa de Maestría y Doctorado en Ciencias Químicas me proporcionó un lugar para formarme académicamente y personalmente, porque al final, por mi raza, hablará el espíritu.

Agradecimientos

Quiero agradecer al Dr. Jorge Martín del Campo Ramírez por formarme académicamente, por las ideas discutidas, por los congresos a donde viajamos, y por todo lo que vivimos juntos. Estando bajo su supervisión aprendí química cuántica, programación, a usar unidades de procesamiento gráfico, inteligencia artificial aplicada a la química, dimos cursos, talleres y desde luego aprendí sobre funcionales de orbitales de naturales. Definitivamente, estos años han sido muy productivos y agradezco toda la motivación otorgada para aprender cosas innovadoras y con mucho potencial. Todavía más, no solo me enseñó a ser un científico, sino también a cambiar la llanta de mi bicicleta, a pedir un buen vino, a convivir con personas, me dio grandes consejos de vida y se convirtió no solo en un excelente asesor, sino también en un gran amigo. De la misma forma quiero agradecer al Dr. Carlos Amador Bedolla porque a lo largo de estos años he tenido la oportunidad de vivir experiencias únicas, porque se tomó el tiempo de formarme como docente mediante su ejemplo y me brindó la oportunidad de dar clases en las asignaturas que tanto me gustan. De igual forma, quiero agradecerle por sus enseñanzas en química cuántica, programación, termodinámica y cálculo. Agradezco también al Dr. Mario Piris, que me ha apoyado desde el otro lado del mundo, ha revisado mi trabajo, y cuya influencia se propaga a lo largo de este trabajo. Doy gracias especiales a estas tres personas porque creyeron en mí y me apoyaron de muchas maneras a lo largo de esta etapa.

Agradezco a las personas que conocí cuando llegué a este grupo de investigación, mis hermanos académicos mayores Rodrigo Cortés Mejía y Xiaomin Huang, así como a mi hermano académico, Demetrio Cumplido, con quienes compartí momentos inolvidables y que definitivamente representan la primera etapa de todo lo que viví aquí. Debo también mencionar a Alfonso Esqueda Rodríguez y Neftali Isaí Rodríguez Rojas, con quienes compartí la parte media de mi estadía aquí. Finalmente, menciono a mis hermanos académicos menores, Lizeth Franco Nolasco, Iván Alejandro Bonfil Rodríguez y Roberto Rojas Hernández, con quienes comparto los días actuales, los aprecio mucho y sé qué están haciendo y que harán grandes cosas. A todas estas personas les agradezco por los cumpleaños que compartimos, por las carreras que corrimos juntos, por cada día que vinimos a entrenar para esas carreras, por compartir cafés, comidas, congresos. Guardo un agradecimiento especial para Alfonso Esqueda Rodríguez, Neftali Isaí Rodríguez Rojas y Lizeth

Franco Nolasco, quienes me brindaron su voto de confianza para ser supervisor técnico de sus trabajos y por lo que estoy muy agradecido.

A las personas con quienes compartí grandes momentos a lo largo de los años, Martha Magdalena Flores Leonar, Mariano Sánchez Castellanos, Humberto Laguna Galindo, Andrés Felipe Marmolejo Valencia, Nancy Cihuapilli Barrueta Flores, Edith Leal Sánchez, José María Castillo Robles, Alejandra del Río Lima, Guillermo Crespo.

A los investigadores con quienes conviví y que influyeron en el químico que quiero ser. A Jorge Martín del Campo Ramírez, Carlos Amador Bedolla, Mario Piris, Roberto Flores Moreno, José Manuel Méndez Stivalet, Luis Emilio Orgaz Baqué, Juan Raúl Álvarez Idaboy, Carlos Federico Bunge Molina, José Eduardo Barrios Vargas, Tomás Rocha Rinza y Rodrigo Alejandro Vargas Hernández.

A mis amigos de la carrera, Luis Alberto Camacho Cruz, Carlos Hernández Fontes, Luis Fernando Valdez, Romina Soto Pérez, Stefani Paulin Martínez.

A mi familia, Leticia Yee López, Victoria Yee López y Felipe Lew León, a quienes agradezco todo el apoyo brindado durante el camino para llegar hasta aquí. A Dulce Consuelo Guzmán Ocampo, a quien conozco desde el 2011, con quien he vivido todo tipo de momentos y que hoy tengo el privilegio de llamar mi esposa. Agradezco por todas las sugerencias, por el apoyo, así como por cada momento de vida compartido.

Creo que somos la suma de las contribuciones que nos dan las personas por las que conocemos a lo largo de la vida. Estas son las personas que estuvieron presentes a lo largo de mi camino por aquí, así que a todas ellas les digo, muchas gracias.

Índice general

Introducción

1

> *The computer firms will not have done their job properly until they have produced a computer that I can talk to, and which will listen to my voice, interpret my instructions, code itself, and then tell me the answer. This attractive prospect -I am assured- is by no means absurdly idealistic.*
>
> **— C. A. Coulson**
> Rev. Mod. Phys. 32(2), 170–177 (1960)

En los últimos años, ha habido un desarrollo impresionante de las herramientas que permiten el estudio computacional de sistemas químicos de interés. Inicialmente, los métodos basados en la función de onda proporcionaron un avance progresivo[a] hacia la mejor descripción teórica de átomos y moléculas, un ejemplo de esto son los métodos de interacción de configuraciones (CI, por sus siglas en inglés), Møller-Plesset (MP) y cúmulos acoplados (CC, por sus siglas en inglés). Sin embargo, la mejora cuantitativa de los resultados vino acompañada de un incremento en el escalamiento computacional, volviéndolos rápidamente prohibitivos para una aplicación práctica. Por otra parte, la teoría de los funcionales de la densidad (DFT, por sus siglas en inglés) proporcionó la promesa de un funcional exacto, que aunque desconocido, motivó el desarrollo de funcionales de la densidad aproximados (DFAs, por sus siglas en inglés) que generan resultados lo suficientemente buenos para estudiar química a un costo aceptable. Bajo esta premisa, se han desarrollado una gran diversidad de funcionales,[1,2] colocando a DFT como la teoría más utilizada de la Química Cuántica actual.[3] A pesar de su gran éxito, los DFAs han encontrado obstáculos. La construcción de los DFAs no es sistemática y aunque se ha propuesto la escalera de Jacob como una analogía para jerarquizar los funcionales,[4] esta analiza cómo son construidos, lo que no necesariamente corresponde a su mejora progresiva en exactitud, como sí sucede en los métodos basados en función de onda. En este sentido, los funcionales diseñados puramente con condiciones teóricas no son tan exactos como se desearía, por lo que se han diseñado funcionales parametrizados para predecir de forma óptima la energía de un conjunto de moléculas. Si bien esto mejora los resultados, también produce un sesgo en el que el funcional se desempeñe mejor en moléculas similares a las del conjunto con el que se ajustaron los parámetros, pero no se desempeña tan bien en el resto de las moléculas. Además, ha surgido un debate sobre que los

[a] Por ejemplo, podemos analizar un sistema considerando un determinante de Slater y sus excitaciones sencillas, luego agregar excitaciones dobles, luego triples y continuar hasta tener determinantes de Slater que contengan todas las excitaciones posibles, cada vez con mejores valores de energía.

DFAs recientes son cada vez mejores prediciendo valores de energía, pero no funcionan bien para otras propiedades como densidades electrónicas, momentos dipolares y cargas, lo que es un indicador de buenos resultados por las razones incorrectas.[5-8] En este sentido, es deseable el uso de una teoría que proporcione resultados con la calidad de altos niveles de métodos de función de onda pero con el costo computacional de DFAs.

La correlación electrónica se origina por la no separabilidad del movimiento electrónico y es un factor clave para poder alcanzar predicciones químicas con buena exactitud. Ya que el método de Hartree-Fock considera el movimiento de un electrón en el campo promedio de los demás electrones, este método no cuantifica adecuadamente la contribución energética de la correlación electrónica. Ante este escenario, sería deseable usar siempre la versión completa del método de interacción de configuraciones (FCI, por sus siglas en inglés), el cual construye la función de onda como una combinación del conjunto completo de determinantes de Slater en una base dada; no obstante, esto es inviable en un tiempo de vida humano con recursos computacionales limitados. En la práctica es común utilizar aproximaciones sencillas como la interacción de configuraciones con excitaciones simples y dobles (CISD, por sus siglas en inglés), Møller-Plesset de segundo orden (MP2) y cúmulos acoplados con excitaciones simples y dobles (CCSD, por sus siglas en inglés). De hecho, agregar excitaciones triples de forma perturbativa a CCSD se considera como el gran estándar[b] de la Química Cuántica, pero esto se debe más al balance entre exactitud y "límites computacionales alcanzables" que a un buen desempeño universal del método. Los métodos anteriores capturan predominantemente correlación dinámica, la cual proviene de las interacciones instantáneas entre electrones y es la dominante en muchas moléculas en su estructura de equilibrio. Sin embargo, la descripción de otros sistemas y fenómenos químicos de interés requiere de correlación estática,[c] la cual se obtiene aumentando el número de determinantes en la función de onda.[9] En este contexto, los sistemas fuertemente correlacionados representan uno de los grandes desafíos para la Química Cuántica actual.[10-12] Estos sistemas tienen una contribución significativa de correlación estática,[d] por lo que requieren de métodos de función de onda computacionalmente demandantes. Alternativamente, se pueden utilizar determinantes selectos para generar nuevos determinantes, dando lugar a los métodos multiconfiguracionales, los cuales son más plausibles, pero siguen siendo costosos. Para añadirle complejidad al problema, existen moléculas en las que la correlación estática es necesaria, pero no suficiente, en estos casos se pueden relajar los orbitales dando lugar a los métodos multireferenciales.[13,14] Respecto a DFT, aunque en principio es capaz de recuperar correlación estática, se ha reportado la falta de efectividad de muchos funcionales para describir sistemas fuertemente correlacionados.[15] El costo

[b] Gold standard, en inglés.
[c] La separación de la correlación electrónica en dinámica y estática es solo una herramienta interpretativa práctica, estrictamente existe una sola correlación electrónica.
[d] En estos sistemas, la correlación estática no puede omitirse.

computacional de los métodos actuales limita el estudio de estos sistemas y genera la necesidad de buscar caminos alternativos para su estudio.

Los sistemas fuertemente correlacionados incluyen una gran diversidad de sistemas químicos interesantes, como moléculas altamente aromáticas, por ejemplo los acenos de más de seis anillos,[16,17] ciclacenos,[18] algunos fulerenos,[19,20] superconductores,[21] sistemas con metales de transición[22] como catalizadores,[23] compuestos de coordinación y organometálicos y la mayor parte de los sistemas fuera de su estructura de equilibrio. Por su interés, se ha investigado bastante sobre la capacidad de los métodos actuales para predecir estos sistemas. Se conoce que los funcionales de la densidad con intercambio local recuperan mejor la correlación estática que los que tienen intercambio de Hartree-Fock, pero en general no representan una solución al problema.[15] Por otra parte, los métodos de función de onda aproximados como CASSCF y CASPT2 se han vuelto la elección de-facto para estudiar sistemas fuertemente correlacionados, aunque su éxito depende de factores como la selección correcta del espacio activo y su demanda de recursos de cómputo limita el tamaño de los sistemas que pueden ser estudiados. Otra alternativa se encuentra en la teoría de matrices de la densidad reducida (RDM, por sus siglas en inglés), cuyo desarrollo se origina en las ideas iniciales de Löwdin, McWeeny y von Neumann y que fue ampliamente impulsado por Coulson[24] y Coleman.[25-27] La premisa de estos métodos es que la función de onda contiene más información de la necesaria para calcular la energía, por lo que puede reducirse a objetos más simples de analizar, como la matriz de la densidad reducida de primer orden (1RDM) y la de segundo orden (2RDM). Esto proporcionó el desarrollo de métodos basados en la RDM,[28] por ejemplo, la propuesta de Valone de un funcional universal de la 1RDM.[29,30] La teoría de matrices de la densidad reducida se basa en que el Hamiltoniano no relativista posee a lo más interacciones entre dos partículas, por lo tanto, la energía es un funcional exacto y conocido de la 2RDM, la cual se puede obtener directamente de la función de onda.[31] El reto se encuentra en construir directamente la 2RDM sujeta a que corresponda a la función de onda del sistema, lo que se conoce como el problema de la N-representabilidad.[32]

El desarrollo de los métodos basados en la RDM perdió impulso con el auge de DFT, al igual que la mayoría de los métodos de Química Cuántica. Es hasta en los últimos años que la RDM ha resurgido como una forma de enfrentar los desafíos a los que se enfrentan los DFAs. La forma en la que se aborda la reconstrucción de la 2RDM ha dado lugar a diversas metodologías, destacando recientemente la 2RDM variacional (v2RDM, por sus siglas en inglés) actualmente representada por los trabajos de David A. Mazziotti[31-34] y DePrince III.[35-38] Estos métodos han sido exitosos, aunque su mejora requiere RDMs de orden superior y su escalamiento se vuelve prohibitivo, por lo que es más común solo usar condiciones de hasta tercer orden.[39] Otra alternativa consiste en la reconstrucción de la 2RDM a partir de la 1RDM antisimetrizada y un cumulante. En este caso, el cumulante contiene la información necesaria para conectar ambas RDMs.[40] Aquí destaca la teoría

del cumulante de la densidad (DCT, por sus siglas en inglés).[41-44] Una consideración adicional se logra a través de expresar las RDMs en la base de orbitales naturales, lo que da lugar a los funcionales de orbitales naturales (NOFs, por sus siglas en inglés), en los que nos centraremos en este trabajo. Los funcionales de orbitales naturales ofrecen como ventaja la diagonalización de la 1RDM, lo que permite tener una expresión del cumulante que depende de los números de ocupación, así como una expresión sencilla de energía, con un escalamiento aritmético de quinto orden.[45] Es en este contexto que la teoría se vuelve prometedora para el estudio de sistemas fuertemente correlacionados.

La computación ha avanzado mucho desde aquellos años en que se desarrollaron los primeros trabajos de la RDM. Por ejemplo, el surgimiento de unidades de procesamiento gráfico ha permitido el cómputo heterogéneo con unidades de procesamiento central y esto ha acelerado los cálculos de los métodos de función de onda y de DFAs de maneras sin precedentes, en el orden de decenas a miles de veces. Por otra parte, el cómputo de integrales y los métodos de convergencia han evolucionado ampliamente. En este sentido, la cita con la que inicia este capítulo, escrita en el artículo de Coulson donde reflexiona sobre la RDM, proporciona una motivación muy interesante.[24] La frase trata sobre el deseo de tener una computadora a la que se le pueda hablar, que nos pueda responder y hasta que se pueda autoprogramar. Si bien en aquellos años (e incluso hace una década) eso sonó a un escenario de película futurista, hoy en día comienza a hacerse una realidad. La computadora que escucha y responde llegó de la mano de *Siri*, *Google Assistant* y *Cortana* y la computadora que se autoprograma llegó de la mano de *GitHub Copilot* y *Amazon Codewhisperer*. Estos parecen haber sido sucedidos recientemente por OpenAI-*ChatGPT* y *Google-Bard*. En ese sentido, el sueño computacional de Coulson ha sido cumplido y ha llegado la hora de poner un pequeño grano de arena para impulsar el otro sueño, volver a la RDM el motor de la Química Cuántica actual.

Teoría

2

2.1 Matrices de la densidad reducida

La ecuación de Schrödinger independiente del tiempo proporciona la información asequible del sistema a partir de la solución a la ecuación:

$$\hat{H}\Psi = E\Psi, \tag{2.1}$$

donde $\hat{H}$ es el Hamiltoniano electrónico, Ψ es la función de onda y E es la energía del sistema. En el caso de átomos y moléculas, la aproximación de Born-Oppenheimer permite desacoplar la parte nuclear de la parte electrónica y centrarnos exclusivamente en resolver el problema

$$\hat{H}_{\text{elec}}\psi = E_{\text{elec}}\psi, \tag{2.2}$$

con ψ la parte electrónica de la función de onda y el Hamiltoniano electrónico dado por

$$\hat{H}_{\text{elec}} = -\frac{1}{2}\sum_i h(i) + \sum_{j>i}\frac{1}{|\mathbf{r}_i - \mathbf{r}_j|}, \tag{2.3}$$

con

$$h(i) = \frac{1}{2}\nabla_i^2 - \sum_{i,A}\frac{Z_A}{|\mathbf{r}_i - \mathbf{R}_A|}, \tag{2.4}$$

en esta ecuación, los índices i y j corresponden a los electrones y el índice A etiqueta a los núcleos, de esta forma $\mathbf{r}_i$ y $\mathbf{R}_A$ corresponden el vector posición del electrón i y del átomo A respectivamente. La solución a la ecuación (2.2) resulta desafiante y analíticamente imposible para más de dos partículas interactuantes, por lo que debemos recurrir a varias aproximaciones que dan lugar a los diversos métodos basados en la función de onda.

Otra alternativa se encuentra en las matrices de la densidad reducida. En general, para un sistema de N electrones cuya función de onda es $\psi(\mathbf{x}_1, \cdots, \mathbf{x}_N)$, donde $\mathbf{x}_i$ representa la coordenada (espacial y de espín) del i-ésimo electrón, la matriz de la densidad de orden-*N* está dada por:

$${}^N\mathrm{D}(\mathbf{x}_1^*, \cdots, \mathbf{x}_N^*; \mathbf{x}_1, \mathbf{x}_2, \cdots, \mathbf{x}_N) = \psi(\mathbf{x}_1^*, \cdots, \mathbf{x}_N^*)\psi(\mathbf{x}_1, \cdots, \mathbf{x}_N), \tag{2.5}$$

mientras que la matriz de la densidad reducida de orden-m está dada por:

$$
\begin{aligned}
&{}^{m}\mathrm{D}(\mathbf{x}_1^*,\cdots,\mathbf{x}_m^*;\mathbf{x}_1,\cdots,\mathbf{x}_m) = \\
&\qquad \binom{N}{m} \int \psi(\mathbf{x}_1^*,\cdots,\mathbf{x}_m^*,\mathbf{x}_{m+1},\cdots,\mathbf{x}_N)\psi(\mathbf{x}_1,\cdots,\mathbf{x}_m,\mathbf{x}_{m+1},\cdots,\mathbf{x}_N)d\mathbf{x}_{m+1}\cdots d\mathbf{x}_N, \quad (2.6)
\end{aligned}
$$

es decir, integrando todas las coordenadas de $(N-m)$ electrones.

Debido a que el Hamiltoniano electrónico contiene a lo más interacciones entre dos electrones, la energía es un funcional exacto y conocido de la 2RDM. Esto se puede entender al expresar el Hamiltoniano en operadores de segunda cuantización

$$
\hat{H}_{\mathrm{elec}} = \sum_{pq} h_{pq} a_p^\dagger a_q + \frac{1}{2}\sum_{pqrs} \langle pq|rs\rangle\, a_p^\dagger a_q^\dagger a_s a_r, \quad (2.7)
$$

con p, q, r y s denotando espín-orbitales y

$$
\begin{aligned}
h_{pq} &= \int d\mathbf{x}\chi_p^*(\mathbf{x})\left(-\frac{1}{2}\nabla^2 - \sum_A \frac{Z_A}{|\mathbf{r}-\mathbf{r}_A|}\right)\chi_q(\mathbf{x}), \quad (2.8)\\
\langle pq|rs\rangle &= \int d\mathbf{x}_1 d\mathbf{x}_2 \chi_p^*(\mathbf{x}_1)\chi_q^*(\mathbf{x}_2)\int r_{12}^{-1}\chi_r(\mathbf{x}_1)\chi_s(\mathbf{x}_2). \quad (2.9)
\end{aligned}
$$

Tomando el valor esperado de la energía se obtiene

$$
E = \langle\psi|\,\hat{H}_{\mathrm{elec}}\,|\psi\rangle = H_{pq}\,{}^{1}\mathrm{D}_{q,p} + \langle pq|rs\rangle\,{}^{2}\mathrm{D}_{rs,pq}, \quad (2.10)
$$

donde se define la 1RDM y la 2RDM como

$$
\begin{aligned}
{}^{1}\mathrm{D}_{p,q} &= \langle\psi|\,a_p^\dagger a_q\,|\psi\rangle\,, \quad (2.11)\\
{}^{2}\mathrm{D}_{rs,pq} &= \langle\psi|\,a_p^\dagger a_q^\dagger a_s a_r\,|\psi\rangle\,. \quad (2.12)
\end{aligned}
$$

Debido a su importancia, se le asigna el símbolo Γ a la 1RDM y el símbolo D a la 2RDM, de tal forma que la expresión de energía resulta

$$
E = \sum_{ij} H_{ij}\Gamma_{j,i} + \sum_{ijkl}\langle ij|kl\rangle\,\mathrm{D}_{kl,ij}. \quad (2.13)
$$

Esta ecuación resulta trascendental, ya que si conociéramos la función de onda exacta del sistema, podríamos reducirla a la 1RDM y 2RDM y usar la ecuación (2.13) para calcular la energía exacta. Además, podemos considerar a la 1RDM en una representación diagonal, es decir,

$$
\Gamma_{p,q} = n_p\delta_{pq}, \quad (2.14)
$$

donde n_p es el número de ocupación del espín-orbital natural, ϕ_p.

2.2 Condiciones de *N*-representabilidad y propiedades de la 2RDM

La ecuación (2.6) proporciona una forma de construir la 2RDM a partir de la función de onda, mientras que la ecuación (2.13) proporciona una forma de usarla para calcular la energía. La existencia de este camino es importante porque muestra que el funcional exacto de la 2RDM es conocido, pero proceder de esta manera es poco práctico, ya que implica realizar un cálculo previo para generar la función de onda. La idea detrás del uso de la 2RDM consiste en construirla directamente sin pasar por la función de onda, lo cual puede hacerse variando la 2RDM en un proceso de optimización de la ecuación (2.13). La ventaja de este enfoque es que la 2RDM generada puede corresponder a la función de onda de cualquier método de estructura electrónica, desde Hartree-Fock, pasando por los métodos multirreferenciales, e idealmente hasta la función de onda correspondiente a FCI. De esta forma sería posible obtener una energía con gran exactitud sin tener que pagar el costo computacional de estos métodos.

Las RDMs deben cumplir ciertas propiedades, por ejemplo, la traza de la 1RDM debe ser el número de electrones N y la traza de la 2RDM debe ser el número de pares de electrones $N(N-1)/2$, a su vez esto genera una vía de contracción de la 2RDM a la 1RDM. Además, la 2RDM debe de cumplir con propiedades como la Hermiticidad y la antisimetría, como se muestra en la Tabla 2.1. Sin embargo, la variación directa de la 2RDM sujeta a estas restricciones lleva a valores de energía más negativos que el exacto, en contradicción aparente con el teorema variacional. La razón es que las condiciones anteriores permiten generar 2RDMs válidas, pero no garantizan que correspondan a la función de onda de N-electrones del sistema, lo que se conoce como el problema de la N-representabilidad.

Tab. 2.1: Propiedades que deben de cumplir la 1RDM y la 2RDM.

Propiedad	Expresión
Traza 1RDM	$\mathrm{Tr}\,\Gamma = \sum_p \Gamma_{p,p} = N$
Traza 2RDM	$\mathrm{Tr}\,\mathrm{D} = \sum_{pq} \mathrm{D}_{pq,pq} = N(N-1)/2$
Contracción	$\sum_r \mathrm{D}_{qr,pr} = \frac{N-1}{2}\Gamma_{qp}$
Hermiticidad	$\mathrm{D}_{rs,pq} = \mathrm{D}^*_{pq,rs}$
Antisimetría	$\mathrm{D}_{rs,pq} = -\mathrm{D}_{rs,qp} = -\mathrm{D}_{sr,pq} = \mathrm{D}_{sr,qp}$

Para solucionar este problema, se proponen condiciones de N-representabilidad. Las condiciones necesarias y suficientes para la N-representabilidad de la 1RDM son[46,47]

- Los números de ocupación deben de encontrarse entre cero y uno, $0 \leq n_p \leq 1$.

- Los números de ocupación deben de sumar el número de electrones, $\sum_p n_p = N$.

Respecto a las condiciones de la 2RDM, resulta conveniente definir tres tipos de matrices a partir de operadores de segunda cuantización, las cuales deben de ser semipositivo definidas:

- $\mathrm{D}_{pq,rs} = \frac{1}{2} \langle \psi | \, a_p^\dagger a_q^\dagger a_s a_r \, | \psi \rangle \geq 0.$

- $\mathrm{Q}_{pq,rs} = \frac{1}{2} \langle \psi | \, a_p a_q a_s^\dagger a_r^\dagger \, | \psi \rangle \geq 0.$

- $\mathrm{G}_{pq,rs} = \frac{1}{2} \langle \psi | \, a_p^\dagger a_q a_s^\dagger a_r \, | \psi \rangle \geq 0.$

Estas ecuaciones se conocen como las condiciones D, Q y G, donde la $\mathbf{D}$ corresponde directamente a la 2RDM, mientras que $\mathbf{Q}$ y $\mathbf{G}$ se obtienen como permutaciones de los operadores de segunda cuantización que forman la matriz $\mathbf{D}$. Es importante señalar que las condiciones D, Q, y G son necesarias, pero no suficientes para lograr la N-representabilidad de la 2RDM. Realizar el proceso de optimización sin las condiciones de N-representabilidad completas lleva a energías menores a las del estado basal. En la medida que se agreguen más condiciones se obtendrán mejores resultados y en el límite en que se tengan todas las condiciones necesarias y suficientes, entonces se podrá alcanzar el límite exacto permitido por la base.

Variar la 2RDM sujeto a las restricciones de N-representabilidad no es algo trivial y a lo largo de los años se han desarrollado varios algoritmos para lograrlo, destacando la programación semidefinida y la optimización restringida no lineal.[33] Por otra parte, por mucho tiempo el conjunto suficiente de estas condiciones fue desconocido, pero recientemente se ha propuesto un método para la inclusión progresiva de las condiciones necesarias y suficientes para lograr la N-representabilidad.[48]

2.3 Expansión cumulante

En paralelo al desarrollo de la optimización directa de la 2RDM, hubo un desarrollo interesante respecto a objetos de menor orden. Por una parte, en 1964 Hohenberg y Kohn formularon su famoso tratamiento del gas de electrones no homogéneo, en el que mostraron la energía del estado basal de un gas de electrones interactuantes con un potencial externo determinado es un funcional de la densidad electrónica.[49] Sin embargo, la prueba proporcionada por Kohn y Sham sólo es aplicable a densidades v-representables, es decir, que provengan de un potencial externo de tipo

local. Posteriormente, en 1975 Gilbert extendió el teorema de Hohenberg y Kohn a potenciales externos no locales, encontrando de manera más general que la energía es un funcional de la 1RDM.[50] En 1979 Levy resolvió el problema de la v-representabilidad y estableció la existencia de un funcional universal de la densidad electrónica y de un funcional universal de la 1RDM, estando ambos conectados.[51] Finalmente, Valone extendió el trabajo de Levy a ensambles.[29,30] Mientras que el uso de la densidad llevó a la actual formulación de DFT, el resto de los trabajos motivaron el desarrollo de la teoría de los funcionales de la matriz de la densidad reducida (RDMFT, por sus siglas en inglés). La representación de la 1RDM en forma diagonal, es decir, en orbitales naturales y sus números de ocupación, fue de gran utilidad para el diseño de los funcionales, surgiendo el funcional de Müller,[52] así como otros funcionales propuestos por Goedecker y Umrigar (GU),[53] Gritsenko, Pernal y Baerends (BBC),[54], Marqués y Lathiotakis (ML),[55] entre otros.[56] En estos casos, la expresión de la energía está basada directamente en alguna función de los números de ocupación y de integrales que dependen de los orbitales naturales.

Otra idea para construir el funcional es a partir del concepto de expansión cumulante propuesto originalmente como un principio matemático,[57] pero aplicado posteriormente en el ámbito de las RDMs.[40] La idea consiste en descomponer una RDM en función de productos de RDMs de orden inferior y una parte no desacoplable, conocida como el cumulante. En el caso de la 2RDM, esta se puede expresar en función de la 1RDM como

$$\mathbf{D} = \mathbf{\Gamma} \wedge \mathbf{\Gamma} + \boldsymbol{\lambda}, \tag{2.15}$$

donde $\wedge$ es el producto antisimetrizado,[a] y $\boldsymbol{\lambda}$ es el cumulante que conecta a la 1RDM con la 2RDM. Haciendo explícito el espín de los índices de la 2RDM y considerando su antisimetría, se cumple

$$\mathrm{D}^{\alpha\alpha\alpha\alpha}_{rs,pq} = \frac{1}{2}\left(\Gamma^{\alpha\alpha}_{rp}\Gamma^{\alpha\alpha}_{sq} - \Gamma^{\alpha\alpha}_{rq}\Gamma^{\alpha\alpha}_{sp}\right) + \lambda^{\alpha\alpha\alpha\alpha}_{rs,pq}, \tag{2.16}$$

$$\mathrm{D}^{\alpha\beta\alpha\beta}_{rs,pq} = \frac{1}{2}\left(\Gamma^{\alpha\alpha}_{rp}\Gamma^{\beta\beta}_{sq}\right) + \lambda^{\alpha\beta\alpha\beta}_{rs,pq}, \tag{2.17}$$

con $\lambda^{\alpha\alpha\alpha\alpha}_{rs,pq}$ siendo antisimétrico ante el intercambio de índices[b] y $\lambda^{\alpha\beta\alpha\beta}_{rs,pq}$ sin ningún requisito particular de simetría. Con esto, la expresión de energía haciendo explícito el espín resulta

$$\begin{aligned} E = \sum_{pq} H_{pq}\Gamma^{\alpha\alpha}_{pq} + \sum_{pq} H_{pq}\Gamma^{\beta\beta}_{pq} + \sum_{pqrs} \langle pq|rs\rangle \, \mathrm{D}^{\alpha\alpha\alpha\alpha}_{rs,pq} \\ + \sum_{pqrs} \langle pq|rs\rangle \, \mathrm{D}^{\alpha\beta\alpha\beta}_{rs,pq} + \sum_{pqrs} \langle pq|rs\rangle \, \mathrm{D}^{\beta\alpha\beta\alpha}_{rs,pq} + \sum_{pqrs} \langle pq|rs\rangle \, \mathrm{D}^{\beta\beta\beta\beta}_{rs,pq}. \end{aligned} \tag{2.18}$$

[a] En inglés, *wedge* product

[b] $\lambda^{\alpha\alpha\alpha\alpha}_{rs,pq} = -\lambda^{\alpha\alpha\alpha\alpha}_{rs,qp} = -\lambda^{\alpha\alpha\alpha\alpha}_{sr,pq} = \lambda^{\alpha\alpha\alpha\alpha}_{sr,qp}$

Se pueden proponer diversos funcionales dependiendo de como se construya el cumulante. Destaca en este sentido la teoría de funcionales del cumulante de la densidad (DCFT, por sus siglas en inglés).[41] Las ecuaciones (2.16) y (2.17) también pueden escribirse utilizando orbitales naturales y sus números de ocupación según la ecuación (2.14) para dar lugar a

$$\mathrm{D}^{\alpha\alpha\alpha\alpha}_{rs,pq} = \frac{1}{2}\left(n_p n_q \delta_{rp}\delta_{sq} - n_p n_q \delta_{rq}\delta_{sp}\right) + \lambda^{\alpha\alpha\alpha\alpha}_{rs,pq}, \tag{2.19}$$

$$\mathrm{D}^{\alpha\beta\alpha\beta}_{rs,pq} = \frac{1}{2}\left(n_p n_q \delta_{rp}\delta_{sq}\right) + \lambda^{\alpha\beta\alpha\beta}_{rs,pq}, \tag{2.20}$$

con la expresión de la energía en función de los números de ocupación y del cumulante

$$E = 2\sum_p n_p H_{pp} + \sum_{pqrs} \langle pq|rs\rangle\, n_p n_q (2\delta_{rp}\delta_{sq} - \delta_{rq}\delta_{sp}) + 2\sum_{pqrs} \langle pq|rs\rangle\, \lambda^{\alpha\alpha\alpha\alpha}_{rs,pq} - 2\sum_{pqrs} \langle pq|rs\rangle\, \lambda^{\alpha\beta\alpha\beta}_{rs,pq}. \tag{2.21}$$

Un caso particular emerge directamente de las ecuaciones (2.19) y (2.20), ya que si restringimos los números de ocupación a “0” y “1” con el cumulante como cero, entonces la ecuación (2.21) se reduce a la energía de Hartree-Fock.

2.3.1 PNOFs

Los funcionales de orbitales naturales de Piris (PNOFs, por sus siglas en inglés) proponen una expresión cumulante en la base de orbitales naturales dada por[58]

$$\lambda^{\alpha\alpha\alpha\alpha}_{pq,rs} = -\frac{\Delta_{pq}}{2}\left(\delta_{pr}\delta_{qs} - \delta_{ps}\delta_{qr}\right), \tag{2.22}$$

$$\lambda^{\alpha\beta\alpha\beta}_{pq;rs} = -\frac{\Delta_{pq}}{2}\delta_{pr}\delta_{qs} + \frac{\Pi_{pr}}{2}\delta_{pq}\delta_{rs}, \tag{2.23}$$

donde Δ_{pq} y Π_{pq} son matrices que se definen según el funcional. Utilizando el cumulante de PNOF dado en las ecuaciones (2.22) y (2.23) podemos usar las ecuaciones (2.19) y (2.20) para reconstruir la 2RDM a partir de los orbitales naturales y sus números de ocupación y a su vez usar la ecuación (2.21) para obtener una expresión de energía. Al efectuar todas las sustituciones se obtiene

$$E = \sum_p n_p(2H_{pp} + J_{pp}) + \sum_{pq,p\neq q}(n_p n_q - \Delta_{qp})(2J_{pq} - K_{pq}) + \sum_{pq,p\neq q}\Pi_{qp}L_{pq}, \tag{2.24}$$

con H_{pp} los elementos diagonales de la matriz del Hamiltoniano de *core*, $J_{pq} = \langle pq|pq\rangle = (pp|qq)$ siendo las integrales de Coulomb, $K_{pq} = \langle pq|qp\rangle = (pq|qp)$ las integrales de intercambio y $L_{pq} = \langle pp|qq\rangle = (pq|pq)$ las integrales de intercambio e inversión del tiempo,[c] todas en la base de

[c] Las integrales de intercambio e inversión del tiempo se han definido en las referencias [59, 60]. Ya que en este trabajo se usan orbitales reales, estas integrales se transforman simplemente en integrales de intercambio, $L_{pq} = K_{pq}$.

orbitales naturales y con los paréntesis indicando la notación química de integrales en orbitales espaciales que se usará por conveniencia a partir de ahora. Esta expresión es importante, ya que permite identificar las integrales que contribuyen a la energía y que dan origen a que a estos funcionales se les conozca como de tipo JKL.

Una vez definida la expresión de energía, solo resta proponer una expresión para las matrices $\mathbf{\Delta}$ y $\mathbf{\Pi}$, lo que da lugar a ocho PNOFs, denominados PNOFi (i=1-7) y un funcional global de orbitales naturales (GNOF, por sus siglas en inglés).[61-68] Aquí destacaremos los más recientes, PNOF5, PNOF7 y GNOF, los cuales se basan en un esquema de apareamiento de electrones,[69] como el que se muestra en la Figura 2.1. Dado un sistema de N electrones en un espacio orbital Ω, este se puede dividir en N_Ω subespacios, cada uno denominado Ω_g con $g = 1, \cdots, N_\Omega$. Del total hay, $N_{\rm II}/2$ subespacios de tipo $\Omega_{\rm II}$ y $N_{\rm I}$ de tipo $\Omega_{\rm I}$, tal que

$$2S + 1 = N_{\rm I} + 1, \tag{2.25}$$

$$N_{\rm II} + N_{\rm I} = N, \tag{2.26}$$

con $2S + 1$ la multiplicidad de espín del sistema determinada por $N_{\rm I}$ y junto con el número total de electrones se determina $N_{\rm II}$. Este esquema permite que la 2RDM cumpla con el valor esperado del operador del cuadrado del espín.[70,71d] Cada subespacio en $\Omega_{\rm I}$ está formado por un orbital natural espacial ($n_p = 1/2$), mientras que cada subespacio en $\Omega_{\rm II}$ está formado por un orbital natural espacial fuertemente doble ocupado ($1/2 \leq n_p \leq 1$) y N_g orbitales naturales espaciales débilmente doble ocupados ($0 \leq n_p \leq 1$), tal que su suma da 2.0, correspondiendo a la ocupación total de un subespacio en $\Omega_{\rm II}$. Cuando solo se acopla un orbital, $N_g = 1$, se dice que se tiene emparejamiento perfecto, mientras que si se acopla más de un orbital, $N_g > 1$, entonces se tiene un esquema de emparejamiento extendido.

Dado el esquema de subespacios, se tienen contribuciones tipo intrasubespacio (intrapar) e intersubespacio (interpar). Las contribuciones intrapares a los bloques de espines opuestos de la 2RDM están dadas por

$$\mathrm{D}^{\alpha\beta\alpha\beta}_{pq,rt} = \frac{n_p\delta_{pr} + \Pi_{pr}(1-\delta_{pr})}{2}\delta_{pq}\delta_{rt}\delta_{p\Omega_g}\delta_{r\Omega_g}, \;\; g \leq N_{\rm II}/2, \tag{2.27}$$

[d] $\left\langle \hat{S}^2 \right\rangle = \frac{N(4-N)}{4} + \sum_{pq}\left(\mathrm{D}^{\alpha\alpha\alpha\alpha}_{pq,pq} + \mathrm{D}^{\beta\beta\beta\beta}_{pq,pq} - 2\mathrm{D}^{\alpha\beta\alpha\beta}_{pq,qp}\right)$

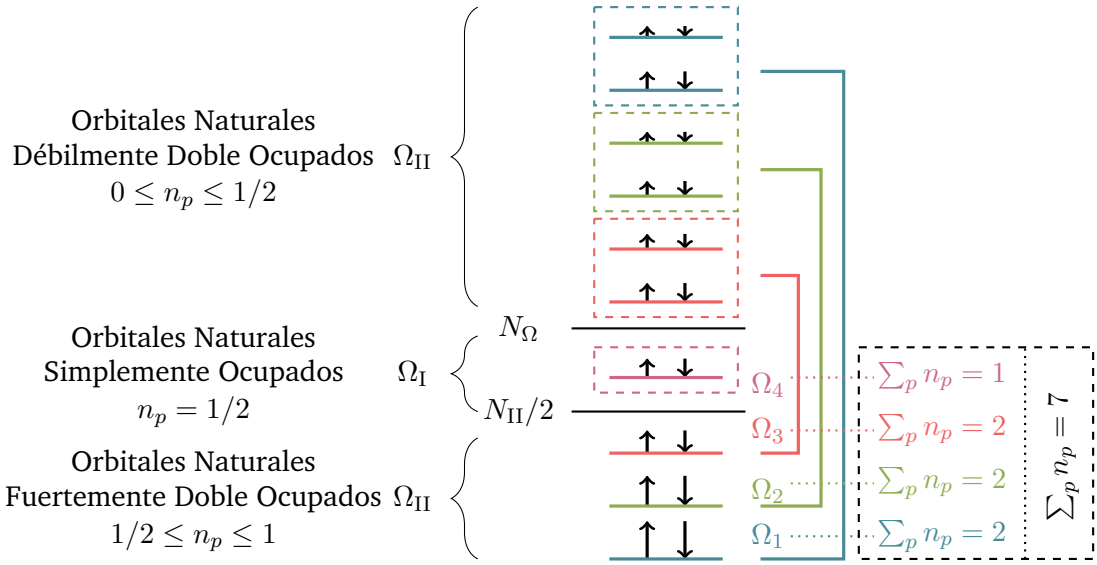

Fig. 2.1: Esquema de acoplamiento orbital usado en PNOF. El ejemplo corresponde a un sistema de $N = 7$ electrones con multiplicidad doblete ($2S+1 = 2$), tal que $N_{\mathrm{I}} = 1$ y $N_{\mathrm{II}} = 6$. El espacio orbital Ω se divide en $N_\Omega = N_{\mathrm{I}} + N_{\mathrm{II}}/2 = 4$ subespacios, de los cuales hay uno en Ω_{I} y tres subespacios en Ω_{II}. Ω_{I} está formado por el subespacio Ω_4 y Ω_{II} está formado por los subespacios Ω_1, Ω_2 y Ω_3, cada uno, con un orbital fuertemente ocupado y dos orbitales débilmente ocupados ($N_g = 2$). De esta forma, los subespacios Ω_1, Ω_2 y Ω_3 aportan una suma de ocupaciones de "dos" cada uno y Ω_4 aporta una ocupación de "uno", para dar el total de 7 electrones del sistema distribuidos en 10 orbitales.

donde el producto $\delta_{p\Omega_f}\delta_{q\Omega_g}$ verifica que los orbitales p y q pertenezcan al mismo subespacio,[e] y

$$\Pi(n_q, n_p) = \sqrt{n_q n_p}(\delta_{q\Omega^{\mathrm{a}}}\delta_{p\Omega^{\mathrm{a}}} - \delta_{qg} - \delta_{pg}), \;\; g \leq N_{\mathrm{II}}/2, \tag{2.28}$$

con δ_{pg} que verifica que el orbital p sea un orbital fuertemente doble ocupado y $\delta_{p\Omega^{\mathrm{a}}}$ que verifica que el orbital p se encuentre arriba de N_Ω, es decir, que sea débilmente doble ocupado.

La contribución interpar al bloque de espines paralelos de la 2RDM está dada por

$$\mathrm{D}^{\alpha\alpha\alpha\alpha}_{pq,rt} = \frac{n_p n_q}{2}\left(\delta_{pr}\delta_{qt} - \delta_{pt}\delta_{qr}\right)\delta_{p\Omega_f}\delta_{q\Omega_g}\,, \tag{2.29}$$

[e] El término $\delta_{p\Omega_g}$ corresponde a la delta de Kronecker definida como

$$\delta_{p\Omega_g} = \begin{cases} 1, & \phi_p \in \Omega_g \\ 0, & \phi_p \notin \Omega_g \end{cases},$$

y que verifica si el orbital ϕ_p pertenece al subespacio Ω_g.

donde el producto $\delta_{p\Omega_f}\delta_{q\Omega_g}$ verifica que p y q pertenezcan a distintos subespacios. Por otra parte, la contribución interpar al bloque de espines opuestos es diferente para cada funcional. En el caso de PNOF5 se propone

$$\mathrm{D}^{\alpha\beta\alpha\beta}_{pq,rt} = \frac{n_p n_q}{2}\delta_{pr}\delta_{qt}\delta_{p\Omega_f}\delta_{q\Omega_g}\,. \tag{2.30}$$

Por otra parte, PNOF7 introduce la función

$$\Phi_p = \sqrt{n_p(1-n_p)}, \tag{2.31}$$

y la contribución interpar de espines opuestos está dada por

$$\mathrm{D}^{\alpha\beta\alpha\beta}_{pq,rt} = \frac{n_p n_q}{2}\delta_{pr}\delta_{qt}\delta_{p\Omega_f}\delta_{q\Omega_g} - \frac{\Phi_p\Phi_r}{2}\delta_{p\Omega_f}\delta_{r\Omega_g} \times \begin{cases} \delta_{pq}\delta_{rt}, & f \leq N_{\mathrm{II}}/2 \text{ ó } g \leq N_{\mathrm{II}}/2 \\ \delta_{pt}\delta_{qr}, & N_{\mathrm{II}}/2 < f,g \leq N_\Omega \end{cases}. \tag{2.32}$$

Es destacable que PNOF7 introduce más correlación respecto a PNOF5 debido al segundo término del lado derecho de la ecuación (2.32), en particular, Φ incrementa su valor cuando los números de ocupación se alejan de 0 y 1, es decir, que se introduce predominantemente correlación interpar de tipo estática. Además, si se utiliza la función $\Phi_p = 2n_p(1-n_p)$ se obtiene una modificación denominada PNOF7s, cuyo propósito es obtener únicamente correlación estática y eliminar la dinámica para evitar conteo doble al recuperarla mediante métodos alternativos como en el esquema NOF-MP2.

Finalmente, GNOF introduce la idea de cuantificar la correlación dinámica a partir de los números de ocupación, n_p. Para ello, a cada uno le asocia un número de ocupación dinámico n_p^{d}, que se calcula como función de n_p y el hueco $h_g = 1 - n_g$ asociado al subespacio Ω_g al que pertenece ϕ_p, según

$$n_p^{\mathrm{d}} = n_p \mathrm{e}^{-\left(\frac{h_g}{h_{\mathrm{c}}}\right)^2}, \;\; \phi_p \in \Omega_g, \tag{2.33}$$

con $h_{\mathrm{c}} = (0.02)\sqrt{2}$ una constante. De esta forma, la contribución interpar de espines opuestos queda dada por

$$\mathrm{D}^{\alpha\beta\alpha\beta}_{pq,rt} = \left(\frac{n_p n_q}{2}\delta_{pr}\delta_{qt} - \frac{\delta_{p\Omega_{\mathrm{I}}}\delta_{q\Omega_{\mathrm{I}}}}{8}\delta_{pq}\delta_{qr}\right)\delta_{p\Omega_f}\delta_{q\Omega_g} - \frac{\Pi^{\mathrm{s}}_{pr} + \Pi^{\mathrm{d}}_{pr}}{2}\delta_{pq}\delta_{rt}\delta_{p\Omega_f}\delta_{r\Omega_g}, \tag{2.34}$$

donde $\delta_{p\Omega_{\mathrm{I}}}$ verifica que el orbital p sea sencillamente ocupado, y

$$\Pi^{\mathrm{s}}_{pr} = \Phi_p\Phi_r\left(\delta_{p\Omega^{\mathrm{b}}}\delta_{r\Omega^{\mathrm{a}}} + \delta_{p\Omega^{\mathrm{a}}}\delta_{r\Omega^{\mathrm{b}}} + \frac{1}{2}(\delta_{p\Omega^{\mathrm{b}}_{\mathrm{II}}}\delta_{r\Omega_{\mathrm{I}}} + \delta_{p\Omega_{\mathrm{I}}}\delta_{r\Omega^{\mathrm{b}}_{\mathrm{II}}})\right), \tag{2.35}$$

$$\Pi^{\mathrm{d}}_{pr} = \left(\sqrt{n_p^{\mathrm{d}}n_r^{\mathrm{d}}} - n_p^{\mathrm{d}}n_r^{\mathrm{d}}\right)\left(\delta_{p\Omega^{\mathrm{b}}_{\mathrm{II}}}\delta_{r\Omega^{\mathrm{a}}} + \delta_{p\Omega^{\mathrm{a}}}\delta_{r\Omega^{\mathrm{b}}_{\mathrm{II}}}\right) - \left(\sqrt{n_p^{\mathrm{d}}n_r^{\mathrm{d}}} + n_p^{\mathrm{d}}n_r^{\mathrm{d}}\right)\delta_{p\Omega^{\mathrm{a}}}\delta_{r\Omega^{\mathrm{a}}}, \tag{2.36}$$

con $\delta_{p\Omega^{\mathrm{b}}}$ que verifica que el orbital p se encuentre por debajo de N_Ω y $\delta_{p\Omega^{\mathrm{b}}_{\mathrm{II}}}$ verifica que el orbital p se encuentre por debajo de $N_{\mathrm{II}}/2$.

Considerando la contribución dada por el esquema de emparejamiento, resulta conveniente expresar la energía como una contribución intrasubespacio, una contribución intersubespacio de tipo Hartree-Fock, de tipo estática y de tipo dinámica. La contribución intrapar está dada por

$$E^{\mathrm{intra}} = \sum_{g=1}^{\frac{N_{\mathrm{II}}}{2}} E_g + \sum_{g=N_{\mathrm{II}}/2+1}^{N_\Omega} H_{gg}, \tag{2.37}$$

con E_g siendo la contribución a la energía de un subespacio doblemente ocupado, dada por

$$E_g = \sum_{p\in\Omega_g} n_p(2H_{pp} + J_{pp}) + \sum_{q,p\in\Omega_g} \Pi_{qp}K_{pq}. \tag{2.38}$$

Por otra parte, la contribución interpar de tipo Hartree-Fock está dada por

$$E^{\mathrm{inter}}_{\mathrm{HF}} = \sum_{\substack{p\in\Omega_g, q\in\Omega_f \\ g\neq f}}^{N_{\mathrm{bf}}} n_q n_p(2J_{pq} - K_{pq}), \tag{2.39}$$

con N_{bf} siendo el número de funciones de base y la prima indicando que se omiten los orbitales dentro de un mismo subespacio. Hasta aquí se tiene la energía de PNOF5, dada por

$$E_{\mathrm{PNOF5}} = E^{\mathrm{intra}} + E^{\mathrm{inter}}_{\mathrm{HF}}. \tag{2.40}$$

La contribución interpar de tipo estática de PNOF7 está dada por

$$E^{\mathrm{inter}}_{\mathrm{sta}} = \sum_{\substack{p\in\Omega_g, q\in\Omega_f \\ g\neq f}}^{N_{\mathrm{bf}}} \Phi_q\Phi_p(2J_{pq} - K_{pq}), \tag{2.41}$$

por lo que la expresión de energía resulta

$$E_{\mathrm{PNOF7}} = E^{\mathrm{intra}} + E^{\mathrm{inter}}_{\mathrm{HF}} + E^{\mathrm{inter}}_{\mathrm{sta}}. \tag{2.42}$$

Finalmente, GNOF modifica la contribución interpar estática y agrega contribución interpar dinámica

$$E_{\mathrm{sta}}^{\mathrm{inter}} = -\left(\sum_{p=1}^{N_\Omega}\sum_{q=N_\Omega+1}^{N_{\mathrm{bf}}} + \sum_{p=N_\Omega+1}^{N_{\mathrm{bf}}}\sum_{q=1}^{N_\Omega} + \sum_{p,q=N_\Omega+1}^{N_{\mathrm{bf}}}\right)' \Phi_q\Phi_p K_{pq} - \frac{1}{2}\left(\sum_{p=1}^{N_{\mathrm{II}}/2}\sum_{q=N_{\mathrm{II}}/2+1}^{N_\Omega} + \sum_{N_{\mathrm{II}}/2+1}^{N_\Omega}\sum_{q=1}^{N_{\mathrm{II}}/2}\right)' \Phi_q\Phi_p K_{pq} - \frac{1}{4}\sum_{p,q=N_{\mathrm{II}}/2+1}^{N_\Omega} K_{pq}, \quad (2.43)$$

con la contribución dinámica interpar dada por

$$E_{\mathrm{dyn}}^{\mathrm{inter}} = \sum_{p,q=1}^{N_{\mathrm{bf}}}{}' \left[n_q^{\mathrm{d}} n_p^{\mathrm{d}} + \Pi(n_q^{\mathrm{d}}, n_p^{\mathrm{d}})\right](1 - \delta_{q\Omega_{\mathrm{II}}^{\mathrm{b}}}\delta_{p\Omega_{\mathrm{II}}^{\mathrm{b}}})K_{pq}, \quad (2.44)$$

donde el apóstrofe significa que se omiten las contribuciones donde p y q pertenecen al mismo subespacio. De esta forma, se obtiene la expresión de energía

$$E_{\mathrm{GNOF}} = E^{\mathrm{intra}} + E_{\mathrm{HF}}^{\mathrm{inter}} + E_{\mathrm{sta}}^{\mathrm{inter}} + E_{\mathrm{dyn}}^{\mathrm{inter}}. \quad (2.45)$$

2.4 Diagnóstico de correlación electrónica

El método de Hartree-Fock aproxima la función de onda como un determinante de Slater y considera el movimiento de un electrón en el campo promedio ejercido por los demás electrones. La diferencia entre esta energía aproximada y la energía exacta del sistema da lugar a la correlación electrónica y aunque representa una fracción pequeña de la energía total del sistema, esta resulta crucial para obtener predicciones químicas acertadas. Suele ser conveniente dividir la correlación electrónica en dos tipos, en correlación dinámica, originada por las interacciones entre los electrones que Hartree-Fock no describe adecuadamente cuando considera el campo promedio, así como en correlación estática, proveniente de aproximar a la función de onda de forma monoconfiguracional. Desde el punto de vista de los métodos basados en función de onda, se suele considerar que métodos como MP2, CCSD y CISD, que utilizan un solo determinante de Slater como referencia para construir a la función de onda, recuperan principalmente correlación dinámica. A estos métodos se les denomina de referencia simple, mientras que para recuperar la correlación estática se requieren métodos con una función de onda con más de un determinante de Slater como referencia, por ejemplo CASPT2, a los que se les conoce como métodos multirreferenciales.

Cuando la correlación dinámica resulta dominante se dice que el sistema es débilmente correlacionado, mientras que cuando la correlación estática es la dominante se dice que el sistema es fuertemente correlacionado. El problema reside en que recuperar la correlación estática mediante los métodos multiconfiguracionales comunes suele ser costoso y complejo, por lo que estos no son usados de forma rutinaria, pero no considerarla da malas predicciones para los sistemas fuertemente correlacionados. Es por esto que bajo el esquema de trabajo habitual resulta deseable poder identificar la correlación electrónica dominante en un sistema para saber si podemos usar un método de referencia sencilla de forma confiable, o si, por el contrario, resulta importante usar un método multirreferencial. Sin embargo, la estructura molecular no suele ser suficiente para determinar directamente cuál es el tipo de correlación dominante en el sistema, por lo que se recurre al uso de varios diagnósticos de correlación,[72] algunos de los cuales se muestran en la Tabla 2.2.

Tab. 2.2: Diagnósticos comunes del tipo de correlación electrónica predominante.

Diagnóstico	Criterio para Correlación Estática	Tipo de Cálculo	Referencia
C_0	1-$C_0^2 \geq 0.05$	CISD	[73]
T1	T1 ≥ 0.02	CCSD	[74]
D1	D1 ≥ 0.05	CCSD y MP2	[75]
D2	D2 ≥ 0.18	CCSD y MP1	[76]
FOD	$N^{FOD} \geq 0.2$	DFT	[77, 78]
TAE	%TAE(T) $\geq 10\,\%$	CCSD(T)	[79]
M	M ≥ 0.1	CASSCF	[80]

Dado que la correlación estática se recupera utilizando funciones de onda con una gran cantidad de determinantes, entonces su importancia puede cuantificarse al evaluar el peso del determinante de Hartree-Fock en la combinación lineal de determinantes. Si el peso de este determinante es suficientemente grande como para despreciar a los demás, entonces el sistema será débilmente correlacionado, pero si no, entonces se requerirán los otros determinantes para describir adecuadamente al sistema. Siendo C_0 el coeficiente que acompaña al determinante de Hartree-Fock en la combinación lineal, se considera que si el determinante de Hartree-Fock representa menos del $95\,\%$ de la función de onda, es decir, $C_0^2 \leq 0.95$, entonces el sistema es fuertemente correlacionado; alternativamente también se puede usar el criterio equivalente $1 - C_0^2 \leq 0.05$. El problema de este criterio es que el método de interacción de configuraciones es costoso, por lo que suele usarse con CISD, en cuyo caso los orbitales moleculares favorecen al determinante de Hartree-Fock, dando falsos negativos a sistemas fuertemente correlacionados. Alternativamente, se han propuesto los diagnósticos T_1, D_1 y D_2 basados en las amplitudes de los respectivos operadores en CCSD, con mejores resultados.[74-76] Sin embargo, estudios más recientes han mostrado que estos pueden tener ciertas inconsistencias al predecir el efecto energético de

pasar de CCSD a órdenes superiores de cúmulos acoplados que recuperan correlación estática.[f] En este sentido se ha propuesto usar la diferencia porcentual entre la energía de atomización total predicha por CCSD y por CCSD(T) como una medida de la correlación estática, dando lugar al diagnóstico $\%\mathrm{TAE}$.[79] Este criterio es conveniente porque da información directa sobre la confiabilidad de un método de referencia única, sin embargo, CCSD(T) puede resultar costoso. Debido a esto, se han propuesto versiones del diagnóstico $\%\mathrm{TAE}$ basadas en DFT,[72] así como otros métodos como las densidades de ocupaciones fraccionarias (FOD, por sus siglas en inglés).[77,78]

Finalmente, los números de ocupación proporcionados por la 1RDM también son un buen indicador de correlación estática conforme estos se alejan de los valores de cero y uno. Se ha propuesto un diagnóstico M en el contexto de la 1RDM de CASSCF que resume los números de ocupación en un solo número y se considera que un diagnóstico M mayor a 0.1 es indicador de correlación estática.[80] En particular, el diagnóstico $\%\mathrm{TAE}$ y el diagnóstico-M son importantes para el desarrollo de este trabajo y como se verá más adelante, el diagnóstico-M se adaptó conforme a los números de ocupación de PNOF. Por último, es importante destacar que estas definiciones son una buena guía para predecir el comportamiento de un método ante diversos tipos de moléculas, pero al final es importante recalcar que la división de la correlación es ficticia y solo se realiza por conveniencia. Al final, existe una sola correlación electrónica.

[f] En general se considera que CCSD solo recupera correlación dinámica y que ir a órdenes superiores empieza a introducir correlación estática.

3 Objetivos

3.1 Objetivo generales

Generar una implementación que permita aprovechar los funcionales de orbitales naturales como un método basado en la RDM para estudiar sistemas químicos fuertemente correlacionados.

3.2 Objetivos particulares

- Reducir el escalamiento aritmético y de memoria de los funcionales de orbitales naturales mediante el uso de la aproximación de resolución de la identidad.
- Mejorar el proceso de convergencia de la optimización de los orbitales naturales y sus números de ocupación.
- Establecer el desempeño de los funcionales en sistemas cargados fuertemente correlacionados.
- Aprovechar la nueva implementación para estudiar un sistema químico fuertemente correlacionado de interés cuyo análisis resulte desafiante.

4 Implementación

En este capítulo se presenta la implementación para la determinación de los NOFs, la cual se centra en optimizar la energía respecto a los orbitales naturales y respecto a los números de ocupación. Esto se puede realizar de forma separada como se muestra en la Figura 4.1, donde se parte de un conjunto de orbitales y números de ocupación de inicio (*guess*) y se entra a un ciclo iterativo donde se optimizan los orbitales naturales manteniendo fijos los números de ocupación (iteraciones externas), para posteriormente optimizar los números de ocupación manteniendo fijos los orbitales naturales (iteraciones internas) y repetir el proceso. La optimización también puede realizarse de forma simultánea, como se verá más adelante.

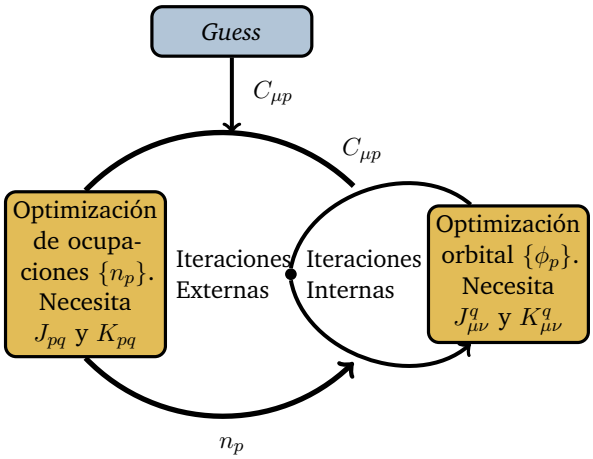

Fig. 4.1: Algoritmo para la optimización de los orbitales naturales ϕ_p y de los números de ocupaciones n_p. Se parte de un conjunto inicial de $\{\phi_p, n_p\}$ y se realiza la optimización de formada separada, es decir, se optimizan los orbitales manteniendo los números de ocupación fijos y luego se optimizan los números de ocupación manteniendo los orbitales fijos. Se muestran también las integrales necesarias para el algoritmo, las cuales se describirán más adelante.

Primero se presenta el proceso de optimización de números de ocupaciones mediante gradientes y de optimización orbital por multiplicadores de Lagrange mediante el algoritmo de diagonalización iterativa (ID, por sus siglas en inglés) que ha sido reportado en la Ref. [81] y que ha sido utilizado por largo tiempo en el contexto de los funcionales PNOF, por ejemplo en el software DoNOF.[82] Posteriormente, se presentan los gradientes para optimizar la energía por rotaciones orbitales desarrollada en este trabajo, seguido de un análisis de como usar la aproximación de la resolución de la identidad para reducir el escalamiento de los algoritmos. Finalmente, se compara el desempeño de los algoritmos utilizando los códigos PyNOF y DoNOF.jl.

4.1 Optimización de números de ocupación

Para fines de implementación, conviene escribir la energía como[a]

$$E = 2\sum_p n_p H_{pp} + \sum_p n_p J_{pp} + \sum_{pq} C^{\mathrm{J}}_{pq} J_{pq} + \sum_{pq} C^{\mathrm{K}}_{pq} K_{pq}, \tag{4.1}$$

donde C^{J}_{pq} y C^{K}_{pq} son funciones de los números de ocupación que acompañan a las integrales de Coulomb J_{pq} e intercambio K_{pq} respectivamente y su expresión da lugar a los diferentes funcionales PNOF.

La optimización de números de ocupación, n, se realiza mediante las variables auxiliares, γ. Para un subespacio Ω_g que pertenece a Ω_{II}, su orbital fuertemente doble ocupado tendrá una ocupación dada por

$$n_g = \frac{1}{2}\left(1 + \cos^2\gamma_g\right), \quad g = 1, \cdots, N_{\mathrm{II}}/2, \tag{4.2}$$

con un hueco asociado dado por $h_g = 1 - n_g$, mientras que habrá N_g orbitales acoplados débilmente doble ocupados con ocupaciones dadas por

$$\begin{aligned}
n_{p_1} &= h_g \,\mathrm{sen}^2\,\gamma_{p_1}, && (4.3)\\
n_{p_2} &= h_g \cos^2\gamma_{p_1}\,\mathrm{sen}^2\,\gamma_{p_2}, && (4.4)\\
&\vdots \\
n_{p_i} &= h_g \cos^2\gamma_{p_1}\cos^2\gamma_{p_2}\cdots\cos^2\gamma_{p_{i-1}}\,\mathrm{sen}^2\,\gamma_{p_i}, && (4.5)\\
&\vdots \\
n_{p_{N_g-1}} &= h_g \cos^2\gamma_{p_1}\cos^2\gamma_{p_2}\cdots\cos^2\gamma_{p_{N_g-2}}\,\mathrm{sen}^2\,\gamma_{p_{N_g-1}}, && (4.6)\\
n_{p_{N_g}} &= h_g \cos^2\gamma_{p_1}\cos^2\gamma_{p_2}\cdots\cos^2\gamma_{p_{N_g-2}}\cos^2\gamma_{p_{N_g-1}}. && (4.7)
\end{aligned}$$

Para un orbital de un subespacio Ω_g que pertenece a Ω_{I}, se tiene

$$n_g = \frac{1}{2}, g = N_{\mathrm{II}}/2 + 1, \cdots, N_\Omega \tag{4.8}$$

La ecuación (4.2) restringe la ocupación del orbital fuertemente doble ocupado a $0.5 \leq n_g \leq 1.0$, mientras que las ecuaciones (4.3)-(4.7) restringen las ocupaciones de los orbitales débilmente ocupados a $0.0 \leq n_g \leq 0.5$, cumpliendo así con el esquema de emparejamiento orbital dado en la Figura 2.1. Las ecuaciones mostradas permiten reemplazar la minimización respecto a $\mathbf{n}$ por una minimización respecto al vector $\boldsymbol{\gamma}$. Esto resulta ventajoso, ya que la minimización directa de la

[a]Esta es una forma conveniente de representar las ecuaciones (2.40), (2.42) y (2.45), resaltando las integrales involucradas.

energía respecto a los números de ocupación requiere de una optimización con restricciones para limitar los números de ocupación a valores entre cero y uno para garantizar que sumen el número total de electrones; sin embargo, la optimización de la energía respecto a γ vuelve al problema una minimización sin restricciones, ya que el cuadrado de senos y cosenos acota naturalmente las ocupaciones a valores entre cero y uno, mientras que la relación trigonométrica pitagórica[b] asegura que todos los números de ocupación por subespacio sumados den uno y sumando todos los subespacios den el número total de electrones, N, cumpliendo así la N-representabilidad de la 1RDM.

La minimización de la energía respecto a los elementos del vector $\boldsymbol{\gamma}$ se puede realizar mediante la regla de la cadena

$$\frac{\partial E}{\partial \gamma_r} = 2\sum_p \frac{\partial n_p}{\partial \gamma_r} H_{pp} + 2\sum_p \frac{\partial n_p}{\partial \gamma_r} J_{pp} + \sum_{pq} \frac{\partial C^{\mathrm{J}}_{pq}}{\partial n_p}\frac{\partial n_p}{\partial \gamma_r} J_{pq} + \sum_{pq} \frac{\partial C^{\mathrm{K}}_{pq}}{\partial n_p}\frac{\partial n_p}{\partial \gamma_r} K_{pq}, \tag{4.9}$$

donde las derivadas $\frac{\partial C^{\mathrm{J}}_{pq}}{\partial n_p}$ y $\frac{\partial C^{\mathrm{K}}_{pq}}{\partial n_p}$ dependen de la expresión del funcional, pero el escalamiento de su evaluación no es un cuello de botella. Por otra parte, las derivadas de los números de ocupación respecto a los elementos de $\boldsymbol{\gamma}$ se realizan por casos. Si el número de ocupación corresponde a un orbital fuertemente doble ocupado del subespacio Ω_g, entonces de la ecuación (4.2) se ve que su derivada solo es distinta de cero si se toma respecto a γ_g y es

$$\frac{\partial n_g}{\partial \gamma_g} = -\frac{1}{2}\operatorname{sen}(2\gamma_g). \tag{4.10}$$

Si el número de ocupación corresponde al orbital débilmente ocupado n_{p_i} del subespacio Ω_g, entonces de la ecuación (4.5) se ve que su derivada puede ser distinta de cero en tres casos, i) al derivar respecto a γ_g, ii) al derivar respecto a γ_{p_j} con $j < i$ y iii) al derivar respecto a γ_{p_i} con $(i \neq N_g)$. Entonces hay que tomar tres derivadas

$$\frac{\partial n_{p_i}}{\partial \gamma_g} = -\frac{\partial n_g}{\partial \gamma_g}\cos^2\gamma_{p_1}\cdots\cos^2\gamma_{p_{i-1}},\operatorname{sen}^2\gamma_{p_i},\ \ p_i \in \Omega_g, \tag{4.11}$$

$$\frac{\partial n_{p_i}}{\partial \gamma_{p_j}} = -h_g\cos^2\gamma_{p_1}\cdots\operatorname{sen}2\gamma_{p_j}\cdots\cos^2\gamma_{p_{i-1}}\operatorname{sen}^2\gamma_{p_i},\ \ j < i, \tag{4.12}$$

$$\frac{\partial n_{p_i}}{\partial \gamma_{p_i}} = h_g\cos^2\gamma_{p_1}\cdots\cos^2\gamma_{p_{i-1}}\operatorname{sen}2\gamma_{p_i},\ \ i \neq N_g. \tag{4.13}$$

De la ecuación (4.1) que proporciona la energía y la ecuación (4.9) que proporciona el cambio de energía respecto a las variables γ_r se ve que se necesitan las integrales H_{pp}, J_{pq} y K_{pq}. La construcción de estas integrales requiere de una transformación de orbital atómico a un orbital

[b] Relación trigonométrica pitagórica: $\operatorname{sen}^2 x + \cos^2 x = 1$.

molecular con un escalamiento aritmético de quinto orden respecto al número de funciones de base, representando el paso más demandante de la optimización de ocupaciones. Sin embargo, como los números de ocupación se optimizan a orbital fijo, las integrales solo deben de evaluarse una vez y se pueden reutilizar durante el proceso de optimización.

4.2 Optimización orbital

Los orbitales ϕ se construyen como una combinación lineal de funciones de base $\mu(\mathbf{r})$

$$\phi_p(\mathbf{r}) = \sum_{\mu} C_{\mu p}\mu(\mathbf{r}), \tag{4.14}$$

siendo C la matriz cuya p-ésima columna contienen los coeficientes para construir el orbital natural $\phi_p(\mathbf{r})$ a partir de las funciones de base $\mu(\mathbf{r})$. La optimización orbital busca minimizar la energía variando los orbitales sujetos a la ortonormalidad, es decir,

$$\langle p, q\rangle = \delta_{pq}. \tag{4.15}$$

La matriz C correspondiente a cada paso del proceso de optimización puede construirse a partir de una matriz de orbitales de referencia C_0 que suelen ser los de la iteración anterior mediante

$$\mathbf{C} = \mathbf{C}_0\mathbf{U}, \tag{4.16}$$

donde $\mathbf{U}$ es una matriz unitaria que nos permite preservar la ortonormalidad, analizaremos como construir esta matriz en las siguientes subsecciones.

4.2.1 Diagonalización iterativa

La optimización de la energía sujeta a la ortonormalidad de los orbitales puede realizarse mediante el método de multiplicadores de Lagrange, para lo que se propone la función auxiliar Ω

$$\Omega = E - 2\sum_{pq} \kappa_{pq}\left(\langle p, q\rangle - \delta_{pq}\right), \tag{4.17}$$

donde κ_{pq} son los multiplicadores de Lagrange. Volviendo estacionaria la variable auxiliar respecto a la variación de Ω se obtiene

$$\delta\Omega = \sum_{p}\int d\mathbf{r}\delta\phi_p(\mathbf{r})\left[\frac{\delta E}{\delta\phi_p(\mathbf{r})} - 4\sum_{q}\kappa_{qp}\phi_q(\mathbf{r})\right] = 0, \tag{4.18}$$

lo que relaciona a los multiplicadores de Lagrange con el cambio en la energía dado por la variación orbital

$$\frac{\delta E}{\delta \phi_p(\mathbf{r})} = 4 n_p \hat{H} \phi_p(\mathbf{r}) + \frac{\delta V_{ee}}{\delta \phi_p(\mathbf{r})} = 4 \sum_q \kappa_{qp} \phi_q(\mathbf{r}). \tag{4.19}$$

Multiplicando por $\phi_q(\mathbf{r})$ e integrando

$$\kappa_{qp} = n_p H_{qp} + g_{pq}, \tag{4.20}$$

con $g_{pq} = \int d\mathbf{r} \frac{\delta V_{ee}}{\delta \phi_p(\mathbf{r})} \phi_q(\mathbf{r})$. Debe recalcarse que dado que se usó un orbital general, la dimensión del índice q corresponde al número de funciones de base, N_{bf}, mientras que la del índice p corresponde al número de orbitales, N_{orb}. Los elementos de g_{pq} contienen información sobre cómo se modifican las integrales de Coulomb e intercambio. Con esto, la expresión de los multiplicadores de Lagrange es

$$\kappa_{qp} = n_p H_{qp} + \sum_{\mu\nu} C_{\mu q} n_p J^p_{\mu\nu} C_{\nu p} + \sum_{\mu\nu} \sum_r C_{\mu q} C^{\mathrm{J}}_{qr} J^r_{\mu\nu} C_{\nu p} - \sum_{\mu\nu} \sum_r C_{\mu q} C^{\mathrm{K}}_{qr} K^r_{\mu\nu} C_{\mu p}, \tag{4.21}$$

donde $J^p_{\mu\nu}$ y $K^p_{\mu\nu}$ son matrices de Coulomb e intercambio en orbital atómico para el orbital molecular p. La expresión de κ_{qp} también puede reformularse como

$$\kappa_{qp} = n_p H_{qp} + n_p (pp|pq) + C^{\mathrm{J}}_{pr} (rr|qp) - C^{\mathrm{K}}_{pr} (qr|pr). \tag{4.22}$$

La matriz de multiplicadores de Lagrange debe de ser simétrica en el extremo, lo que permite proponer la función,

$$F_{qp} = \begin{cases} \kappa_{qp} - \kappa_{pq}, & p > q \\ \kappa_{pq} - \kappa_{qp}, & p < q \end{cases}, \tag{4.23}$$

esta matriz puede descomponerse en sus valores $\mathbf{v}$ y vectores propios $\mathbf{U}$

$$\mathbf{F} = \mathbf{U} \mathbf{v} \mathbf{U}^T, \tag{4.24}$$

donde $\mathbf{v}$ es una matriz diagonal. De esta forma, el proceso de optimización orbital está impulsado por la transformación que diagonalice la matriz $\mathbf{F}$, lo que por la ecuación 4.23 implica volver simétrica la matriz de multiplicadores de Lagrange. Un detalle de la definición de $\mathbf{F}$ dada en la ecuación (4.23) es que la simetría de los multiplicadores no proporciona un criterio para construir los elementos diagonales F_{pp}. En el algoritmo de ID, se proponen elementos diagonales iniciales y en cada iteración se usa la diagonal de la iteración anterior como entrada para la nueva matriz. Además, se pueden utilizar métodos como la inversión directa en el espacio iterativo (DIIS, por sus siglas en inglés),[83] así como escalamiento en la matriz $\mathbf{F}$. Cuando se ha alcanzado la convergencia,

la matriz de multiplicadores de Lagrange se vuelve simétrica y por la ecuación (4.23), la matriz $\mathbf{F}$ se vuelve diagonal, razón por la que este algoritmo se denomina diagonalización iterativa. Cabe mencionar que la evaluación de la matriz de multiplicadores de Lagrange mediante la ecuación (4.21) puede realizarse separando las sumas con un escalamiento de cuarto orden. Sin embargo, la evaluación de $J^r_{\mu\nu}$ y $K^r_{\mu\nu}$ tiene un escalamiento de quinto orden, lo que determina el costo del algoritmo.

4.2.2 Rotaciones orbitales

La matriz ortogonal $\mathbf{U}$ también puede parametrizarse a partir de la función exponencial dada por[84-86]

$$\mathbf{U} = e^{\mathbf{Y}}, \tag{4.25}$$

con $\mathbf{Y}$ una matriz antisimétrica tal que $y_{ab} = -y_{ba}$. De esta forma, un orbital puede expresarse como una combinación de los orbitales de referencia como

$$\phi_p = \sum_r U_{rp}\phi^0_r. \tag{4.26}$$

La derivada de un orbital respecto a un elemento de la matriz $\mathbf{Y}$ está dada por

$$\frac{\partial \phi_p}{\partial y_{ab}}\Big|_{y=0} = \delta_{bp}\phi_a - \delta_{ap}\phi_b. \tag{4.27}$$

Derivando la expresión de energía dada por la ecuación (4.1) respecto a y_{ab} obtenemos la expresión del gradiente para un funcional JKL como PNOF, dada por

$$\begin{aligned}\frac{\partial E}{\partial y_{ab}}\Big|_{y=0} &= 4\left(n_b H_{ab} - n_a H_{ba}\right) + 4\left(n_b(ab|bb) - n_a(ba|aa)\right) \\ &\quad + 4\sum_q \left(C^{\mathrm{J}}_{bq}(ab|qq) - C^{\mathrm{J}}_{aq}(ba|qq)\right) + 4\sum_q \left(C^{\mathrm{K}}_{bq}(aq|bq) - C^{\mathrm{K}}_{aq}(bq|aq)\right).\end{aligned} \tag{4.28}$$

Este tipo de optimización se ha utilizado antes en métodos multiconfiguracionales,[87] en DFT,[88] y en otros métodos de orbitales naturales.[89] En la práctica conviene ordenar los elementos de la parte triangular superior de $\mathbf{Y}$ en un vector a optimizar.

Por comparación de $\frac{\partial E}{\partial y_{ab}}$ dado por la ecuación (4.28) y de los multiplicadores de Lagrange κ_{ab} dados por la ecuación (4.21), resulta bastante interesante hacer notar la relación

$$\frac{\partial E}{\partial y_{ab}} = \kappa_{ab} - \kappa_{ba} = F_{ab}, \tag{4.29}$$

que justo es la definición de la $\mathbf{F}$ dada en la ecuación (4.23) que se usa en el método de diagonalización iterativa. En otras palabras, el método de ID y el método de rotaciones orbitales están relacionados. La ID está impulsada por aumentar la simetría de la matriz de multiplicadores de Lagrange y es compatible con DIIS, mientras que en el proceso esto reduce el gradiente y dirige la función hacia un extremo. Sin embargo, esto no garantiza que la energía disminuya una iteración tras otra. Por otra parte, el método de rotaciones proporciona un gradiente, lo que permite usar métodos como descenso del gradiente, gradiente conjugado (CG, por sus siglas en inglés),[90] y Broyden-Fletcher-Goldfarb-Shanno (BFGS, por sus siglas en inglés)[91-94] que han sido diseñados para minimizar la energía una iteración tras otra, lo que a su vez vuelve simétrica a la matriz de multiplicadores de Lagrange. Una diferencia entre ambos métodos es que como y_{ab} es antisimétrica, entonces su diagonal siempre es cero, por lo que los elementos diagonales y_{aa} no forman parte de los elementos a optimizar, como ocurre en ID con F_{pp} para cuyos valores no se tiene una expresión definida y se toman de la iteración anterior.

4.3 Optimización combinada

Hasta ahora se ha considerado la optimización de los números de ocupación y de los orbitales naturales de forma separada, sin embargo, estos pueden optimizarse de forma conjunta. Para ver esto, resulta conveniente considerar a la energía como una función de los parámetros del vector $\boldsymbol{\gamma}$ de la optimización de números de ocupación y de los parámetros del vector y de la optimización orbital. Todos los parámetros pueden agruparse en un solo vector $\mathbf{x}$, es decir,

$$\{\mathbf{x}\} = \{\boldsymbol{\gamma}\} + \{\mathbf{y}\}\,, \tag{4.30}$$

esto ocasiona que la energía sea una función especificada completamente dependiente de los parámetros que forman el vector x. De esta manera, el gradiente de la energía respecto a estos parámetros es simplemente la unión de los gradientes de la optimización orbital y de ocupaciones

$$\left\{\frac{\mathrm{d}E}{\mathrm{d}\mathbf{x}}\right\} = \left\{\frac{\mathrm{d}E}{\mathrm{d}\boldsymbol{\gamma}}\right\} + \left\{\frac{\mathrm{d}E}{\mathrm{d}\mathbf{y}}\right\}. \tag{4.31}$$

Las derivadas de la energía respecto a los elementos del vector $\mathbf{x}$ pueden usarse nuevamente en métodos como CG[90] y BFGS[91-94] para seguir una ruta de minimización que considere el acoplamiento entre la variación de números de ocupación y orbitales naturales. Es de esperar que esta ruta minimice la energía en una menor cantidad de iteraciones, pero también debe de tenerse en cuenta que cada iteración es más costosa porque la dimensión de los parámetros a optimizar es mayor.

4.4 Análisis de escalamiento

El costo de realizar la minimización del funcional de energía está dominado por la construcción de integrales. Considerando un algoritmo de tipo *incore* en el que las integrales monoelectrónicas y bielectrónicas se evalúen una vez y se guarden en memoria, entonces la parte más demandante del algoritmo se encuentra en la transformación de las integrales bielectrónicas de orbitales atómicos (OA) a orbitales naturales (ON). Las integrales necesarias son:

- J_{pq} y K_{pq} para calcular la energía y su gradiente en la optimización de números de ocupación según las ecuaciones (4.1) y (4.9).

- $J^q_{\mu\nu}$ y $K^q_{\mu\nu}$ para calcular los multiplicadores de Lagrange en la optimización de orbitales naturales según la ecuación (4.21).

- $(pp|pq)$, $(rr|pq)$ y $(rp|rq)$ pueden usarse en un algoritmo alternativo a la opción anterior según la ecuación (4.22).

La Tabla 4.1 presenta el costo computacional de calcular las integrales necesarias para realizar la optimización orbital que requiere de $J^p_{\mu\nu}$ y $K^p_{\mu\nu}$ según la ecuación (4.21) y para realizar la optimización de ocupaciones que requiere de J_{pq} y K_{pq} según las ecuaciones (4.1) y (4.9). Como referencia, se vuelve a mencionar que el número de funciones de base se representa con el símbolo N_{bf} y el número de orbitales naturales con N_{orb}, recordando que en general $N_{\mathrm{orb}} \leq N_{\mathrm{bf}}$. El paso cero consiste en la evaluación de las integrales bielectrónicas $(\mu\nu|\sigma\lambda)$ en la base de orbital atómico, con un escalamiento tanto aritmético y de memoria de cuarto orden respecto al número de funciones de base. Este paso determina la demanda de memoria, pero no representa un cuello de botella aritmético, además, se hace una sola vez al inicio del cálculo. El siguiente paso, también común a ambas integrales, consiste en construir una matriz de densidad por cada orbital natural p,

$$P^p_{\mu\nu} = C_{\mu p} C_{\nu p}, \tag{4.32}$$

lo cual tiene un escalamiento aritmético de tercer orden dado por $N^2_{\mathrm{bf}} N_{\mathrm{orb}}$. Posteriormente, esta matriz se usa para construir las matrices de Coulomb e intercambio por orbital natural,

$$J^q_{\mu\nu} = \sum_{\sigma\lambda} P^q_{\sigma\lambda} (\mu\nu|\sigma\lambda), \tag{4.33}$$

$$K^q_{\mu\sigma} = \sum_{\nu\lambda} P^q_{\nu\lambda} (\mu\nu|\sigma\lambda). \tag{4.34}$$

La transformación a $J^q_{\mu\nu}$ y $K^q_{\mu\nu}$ tiene un escalamiento aritmético de quinto orden, $N_{\mathrm{orb}} N^4_{\mathrm{bf}}$, siendo esta la parte más demandante del algoritmo. Una vez calculadas las matrices de intercambio y

de Coulomb por orbital natural, se procede a construir los multiplicadores de Lagrange para la optimización orbital. En el caso de la optimización de los números de ocupación, las matrices $J^q_{\mu\nu}$ y $K^q_{\mu\nu}$ se continúan contrayendo para generar

$$J_{pq} = \sum_{\mu\nu} P^p_{\mu\nu} J^q_{\mu\nu}, \tag{4.35}$$

$$K_{pq} = \sum_{\mu\sigma} P^p_{\mu\sigma} K^q_{\mu\sigma}, \tag{4.36}$$

ambos pasos con un escalamiento aritmético de cuarto orden y de memoria de segundo orden. Ambas matrices se emplean en la optimización de los números de ocupación, sin embargo, como J_{pq} y K_{pq} dependen de $J^q_{\mu\nu}$ y $K^q_{\mu\nu}$, el escalamiento global de la optimización de números de ocupación también es de quinto orden.

Tab. 4.1: Algoritmo utilizado para calcular $\mathbf{J}^q$ y $\mathbf{K}^q$ necesarios durante la optimización de los orbitales naturales según la ecuación (4.21), así como $\mathbf{J}$ y $\mathbf{K}$ necesarias para la optimización de números de ocupación según las ecuaciones (4.1) y (4.9). N_{bf} corresponde al número de funciones de base y N_{orb} al número de orbitales.

Tipo de Integral	Paso	Operación	Escalamiento	
			Memoria	Aritmético
Común	0	Evaluación de $(\mu\nu\|\sigma\lambda)$	N^4_{bf}	N^4_{bf}
	1	$P^p_{\mu\nu} = C_{\mu p} C_{\nu p}$	$N^2_{\mathrm{bf}} N_{\mathrm{orb}}$	$N^2_{\mathrm{bf}} N_{\mathrm{orb}}$
Coulomb	2	$J^q_{\mu\nu} = \sum_{\sigma\lambda} P^q_{\sigma\lambda} (\mu\nu\|\sigma\lambda)$	$N^2_{\mathrm{bf}} N_{\mathrm{orb}}$	$N^4_{\mathrm{bf}} N_{\mathrm{orb}}$
	3	$J_{pq} = \sum_{\mu\nu} P^p_{\mu\nu} J^q_{\mu\nu}$	N^2_{orb}	$N^2_{\mathrm{bf}} N^2_{\mathrm{orb}}$
Intercambio	2	$K^q_{\mu\sigma} = \sum_{\nu\lambda} P^q_{\nu\lambda} (\mu\nu\|\sigma\lambda)$	$N^2_{\mathrm{bf}} N_{\mathrm{orb}}$	$N^4_{\mathrm{bf}} N_{\mathrm{orb}}$
	3	$K_{pq} = \sum_{\mu\sigma} P^p_{\mu\sigma} K^q_{\mu\sigma}$	N^2_{orb}	$N^2_{\mathrm{bf}} N^2_{\mathrm{orb}}$

La construcción de los multiplicadores de Lagrange con $J^q_{\mu\nu}$ y $K^q_{\mu\nu}$ acorde a la ecuación (4.21) tiene como ventaja que se conserva la noción de matrices de Coulomb e intercambio en orbital atómico, similar a como se haría en otros métodos como Hartree-Fock. El uso de la ecuación (4.22) proporciona un procedimiento alternativo como se muestra en la Tabla 4.2, donde la primera columna identifica el coeficiente con el que se multiplica la integral. Se necesitan tres tipos de integrales bielectrónicas que se pueden identificar acorde a los coeficientes que las acompañan:

- La que proviene del término de los elementos diagonales de la matriz de Coulomb con coeficientes n_p, que requiere las integrales $(pp|pq)$.

- La que proviene de la matriz de Coulomb con coeficientes C^{J}, que requiere las integrales $(rr|qp)$.

- La que proviene de la matriz de intercambio con coeficientes C^{K}, que requiere las integrales $(qr|pr)$.

Sin embargo, en todos los casos sigue habiendo algún paso con escalamiento de quinto orden.

Tab. 4.2: Algoritmo utilizado para calcular las integrales necesarias para construir los multiplicadores de Lagrange durante la optimización orbital acorde a la ecuación (4.22). N_{bf} corresponde al número de funciones de base y N_{orb} al número de orbitales.

Coeficiente a Multiplicar	Paso	Operación	Escalamiento	
			Memoria	Aritmético
Común	0	Evaluación de $(\mu\nu\|\sigma\lambda)$	N_{bf}^4	N_{bf}^4
n_p	1	$(pp\|p\lambda) = \sum_p C_{\mu p} C_{\nu p} C_{\sigma p} (\mu\nu\|\sigma\lambda)$	$N_{\mathrm{bf}} N_{\mathrm{orb}}$	$N_{\mathrm{bf}}^4 N_{\mathrm{orb}}$
	2	$(pp\|pq) = \sum_q C_{\lambda q} (pp\|p\lambda)$	$N_{\mathrm{bf}} N_{\mathrm{orb}}$	$N_{\mathrm{bf}}^2 N_{\mathrm{orb}}$
C^{J}	1	$(\mu\nu\|\sigma p) = \sum_\lambda C_{\lambda p} (\mu\nu\|\sigma\lambda)$	$N_{\mathrm{bf}}^3 N_{\mathrm{orb}}$	$N_{\mathrm{bf}}^4 N_{\mathrm{orb}}$
	2	$(rr\|\sigma p) = \sum_{\mu\nu} C_{\mu r} C_{\nu r} (\mu\nu\|\sigma p)$	$N_{\mathrm{bf}} N_{\mathrm{orb}}^2$	$N_{\mathrm{bf}}^3 N_{\mathrm{orb}}^2$
	3	$(rr\|qp) = \sum_\sigma C_{\sigma q} (rr\|\sigma p)$	$N_{\mathrm{bf}} N_{\mathrm{orb}}^2$	$N_{\mathrm{bf}}^2 N_{\mathrm{orb}}^2$
C^{K}	1	$(\mu\nu\|p\lambda) = \sum_\sigma C_{\sigma p} (\mu\nu\|\sigma\lambda)$	$N_{\mathrm{bf}}^3 N_{\mathrm{orb}}$	$N_{\mathrm{bf}}^4 N_{\mathrm{orb}}$
	2	$(\mu r\|pr) = \sum_{\nu\lambda} C_{\nu r} C_{\lambda r} (\mu\nu\|p\lambda)$	$N_{\mathrm{bf}} N_{\mathrm{orb}}^2$	$N_{\mathrm{bf}}^3 N_{\mathrm{orb}}^2$
	3	$(qr\|pr) = \sum_\mu C_{\mu q} (\mu r\|pr)$	$N_{\mathrm{bf}} N_{\mathrm{orb}}^2$	$N_{\mathrm{bf}}^2 N_{\mathrm{orb}}^2$

Un punto clave a destacar es que en la optimización de números de ocupación se mantienen fijos los orbitales, por lo que la transformación solo se necesita hacer una vez por iteración externa; en contraste, la transformación tiene que llevarse a cabo en cada iteración interna de la optimización orbital porque los orbitales cambian con cada iteración. Es por esta razón que la optimización orbital representa el mayor tiempo de cómputo de la evaluación de los NOF.

4.5 Resolución de la identidad

El escalamiento aritmético y de memoria puede reducirse mediante la aproximación de resolución de la identidad (RI, por sus siglas en inglés). Esta consiste en aproximar las integrales bielectrónicas de cuatro centros a partir de integrales bielectrónicas de tres y dos centros, mediante

$$\begin{aligned}(\mu\nu|\sigma\lambda) &= \sum_k (\mu\nu|k) \sum_l G_{kl}^{-1} (l|\sigma\lambda) \\ &= \sum_k (\mu\nu|k) \sum_l G_{kl}^{-1/2} \sum_m G_{lm}^{-1/2} (m|\sigma\lambda),\end{aligned} \tag{4.37}$$

con los elementos de la matriz **G** dados por las integrales de repulsión electrónica de dos centros

$$G_{kl} \quad = \quad (k|l), \tag{4.38}$$

y los índices k y l representando las funciones de base auxiliares de dimensión N_{aux}. Al sustituir la aproximación de la resolución de la identidad de la ecuación (4.37) en las ecuaciones (4.33)-(4.34) para los orbitales naturales y en las ecuaciones (4.35)-(4.36) para los números de ocupación, podemos generar ecuaciones más sencillas que llevan a una reducción en el escalamiento aritmético y de memoria.

En el caso de la optimización orbital, los nuevos pasos se resumen en la Tabla 4.3. El paso cero consiste en la evaluación de las integrales bielectrónicas $(\mu\nu|k)$ y $(k|l)$, las cuales en este caso tienen un menor escalamiento de memoria, reduciéndola de cuarto orden (N^4) a tercer orden ($N^2 N_{\text{aux}}$). El siguiente paso consiste en la formación del tensor $\mathbf{b}$ dado por

$$b^l_{\mu\nu} = \sum_k (\mu\nu|k) G^{-1/2}_{kl}, \tag{4.39}$$

este paso tiene un escalamiento aritmético de cuarto orden, dado por $N^2 N^2_{\text{aux}}$, siendo el más alto de todo el procedimiento, sin embargo, se hace una sola vez al inicio del cálculo. Esto es seguido por la transformación de un índice de OA a ON para construir

$$b^l_{q\nu} = \sum_\mu C_{\mu q} b^l_{\mu\nu}, \tag{4.40}$$

con escalamiento aritmético de cuarto orden $N^2_{\text{bf}} N_{\text{orb}} N_{\text{aux}}$, este es el paso más demandante y que se realiza en cada iteración. Los siguientes pasos consisten en otra transformación de b y su uso para generar la matriz de Coulomb en orbital atómico por orbital natural $J^q_{\mu\nu}$

$$b^l_{qq} \quad = \quad \sum_\nu C_{\nu q} b^l_{q\nu}, \tag{4.41}$$

$$J^q_{\mu\nu} \quad = \quad \sum_l b^l_{qq} b^l_{\mu\nu}, \tag{4.42}$$

y de intercambio $K^q_{\mu\nu}$,

$$K^q_{\mu\nu} \quad = \quad \sum_l b^l_{q\mu} b^l_{q\nu}, \tag{4.43}$$

en ambos casos los pasos finales tienen un escalamiento aritmético de cuarto orden, dado por $N^2_{\text{bf}} N_{\text{aux}} N_{\text{orb}}$.

Tab. 4.3: Algoritmo para calcular $\mathbf{J}^q$ y $\mathbf{K}^q$ usando la aproximación de resolución de la identidad para usarse en la optimización orbital. N_{bf} corresponde al número de funciones de base, N_{orb} al número de orbitales y N_{aux} al número de funciones de la base auxiliar.

Tipo de Integral	Paso	Operación	Escalamiento	
			Memoria	Aritmético
Común	0	Evaluación de $(\mu\nu\|k)$	$N_{\mathrm{bf}}^2 N_{\mathrm{aux}}$	$N_{\mathrm{bf}}^2 N_{\mathrm{aux}}$
	1	$b^l_{\mu\nu} = \sum_k (\mu\nu\|k) G^{-1/2}_{kl}$	$N_{\mathrm{bf}}^2 N_{\mathrm{aux}}$	$N_{\mathrm{bf}}^2 N_{\mathrm{aux}}^2$
	2	$b^l_{q\nu} = \sum_\mu C_{\mu q} b^l_{\mu\nu}$	$N_{\mathrm{bf}} N_{\mathrm{aux}} N_{\mathrm{orb}}$	$N_{\mathrm{bf}}^2 N_{\mathrm{aux}} N_{\mathrm{orb}}$
$J^q_{\mu\nu}$	3	$b^l_{qq} = \sum_\nu C_{\nu q} b^l_{q\nu}$	$N_{\mathrm{aux}} N_{\mathrm{orb}}$	$N_{\mathrm{bf}} N_{\mathrm{aux}} N_{\mathrm{orb}}$
	4	$J^q_{\mu\nu} = \sum_l b^l_{qq} b^l_{\mu\nu}$	$N_{\mathrm{bf}}^2 N_{\mathrm{orb}}$	$N_{\mathrm{bf}}^2 N_{\mathrm{aux}} N_{\mathrm{orb}}$
$K^q_{\mu\nu}$	3	$K^q_{\mu\nu} = \sum_l b^l_{q\mu} b^l_{q\nu}$	$N_{\mathrm{bf}}^2 N_{\mathrm{orb}}$	$N_{\mathrm{bf}}^2 N_{\mathrm{aux}} N_{\mathrm{orb}}$

En el caso de los elementos de la optimización de ocupaciones, el esquema de contracción para los elementos de b cambia. Resulta conveniente transformar los índices de b a orbital natural

$$b^l_{p\nu} = \sum_\mu C_{\mu p} b^l_{\mu\nu}, \tag{4.44}$$

$$b^l_{pq} = \sum_\mu C_{\nu q} b^l_{p\nu}, \tag{4.45}$$

estas transformaciones tienen un escalamiento de cuarto orden. Posteriormente, las matrices de Coulomb e intercambio se construyen fácilmente mediante con un escalamiento de tercer orden,

$$J_{pq} = \sum_l b^l_{pp} b^l_{qq}, \tag{4.46}$$

$$K_{pq} = \sum_l b^l_{pq} b^l_{pq}. \tag{4.47}$$

La construcción de los multiplicadores de Lagrange mediante la ecuación (4.22) también se puede beneficiar de la aproximación RI. La Tabla 4.5 muestra el análisis del escalamiento de las integrales involucradas y la primera columna hace referencia al coeficiente que acompaña a la integral. Los primeros pasos comunes consisten en la construcción de b y su contracción a orbital molecular, con un escalamiento de cuarto orden como ya se ha visto. Posteriormente, se construye la integral $(pp|pp)$ que acompaña a n_p mediante

$$(pp|pp) = \sum_l b^l_{pp} b^l_{pp}, \tag{4.48}$$

Tab. 4.4: Algoritmo para calcular las integrales **J** y **K** necesarias para la optimización de números de ocupación con la aproximación de resolución de la identidad. N_{bf} corresponde al número de funciones de base, N_{orb} al número de orbitales y N_{aux} al número de funciones de la base auxiliar.

	Paso	Operación	Escalamiento	
			Memoria	Aritmético
Común	0	Evaluación de $(\mu\nu\|k)$	$N_{\mathrm{bf}}^2 N_{\mathrm{aux}}$	$N_{\mathrm{bf}}^2 N_{\mathrm{aux}}$
	1	$b_{\mu\nu}^l = \sum_k (\mu\nu\|k) G_{kl}^{-1/2}$	$N_{\mathrm{bf}}^2 N_{\mathrm{aux}}$	$N_{\mathrm{bf}}^2 N_{\mathrm{aux}}^2$
	2	$b_{p\nu}^l = \sum_\mu C_{\mu p} b_{\mu\nu}^l$	$N_{\mathrm{bf}} N_{\mathrm{aux}} N_{\mathrm{orb}}$	$N_{\mathrm{bf}}^2 N_{\mathrm{aux}} N_{\mathrm{orb}}$
	3	$b_{pq}^l = \sum_\nu C_{\nu q} b_{p\nu}^l$	$N_{\mathrm{aux}} N_{\mathrm{orb}}^2$	$N_{\mathrm{bf}} N_{\mathrm{aux}} N_{\mathrm{orb}}^2$
J_{pq}	4	$J_{pq} = \sum_l b_{pp}^l b_{qq}^l$	N_{orb}^2	$N_{\mathrm{aux}} N_{\mathrm{orb}}^2$
K_{pq}	4	$K_{pq} = \sum_l b_{pq}^l b_{pq}^l$	N_{orb}^2	$N_{\mathrm{aux}} N_{\mathrm{orb}}^2$

con un escalamiento de segundo orden. La integral $(rr|qp)$ que acompaña a C^{J} se construye mediante

$$(rr|qp) = \sum_l b_{rr}^l b_{qp}^l, \tag{4.49}$$

con un escalamiento de cuarto orden. Finalmente, la integral $(qr|pr)$ que acompaña a C^{K} se construye mediante

$$(qr|pr) = \sum_l b_{qr}^l b_{pr}^l, \tag{4.50}$$

también con un escalamiento de cuarto orden.

Los procedimientos dados en las Tablas 4.3 y 4.5 proporcionan la misma matriz de multiplicadores con escalamiento de cuarto orden. Sin embargo, el último procedimiento introduce pasos con escalamiento de $N_{\mathrm{bf}} N_{\mathrm{aux}} N_{\mathrm{orb}}^2$ en lugar de $N_{\mathrm{bf}}^2 N_{\mathrm{aux}} N_{\mathrm{orb}}$; considerando que $N_{\mathrm{orb}} \leq N_{\mathrm{bf}}$, entonces el segundo procedimiento conduce a un prefactor más pequeño que vuelve más eficiente el proceso de optimización orbital.

4.6 Comparación entre algoritmos: ID, rotaciones y combinado

Tab. 4.5: Algoritmo para calcular las integrales necesarias para construir los multiplicadores de Lagrange durante la optimización orbital acorde a la ecuación (4.22) utilizando la aproximación de resolución de la identidad. N_{bf} corresponde al número de funciones de base, N_{orb} al número de orbitales y N_{aux} al número de funciones de la base auxiliar.

	Paso	Operación	Escalamiento	
			Memoria	Aritmético
Común	0	Evaluación de $(\mu\nu\|k)$	$N_{\mathrm{bf}}^2 N_{\mathrm{aux}}$	$N_{\mathrm{bf}}^2 N_{\mathrm{aux}}$
	1	$b^l_{\mu\nu} = \sum_k (\mu\nu\|k) G^{-1/2}_{kl}$	$N_{\mathrm{bf}}^2 N_{\mathrm{aux}}$	$N_{\mathrm{bf}}^2 N_{\mathrm{aux}}^2$
	2	$b^l_{p\nu} = \sum_\mu C_{\mu p} b^l_{\mu\nu}$	$N_{\mathrm{bf}} N_{\mathrm{aux}} N_{\mathrm{orb}}$	$N_{\mathrm{bf}}^2 N_{\mathrm{aux}} N_{\mathrm{orb}}$
	3	$b^l_{pq} = \sum_\nu C_{\nu q} b^l_{p\nu}$	$N_{\mathrm{bf}} N_{\mathrm{aux}} N_{\mathrm{orb}}$	$N_{\mathrm{bf}}^2 N_{\mathrm{aux}} N_{\mathrm{orb}}$
n_p	4	$(pp\|pq) = \sum_l b^l_{pp} b^l_{pq}$	$N_{\mathrm{bf}} N_{\mathrm{orb}}$	$N_{\mathrm{bf}} N_{\mathrm{aux}} N_{\mathrm{orb}}$
C^{J}	4	$(rr\|qp) = \sum_l b^l_{rr} b^l_{qp}$	$N_{\mathrm{bf}} N_{\mathrm{orb}}^2$	$N_{\mathrm{bf}} N_{\mathrm{aux}} N_{\mathrm{orb}}^2$
C^{K}	4	$(qr\|pr) = \sum_l b^l_{qr} b^l_{pr+}$	$N_{\mathrm{bf}} N_{\mathrm{orb}}^2$	$N_{\mathrm{bf}} N_{\mathrm{aux}} N_{\mathrm{orb}}^2$

4.6.1 Escalamiento en cadenas lineales de alcanos

El uso de la resolución de la identidad permite reducir el escalamiento del método de quinto a cuarto orden. Si bien las integrales son la parte más demandante del proceso de solución, no son el único paso, por lo que es importante verificar el desempeño del programa mediante cálculos prácticos. Para ello se plantean los siguientes tres algoritmos a revisar:

- Diagonalización Iterativa (ID): la optimización de números de ocupación y de orbitales se realizan de manera separada, usando la diagonalización iterativa con DIIS para la última.
- Rotaciones: la optimización de números de ocupación y de orbitales se realizan de manera separada, usando el método de rotaciones con gradientes conjugados para la última.
- Combinado: la optimización de números de ocupación y de orbitales se realizan de manera conjunta usando el método de gradientes conjugados. Para ello se unen el gradiente de los números de ocupación y de los orbitales en un solo vector.

Se realizaron cálculos con cadenas lineales de alcanos desde metano CH_4 hasta pentadecano $C_{15}H_{32}$ utilizando el conjunto de base cc-pVDZ[95] y la base auxiliar cc-pVDZ-jkfit en el código PyNOF. La arquitectura de cómputo corresponde a un procesador AMD Ryzen 7 5800X de 8 procesadores y 16 hilos. La mayor parte del programa utiliza Numba,[96] el cual es un compilador en

tiempo real[c] que le permite alcanzar mayor eficiencia de cómputo. Además, las transformaciones de integrales se hicieron mediante CuPy[97] en una GPU NVIDIA RTX 4080.

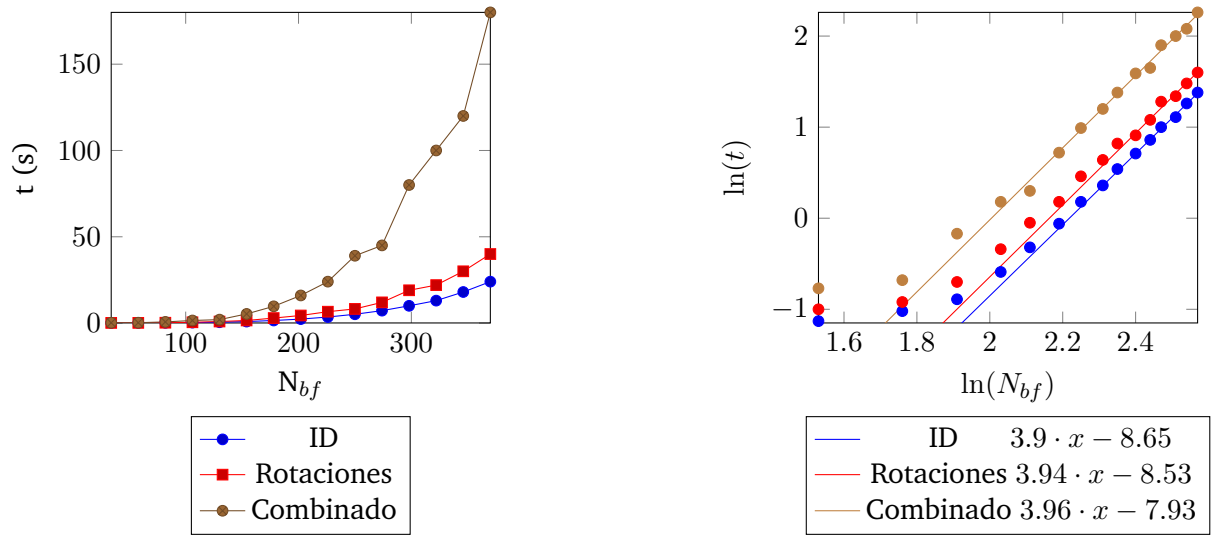

(a) (b)

Fig. 4.2: Análisis de escalamiento para los métodos de diagonalización iterativa (ID), optimización por rotaciones y optimización combinada. La Figura 4.2a muestra el tiempo por iteración externa según el número de funciones de base del sistema y cada punto corresponde a un alcano lineal desde metano (CH_4) hasta pentadecano ($C_{10}H_{22}$). La Figura 4.2b muestra el análisis logarítmico cuya pendiente proporciona el escalamiento respecto a N_{bf}, siendo muy cercano a cuarto orden.

La Figura 4.2a muestra el tiempo de cómputo por iteración externa, donde cada punto corresponde a un alcano lineal; en todos los casos se ha impuesto un máximo de 30 iteraciones internas por iteración externa o conjunta. Se observa que la diagonalización iterativa (azul) es el método que consume menor tiempo por iteración externa, seguido de la optimización por rotaciones (rojo) que consume un poco más de tiempo, y de la optimización combinada (café) que consume significativamente más tiempo. Es interesante notar que los tres métodos construyen los multiplicadores de Lagrange para la optimización orbital, el cual acorde a la Tabla 4.5 es el proceso con escalamiento de cuarto orden. Por lo tanto, la diferencia que se observa entre la curva de ID y de rotaciones se debe a otros pasos, particularmente el algoritmo de DIIS en el caso de ID y de gradientes conjugados en el caso de rotaciones. En el caso de la optimización combinada, el tiempo de cómputo es sustancialmente mayor, ya que hay un aumento en la dimensión del vector a optimizar aumenta. Suponiendo un comportamiento polinomial del tiempo de cómputo respecto a las funciones de base del tipo

$$t = bN_{\text{bf}}^{m} \tag{4.51}$$

[c]En inglés, just-in-time (JIT) compilator.

donde b es un prefactor y m es el grado del escalamiento, se tiene

$$\ln(t) = m \ln(N_{\text{bf}}) + \ln(b) \tag{4.52}$$

por lo tanto la regresión lineal de $\ln(N_{\text{bf}})$ contra $\ln(t)$ da como pendiente el factor de escalamiento y como ordenada al origen el prefactor. Esto se muestra en la Figura 4.2b, donde se ha realizado la regresión lineal con las moléculas de undecano a pentadecano con los tres métodos de optimización, mostrando una pendiente muy cercana a cuatro; así mismo, ID tiene el menor prefactor, seguido por la optimización por rotaciones y la optimización combinada de acuerdo con todo el análisis realizado previamente.

4.6.2 Análisis del proceso de convergencia

Si bien es importante generar métodos que requieran poco tiempo por iteración, también es importante que puedan llegar correctamente a la solución. Podemos definir el camino a la convergencia como el conjunto de parámetros y valores de la función objetivo que sigue el método de optimización desde su punto inicial hasta su punto final. El camino a la convergencia de los NOF depende de muchos factores, como los orbitales y números de ocupación de partida, los criterios de convergencia y hasta de la precisión numérica de la arquitectura de cómputo utilizada. A fin de tener una idea general del desempeño de los métodos de optimización, la Figura 4.3 muestra el camino de convergencia de tres moléculas, en particular en la Figura 4.3a se muestra el camino de CH_4 el cual es un sistema débilmente correlacionado, en la Figura 4.3b se muestra el camino de FO_2 el cual es un sistema fuertemente correlacionado, en la Figura 4.3c se muestra el camino de $ClOO^-$ que además de ser fuertemente correlacionado también es un sistema cargado y en la Figura 4.3d se muestra el camino de naftaleno, un sistema químico de mayor tamaño y más complejo. Todos los sistemas se han iniciado desde un punto de partida de Hartree-Fock.

Un fenómeno común en CH_4, OF y $ClOO^-$ es que al inicio la optimización por diagonalización iterativa desciende más rápido en energía que los otros métodos, sin embargo, esta se detiene antes y en una energía más positiva, como se puede ver en las Figuras 4.3a, Figuras 4.3b y Figuras 4.3c. Otro punto a considerar es que después de descender, la energía puede subir localmente, como se puede ver en la Figura 4.3c del sistema de $ClOO^-$, e incluso puede oscilar como ocurre en la Figura 4.3d del naftaleno. Por otra parte, si bien la optimización por rotaciones y combinada inician más lento y realizan más iteraciones, también llegan a energías más negativas, garantizando un descenso en la energía en cada paso. De esta forma, puede concluirse que la optimización por ID funciona bien para una etapa inicial del proceso de convergencia, que incluso puede quedarse como la única etapa dependiendo de la exactitud deseada. Sin embargo, si se requiere una mayor exactitud o un camino de convergencia más estable, el cálculo puede continuarse utilizando

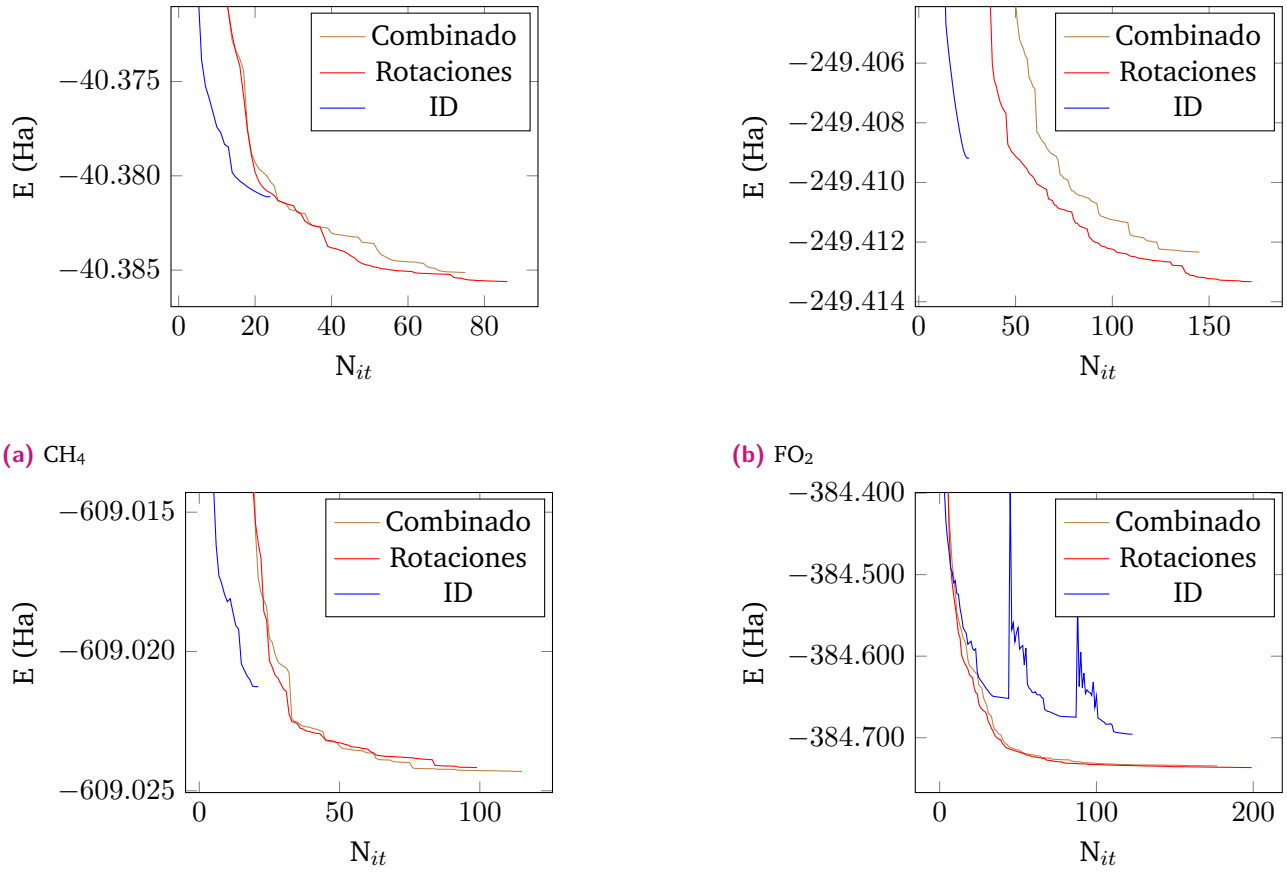

(a) CH_4

(b) FO_2

(c) $ClOO^-$

(d) Naftaleno

Fig. 4.3: Comparación del camino de convergencia seguido por los métodos de optimización ID, rotaciones y combinado para los sistemas a) CH_4, b) FO_2, c) $ClOO^-$ y d) Naftaleno.

la optimización por rotaciones o combinada, donde por relación costo-beneficio el método de rotaciones será preferible en la mayoría de los casos.

5 Sistemas seleccionados

En este capítulo se aborda el desempeño de los funcionales en sistemas de interés. En particular, se cubrirá el error de deslocalización de la carga estudiado sobre los sistemas del conjunto molecular W4-17-MR[a] y la competencia de estabilidad entre los estados triplete y quintuplete de la hierro-porfirina.

5.1 Desempeño en el error de deslocalización de la carga

El error de deslocalización de la carga representa uno de los grandes desafíos de la Química Cuántica actual,[10,99] y tiene implicaciones en el estudio de superficies de energía potencial, *band-gaps*,[100] energías de ionización,[101] reactividad química y análisis de transferencia de carga. Este error ha sido relacionado con varios fenómenos como la autointeracción[102,103] y su versión de muchos electrones[104], un error de concavidad o convexidad en la energía de electrones fraccionarios,[105] o una mala descripción de la discontinuidad en la derivada de la energía respecto al número de electrones,[106,107] aunque esto último ha sido criticado.[108] El hecho es que el fenómeno se manifiesta como una sobreestablización incorrecta de cargas fraccionarias que ocurre en varios métodos (*vide infra*). Para entender esto, consideremos un sistema como el de la Figura 5.1a, donde cada esfera representa un fragmento y estos están separados por una distancia r, la cual es lo suficientemente grande para considerar que no hay interacciones entre los fragmentos. Si a este sistema se le remueve un electrón, la energía del nuevo sistema será la energía de un fragmento cargado, E_+, más la energía de los fragmentos neutros, E_0, es decir:

$$E_{\text{cadena cargada}} = E_+ + (n-1)E_0, \tag{5.1}$$

donde n representa el número de fragmentos del sistema.

Este fenómeno se puede representar como en la Figura 5.1b, donde la carga se encuentra completamente localizada en el fragmento de la izquierda marcado con verde. Sin embargo, esta no es la única distribución de carga posible, ya que también podría encontrarse localizada en cualquiera de los otros fragmentos. Además, la carga podría estar completamente deslocalizada entre todos los fragmentos, representando un ensamble de los casos anteriores, como se muestra en la Figura 5.1c, donde cada uno tiene una carga fraccionaria.[106] Estas distribuciones, completa-

[a] Este es un conjunto con 17 moléculas cuyo análisis requieren de métodos multirreferenciales.[98]

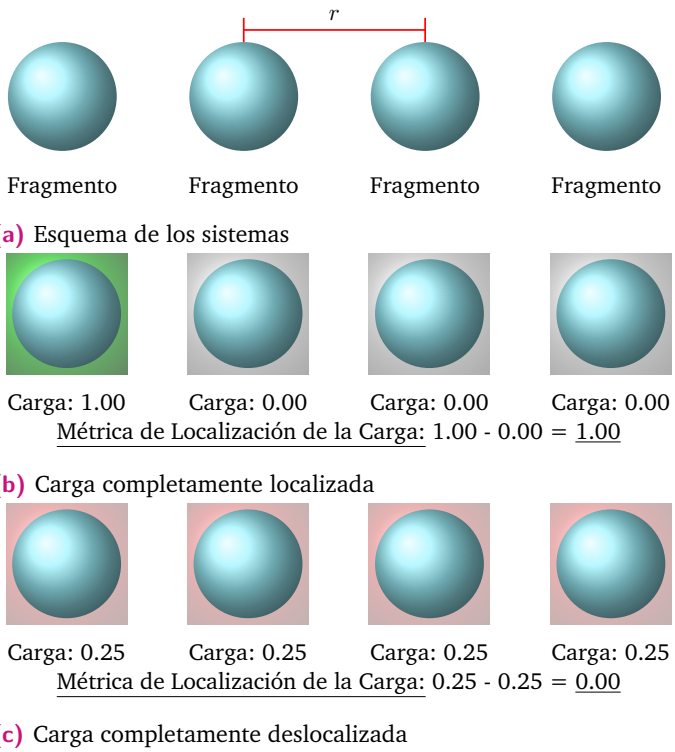

Fig. 5.1: Representación de los sistemas estudiados, los cuales consisten en cadenas de fragmentos repetidos y bien separados, como se muestra en la Figura 5.1a, donde cada fragmento es simbolizado por una esfera con distancia de separación r. En la Figura 5.1c se muestra el caso completamente localizado, con la carga concentrada en el fragmento señalado con verde, tal que la métrica de localización de la carga da 1.0 y en la Figura 5.1b se muestra el caso completamente deslocalizado, donde cada fragmento de color rojo tiene la misma carga y, por tanto, la métrica de localización de la carga da 0.0.

mente localizadas y completamente deslocalizadas, deben de tener la misma energía, dada por la ecuación (5.1), sin embargo, es un problema conocido que la gran mayoría de los funcionales de la densidad,[109] y algunos otros métodos como Møller-Plesset,[110] sobreestabilizan el caso de la carga completamente deslocalizada.

En esta sección estudiamos el comportamiento de los NOFs respecto al error de deslocalización de la carga en sistemas de moléculas repetidas y suficientemente separadas. Para poder caracterizar la distribución de la carga en estos sistemas, proponemos una métrica de localización de la carga, (CLM, por sus siglas en inglés), dada por la diferencia entre la carga del fragmento más cargado y la carga del fragmento menos cargado

$$\mathrm{CLM} = q_{\substack{\text{Fragmento}\\ \text{más cargado}}} - q_{\substack{\text{Fragmento}\\ \text{menos cargado}}} . \tag{5.2}$$

Si la carga está completamente localizada como en la Figura 5.1b, entonces el fragmento más cargado tendrá una carga de “1” y el fragmento una carga de “0”, por lo tanto, la métrica de localización de la carga tomará el valor de la unidad. En contraste, cuando se tiene la carga completamente deslocalizada entre todos los n fragmentos, como en la Figura 5.1c, todos tendrán una carga de $1/n$ y la métrica tomará el valor de la diferencia entre el más cargado y el menos cargado que será de cero. Cualquier valor entre cero y uno indicará una localización parcial de la carga, es decir, estará distribuida entre los fragmentos, pero al menos uno tiene un poco más de carga que los demás. A continuación aplicaremos la métrica a varios sistemas.

5.1.1 Cadenas de helio

Para entender el efecto del error de deslocalización de la carga, consideremos la energía de ionización de cadenas lineales de átomos de helio, como se muestra en la Figura 5.2. Para ello, se construyeron cadenas de 2 hasta 20 átomos de helio y se removió un electrón de cada una de las cadenas, generando una carga positiva. La energía de ionización de la cadena deberá estar dada por la diferencia de energía entre la cadena cargada y la cadena neutra,

$$\mathrm{IP}_{\text{cadena}} = E_{\text{cadena cargada}} - E_{\text{cadena neutra}}. \tag{5.3}$$

Si la energía de la cadena neutra está dada por:

$$E_{\text{cadena neutra}} = nE_0, \tag{5.4}$$

entonces la energía de ionización será

$$\begin{aligned} \mathrm{IP}_{\text{cadena}} &= E_+ + (n-1)E_0 - nE_0 \\ &= E_+ - E_0 \\ &= \mathrm{IP}_{\text{fragmento}}. \end{aligned} \tag{5.5}$$

Es decir, la energía de ionización es independiente de la cantidad de fragmentos en la cadena y es igual a la energía de ionización de un solo fragmento, lo cual concuerda con la idea de fragmentos suficientemente separados e independientes.

Considerando que la energía de ionización de la cadena debe de ser la misma que la de un fragmento, podemos plantear la desviación de ambas energías como una medida del error debido a la deslocalización de la carga, dada por

$$\text{Error} = \mathrm{IP}_{\text{fragmento}} - \mathrm{IP}_{\text{cadena}}. \tag{5.6}$$

Los resultados del error para cadenas de helio se muestran en la Figura 5.2a, donde cada punto representa una cadena, el eje horizontal muestra el número de átomos de la cadena y el eje vertical muestra el error en la energía de ionización de las cadenas respecto a la de un solo átomo de helio. Además, se muestra el conjunto de datos para los NOF, así como algunos funcionales aproximados de la densidad representativos de cada escalón de la escalera de Jacob. Puede verse que los funcionales semilocales presentan un mayor error que sus contrapartes híbridas, por ejemplo, la curva de TPSS (diamantes rojos) se encuentra por debajo de la de TPSSh (pentágonos cafés) y la curva de MN15-L (cruces verdes) se encuentra por debajo de la de MN15 (cruces moradas), por otra parte, el funcional de correlación de rango separado[b], ωB97X-D es el que presenta menor error, todo esto en concordancia con lo reportado previamente para los DFAs. En cambio, los funcionales PNOF5 y PNOF7 se encuentran en la parte superior de la gráfica, con un error prácticamente de cero eV, independientemente de la cantidad de átomos en la cadena. El comportamiento de las gráficas puede entenderse a partir de la Figura 5.2b, la cual muestra la métrica de localización de la carga en función del número de fragmentos y donde puede verse que en todos los casos las DFAs tienen una métrica muy cercana a cero, indicando que la carga está significativamente deslocalizada, mientras que en PNOF5 y PNOF7 la métrica es de uno, indicando que la carga está localizada en un solo átomo.

[b]En inglés, long-range correlated.

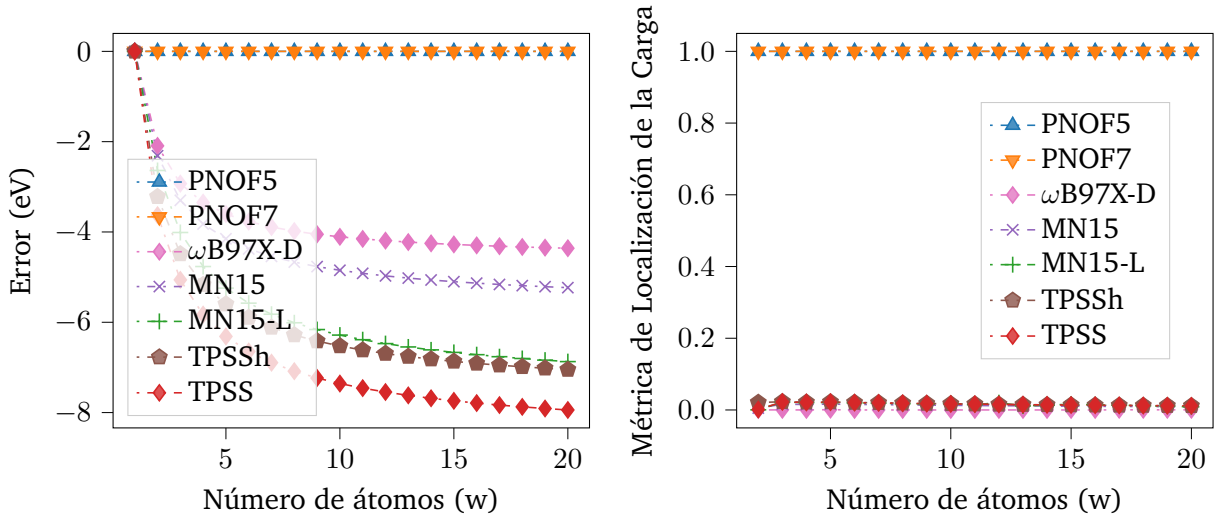

(a) Desviación de la energía de ionización de cadenas de helio $(He)_w$ respecto a la energía de ionización de un solo átomo.

(b) Métrica de localización de cadenas de helio $(He)_w$.

Fig. 5.2: Análisis de la ionización de cadenas de átomos de helio separados por una distancia $r = 7$ Å, calculado con PNOF5, PNOF7 y varios funcionales aproximados de la densidad representativos de la escalera de Jacob. La energía de ionización debería de ser constante e igual a la de un solo átomo de helio, independientemente de la cantidad de átomos en la cadena. El error respecto a esta energía es un efecto del error de deslocalización de la carga y se puede relacionar con valores de CLM muy cercanos a cero.

5.1.2 Cadenas de sistemas fuertemente correlacionados: conjunto W4-17-MR

Evaluación de la correlación mediante el Diagnóstico-M

Los resultados para las cadenas de helio muestran un desempeño prometedor de PNOF en el error de deslocalización de la carga y motiva investigar si este comportamiento se mantiene en sistemas más complejos. Debido a que el uso de los funcionales PNOF ha destacado en sistemas fuertemente correlacionados, se han elegido los sistemas del conjunto W4-17-MR,[98] el cual contiene 17 moléculas multirreferenciales. Se utilizó el diagnóstico-M para evaluar la descripción de PNOF sobre estas moléculas. Este diagnóstico toma valores entre cero y uno y se considera que un diagnóstico mayor a 0.10 es indicativo de que un sistema es fuertemente correlacionado. Los resultados del diagnóstico aplicado a cadenas formadas por cuatro fragmentos repetidos se muestran en la Figura 5.3, donde cada renglón corresponde a la molécula base de la cadena, la primera columna corresponde a resultados de PNOF5 y la segunda columna a resultados de PNOF7. Además, la etiqueta $M^{(0)}$ corresponde al diagnóstico del sistema neutro, mientras que la

etiqueta $M^{(1)}$ corresponde al diagnóstico del sistema con carga positiva. Los resultados muestran que PNOF5 es capaz de detectar varios sistemas como fuertemente correlacionados, en particular, B_2, BN, C_2, ClOO, FO_2, FOOF, O_3, S_3 y S_4. Sin embargo, falla en caracterizar al resto de los sistemas. Estos resultados son mejorados sustancialmente por PNOF7, el cual detecta correlación fuerte en todos los sistemas, aunque cabe señalar que existe un desbalance en la correlación de los sistemas neutros ($M^{(0)}$) y cargados ($M^{(1)}$) de ClF_5, ClO_3, ClOO y OClO.

Deslocalización de la carga

La Figura 5.4 muestra la CLM para las 17 cadenas cargadas estudiadas con PNOF y DFAs. En particular, los DFAs producen valores de CLM muy cercanos a cero, mientras que PNOF5 y PNOF7 producen valores de CLM más cercanas a uno, similar a lo observado en las cadenas de helio. Hay ciertos casos que destacan en los resultados de PNOF7. En particular, S_3, ClOO, FO_2 y S_4 muestran distribuciones de carga parcialmente deslocalizadas y las cadenas que tienen como base a B_2, BN y C_2 muestran una deslocalización importante de la carga.

La distribución de la carga observada en los diferentes funcionales puede relacionarse con la desviación de la energía de la cadena cargada de cuatro fragmentos respecto a la suma de la energía de los fragmentos separados, como se muestra en la Figura 5.5. Cualquier punto con desviación cero de energía es correcto, independientemente de su distribución de carga. Sin embargo, lo que se observa en la Figura es que los DFAs se encuentran en la región izquierda con valores de métrica de localización de la carga muy cercanos a cero, indicando que la carga está mayormente deslocalizada entre los fragmentos y con errores de hasta 5 eV. Además, se observa la misma tendencia encontrada en el caso de las cadenas de helio respecto a la escalera de Jacob. Por otra parte, PNOF5 (triángulos azules) se encuentra concentrado en la esquina superior derecha, indicando que localiza la carga en un solo fragmento sin desviarse de la energía. En contraste, los puntos de PNOF7 (triángulos naranjas) se distribuyen en un intervalo más amplio de métrica de localización de la carga, en general manteniéndose cerca de la línea de no desviación.

Resulta muy interesante que la tendencia a distribuir la carga a través de las cadenas puede ser relacionada con el régimen de correlación en el sistema, como se muestra en la Figura 5.6. En esta figura se han colocado las moléculas del conjunto W4-17-MR con diferentes colores:

- Verde si no presentan desviaciones en la energía,
- Naranja si presentan desviaciones pequeñas,
- Rojo si presentan desviaciones significativas.

(a) PNOF5 **(b)** PNOF7

Fig. 5.3: Diagnóstico-M aplicado a las cadenas suficientemente separadas de cuatro unidades, cada una tomada del conjunto W4-17-MR, neutras ($M^{(0)}$) y cargadas ($M^{(1)}$). Moléculas con diagnóstico-M igual o superior a 0.10 son consideradas como fuertemente correlacionadas y se indican con color verde, mientras que las moléculas con valores por debajo de dicho límite se indican en amarillo.

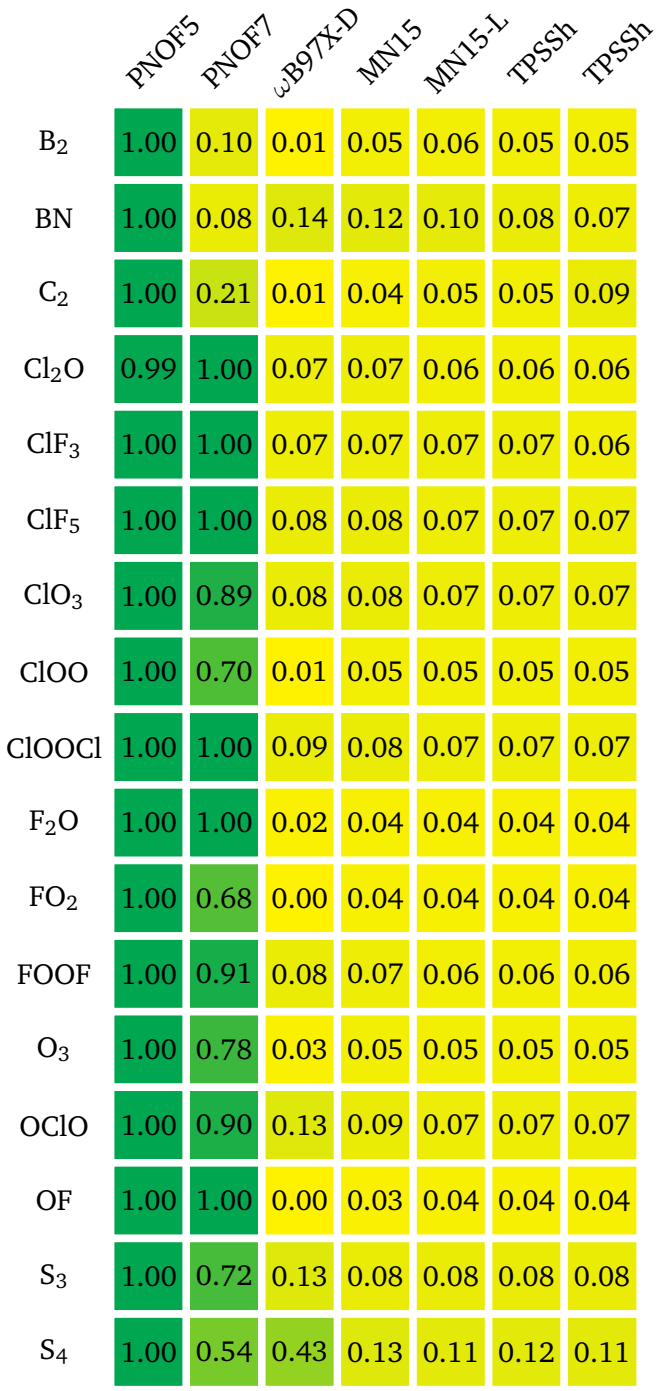

Fig. 5.4: Métrica de localización de la carga para las cadenas de cuatro fragmentos en su estado ionizado, calculada con PNOF5, PNOF7 y varios DFAs aproximados. Valores cercanos a 1.0 indican localización de la carga y se encuentran marcados en verde, mientras que valores cercanos a 0.0 indican deslocalización de la carga y se encuentran marcados en amarillo.

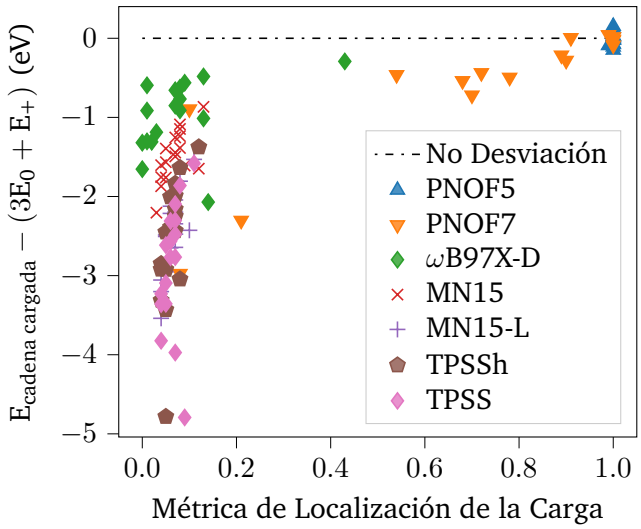

Fig. 5.5: Desviación de la energía de cadenas cargadas de cuatro fragmentos de las unidades de W4-17-MR como función de la métrica de localización de la carga para cadenas de PNOF5, PNOF7 y DFAs comunes. Puntos a la izquierda indican que la carga está deslocalizada entre todos los fragmentos, mientras que puntos a la derecha indican que la carga está localizada en un solo fragmento. Puntos cercanos a cero en el eje vertical son deseables e indican que no hay desviación en la energía, mientras que entre más abajo estén los puntos en el eje vertical indican que hay una sobreestabilización de la cadena cargada respecto a los fragmentos separados.

Además, se ha colocado una línea roja para señalar la tendencia de PNOF7 a proporcionar soluciones más deslocalizadas entre mayor sea el carácter fuertemente correlacionado del sistema. De las diferentes figuras presentadas hasta este punto se concluye que PNOF5 no presenta error de deslocalización de la carga, pero tampoco captura el carácter multiconfiguracional de todos los sistemas, por otra parte, PNOF7 sí recupera el carácter multiconfiguracional de los sistemas, pero presenta error de deslocalización de la carga conforme aumenta el carácter multiconfiguracional del sistema. Sin embargo, esto implica que PNOF7 está libre de error de deslocalización de la carga para sistemas fuertemente correlacionados con diagnóstico-M de hasta 0.3 y para sistemas con valores mayores sí presenta desviaciones energéticas, pero menores a los DFAs comunes.

Desempeño de GNOF

Una vez discutido el desempeño de PNOF5 y PNOF7 en relación con DFAs comunes, se presenta el desempeño de GNOF, el cual tiene como propósito proporcionar un balance adecuado entre correlación estática y dinámica. Para evaluar el desempeño, la Figura 5.7 muestra la desviación de energía de dímeros cargados respecto a la suma de la energía de una unidad neutra y una unidad cargada, calculados con PNOF7 y GNOF. El comportamiento de PNOF7 es similar al observado previamente, mientras que los puntos verdes de GNOF muestran que este se encuentra más cerca de la línea de desviación cero en la mayoría de los casos, salvo por tres sistemas, ClO_3, OClO y B_2.

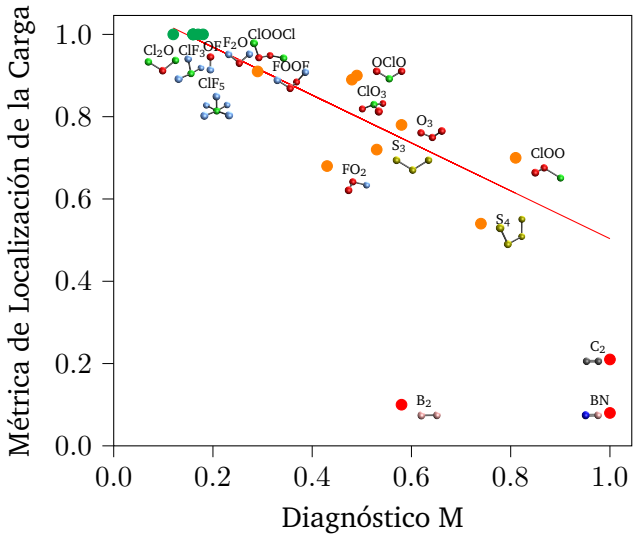

Fig. 5.6: Distribución de las moléculas del conjunto W4-17-MR acorde al diagnóstico-M y el valor de CLM para las cadenas cargadas de cuatro fragmentos calculadas con PNOF7. Los puntos en color verde corresponden a sistemas completamente localizados, en color naranja a sistemas con localización parcial de la carga y los puntos en color rojo a sistemas con la carga completamente deslocalizada.

Por tanto, aunque GNOF no está exento del error de deslocalización de la carga, sí presenta un mejor desempeño respecto a PNOF7 y corrige el comportamiento en la mayoría de los casos.

Para verificar el buen desempeño de GNOF en el estudio de sistemas cargados, la Figura 5.8 muestra la energía de ionización de cadenas de ozono de hasta diez fragmentos, el cual tiene una energía de ionización de 12.5 eV. En el caso de PNOF7 (puntos naranjas), este predice una energía de ionización de 11.2 eV para una unidad, mientras que la energía de ionización disminuye en función del número de fragmentos en la cadena hasta llegar a 10.0 eV para la cadena de diez fragmentos, como consecuencia del error de deslocalización de la carga. En la figura también se muestra el comportamiento de varios DFAs, los cuales presentan la carga completamente deslocalizada. Si bien varios de los DFAs presentan predicciones correctas para la energía de ionización de una sola molécula de ozono, la predicción se degrada rápidamente y en general PNOF7 proporciona mejores resultados a partir de dos fragmentos que TPSS, TPSSh y MN15-L. En el caso de GNOF, este proporciona una predicción acertada y constante de energía de ionización, mostrando que no es afectado por el error de deslocalización de la carga.

Otro efecto donde resulta importante dar un tratamiento adecuado a sistemas cargados es en las curvas de energía potencial, como la que se muestra en la parte inferior de la Figura 5.9 para el hidruro de litio, junto a las correspondientes carga de Löwdin del litio en la parte superior. En particular, en la Figura 5.9a se presenta la información para la especie neutra, LiH, con los datos

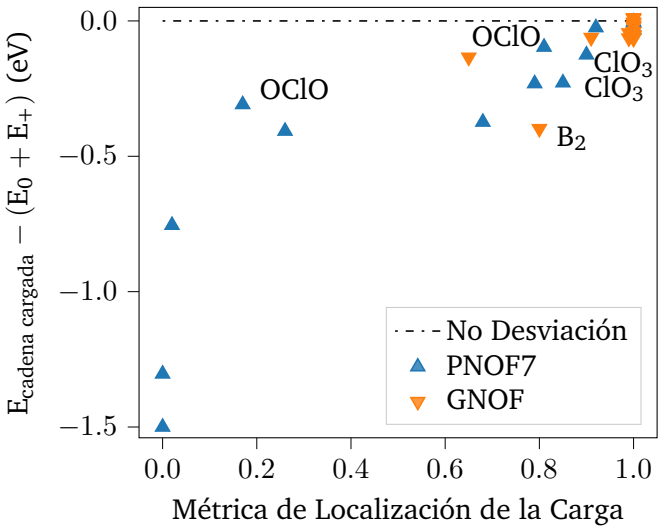

Fig. 5.7: Desviación de la energía de los sistemas con respecto a la energía sumada de un fragmento neutro y un fragmento cargado, $\Delta E = E_{\text{cadena cargada}} - (E_0 + E_+)$, como función de la métrica de localización de la carga.

de FCI en rojo como referencia, PNOF5 en azul, PNOF7 en naranja y GNOF en verde. En general se observa una buena reproducción de todos los PNOF respecto a FCI en todos los casos, tanto en energía como en carga. Cabe destacar que en la región del enlace la energía de PNOF5 queda por arriba del valor correspondiente a FCI, evidenciando que es variacional, pero GNOF queda por debajo debido a que no es completamente N-representable. PNOF7 queda por arriba de FCI en la región de enlace, pero en la región de disociación tanto PNOF7 como GNOF quedan por debajo de FCI. Por otra parte, el comportamiento de la carga en el proceso de disociación de la carga es correcto y comparable al de FCI en todo el intervalo estudiado, convergiendo a cero en la región de disociación y solo con pequeñas diferencias por parte de GNOF. El mismo efecto puede observarse en la Figura 5.9b para la especie cargada, LiH^+. En este caso PNOF7 y GNOF quedan por debajo de FCI en todo el intervalo, sin embargo, cabe destacar que se ha ampliado la escala de energía en el eje vertical para hacer más evidente el resultado y que la diferencia de energía entre las curvas es realmente pequeña. Además, la reproducción de la distribución de la carga coincide perfectamente con FCI en todo el intervalo, convergiendo asintóticamente a la unidad para litio, como es de esperarse debido al buen desempeño respecto al error de deslocalización de la carga.

5.2 Sistema Hierro-Porfirina (FeP)

El sistema hierro-porfirina (FeP) consiste en un núcleo de hierro (II) coordinado con los cuatro nitrógenos del anillo de la porfirina, como se puede ver en la Figura 5.10. Durante varios años se ha debatido sobre la multiplicidad del estado basal del sistema hierro porfirina, con evidencias

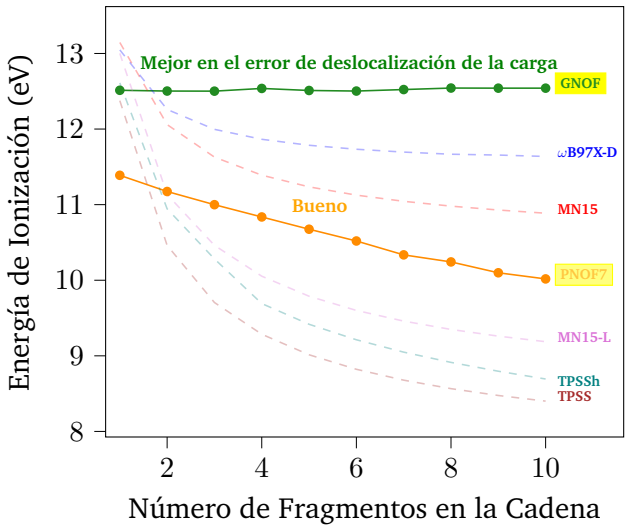

Fig. 5.8: Potenciales de ionización de cadenas repetidas y suficientemente separadas, tomando como unidad de construcción la molécula de ozono, O_3. Cada marca corresponde a una cadena compuesta por el número de unidades indicado en el eje horizontal.

encontradas que apoyan al estado triplete o al estado quintuplete.[111] El estado quintuplete fue sugerido inicialmente por los métodos como CASSCF y CASPT2.[112,113] Posteriormente, se utilizó DFT y métodos perturbativos que indicaban que el estado triplete es el más estable.[114] Más recientemente, se ha sugerido que la preferencia de los métodos multirreferenciales por el estado quintuplete se debe a incompletés del espacio activo y que cálculos con espacios activos lo suficientemente grandes vuelven a favorecer el estado triplete como el más estable.[115]

En este trabajo se han calculado los estados singulete (S), triplete (T) y quintuplete (Q) del sistema FeP utilizando PNOF5, PNOF7 y GNOF con la base cc-pVDZ.[95] En esta base, el sistema tiene cuatro orbitales débilmente doble ocupados acoplados a cada orbital fuertemente doble ocupado, dando un total de 462 orbitales naturales para el estado triplete.[c] Este se trata de un cálculo retador considerando que contiene correlación estática y que en términos de métodos con espacio activo se trataría de un cálculo de 184 electrones en 462 orbitales. Los resultados se muestran en la Tabla 5.1, donde la primera columna muestra el estado (S, T y Q) en Hartrees, así como la diferencia de energía del estado triplete respecto al estado singulete (S-T) y al estado quintuplete (Q-T) en kcal/mol para los PNOFs que se muestran en el resto de las columnas. Para todos los funcionales se observa una diferencia de energía positiva de S-T, lo que indica que el estado triplete es más estable que el estado singulete. Por otra parte, PNOF5, PNOF7s y PNOF7 presentan valores negativos de Q-T indicando que favorecen el estado quintuplete frente

[c]Con referencia a la Figure 2.1, el sistema de FeP tiene $N = 186$ electrones. En estado triplete se tiene $N_I = 2, N_{II} = 92$, tal que $N_I + 2N_{II} = 186$. Hay cuatro orbitales débilmente doble ocupados acoplados ($N_g = 4$) a cada orbital fuertemente doble ocupado, por lo que hay $92(4 + 1) = 460$ orbitales en Ω_{II} y 2 orbitales en Ω_I, dando un total de 462 orbitales.

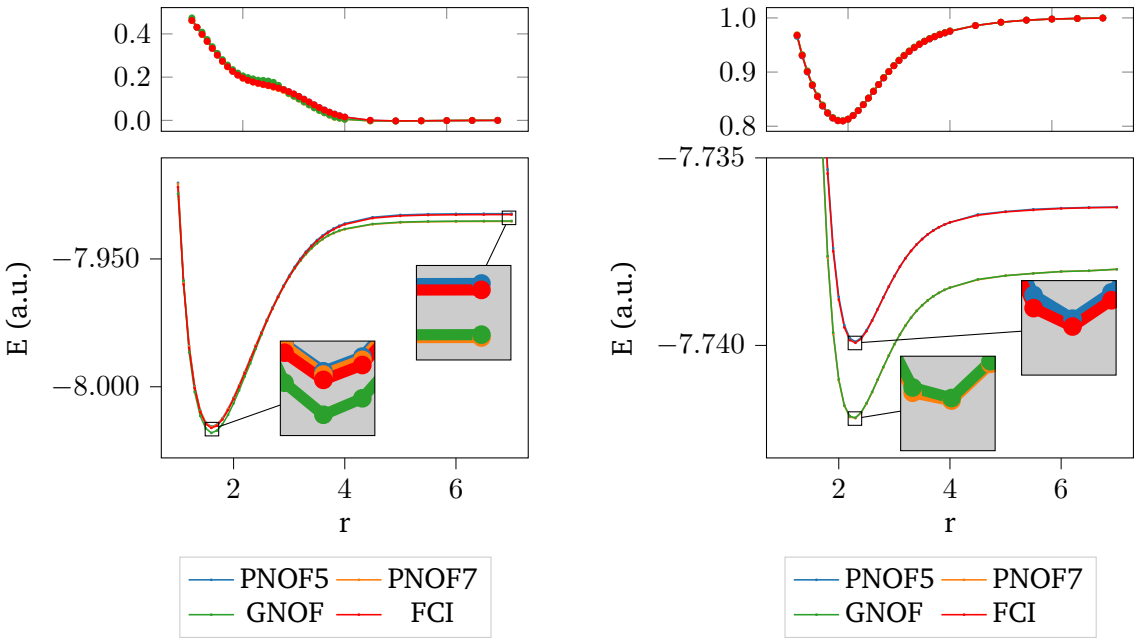

(a) LiH **(b)** LiH^+

Fig. 5.9: Curvas de disociación de hidruro de litio, (a) neutro (LiH) y (b) cargado (LiH^+). Los paneles superiores presentan el comportamiento de la carga del átomo de litio a lo largo de la curva de disociación, calculada mediante un análisis de poblaciones de Löwdin. En la Figura 5.9b, la curva de PNOF7, las curvas de PNOF7 y GNOF están sobrepuestas y las curvas de PNOF5 y FCI están sobrepuestas.

al triplete, es decir, estos funcionales predicen el orden de energía como Q <T <S. Estos tres funcionales tienen en común que tienden a favorecer la correlación estática frente a la dinámica y resulta interesante que PNOF7s, el funcional desarrollado explícitamente para tomar en cuenta solo la correlación estática sin la dinámica, es el que más sobreestabiliza el estado quintuplete. Por otra parte, agregar correlación dinámica a PNOF7s da lugar a NOF-MP2, el cual estabiliza el estado triplete. Estos resultados concuerdan con GNOF, el cual busca proporcionar un balance adecuado entre correlación estática y dinámica y que también apoya al triplete como el estado basal. Esto resalta la importancia de un balance correcto entre correlación dinámica y estática para poder capturar la estabilidad del estado triplete y muestra la superioridad de GNOF respecto a PNOF5 y PNOF7.

Respecto a las soluciones proporcionadas por cada uno de los PNOFs, su diagnóstico-M se presenta en la Tabla 5.2, donde se puede ver un valor de 1.0 para el singulete predicho por todos los NOFs, indicando una solución diradical, en concordancia con otros reportes.[20] En los casos del triplete y el quintuplete, el diagnóstico-M de PNOF5 y PNOF7s muestra que estos no capturan el carácter multiconfiguracional del sistema; sin embargo, PNOF7 proporciona valores que indican

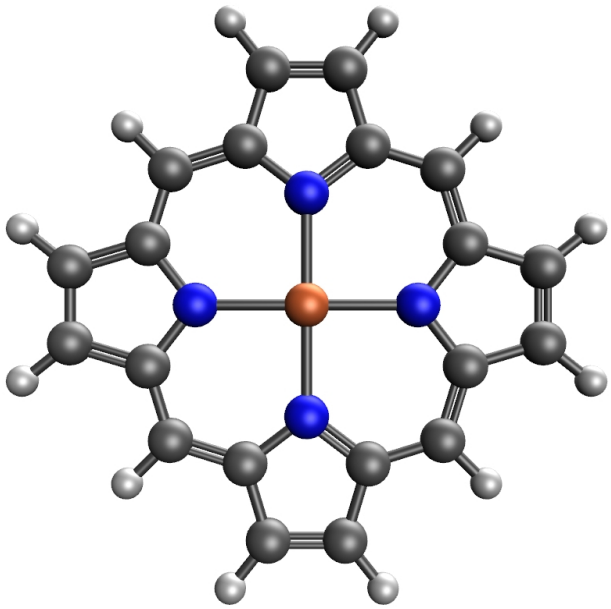

Fig. 5.10: Estructura del sistema de hierro-porfirina (FeP)

una fuerte importancia de correlación estática para estos estados. Desafortunadamente, esta importancia se ve opacada en el caso de GNOF, cuyos diagnósticos-M toman valores pequeños.

También resulta de interés el análisis de ciertos orbitales, particularmente los del estado triplete. La Tabla 5.3 muestra el orbital natural más ocupado más alto[d] (HONO, por sus siglas en inglés) en el primer renglón, los dos orbitales naturales simplemente ocupados (SONOs, por sus siglas

[d]Considerando un ordenamiento de los orbitales acorde a los elementos diagonales de la matriz de multiplicadores de Lagrange. Estos valores se interpretan como energías orbitales en Hartree-Fock, pero esta interpretación no es válida en NOF, ya que en general la matriz de multiplicadores no es estrictamente diagonal. Sin embargo, este ordenamiento también suele coincidir con el ordenamiento por números de ocupación.

Tab. 5.1: Energía (Hartree) de los diferentes estados de espín para el compuesto hierro-porfirina (FeP), calculados con PNOF5, PNOF7s, PNOF7, NOF-MP2 y GNOF, con sus correspondientes gaps adiabáticos singulete-triplete (ST), $E_{singlet} - E_{triplet}$ y gaps adiabáticos triplete-quintuplete (QT) , $E_{quintet} - E_{triplet}$, en kcal/mol. Los valores corresponden a cálculos con la geometría optimizada reportada en la referencia Ref. [114].

MUL	PNOF5	PNOF7s	PNOF7	NOF-MP2	GNOF
S	-2245.417	-2245.436	-2245.989	-2248.384	-2247.769
T	-2245.484	-2245.492	-2246.014	-2248.456	-2247.869
S-T	42	35	16	45	63
Q	-2245.549	-2245.560	-2246.042	-2248.416	-2247.766
Q-T	-29	-36	-17	25	65

Tab. 5.2: Diagnóstico M para los estados de espín del sistema FeP calculados con PNOF5, PNOF7 y GNOF.

MUL	PNOF5	PNOF7s	PNOF7	GNOF
S	1.00	1.00	1.00	1.00
T	0.07	0.07	0.60	0.04
Q	0.07	0.08	0.56	0.04

en inglés) en el segundo y tercer renglón y el orbital natural desocupado más bajo (LUNO, por sus siglas en inglés) en el cuarto renglón para los funcionales PNOF5, PNOF7s, PNOF7 y GNOF, situados en las columnas. Los SONOs son similares independientemente del PNOF usado, aunque en el caso de GNOF están un poco más deslocalizados. Sin embargo, existe un cambio en el HONO y en el LUNO entre los diferentes funcionales. Existe un aumento de la correlación electrónica de izquierda a derecha y junto con este, una tendencia a involucrar al átomo de hierro en estos orbitales. En particular, el átomo de hierro no está involucrado en PNOF5 y PNOF7s, pero sí lo está en PNOF7 y GNOF. Este fenómeno se ha observado también en otros métodos que establecen el triplete como estado basal.[116] Si bien este hecho se observa tanto en el HONO de PNOF7 y GNOF, el hecho de que GNOF contiene correlación dinámica es el factor clave para que el triplete resulte como el estado más estable.

Tab. 5.3: Orbitales naturales del estado triplete del sistema FeP calculados con PNOF5, PNOF7s, PNOF7 y GNOF.

PNOF5	PNOF7s	PNOF7	GNOF
HONO Ω_b			
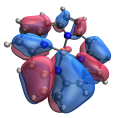	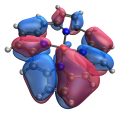	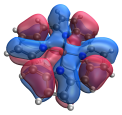	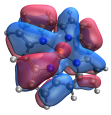
SONO-1 del subespacio Ω_I			
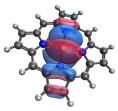	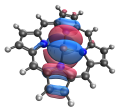	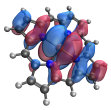	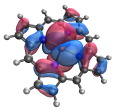
SONO-2 del subespacio Ω_I			
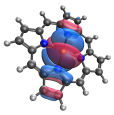	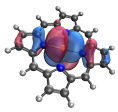	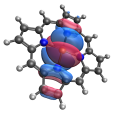	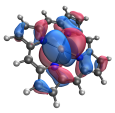
LUNO Ω_a			
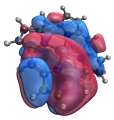	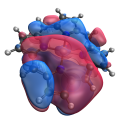	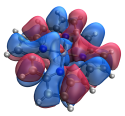	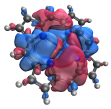

Conclusiones y Perspectivas

6

En este trabajo se han implementado funcionales de orbitales naturales basados en la teoría de matrices de la densidad reducida en PyNOF y DoNOF.jl, los cuales son programas de estructura electrónica escritos en lenguajes de programación modernos, Python y Julia respectivamente. En este sentido, el uso de aproximaciones como la resolución de la identidad y de arquitecturas de cómputo heterogéneo CPU/GPU permitieron tener una implementación competitiva que vuelve accesible el realizar cálculos de sistemas fuertemente correlacionados a un costo computacional intermedio entre métodos multirreferenciales y de referencia simple. Esto, junto con el acoplamiento a diversos métodos de convergencia, permitió explorar sistemas químicos de interés, mostrar su buen desempeño, por ejemplo, en sistemas cargados, y explorar sistemas químicos tan grandes como la hierro-porfirina.

Se espera que la implementación generada popularice el uso de la teoría de matrices de la densidad reducida, a través de los funcionales de orbitales naturales, y permita afrontar retos que siguen siendo inalcanzable para la química computacional actual. También existe otra oportunidad de aprovechar la localización orbital para reducir el costo de integración a tercer orden, lo que tendría un impacto aún mayor en la misma dirección que este trabajo. Finalmente, una vez establecido el éxito de los funcionales en el estado basal, se vuelve deseable extenderlos al estudio de estados excitados, lo que permitiría estudiar sistemas muy interesantes como los involucrados en procesos fotoquímicos.

Referencias

[1]L. Goerigk, A. Hansen, C. Bauer et al., “A look at the density functional theory zoo with the advanced GMTKN55 database for general main group thermochemistry, kinetics and noncovalent interactions”, Phys. Chem. Chem. Phys. **19**, 32184-32215 (2017).

[2]L. Goerigk y N. Mehta, “A trip to the density functional theory zoo: Warnings and recommendations for the user”, Aust. J. Chem. **72**, 563 (2019).

[3]R. Van Noorden, B. Maher y R. Nuzzo, “The top 100 papers”, Nature **514**, 550-553 (2014).

[4]J. P. Perdew, A. Ruzsinszky, J. Tao et al., “Prescription for the design and selection of density functional approximations: more constraint satisfaction with fewer fits”, J. Chem. Phys. **123**, 62201 (2005).

[5]M. G. Medvedev, I. S. Bushmarinov, J. Sun, J. P. Perdew y K. A. Lyssenko, “Response to Comment on “Density functional theory is straying from the path toward the exact functional””, Science **356**, 496 (2017).

[6]K. P. Kepp, “Comment on “Density functional theory is straying from the path toward the exact functional””, Science **356**, 496 (2017).

[7]M. G. Medvedev, I. S. Bushmarinov, J. Sun, J. P. Perdew y K. A. Lyssenko, “Density functional theory is straying from the path toward the exact functional”, Science **355**, 49-52 (2017).

[8]S. Hammes-Schiffer, “A conundrum for density functional theory”, Science **355**, 28-29 (2017).

[9]C. L. Benavides-Riveros, N. N. Lathiotakis y M. A. L. Marques, “Towards a formal definition of static and dynamic electronic correlations”, Phys. Chem. Chem. Phys. **19**, 12655-12664 (2017).

[10]A. J. Cohen, P. Mori-Sánchez y W. Yang, “Insights into current limitations of density functional theory”, Science **321**, 792-794 (2008).

[11]A. J. Cohen, P. Mori-Sánchez y W. Yang, “Challenges for density functional theory”, Chem. Rev. **112**, 289-320 (2012).

[12]K. Burke, “Perspective on density functional theory”, J. Chem. Phys. **136** (2012).

[13]J. W. Park, R. Al-Saadon, M. K. MacLeod, T. Shiozaki y B. Vlaisavljevich, “Multireference electron correlation methods: journeys along potential energy surfaces”, Chem. Rev. **120**, 5878-5909 (2020).

[14]J. G. Vitillo, C. J. Cramer y L. Gagliardi, “Multireference methods are realistic and useful tools for modeling catalysis”, Isr. J. Chem. **62** (2022).

[15]D. Zhang y D. G. Truhlar, “Unmasking static correlation error in hybrid Kohn-Sham density functional theory”, J. Chem. Theory Comput. **16**, 5432-5440 (2020).

[16]K. Pelzer, L. Greenman, G. Gidofalvi y D. A. Mazziotti, “Strong correlation in acene sheets from the active-space variational two-electron reduced density matrix method: Effects of symmetry and size”, J. Phys. Chem. A **115**, 5632-5640 (2011).

[17]C. U. Ibeji y D. Ghosh, “Singlet-triplet gaps in polyacenes: A delicate balance between dynamic and static correlations investigated by spin-flip methods”, Phys. Chem. Chem. Phys. **17**, 9849-9856 (2015).

[18]C.-S. Wu, P.-Y. Lee y J.-D. Chai, “Electronic properties of cyclacenes from TAO-DFT”, Sci. Rep. **6**, 37249 (2016).

[19]J. Lee y M. Head-Gordon, “Distinguishing artificial and essential symmetry breaking in a single determinant: Approach and application to the C60, C36, and C20 fullerenes”, Phys. Chem. Chem. Phys. **21**, 4763-4778 (2019).

[20]J. Lee, F. D. Malone y M. A. Morales, “Utilizing essential symmetry breaking in auxiliary-field quantum Monte Carlo: application to the spin gaps of the C36 fullerene and an iron porphyrin model complex”, J. Chem. Theory Comput. **16**, 3019-3027 (2020).

[21]J. K. Perry, “Importance of static correlation in the band structure of high-temperature superconductors”, J. Phys. Chem. A **104**, 2438-2444 (2000).

[22]E. R. Johnson y A. D. Becke, “Communication: DFT treatment of strong correlation in 3d transition-metal diatomics”, J. Chem. Phys. **146**, 211105 (2017).

[23]C. Biz, M. Fianchini y J. Gracia, “Strongly correlated electrons in catalysis: Focus on quantum exchange”, ACS Catal. **11**, 14249-14261 (2021).

[24]C. A. Coulson, “Present state of molecular structure calculations”, Rev. Mod. Phys. **32**, 170-177 (1960).

[25]A. J. Coleman, “Structure of fermion density matrices”, Rev. Mod. Phys. **35**, 668-686 (1963).

[26]A. J. Coleman, “Structure of fermion density matrices. II. antisymmetrized geminal powers”, J. Math. Phys. **6**, 1425-1431 (1965).

[27]A. J. Coleman, “The structure of fermion density matrices. III. Long-range order”, J. Low Temp. Phys. **74**, 1-17 (1989).

[28]R. Mitja, “Historical introduction”, en *Reduced-density-matrix mechanics: with application to many-electron atoms and molecules*, Advances in chemical physics (John Wiley & Sons, Inc., Hoboken, NJ, USA, 2007), págs. 11-18.

[29]S. M. Valone, “A one-to-one mapping between one-particle densities and some n-particle ensembles”, J. Chem. Phys. **73**, 4653-4655 (1980).

[30]S. M. Valone, “Consequences of extending 1-matrix energy functionals from pure–state representable to all ensemble representable 1 matrices”, J. Chem. Phys. **73**, 1344-1349 (1980).

[31]D. A. Mazziotti, “Two-electron reduced density matrix as the basic variable in many-electron quantum chemistry and physics”, Chem. Rev. **112**, 244-262 (2012).

[32]D. A. Mazziotti, “Quantum chemistry without wave functions: Two-electron reduced density matrices”, Acc. Chem. Res. **39**, 207-215 (2006).

[33]D. A. Mazziotti, "Realization of quantum chemistry without wave functions through first-order semidefinite programming", Phys. Rev. Lett. **93**, 19-22 (2004).

[34]D. A. Mazziotti, "Variational two-electron reduced-density-matrix theory", en *Reduced-Density-Matrix Mechanics: With Application to Many-Electron Atoms and Molecules*, Advances in chemical physics (John Wiley & Sons, Inc., Hoboken, NJ, USA, 2007), págs. 19-59.

[35]J. Wayne Mullinax, E. Maradzike, L. N. Koulias et al., "Heterogeneous CPU + GPU algorithm for variational two-electron reduced-density matrix-driven complete active-space self-consistent field theory", J. Chem. Theory Comput. **15**, 6164-6178 (2019).

[36]E. Maradzike, G. Gidofalvi, J. M. Turney, H. F. Schaefer y A. E. DePrince, "Analytic energy gradients for variational two-electron reduced-density-matrix-driven complete active space self-consistent field theory", J. Chem. Theory Comput. **13**, 4113-4122 (2017).

[37]J. W. Mullinax, E. Epifanovsky, G. Gidofalvi y A. Eugene Deprince, "Analytic Energy Gradients for Variational Two-Electron Reduced-Density Matrix Methods within the Density Fitting Approximation", J. Chem. Theory Comput. **15**, 276-289 (2019).

[38]J. Fosso-Tande, T. S. Nguyen, G. Gidofalvi y A. E. Deprince, "Large-scale variational two-electron reduced-density-matrix-driven complete active space self-consistent field methods", J. Chem. Theory Comput. **12**, 2260-2271 (2016).

[39]R. R. Li, M. D. Liebenthal y A. E. DePrince III, "Challenges for variational reduced-density-matrix theory with three-particle N-representability conditions", J. Chem. Phys. **155**, 174110 (2021).

[40]W. Kutzelnigg y D. Mukherjee, "Cumulant expansion of the reduced density matrices", J. Chem. Phys. **110**, 2800-2809 (1999).

[41]A. C. Simmonett, J. J. Wilke, H. F. Schaefer y W. Kutzelnigg, "Density cumulant functional theory: First implementation and benchmark results for the DCFT-06 model", J. Chem. Phys. **133**, 28-33 (2010).

[42]A. Y. Sokolov, J. J. Wilke, A. C. Simmonett y H. F. Schaefer, "Analytic gradients for density cumulant functional theory: The DCFT-06 model", J. Chem. Phys. **137** (2012).

[43]A. Y. Sokolov, A. C. Simmonett y H. F. Schaefer, "Density cumulant functional theory: The DC-12 method, an improved description of the one-particle density matrix", J. Chem. Phys. **138** (2013).

[44]J. W. Mullinax, A. Y. Sokolov y H. F. Schaefer 3rd, "Can density cumulant functional theory describe static correlation effects?", J. Chem. Theory Comput. **11**, 2487-2495 (2015).

[45]M. Piris, "A natural orbital functional based on an explicit approach of the two-electron cumulant", Int. J. Quantum Chem. **113**, 620-630 (2013).

[46]D. W. Smith, "N-representability problem for fermion density matrices. I. the second-order density matrix with N =3", J. Chem. Phys. **43**, S258-S264 (1965).

[47]D. W. Smith, "N-Representability problem for fermion density matrices. II. The first-order density matrix with N even", Phys. Rev. **147**, 896-898 (1966).

[48]D. A. Mazziotti, "Structure of fermionic density matrices: complete N-representability conditions", Phys. Rev. Lett. **108**, 263002 (2012).

[49]P. Hohenberg y W. Kohn, "Inhomogeneous electron gas", Physical Review **136**, B864 (1964).

[50]T. L. Gilbert, “Hohenberg-Kohn theorem for nonlocal external potentials”, Phys. Rev. B Condens. Matter **12**, 2111-2120 (1975).

[51]M. Levy, “Universal variational functionals of electron densities, first-order density matrices, and natural spin-orbitals and solution of the *v* -representability problem”, Proc. Natl. Acad. Sci. U. S. A. **76**, 6062-6065 (1979).

[52]A. M. K. Müller, *Explicit approximate relation between reduced two- and one-particle density matrices*, 1984.

[53]S. Goedecker y C. J. Umrigar, “Natural orbital functional for the many-electron problem”, Phys. Rev. Lett. **81**, 866-869 (1998).

[54]O. Gritsenko, K. Pernal y E. J. Baerends, “An improved density matrix functional by physically motivated repulsive corrections”, J. Chem. Phys. **122**, 204102 (2005).

[55]N. N. Lathiotakis y M. A. L. Marques, “Benchmark calculations for reduced density-matrix functional theory”, J. Chem. Phys. **128** (2008).

[56]M. Rodríguez-Mayorga, E. Ramos-Cordoba, M. Via-Nadal, M. Piris y E. Matito, “Comprehensive benchmarking of density matrix functional approximations”, Phys. Chem. Chem. Phys. **19**, 24029-24041 (2017).

[57]R. Kubo, “Generalized cumulant expansion method”, J. Phys. Soc. Jpn. **17**, 1100-1120 (1962).

[58]M. Piris, “A new approach for the two-electron cumulant in natural orbital functional theory”, Int. J. Quantum Chem. **106**, 1093-1104 (2006).

[59]M. Piris, L. A. Montero y N. Cruz, “The Bardeen–Cooper–Schrieffer approach to electron correlation in the density matrix formalism”, J. Chem. Phys. **107**, 180-187 (1997).

[60]M. Piris, “A generalized self-consistent-field procedure in the improved BCS theory”, J. Math. Chem. **25**, 47-54 (1999).

[61]P. Leiva y M. Piris, “Assessment of a new approach for the two-electron cumulant in natural-orbital-functional theory”, J. Chem. Phys. **123**, 214102 (2005).

[62]M. Piris, X. Lopez y J. M. Ugalde, “Dispersion interactions within the Piris natural orbital functional theory: the helium dimer”, J. Chem. Phys. **126**, 214103 (2007).

[63]M. Piris, J. M. Matxain, X. Lopez y J. M. Ugalde, “Communications: accurate description of atoms and molecules by natural orbital functional theory”, J. Chem. Phys. **132**, 031103 (2010).

[64]M. Piris, J. M. Matxain, X. Lopez y J. M. Ugalde, “Communication: the role of the positivity N-representability conditions in natural orbital functional theory”, J. Chem. Phys. **133**, 111101 (2010).

[65]M. Piris, X. Lopez, F. Ruipérez, J. M. Matxain y J. M. Ugalde, “A natural orbital functional for multiconfigurational states”, J. Chem. Phys. **134**, 164102 (2011).

[66]M. Piris, “Interacting pairs in natural orbital functional theory”, J. Chem. Phys. **141**, 044107 (2014).

[67]M. Piris, “Global method for electron correlation”, Phys. Rev. Lett. **119**, 063002 (2017).

[68]M. Piris, “Global natural orbital functional: towards the complete description of the electron correlation”, Phys. Rev. Lett. **127**, 233001 (2021).

[69]M. Piris, J. M. Matxain y X. Lopez, "The intrapair electron correlation in natural orbital functional theory", J. Chem. Phys. **139**, 234109 (2013).

[70]M. Piris, J. M. Matxain, X. Lopez y J. M. Ugalde, "Spin conserving natural orbital functional theory", J. Chem. Phys. **131** (2009).

[71]M. Piris, "Natural orbital functional for multiplets", Phys. Rev. A **100**, 032508 (2019).

[72]U. R. Fogueri, S. Kozuch, A. Karton y J. M. L. Martin, "A simple DFT-based diagnostic for nondynamical correlation", Theor. Chem. Acc. **132**, 1-9 (2013).

[73]I. Shavitt, "The method of configuration interaction", en *Methods of electronic structure theory*, ed. por H. F. Schaefer (Springer US, Boston, MA, 1977), págs. 189-275.

[74]T. J. Lee y P. R. Taylor, "A diagnostic for determining the quality of single-reference electron correlation methods", International Journal of Quantum Chemistry **36**, 199-207 (1989).

[75]C. L. Janssen e I. M. B. Nielsen, "New diagnostics for coupled-cluster and Møller–Plesset perturbation theory", Chem. Phys. Lett. **290**, 423-430 (1998).

[76]I. M. B. Nielsen y C. L. Janssen, "Double-substitution-based diagnostics for coupled-cluster and Møller–Plesset perturbation theory", Chem. Phys. Lett. **310**, 568-576 (1999).

[77]S. Grimme y A. Hansen, "A practicable real-space measure and visualization of static electron-correlation effects", Angewandte Chemie - International Edition **54**, 12308-12313 (2015).

[78]C. A. Bauer, A. Hansen y S. Grimme, "The fractional occupation number weighted density as a versatile analysis tool for molecules with a complicated electronic structure", Chemistry - A European Journal **23**, 6150-6164 (2017).

[79]A. Karton, E. Rabinovich, J. M. L. Martin y B. Ruscic, "W4 theory for computational thermochemistry: In pursuit of confident sub-kJ/mol predictions", J. Chem. Phys. **125** (2006).

[80]O. Tishchenko, J. Zheng y D. G. Truhlar, "Multireference model chemistries for thermochemical kinetics", J. Chem. Theory Comput. **4**, 1208-1219 (2008).

[81]M. Piris y J. M. Ugalde, "Iterative diagonalization for orbital optimization in natural orbital functional theory", J. Comput. Chem. **30**, 2078-2086 (2009).

[82]M. Piris e I. Mitxelena, "DoNOF: An open-source implementation of natural-orbital-functional-based methods for quantum chemistry", Comput. Phys. Commun. **259**, 107651 (2021).

[83]P. Pulay, "Convergence acceleration of iterative sequences. the case of scf iteration", Chem. Phys. Lett. **73**, 393-398 (1980).

[84]B. Levy, "Multi-configuration self-consistent wavefunctions of formaldehyde", Chem. Phys. Lett. **4**, 17-19 (1969).

[85]H. F. King, R. N. Camp y J. W. McIver Jr, "Parametrization of molecular orbital transformations", J. Chem. Phys. **80**, 1171-1174 (1984).

[86]J. Hutter, M. Parrinello y S. Vogel, "Exponential transformation of molecular orbitals", J. Chem. Phys. **101**, 3862-3865 (1994).

[87]G. Chaban, M. W. Schmidt y M. S. Gordon, “Approximate second order method for orbital optimization of SCF and MCSCF wavefunctions”, Theor. Chem. Acc. **97**, 88-95 (1997).

[88]B. Helmich-Paris, “A trust-region augmented Hessian implementation for restricted and unrestricted Hartree-Fock and Kohn-Sham methods”, J. Chem. Phys. **154**, 164104 (2021).

[89]I. A. Elayan, R. Gupta y J. W. Hollett, “ΔNO and the complexities of electron correlation in simple hydrogen clusters”, J. Chem. Phys. **156**, 094102 (2022).

[90]M. R. Hestenes y E. Stiefel, “Methods of conjugate gradients for solving linear systems”, Journal of Research of the National Bureau of Standards **49** (1952).

[91]C. G. Broyden, “The convergence of a class of double-rank minimization algorithms: 2. The new algorithm”, IMA J Appl Math **6**, 222-231 (1970).

[92]R. Fletcher, “A new approach to variable metric algorithms”, Comput. J. **13**, 317-322 (1970).

[93]D. Goldfarb, “A family of variable-metric methods derived by variational means”, Math. Comput. **24**, 23-26 (1970).

[94]D. F. Shanno, “Conditioning of quasi-Newton methods for function minimization”, Math. Comput. **24**, 647-656 (1970).

[95]T. H. Dunning, “Gaussian basis sets for use in correlated molecular calculations. I. The atoms boron through neon and hydrogen”, J. Chem. Phys. **90**, 1007-1023 (1989).

[96]S. K. Lam, A. Pitrou y S. Seibert, “Numba”, en Proceedings of the Second Workshop on the LLVM Compiler Infrastructure in HPC (2015).

[97]R. Okuta, Y. Unno, D. Nishino, S. Hido y C. Loomis, “CuPy: A NumPy-compatible library for NVIDIA GPU calculations”, en Proceedings of workshop on machine learning systems (LearningSys) in The thirty-first annual conference on neural information processing systems (NIPS) (2017).

[98]A. Karton, N. Sylvetsky y J. M. L. Martin, “W4-17: a diverse and high-confidence dataset of atomization energies for benchmarking high-level electronic structure methods”, J. Comput. Chem. **38**, 2063-2075 (2017).

[99]K. R. Bryenton, A. A. Adeleke, S. G. Dale y E. R. Johnson, “Delocalization error: The greatest outstanding challenge in density-functional theory”, Wiley Interdiscip. Rev. Comput. Mol. Sci. (2022).

[100]P. Mori-Sánchez, A. J. Cohen y W. Yang, “Localization and delocalization errors in density functional theory and implications for band-gap prediction”, Phys. Rev. Lett. **100**, 146401 (2008).

[101]S. R. Whittleton, X. A. Sosa Vazquez, C. M. Isborn y E. R. Johnson, “Density-functional errors in ionization potential with increasing system size”, J. Chem. Phys. **142**, 184106 (2015).

[102]Y. Zhang y W. Yang, “A challenge for density functionals: Self-interaction error increases for systems with a noninteger number of electrons”, J. Chem. Phys. **109**, 2604-2608 (1998).

[103]A. Ruzsinszky, J. P. Perdew, G. I. Csonka, O. A. Vydrov y G. E. Scuseria, “Spurious fractional charge on dissociated atoms: pervasive and resilient self-interaction error of common density functionals”, J. Chem. Phys. **125**, 194112 (2006).

[104]P. Mori-Sánchez, A. J. Cohen y W. Yang, “Many-electron self-interaction error in approximate density functionals”, J. Chem. Phys. **125**, 201102 (2006).

[105]W. Yang, Y. Zhang y P. W. Ayers, “Degenerate ground states and a fractional number of electrons in density and reduced density matrix functional theory”, Phys. Rev. Lett. **84**, 5172-5175 (2000).

[106]J. P. Perdew, R. G. Parr, M. Levy y J. L. Balduz, “Density-functional theory for fractional particle number: derivative discontinuities of the energy”, Phys. Rev. Lett. **49**, 1691-1694 (1982).

[107]M. Hellgren y T. Gould, “Strong correlation and charge localization in Kohn-Sham theories with fractional orbital occupations”, J. Chem. Theory Comput. **15**, 4907-4914 (2019).

[108]E. J. Baerends, “Chemical potential, derivative discontinuity, fractional electrons, jump of the Kohn-Sham potential, atoms as thermodynamic open systems, and other (mis)conceptions of the density functional theory of electrons in molecules”, Phys. Chem. Chem. Phys. **24**, 12745-12766 (2022).

[109]D. Hait y M. Head-Gordon, “Delocalization errors in density functional theory are essentially quadratic in fractional occupation number”, J. Phys. Chem. Lett. **9**, 6280-6288 (2018).

[110]A. J. Cohen, P. Mori-Sánchez y W. Yang, “Second-order perturbation theory with fractional charges and fractional spins”, J. Chem. Theory Comput. **5**, 786-792 (2009).

[111]H. Chen, W. Lai y S. Shaik, “Multireference and multiconfiguration ab initio methods in heme-related systems: what have we learned so far?”, J. Phys. Chem. B **115**, 1727-1742 (2011).

[112]Y.-K. Choe, T. Hashimoto, H. Nakano y K. Hirao, “Theoretical study of the electronic ground state of iron(II) porphine”, Chem. Phys. Lett. **295**, 380-388 (1998).

[113]Y.-K. Choe, T. Nakajima, K. Hirao y R. Lindh, “Theoretical study of the electronic ground state of iron(II) porphine. II”, J. Chem. Phys. **111**, 3837-3845 (1999).

[114]A. R. Groenhof, M. Swart, A. W. Ehlers y K. Lammertsma, “Electronic ground states of iron porphyrin and of the first species in the catalytic reaction cycle of cytochrome P450s”, J. Phys. Chem. A **109**, 3411-3417 (2005).

[115]J. E. T. Smith, B. Mussard, A. A. Holmes y S. Sharma, “Cheap and near exact CASSCF with large active spaces”, J. Chem. Theory Comput. **13**, 5468-5478 (2017).

[116]G. Li Manni y A. Alavi, “Understanding the mechanism stabilizing intermediate spin states in Fe(II)-Porphyrin”, J. Phys. Chem. A **122**, 4935-4947 (2018).

JCTC Journal of Chemical Theory and Computation

pubs.acs.org/JCTC Article

Electron Correlation in the Iron(II) Porphyrin by Natural Orbital Functional Approximations

Juan Felipe Huan Lew-Yee, Jorge M. del Campo,* and Mario Piris*

Cite This: J. Chem. Theory Comput. 2023, 19, 211−220 Read Online

ACCESS | Metrics & More | Article Recommendations

ABSTRACT: The relative stability of the singlet, triplet, and quintet spin states of iron(II) porphyrin (FeP) represents a challenging problem for electronic structure methods. While it is currently accepted that the ground state is a triplet, multiconfigurational wave function-based methods predict a quintet, and density functional approximations vary between triplet and quintet states, leading to a prediction that highly depends on the features of the method employed. The recently proposed Global Natural Orbital Functional (GNOF) aims to provide a balanced treatment between static and dynamic correlation, and together with the previous Piris Natural Orbital Functionals (PNOFs), allowed us to explore the importance of each type of correlation in the stability order of the states of FeP with a method that conserves the spin of the system. It is noteworthy that GNOF correlates all electrons in all available orbitals for a given basis set; in the case of the FeP with a double-ζ basis set as used in this work, this means that GNOF can properly correlate 186 electrons in 465 orbitals, significantly increasing the sizes of systems amenable to multiconfigurational treatment. Results show that PNOF5, PNOF7s, and PNOF7 predict the quintet to have a lower energy than the triplet state; however, the addition of dynamic correlation via second-order Møller−Plesset corrections (NOF-MP2) turns the triplet state to be lower than the quintet state, a prediction also reproduced by GNOF that incorporates much more dynamic correlation than its predecessors.

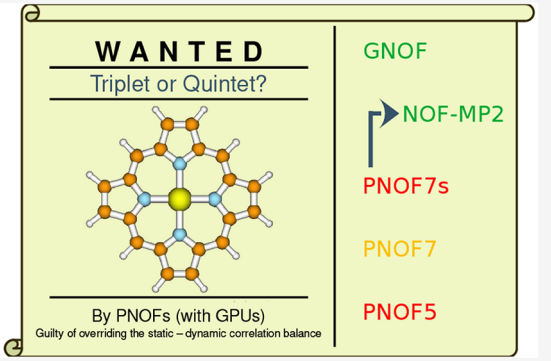

1. INTRODUCTION

As early as the 1970s, it was suggested that one-particle reduced density matrix (RDM) functional theory[1−4] could be an attractive alternative formalism to wave function-based methods. Unfortunately, calculations based on exact functionals generated by the constrained-search formulation are computationally too expensive, which has prompted the development of approximate functionals for practical applications. The functionals currently in use are constructed on the basis where the one-particle RDM is diagonal, which is the definition of a natural orbital functional (NOF).[5,6] In fact, it is more appropriate to speak of a NOF rather than a one-particle RDM functional when dealing with approximate functionals, since a two-particle RDM dependence persists[7] and leads to the functional N-representability problem.[8,9] An extensive account on the evolution of approximate NOFs up to the year 2018 can be found elsewhere.[10−13]

Recent developments[14−47] show that NOF theory has become an active field of research. Nowadays, an open-source implementation of NOF-based methods is available (github.com/DoNOF) to the scientific community. The associated computer program DoNOF (Donostia Natural Orbital Functional)[48] is designed to solve the energy minimization problem of an approximate NOF, describing the ground state of an N-electron system in terms of natural orbitals (NOs) and their occupation numbers (ONs). Fractional occupancies naturally allow NOFs to recover the static correlation. In fact, approximate NOFs have demonstrated[41,49] to be more accurate than their electron density-dependent counterparts for highly multiconfigurational systems and scale satisfactorily compared to wave function-type methods with respect to the number of basis functions.

Particularly successful in describing static electronic correlation are electron-pairing-based NOFs,[50] namely, PNOF5,[51,52] PNOF6,[53] and PNOF7.[54,55] For instance, the PNOF6 dissociation curve of the carbon dimer closely resembles that obtained from the optimized complete active space self-consistent field wave function.[56] So far, only NOFs that satisfy the electron-pairing constraints have provided the correct number of electrons in the fragments after homolytic dissociation.[57,58] PNOF5−PNOF7 take into account most of the nondynamical effects, and also an important part of the

Received: November 2, 2022
Published: December 29, 2022

https://doi.org/10.1021/acs.jctc.2c01093
J. Chem. Theory Comput. 2023, 19, 211−220

dynamic electron correlation corresponding to the intrapair interactions; hence they produce results that are in good agreement with accurate wave function-based methods for small systems, where electron correlation effects are almost entirely intrapair. However, when the number of pairs increases, the total energy values deteriorate, especially in those regions where dynamic correlation prevails.

There are several strategies for adding the missing dynamic correlation to an approximate NOF, but second-order perturbative corrections are probably the simplest and cheapest way to properly incorporate dynamical correlation effects, which has given rise to two methods. The first uses a size-consistent multiconfigurational second-order perturbation theory (PT2), taking as reference the generating wave function of PNOF5, which leads to the PNOF5-PT2 method.[59,60] The other proposal, called NOF-MP2,[54] adds second-order Møller−Plesset (MP2) corrections to a reference Slater determinant wave function formed with the NOs of PNOF7. Let us note that PNOF5 is strictly N-representable; i.e., the functional can be derived from a wave function that is antisymmetric in N-particles, so PNOF5-PT2 is well-defined and the perturbative corrections are added to PNOF5 energy. On the contrary, for PNOF7 the generating wave function is unknown, and in the NOF-MP2 method static and dynamic corrections are added to a Hartree−Fock (HF) type energy.

The reformulation[61] of NOF-MP2 based on the static part of PNOF7 (PNOF7s) and the orbital-invariant MP2 allowed us to prevent reference ONs and NOs from being spuriously influenced by nondynamic correlation in dynamic correlation domains and extend the NOF-MP2 method to any type of orbitals, including localized ones, respectively. NOF-MP2 has been shown to provide quantitative agreement for dissociation energies, with performance comparable to that of the accurate complete active space second-order perturbation theory in hydrogen abstraction reactions,[19] and is highly reliable for accurate chemical reaction mechanistic studies in elementary reactions of transition metal compounds.[31]

A canonicalization procedure applied to the NOs gave us the possibility to combine any many-body perturbation method,[62] like random-phase approximation or coupled-cluster singles and doubles, with a NOF. The inclusion of perturbative corrections improves the absolute energies over the reference NOF values and approaches the energies obtained by accurate wave function-based methods; however, it does not improve the quality of the reference NOs and ONs. A full optimization would be the only way to obtain completely correlated ONs and NOs. Unfortunately, such a self-consistent procedure makes perturbative methods incredibly computationally expensive, so it is preferable to recover the missing dynamic correlation using a more general NOF than PNOF7.

An important recent development that reinforced this strategy was the implementation of the resolution of the identity approximation (RI) in DoNOF[30] and in the FermiONs++ program package.[40] The RI implementation substantially reduces memory and arithmetic scaling factors in NOF calculations. Such developments have made it possible to perform calculations on large systems of chemical interest with tens of atoms, hundreds of electrons, and thousands of basis functions, for example, the 117-atom 2′-carbamate taxol and the 168-atom valinomycin molecule.[40]

Recently,[38] a NOF was proposed for electronic systems with any spin value regardless of the external potential, that is, a global NOF (GNOF). The adjective "global" is used instead of "universal" to differentiate this approximate multipurpose NOF from Valone's exact one.[4] GNOF is able to achieve a balanced treatment of static and dynamic electron correlations even for those systems with significant multiconfigurational character, preserving the total spin of multiplets.[14] It should be noted that the agreement obtained by GNOF with accurate wave function-based methods is not only for relative energies but also for absolute energies, a sign of good results for good reasons. An example is the agreement obtained between GNOF and Full Configuration Interaction (FCI) for challenging dissociation processes in one, two, and three dimensions.[41] Nevertheless, we must point out that GNOF, like its predecessors, is not variational since only some necessary N-representability conditions have been imposed, with the sole exception of PNOF5 for which we know the generating wave function.

The simple construction of GNOF allowed us to examine the effects of different types of electron correlations. The functional has a term that fully recovers the intrapair electron correlation, that corresponds to the independent-pair model, followed by a second term that corresponds to the static interpair correlation, and it also takes into account the dynamic correlation between electron pairs. The aim of this work is to analyze the influence of different types of correlation on the spin state stability of iron(II) porphyrin molecule (FeP), as shown in Figure 1, a system with 37 atoms and 186 electrons.

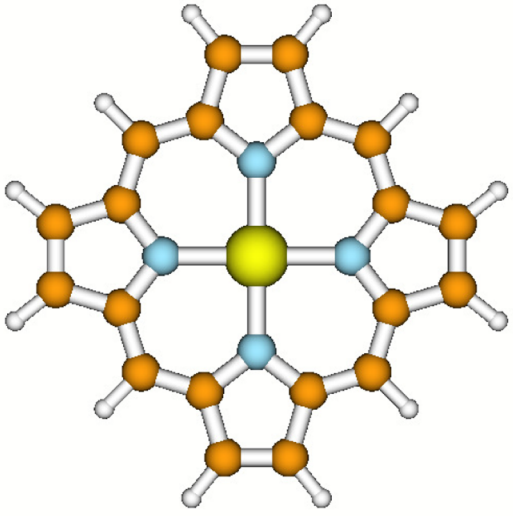

Figure 1. Iron(II) Porphyrin.

FeP is a model system for more general substituted iron porphyrins that play a vital role in many biological processes, including oxygen transport, electron transfer, and catalyzing the incorporation of oxygen into other molecules.[63] The relationship between spin state and structure of FeP constitutes an active research topic[64] due to its implications for the biological activity of heme proteins.[65,66]

The iron porphyrins have proven to be challenging for any theoretical method and an attractive system for testing the GNOF. Initial single reference studies considered a triplet state,[67−70] but subsequent multireference studies favored a quintet state.[71,72] The controversy about the spin of the ground state of FeP continues to this day, and the discussion has become enriched with the increase of computational power

https://doi.org/10.1021/acs.jctc.2c01093
J. Chem. Theory Comput. 2023, 19, 211−220

and the development of innovative methods to include electronic correlation more accurately.

Calculations with currently used single reference methods such as coupled cluster and modern density functional approximations tend to favor the triplet as the ground state,[73−75] and the triplet and quintet states have been reported to not present essential symmetry breaking.[76] In addition, typical complete active space (CAS) calculations point to the quintet,[77] but increasing the size of the active space changes the prediction to the triplet; it has been stated that the preference for a quintet may be an artifact caused by an insufficiently large active space.[78,79] Pair density functional theory (PDFT) points to the triplet,[80] as well as calculations of stochastic generalized active space self-consistent field.[81] However, the discussion is not so easy to conclude, as the density matrix renormalization group (DMRG) points to a quintet state,[82] even after coupling with the adiabatic connection to include dynamic correlation.[83] Studies on the influence of the exact exchange on DFAs concluded that the inclusion of a large amount of it favors high-spin states, while smaller contributions favor low-spin states,[84,85] and this becomes relevant as a recent study of PDFT has found that the use of hybrid functionals reverts the tendency to the quintet state for some on-top functional.[86] Hence, the controversy remains of active interest.

This study provides important information in many ways. First, the analysis of FeP from the perspective of PNOF functionals might provide information on the static and dynamic correlation effects on the problem. At the same time, it will allow us to compare the set of PNOFs with the different methods previously used to study FeP. Note further that GNOF correlates all electrons into all available orbitals for a given basis set, which in the case of FeP using a double-ζ basis set correlates 186 electrons in 465 orbitals. To the best of our knowledge, such a correlation calculation is not possible with current wave function-based methods, such as CAS or DMRG.

The work is organized as follows. First, Section 2 presents a brief review of GNOF and the M diagnostic used to characterize the NOFs solutions. This is followed by the computational details related to the NOF calculations in Section 3. Section 4 presents an analysis of the performance of PNOF5, PNOF7, PNOF7s, NOF-MP2, and GNOF over the spin-stability order of FeP, together with a discussion of the electron correlation effects provided by each functional. Finally, conclusions are given in Section 5.

2. THEORY

In this section, we briefly describe GNOF, and a more detailed description can be found in ref 38. The nonrelativistic Hamiltonian under consideration is spin coordinate free; therefore, a state with total spin S is a multiplet, i.e., a mixed quantum state that allows all possible S_z values. We consider N_I single electrons which determine the spin S of the system, and the rest of electrons ($N_{II} = N - N_I$) are spin-paired so that all spins corresponding to N_{II} electrons altogether provide a zero spin. In the absence of single electrons ($N_I = 0$), the energy obviously reduces to a NOF that describes singlet states.

We focus on the mixed state of highest multiplicity: $2S + 1 = N_I + 1$, $S = N_I/2$.[14] For an ensemble of pure states $\{|SM_s\rangle\}$, we note that the expected value of $\hat{S}_z$ for the whole ensemble is zero. Consequently, the spin-restricted theory can be adopted even if the total spin of the system is not zero. We use a single set of orbitals for α and β spins. All the spatial orbitals will be then doubly occupied in the ensemble so that occupancies for particles with α and β spins are equal: $n_p^\alpha = n_p^\beta = n_p$.

We divide the orbital space Ω into two subspaces: $\Omega = \Omega_I \oplus \Omega_{II}$. Ω_{II} is composed of $N_{II}/2$ mutually disjoint subspaces Ω_g. Each of which contains one orbital $|g\rangle$ with $g \le N_{II}/2$ and N_g orbitals $|p\rangle$ with $p > N_{II}/2$, namely,

$$\Omega_g = \{|g\rangle, |p_1\rangle, |p_2\rangle, ..., |p_{N_g}\rangle\} \tag{1}$$

Taking into account the spin, the total occupancy for a given subspace Ω_g is 2, which is reflected in the following sum rule:

$$\sum_{p\in\Omega_{II}} n_p = n_g + \sum_{i=1}^{N_g} n_{p_i} = 1, \quad g = 1, 2, ..., \frac{N_{II}}{2} \tag{2}$$

Here, the notation $p \in \Omega_{II}$ represents all the indexes of $|p\rangle$ orbitals belonging to Ω_{II}. In general, N_g can be different for each subspace as long as it describes the electron pair well. For convenience, in this work we take it to be equal for all subspaces $\Omega_g \in \Omega_{II}$ to the maximum possible value determined by the basis set used in calculations. From eq 2, it follows that

$$2\sum_{p\in\Omega_{II}} n_p = 2\sum_{g=1}^{N_{II}/2}\left(n_g + \sum_{i=1}^{N_g} n_{p_i}\right) = N_{II} \tag{3}$$

Similarly, Ω_I is composed of N_I mutually disjoint subspaces Ω_g. In contrast to Ω_{II}, each subspace $\Omega_g \in \Omega_I$ contains only one orbital g with $2n_g = 1$. It is worth noting that each orbital is completely occupied individually, but we do not know whether the electron has α or β spin: $n_g^\alpha = n_g^\beta = n_g = 1/2$. It follows that

$$2\sum_{p\in\Omega_I} n_p = 2\sum_{g=N_{II}/2+1}^{N_\Omega} n_g = N_I \tag{4}$$

In eq 4, $N_\Omega = N_{II}/2 + N_I$ denotes the total number of suspaces in Ω. Taking into account eqs 3 and 4, the trace of the 1RDM is verified equal to the number of electrons:

$$2\sum_{p\in\Omega} n_p = 2\sum_{p\in\Omega_{II}} n_p + 2\sum_{p\in\Omega_I} n_p = N_{II} + N_I = N \tag{5}$$

Using ensemble N-representability conditions, we can generate a reconstruction functional for the 2RDM in terms of the ONs that leads to GNOF:

$$E = E^{intra} + E_{HF}^{inter} + E_{sta}^{inter} + E_{dyn}^{inter} \tag{6}$$

The intrapair component is formed by the sum of the energies of the pairs of electrons with opposite spins and the single-electron energies of the unpaired electrons, namely,

$$E^{intra} = \sum_{g=1}^{N_{II}/2} E_g + \sum_{g=N_{II}/2+1}^{N_\Omega} H_{gg} \tag{7}$$

$$E_g = \sum_{p\in\Omega_g} n_p(2H_{pp} + J_{pp}) + \sum_{q,p\in\Omega_g, p\neq q} \Pi(n_q, n_p)L_{pq} \tag{8}$$

where

$$\Pi(n_q, n_p) = \sqrt{n_q n_p}(\delta_{q\Omega^a}\delta_{p\Omega^a} - \delta_{qg} - \delta_{pg}) \tag{9}$$

https://doi.org/10.1021/acs.jctc.2c01093
J. Chem. Theory Comput. 2023, 19, 211−220

Table 1. Spin State Energies (Hartree) for FeP Calculated by a Perfect Pairing PNOF5, PNOF7s, PNOF7, NOF-MP2, and GNOF, with its Corresponding Singlet−Triplet Adiabatic Gap (ST), $E_{singlet}-E_{triplet}$, and Quintet−Triplet Adiabatic Gap (QT), $E_{quintet}-E_{triplet}$, in kcal/mol[a]

MUL	PNOF5	PNOF7s	PNOF7	NOF-MP2	GNOF
S	−2245.417	−2245.436	−2245.989	−2248.384	−2247.769
T	−2245.484	−2245.492	−2246.014	−2248.456	−2247.869
ST	42	35	16	45	63
Q	−2245.549	−2245.560	−2246.042	−2248.416	−2247.766
QT	−29	−36	−17	25	65

[a]The values correspond to calculations using the optimized geometries of ref 74 and the RI approximation.

and H_{pp} are the diagonal one-electron matrix elements of the kinetic energy and external potential operators. $J_{pq} = \langle pq|pq\rangle$ and $L_{pq} = \langle pp|qq\rangle$ are the Coulomb and exchange-time-inversion integrals, respectively. Ω^a denotes the subspace composed of orbitals above the level N_Ω ($p > N_\Omega$). The intersubspace HF term is

$$E_{HF}^{inter} = {\sum_{p,q=1}^{N_B}}' n_q n_p (2J_{pq} - K_{pq}) \tag{10}$$

where $K_{pq} = \langle pq|qp\rangle$ are the exchange integrals. The prime in the summation indicates that only the intersubspace terms are taking into account ($p \in \Omega_f$, $q \in \Omega_g$, $f \neq g$). N_B represents the number of basis functions considered. The intersubspace static component is written as

$$\begin{aligned} E_{sta}^{inter} = &-\left(\sum_{p=1}^{N_\Omega}\sum_{q=N_\Omega+1}^{N_B} + \sum_{p=N_\Omega+1}^{N_B}\sum_{q=1}^{N_\Omega} + \sum_{p,q=N_\Omega+1}^{N_B}\right)' \\ &\Phi_q\Phi_p L_{pq} - \frac{1}{2}\left(\sum_{p=1}^{N_{II}/2}\sum_{q=N_{II}/2+1}^{N_\Omega} + \sum_{p=N_{II}/2+1}^{N_\Omega}\sum_{q=1}^{N_{II}/2}\right)' \\ &\Phi_q\Phi_p L_{pq} - \frac{1}{4}\sum_{p,q=N_{II}/2+1}^{N_\Omega} K_{pq} \end{aligned} \tag{11}$$

where $\Phi_p = \sqrt{n_p h_p}$ with the hole $h_p = 1 - n_p$. Note that Φ_p has significant values only when the occupation number n_p differs substantially from 1 and 0. Finally, the intersubspace dynamic energy can be conveniently expressed as

$$E_{dyn}^{inter} = {\sum_{p,q=1}^{N_B}}' [n_q^d n_p^d + \Pi(n_q^d, n_p^d)](1 - \delta_{q\Omega_{II}^b}\delta_{p\Omega_{II}^b})L_{pq} \tag{12}$$

In eq 12, Ω_{II}^b denotes the subspace composed of orbitals below the level $N_{II}/2$ ($p \leq N_{II}/2$), so interactions between orbitals belonging to Ω_{II}^b are excluded from E_{dyn}^{inter}. The dynamic part of the ON n_p is defined as

$$n_p^d = n_p \cdot e^{-\left(\frac{h_g}{h_c}\right)^2}, \quad p \in \Omega_g \tag{13}$$

with $h_c = 0.02\sqrt{2}$.[38] The maximum value of n_p^d is around 0.012 in accordance with the Pulay's criterion that establishes an occupancy deviation of approximately 0.01 with respect to 1 or 0 for a NO to contribute to the dynamic correlation. Clearly, GNOF does not take into account the dynamic correlation of single electrons ($p \in \Omega_I$) via the E_{dyn}^{inter} term. Considering real spatial orbitals ($L_{pq} = K_{pq}$) and $n_p \approx n_p^d$, it is not difficult to verify that the terms proportional to the product of the ONs will cancel out, so that only those terms proportional to Π will contribute significantly to the energy.

It is important to note that GNOF preserves the total spin of the multiplet: $\langle \hat{S}^2 \rangle = S(S+1)$.[14] Taking into account that GNOF does not contain intersubspace terms between orbitals below N_B, except for the HF-like terms of the eq 10, eq 6 reduces to the PNOF7-like functional[54,55] when the interpair dynamic term (E_{dyn}^{inter}) is neglected. Furthermore, taking $\Phi_p = 2n_p h_p$ in eq 11 the PNOF7s-like version of the functional is obtained.[61] Finally, if the intersubspace static term (E_{sta}^{inter}) is also disregarded, then GNOF reduces to PNOF5.[52]

The solutions of PNOFs can be characterized according to the recently proposed M-diagnostic[87] adapted to the NOF multiplet calculations,[47] namely,

$$M = [1 - n_{LSONO}] + n_{LWONO} \tag{14}$$

where LSONO stands for the least strongly occupied NO, that is, the orbital with ON farthest from 1 below $N_{II}/2$, so it belongs to Ω_{II}^b subspace, and LWONO for the least weakly occupied NO, that is, the orbital with ON farthest from 0 above N_Ω, so it belongs to Ω^a subspace. Recall that M values close to zero indicate the predominance of dynamic correlation, while values beyond 0.1 indicate the predominance of static correlation.

3. COMPUTATIONAL DETAILS

In this work, we have used the optimized structures of FeP reported in ref 74 for the singlet, triplet, and quintet states, as has been used in subsequent studies;[40,76,88] hence the energy gaps are computed adiabatically. The Fe−N distance might be relevant for the energetics of the problem; in the used structures this distance corresponds to 1.979 Å for the singlet, 1.976 Å for the triplet, and 2.053 Å for the quintet. The solution of the NOF equations has been established by optimizing the energy separately with respect to the ONs and to the NOs. Therefore, orbitals vary along the optimization process until the most favorable orbital interactions are found. NOF-MP2 calculations have been carried out as described in ref 62. We have taken this opportunity to test an in-house piece of software written in Julia, currently named DoNOF.jl, and with integral transformation accelerated by graphic processing units (GPUs) in the calculations of the perfect pairing approach ($N_g = 1$), while the extended pairing calculations ($N_g = 4$) have been carried out using the DoNOF code.[48] The correlation-consistent valence double-basis set including polarization (cc-pVDZ)[89,90] was used throughout, as has been previously reported that the active space is more important than using a larger basis set (e.g., cc-pVTZ) to achieve the correct prediction.[40,78] The resolution of the identity (RI) was used to reduce the computational cost of

https://doi.org/10.1021/acs.jctc.2c01093
J. Chem. Theory Comput. 2023, 19, 211−220

the calculations, as reported in ref 91 (including for NOF-MP2), and the cc-pVDZ-jkfit[92] auxiliary basis set was used for all atoms except iron, for which the def2-universal-jkfit[93] auxiliary basis set was used.

4. RESULTS AND DISCUSSION

We aim to understand the stabilization of the spin states in terms of the static and dynamic correlation effects by means of PNOF5, PNOF7s, PNOF7, NOF-MP2, and GNOF calculations. For this purpose, a discussion is given for both the perfect pairing and the extended PNOF approaches, with special attention to the features of the solutions given by each functional.

4.1. Perfect Pairing. Here we study the spin-state stability of FeP using the most simple approach for electron-pairing-based NOFs, that is, pairing a single weakly occupied orbital to each strongly occupied orbital in each subspace, namely, the perfect-pairing approach. Table 1 presents the energy values of the singlet, triplet, and quintet states of FeP in its rows, calculated with PNOF5, PNOF7s, PNOF7, NOF-MP2, and GNOF as shown in each column. First, we observe that the energy decreases according to the order PNOF5 > PNOF7s > PNOF7 > GNOF > NOF-MP2 for all spin states, which corresponds to the order of increase of electron correlation in perfect-pairing coupling. In addition, the singlet−triplet (ST) gaps and the quintet-triplet (QT) gaps allow us to check whether the spin state is more stable with respect to the triplet. Positive values indicate that the triplet state is lower in energy, whereas negative values indicate that either the singlet or the quintet state is lower in energy than the triplet state. Overall, PNOF5, PNOF7s, and PNOF7 predict the quintet as the ground state of FeP, which agrees with the multiconfigurational wave functions that include more static correlation, whereas, NOF-MP2 and GNOF afford the expected triplet ground state. The case of GNOF requires a more detailed analysis of the singlet state (vide infra).

Take the PNOF5 QT gap as a reference to analyze the results obtained and recall that it considers only static and dynamic intrapair correlation but does not have intersubspace correlation terms that are important for medium and large size systems. These terms are found in PNOF7s and PNOF7 leading to deeper total energy values but predict QT gaps with the wrong sign. It should be noted that PNOF7 predicts a lower QT gap than PNOF7s, a performance associated with the PNOF7 static overcorrelation at the equilibrium structures where the dynamic correlation predominates. In contrast, PNOF7s takes into account the correct amount of static intersubspace correlation; therefore, its energy is in between PNOF5 and PNOF7, but the QT gap prediction is worse due to the lack of the intersubspace dynamic correlation.

NOF-MP2 includes the dynamic correlation taking as reference the Slater determinant formed with the PNOF7s NOs[61] and predicts the triplet as the ground state, with a QT gap of 25 kcal/mol with the expected sign. This outcome supports the thesis that dynamic correlation is crucial for predicting the triplet as the ground state. In order to obtain GNOF energies, PNOF7s NOs and ONs were used as starting solutions. Since GNOF accounts for static and dynamic correlations, this functional is also capable of predicting the triplet state to be lower in energy than the quintet.

Regarding the singlet state, we must note that all functionals provide a state with a marked multiconfigurational character, as has been reported in previous studies.[76,94] Remarkably, a ST gap of 17 kcal/mol is achieved by a traditional HF-MP2 calculation that is even lower than the QT gap obtained with the NOF-MP2 method. This result confirms the importance of dynamic correlation and points out the existence of a singlet with a predominant single-reference character.

It should be noted that the total energies of PNOF7s shown in Table 1 are well below the values obtained by Lemke et al.,[40] namely, −2244.6016 and −2244.6514 for the triplet and quintet states, respectively. The latter are very close to the HF energies and must then correspond to local minima. In contrast, our PNOF7s energies are in better agreement with the results of CAS(44,44).[78] They are also lower in energy, since they correlate 186 electrons in 184 and 182 orbitals for triplet and quintet states, respectively. Recall that in multiplet states, single-electron subspaces are made up of a single orbital with $2n_g = 1$, while electron-paired subspaces are those that follow the perfect pairing.

The M diagnostic of the PNOFs solutions for the spin states of FeP are shown in Table 2. For the triplet and quintet states, PNOF5, PNOF7s, and GNOF provide solutions below 0.1, which indicates that dynamic correlation is the dominant contribution. Note that the solutions of PNOF5 and PNOF7s are close to 0.1, indicating that the static correlation is important despite not being the dominant contribution. In contrast, the results of PNOF7 are strongly dominated by static correlation. It is noteworthy that the singlet states achieved with all functionals present an M-diagnostic value of 1.0, which in the perfect-paring approach directly indicates a diradical character, in agreement with previous reports.[76,94]

Table 2. M Diagnostic for the Spin States of FeP Computed with PNOF5, PNOF7s, and PNOF7

MUL	PNOF5	PNOF7s	PNOF7	GNOF
S	1.00	1.00	1.00	1.00
T	0.07	0.07	0.60	0.04
Q	0.07	0.08	0.56	0.04

It has been stated that the NO picture can be used to earn chemical relevant information.[95] Following this idea, Table 3 presents selected frontier orbitals of each NOF considered in this work for the triplet state. A gradual transformation can be observed from left (PNOF5) to right (GNOF) through an increase in correlation. The main change can be observed in the first row corresponding to the LSNO (equivalent to the HF HOMO), where the effect of the increase of electron correlation is to allow the "d" orbitals of the iron atom to interact with the π orbitals of the porphyrin, as can be seen in PNOF7 and GNOF. A similar effect can be seen in the second and third rows corresponding to the single-electron NOs of the Ω_I subspace, where the "d" orbital of the iron atoms appears for all PNOFs; however, the NO of GNOFs spreads throughout the molecule. These results are in accordance with the results reported in ref 96, where it is stated that these orbital interactions are the key factor for the correct ordering between the triplet and the quintet states, as achieved by GNOF.

4.2. Extended Pairing. In this section, the extended-pairing approach is used to go beyond the results of the previous section. For this purpose, the number of weakly occupied orbitals coupled to each strongly occupied orbital was increased to four; that is, the highest possible coupling with the cc-pVDZ basis set was used. Once again, we used the

https://doi.org/10.1021/acs.jctc.2c01093
J. Chem. Theory Comput. 2023, 19, 211−220

Table 3. Natural Orbitals of the Triplet State of FeP Computed with PNOF5, PNOF7s, PNOF7, and GNOF

PNOF5	PNOF7s	PNOF7	GNOF
Orbital of highest energy in the Ω_b subspace			
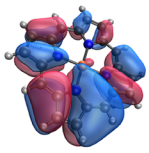	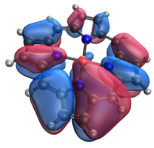	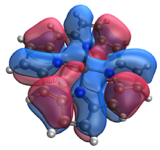	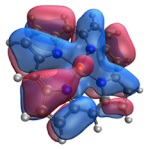
First orbital of the Ω_I subspace			
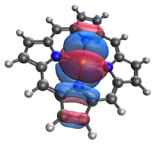	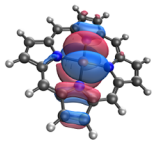	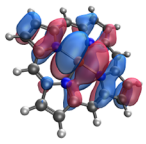	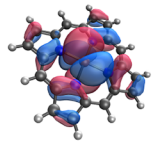
Second orbital of the Ω_I subspace			
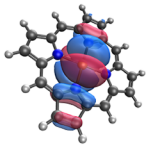	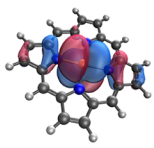	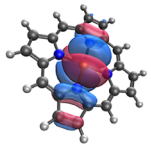	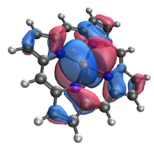
Orbital of lowest energy in the Ω_a subspace			
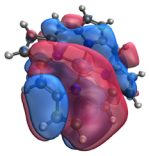	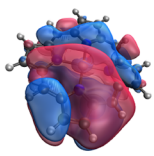	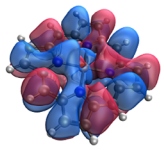	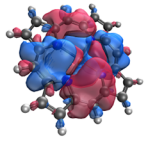

NOs and ONs obtained with the PNOF7s as inputs to achieve the GNOF solutions. In addition, the full electron repulsion integrals are used.

It can be seen from Table 4 that there is an improvement in the PNOF5 QT gap as the amount of intrapair correlation is increased. As expected, the QT gaps of PNOF7s and GNOF are significantly improved due to an increase in the electron correlation between orbitals that form the single- and paired-electron subspaces, which are not present in the independent pair approximation leading to PNOF5. As noted in the previous section, PNOF7 tends to overestimate the non-dynamic electronic correlation between subspaces in the equilibrium region, so these results were not included in the table.

Table 4. Spin State Energies (Hartree) for FeP Calculated by Extended Pairing PNOF5, PNOF7s, and GNOF, with Its Corresponding Singlet−Triplet Adiabatic Gap (ST) and Quintet−Triplet Adiabatic Gap (QT), in kcal/mol[a]

MUL	PNOF5	PNOF7s	GNOF
S	−2245.644	−2245.696	−2248.830
T	−2245.742	−2245.748	−2248.855
ST	62	33	16
Q	−2245.766	−2245.776	−2248.784
QT	−15	−16	45

[a]The optimized geometries of ref 74 are used.

4.2.1. Singlet State with Predominant Dynamic Correlation. As the results of the previous section demonstrate, the inclusion of intersubspace dynamic correlation is crucial for GNOF to favor the intermediate spin state over the low and high spin states. We also noted that the singlet obtained by GNOF from the PNOF7s solution has a marked multiconfigurational character. However, as mentioned above, a traditional MP2 calculation based on the HF reference affords a ST gap that is below the NOF-MP2 result obtained from the reference multiconfigurational PNOF7s singlet. Consequently, we wonder if there is another GNOF singlet state where dynamic correlation predominates. In fact, starting from HF solutions, we have obtained GNOF singlet states with energies of −2247.914 and −2248.918 hartree corresponding to perfect and extended couplings, respectively. Clearly, these energy values favor the singlet with predominant dynamic correlation as the lowest energy state in the GNOF case.

On the other hand, we must be cautious in claiming that this singlet is the state of minimum energy in FeP. If we look more closely at expression 12 that determines the dynamic correlation in GNOF, we can conclude that orbitals with ONs close to half do not contribute to the intersubspace dynamic correlation; that is, it is actually a dynamic correlation term between the electron pairs. Consequently, GNOF does not contain dynamic correlation terms of the single electrons

https://doi.org/10.1021/acs.jctc.2c01093
J. Chem. Theory Comput. 2023, 19, 211−220

that appear in spin multiplets. This behavior has been observed in other systems, such as molecular oxygen, for which the ST gap is underestimated. In the case of FeP, it could be that GNOF is underestimating the energy of the triplet and quintet states as well as that of the open-shell singlet. It is evident that until we have an improved GNOF that includes the dynamic correlation of those orbitals with total occupancies equal to one (half in the case of the NO), we can only give a partial answer as this study shows.

4.3. Computational Times. This work ends with some details related to the time required for the calculations. In particular, the calculations presented in this section were performed in a Julia version of the DoNOF software.[30,48] Similar codes have been reported[97] for other electronic structure methods. As noted above, the NOF equations are solved by optimizing the NOs and ONs separately, and these steps together form an outer iteration in the optimization procedure. Our implementation has been tested on an AMD Ryzen 5800 and in two GPUs, the first being a NVIDIA Turing RTX2080 and the second a NVIDIA Tesla V100. For reference, the hardware configurations are the following:

- CPU-only calculations: AMD Ryzen 5800X with 8 cores-16 threads
- GPU calculations:
  - NVIDIA GeForce RTX 2080 with a 8 cores-16 threads AMD Ryzen 5800X CPU
  - NVIDIA Tesla V100 with a 4 cores Intel Xeon Gold 5122 CPU

The integral transformation on the CPU is currently based on Tullio.jl,[98] while the transformation on the GPU depends mainly on TensorOperations.jl.[99] Table 5 presents the computational times for an outer iteration composed of 30 inner iterations of orbital optimization through the iterative diagonalization algorithm[100] and the ON optimization using the BFGS algorithm up to |grad| < 10^{-4}.

Table 5. Computational Times (s) for Calculations Corresponding to the RI Approximation Using a CPU, a NVIDIA GeForce RTX2080 GPU, and a NVIDIA Tesla V100 GPU

	Perfect Pairing (N_g = 1)			Extended Pairing (N_g = 4)		
Optimization Type	CPU	RTX2080	V100	CPU	RTX2080	V100
NO Optimization	253	10	8	762	22	42
ON Optimization	3	0.2	0.7	109	113	113
Outer Iteration	256	10.2	8.7	871	110	155

A significant improvement in computational time has been achieved in all cases with the GPU implementation, with the cuTENSOR library being a key factor for this success. The integral transformation is the dominating step in both the NO and the ON minimization when the perfect pairing approach is employed; hence the time of an outer iteration is directly benefited when it is performed in a GPU, achieving a speed-up of around 25 times relative to the CPU for the GeFroce RTX2080 GPU and 29 times for the Tesla V100 GPU.

On the other hand, when the CPU is used for the calculations using the extended pairing approach, the NO optimization remains the bottleneck, but the contribution of the ON optimization to the time of an outer iteration increases significantly. In fact, when the GPU is introduced for the integral transformations, the NO optimization time is significantly reduced, as can be seen by going from 762 s on the CPU to 22 s in the RTX2080 hardware configuration, but the ON optimization time remains almost the same; this is the reason the speed-up is reduced to eight times for the extended pairing approach. It is worth noting that the integral transformation is performed only once in the ON optimization; hence, this is not the bottleneck but the calculation of the gradients performed in the CPU. We expect to present further details of this implementation in a future article.

5. CONCLUSIONS

The PNOFs were used to elucidate the picture of the spin stability order of iron porphyrin. It has been found that NOFs that do not consider a significant amount of dynamic correlation, such as PNOF5, PNOF7s, and PNOF7, favor the quintet as the ground state. In these functionals, the increase of the subspace size improves the results due to the inclusion of dynamic intrapair correlation, but the wrong sign of the quintet−triplet gap remains. On the other hand, methods incorporating significant amounts of dynamic correlation, such as NOF-MP2 and GNOF, achieve the correct prediction for the quintet−triplet gap of FeP and predict the triplet as the ground state if we consider the singlet with multiconfigurational character for GNOF.

Surprisingly, there is another singlet state predicted by GNOF with a predominant dynamic correlation. In principle, this state is the one with the lowest energy, which reinforces the importance of the dynamic correlation in the stability of the iron porphyrin; however, GNOF does not contain dynamic correlation terms for the single electrons that appear in spin multiplets, so we cannot provide a definitive answer at this time, for this finding.

Larger systems, such as FeP with 37 atoms and 186 electrons, have been shown to be affordable for NOFs to handle high levels of correlation. This significantly increases the size of the systems susceptible to multiconfigurational treatment, especially when it comes to graphic processing units, such as those used in this work for the two-electron integral transformation.

In addition, GNOF correlates all electrons in all available orbitals preserving the total spin of multiplet states, which in the case of FeP using a double-ζ basis set implies 186 electrons into 465 orbitals. To the best of our knowledge, such calculations have not been done so far with current wave function-based methods, and they are expected to become a reference calculation.

AUTHOR INFORMATION

Corresponding Authors

Jorge M. del Campo − *Departamento de Física y Química Teórica, Facultad de Química, Universidad Nacional Autónoma de México, México City C.P. 04510, México;* orcid.org/0000-0002-4195-3487; Email: jmdelc@unam.mx

Mario Piris − *Kimika Fakultatea, Euskal Herriko Unibertsitatea (UPV/EHU), 20080 Donostia, Euskadi, Spain; Donostia International Physics Center (DIPC), 20018 Donostia, Euskadi, Spain; IKERBASQUE, Basque Foundation for Science, 48013 Bilbao, Euskadi, Spain;* orcid.org/0000-0003-0222-2953; Email: mario.piris@ehu.eus

https://doi.org/10.1021/acs.jctc.2c01093
J. Chem. Theory Comput. 2023, 19, 211−220

Author

Juan Felipe Huan Lew-Yee − *Departamento de Física y Química Teórica, Facultad de Química, Universidad Nacional Autónoma de México, México City C.P. 04510, México;* orcid.org/0000-0002-3908-3144

Complete contact information is available at: https://pubs.acs.org/10.1021/acs.jctc.2c01093

Funding

Support comes from Ministerio de Economía y Competitividad (ref. PID2021-126714NB-I00). The authors are grateful for technical and human support provided by IZO-SGI SGIker of UPV/EHU and European funding (ERDF and ESF). J.F.H. Lew-Yee with CVU Grant No. 867718 acknowledges CONACyT for the Ph.D. scholarship. J.M. del Campo acknowledges funding from Project Grant Nos. CB-2016-282791 and PAPIIT-IN201822 and computing resources from the LANCAD-UNAM-DGTIC-270 project.

Notes

The authors declare no competing financial interest.

REFERENCES

(1) Gilbert, T. L. Hohenberg-Kohn theorem for nonlocal external potentials. *Phys. Rev. B* **1975**, *12*, 2111−2120.

(2) Donnelly, R. A.; Parr, R. G. Elementary properties of an energy functional of the first-order reduced density matrix. *J. Chem. Phys.* **1978**, *69*, 4431−4439.

(3) Levy, M. Universal variational functionals of electron densities, first-order density matrices, and natural spin-orbitals and solution of the v-representability problem. *Proc. Natl. Acad. Sci. U.S.A.* **1979**, *76*, 6062−6065.

(4) Valone, S. M. Consequences of extending 1 matrix energy functionals pure-state representable to all ensemble representable 1 matrices. *J. Chem. Phys.* **1980**, *73*, 1344−1349.

(5) Goedecker, S.; Umrigar, C. J. In *Many-electron densities and reduced density matrices*; Cioslowski, J., Ed.; Kluwer Academic/Plenum Publishers: New York, 2000; pp 165−181.

(6) Piris, M. In *Reduced-Density-Matrix Mechanics with Application to Many-Electron Atoms and Molecules*; Mazziotti, D. A., Ed.; John Wiley and Sons: Hoboken, NJ, U.S.A., 2007; Vol. *134*; Chapter 14, pp 387−427.

(7) Donnelly, R. A. On fundamental difference between energy functionals based on first- and second-order density matrices. *J. Chem. Phys.* **1979**, *71*, 2874−2879.

(8) Ludeña, E. V.; Torres, F. J.; Costa, C. Functional N-Representability in 2-Matrix, 1-Matrix, and Density Functional Theories. *J. Mod. Phys.* **2013**, *04*, 391−400.

(9) Piris, M. In *Many-body approaches at different scales: a tribute to Norman H. March on the occasion of his 90th Birthday*; Angilella, G. G. N., Amovilli, C., Eds.; Springer: New York, 2018; Chapter 22, pp 261−278.

(10) Piris, M.; Ugalde, J. J. M. Perspective on natural orbital functional theory. *Int. J. Quantum Chem.* **2014**, *114*, 1169−1175.

(11) Pernal, K.; Giesbertz, K. J. H. Reduced Density Matrix Functional Theory (RDMFT) and Linear Response Time-Dependent RDMFT (TD-RDMFT). *Top Curr. Chem.* **2015**, *368*, 125−184.

(12) Schade, R.; Kamil, E.; Blöchl, P. Reduced density-matrix functionals from many-particle theory. *Eur. Phys. J. Spec. Top.* **2017**, *226*, 2677−2692.

(13) Mitxelena, I.; Piris, M.; Ugalde, J. M. In *State of The Art of Molecular Electronic Structure Computations: Correlation Methods, Basis Sets and More*; Hoggan, P., Ancarani, U., Eds.; Advances in Quantum Chemistry; Academic Press: 2019; Vol. *79*, Chapter 7, pp 155−177.

(14) Piris, M. Natural orbital functional for multiplets. *Phys. Rev. A* **2019**, *100*, 032508.

(15) Benavides-Riveros, C. L.; Marques, M. A. On the time evolution of fermionic occupation numbers. *J. Chem. Phys.* **2019**, *151*, 044112.

(16) Cioslowski, J.; Mihalka, Z. E.; Szabados, A. Bilinear Constraints Upon the Correlation Contribution to the Electron-Electron Repulsion Energy as a Functional of the One-Electron Reduced Density Matrix. *J. Chem. Theory Comput.* **2019**, *15*, 4862−4872.

(17) Giesbertz, K. J.; Ruggenthaler, M. One-body reduced density-matrix functional theory in finite basis sets at elevated temperatures. *Phys. Rep.* **2019**, *806*, 1−47.

(18) Gritsenko, O. V.; Pernal, K. Approximating one-matrix functionals without generalized Pauli constraints. *Phys. Rev. A* **2019**, *100*, 012509.

(19) Lopez, X.; Piris, M. Performance of the NOF-MP2 method in hydrogen abstraction reactions. *Theor. Chem. Acc.* **2019**, *138*, 89.

(20) Quintero-Monsebaiz, R.; Mitxelena, I.; Rodríguez-Mayorga, M.; Vela, A.; Piris, M. Natural orbital functional for spin-polarized periodic systems. *J. Phys.: Condens. Matter* **2019**, *31*, 165501−8.

(21) Schilling, C.; Schilling, R. Diverging Exchange Force and Form of the Exact Density Matrix Functional. *Phys. Rev. Lett.* **2019**, *122*, 013001−7.

(22) Schmidt, J.; Benavides-Riveros, C. L.; Marques, M. A. L. Reduced Density Matrix Functional Theory for Superconductors. *Phys. Rev. B* **2019**, *99*, 224502.

(23) Buchholz, F.; Theophilou, I.; Nielsen, S. E. B.; Ruggenthaler, M.; Rubio, A. Reduced Density-Matrix Approach to Strong Matter-Photon Interaction. *ACS Photonics* **2019**, *6*, 2694−2711.

(24) Benavides-Riveros, C. L.; Wolff, J.; Marques, M. A.; Schilling, C. Reduced Density Matrix Functional Theory for Bosons. *Phys. Rev. Lett.* **2020**, *124*, 180603.

(25) Giesbertz, K. J. Implications of the unitary invariance and symmetry restrictions on the development of proper approximate one-body reduced-density-matrix functionals. *Phys. Rev. A* **2020**, *102*, 052814.

(26) Cioslowski, J. The One-Electron Reduced Density Matrix Functional Theory of Spin-Polarized Systems. *J. Chem. Theory Comput.* **2020**, *16*, 1578−1585.

(27) Mitxelena, I.; Piris, M. An efficient method for strongly correlated electrons in one dimension. *J. Phys.: Condens. Matter* **2020**, *32*, 17LT01.

(28) Mitxelena, I.; Piris, M. An efficient method for strongly correlated electrons in two-dimensions. *J. Chem. Phys.* **2020**, *152*, 064108.

(29) Mitxelena, I.; Piris, M. Analytic gradients for spin multiplets in natural orbital functional theory. *J. Chem. Phys.* **2020**, *153*, 044101.

(30) Lew-Yee, J. F. H.; Piris, M.; del Campo, J. M. Resolution of the identity approximation applied to PNOF correlation calculations. *J. Chem. Phys.* **2021**, *154*, 064102.

(31) Mercero, J. M.; Ugalde, J. M.; Piris, M. Chemical reactivity studies by the natural orbital functional second-order Møller−Plesset (NOF-MP2) method: water dehydrogenation by the scandium cation. *Theor. Chem. Acc.* **2021**, *140*, 74.

(32) Quintero-Monsebaiz, R.; Perea-Ramirez, L. I.; Piris, M.; Vela, A. Spectroscopic properties of open shell diatomic molecules using Piris Natural Orbital Functionals. *Phys. Chem. Chem. Phys.* **2021**, *23*, 2953−2963.

(33) Schilling, C.; Pittalis, S. Ensemble Reduced Density Matrix Functional Theory for Excited States and Hierarchical Generalization of Pauli's Exclusion Principle. *Phys. Rev. Lett.* **2021**, *127*, 023001.

(34) Liebert, J.; Schilling, C. Functional theory for Bose−Einstein condensates. *Phys. Rev. Res.* **2021**, *3*, 013282.

(35) Wang, Y.; Knowles, P. J.; Wang, J. Information entropy as a measure of the correlation energy associated with the cumulant. *Phys. Rev. A* **2021**, *103*, 062808.

(36) Yao, Y.-F.; Fang, W.-H.; Su, N. Q. Handling Ensemble N-Representability Constraint in Explicit-by-Implicit Manner. *J. Phys. Chem. Lett.* **2021**, *12*, 6788−6793.

(37) Gibney, D.; Boyn, J. N.; Mazziotti, D. A. Toward a Resolution of the Static Correlation Problem in Density Functional Theory from Semidefinite Programming. *J. Phys. Chem. Lett.* **2021**, *12*, 385−391.
(38) Piris, M. Global Natural Orbital Functional: Towards the Complete Description of the Electron Correlation. *Phys. Rev. Lett.* **2021**, *127*, 233001.
(39) Di Sabatino, S.; Koskelo, J.; Berger, J. A.; Romaniello, P. Introducing screening in one-body density matrix functionals: impact on the Extended Koopmans' Theorem's charged excitations of model systems. *Phys. Rev. B* **2022**, *105*, 235123.
(40) Lemke, Y.; Kussmann, J.; Ochsenfeld, C. Efficient Integral-Direct Methods for Self-Consistent Reduced Density Matrix Functional Theory Calculations on Central and Graphics Processing Units. *J. Chem. Theory Comput.* **2022**, *18*, 4229−4244.
(41) Mitxelena, I.; Piris, M. Benchmarking GNOF against FCI in challenging systems in one, two, and three dimensions. *J. Chem. Phys.* **2022**, *156*, 214102.
(42) Liebert, J.; Castillo, F.; Labbé, J.-P.; Schilling, C. Foundation of one-particle reduced density matrix functional theory for excited states. *J. Chem. Theory Comput.* **2022**, *18*, 124−140.
(43) Wang, J.; Baerends, E. J. Self-Consistent-Field Method for Correlated Many-Electron Systems with an Entropic Cumulant Energy. *Phys. Rev. Lett.* **2022**, *128*, 013001.
(44) Ding, L.; Liebert, J.; Schilling, C.Comment on "Self-Consistent-Field Method for Correlated Many-Electron Systems with an Entropic Cumulant Energy. *arXiv*, 2022, 2202.05532.
(45) Rodríguez-Mayorga, M.; Giesbertz, K. J. H.; Visscher, L. Relativistic reduced density matrix functional theory. *SciPost Chem.* **2022**, *1*, 004.
(46) Senjean, B.; Yalouz, S.; Nakatani, N.; Fromager, E. Reduced density matrix functional theory from an ab initio seniority-zero wave function: Exact and approximate formulations along an adiabatic connection path. *Phys. Rev. A* **2022**, *106*, 032203.
(47) Lew-Yee, J. F. H.; Del Campo, J. M. Charge delocalization error in Piris natural orbital functionals. *J. Chem. Phys.* **2022**, *157*, 104113.
(48) Piris, M.; Mitxelena, I. DoNOF: an open-source implementation of natural-orbital-functional-based methods for quantum chemistry. *Comput. Phys. Commun.* **2021**, *259*, 107651−14.
(49) Mitxelena, I.; Piris, M.; Rodriguez-Mayorga, M. On the performance of natural orbital functional approximations in the Hubbard model. *J. Phys.: Condens. Matter* **2017**, *29*, 425602.
(50) Piris, M. In *Theoretical and Quantum Chemistry at the Dawn of the 21st Century*; Carbó-Dorca, R., Chakraborty, T., Eds.; Innovations in Computational Chemistry; Apple Academic Press: 2018; Chapter 22, pp 593−620.
(51) Piris, M.; Lopez, X.; Ruipérez, F.; Matxain, J. M.; Ugalde, J. M. A natural orbital functional for multiconfigurational states. *J. Chem. Phys.* **2011**, *134*, 164102.
(52) Piris, M.; Matxain, J. M.; Lopez, X. The intrapair electron correlation in natural orbital functional theory. *J. Chem. Phys.* **2013**, *139*, 234109−9.
(53) Piris, M. Interacting pairs in natural orbital functional theory. *J. Chem. Phys.* **2014**, *141*, 044107.
(54) Piris, M. Global Method for Electron Correlation. *Phys. Rev. Lett.* **2017**, *119*, 063002−5.
(55) Mitxelena, I.; Rodríguez-Mayorga, M.; Piris, M. Phase Dilemma in Natural Orbital Functional Theory from the N-representability Perspective. *Eur. Phys. J. B* **2018**, *91*, 109.
(56) Piris, M.; Lopez, X.; Ugalde, J. J. M. J. The Bond Order of C 2 from an Strictly N-Representable Natural Orbital Energy Functional Perspective. *Chem. - A Eur. J.* **2016**, *22*, 4109.
(57) Matxain, J. M.; Piris, M.; Ruipérez, F.; Lopez, X.; Ugalde, J. M. Homolytic molecular dissociation in natural orbital functional theory. *Phys. Chem. Chem. Phys.* **2011**, *13*, 20129−20135.
(58) Ruipérez, F.; Piris, M.; Ugalde, J. M.; Matxain, J. M. The natural orbital functional theory of the bonding in Cr(2), Mo(2) and W(2). *Phys. Chem. Chem. Phys.* **2013**, *15*, 2055−2062.
(59) Piris, M. Interpair electron correlation by second-order perturbative corrections to PNOF5. *J. Chem. Phys.* **2013**, *139*, 064111−7.
(60) Piris, M.; Ruipérez, F.; Matxain, J. Assessment of the second-order perturbative corrections to PNOF5. *Mol. Phys.* **2014**, *112*, 1−8.
(61) Piris, M. Dynamic electron-correlation energy in the natural-orbital-functional second-order-Møller-Plesset method from the orbital-invariant perturbation theory. *Phys. Rev. A* **2018**, *98*, 022504−6.
(62) Rodríguez-Mayorga, M.; Mitxelena, I.; Bruneval, F.; Piris, M. Coupling Natural Orbital Functional Theory and Many-Body Perturbation Theory by Using Nondynamically Correlated Canonical Orbitals. *J. Chem. Theory Comput.* **2021**, *17*, 7562−7574.
(63) Lever, A. B. P.; Gray, H. B.*Iron Porphyrins Part 3*; Wiley-VCH: 1989; p 322.
(64) Ugalde, J. M.; Dunietz, B.; Dreuw, A.; Head-Gordon, M.; Boyd, R. J. The spin dependence of the spatial size of Fe(II) and of the structure of Fe(II)-porphyrins. *J. Phys. Chem. A* **2004**, *108*, 4653−4657.
(65) Perutz, M. F.; Wilkinson, A. J.; Paoli, M.; Dodson, G. G. The stereochemical mechanism of the cooperative effects in hemoglobin revisited. *Annu. ReV. Biophys. Biomol. Struct.* **1998**, *27*, 1.
(66) Dayan, F.; Dayan, E. Porphyrins: One ring in the colors of life. *Am. Sci.* **2011**, *99*, 236.
(67) Obara, S.; Kashiwagi, H. Ab initio MO studies of electronic states and Mössbauer spectra of high-, intermediate-, and low-spin Fe(II)-porphyrin complexes. *J. Chem. Phys.* **1982**, *77*, 3155−3165.
(68) Sontum, S. F.; Case, D. A.; Karplus, M. Xα multiple scattering calculations on iron(II) porphine. *J. Chem. Phys.* **1983**, *79*, 2881−2892.
(69) Rohmer, M.-M. Electronic ground state of iron(II)porphyrin. Ab initio SCF and CI calculations and computed electron deformation densities. *Chem. Phys. Lett.* **1985**, *116*, 44−49.
(70) Rawlings, D. C.; Gouterman, M.; Davidson, E. R.; Feller, D. Theoretical investigations of the electronic states of porphyrins. III. Low-lying electronic states of porphinatoiron(II). *Int. J. Quantum Chem.* **1985**, *28*, 773−796.
(71) Choe, Y. K.; Hashimoto, T.; Nakano, H.; Hirao, K. Theoretical study of the electronic ground state of iron(II) porphine. *Chem. Phys. Lett.* **1998**, *295*, 380−388.
(72) Choe, Y. K.; Nakajima, T.; Hirao, K.; Lindh, R. Theoretical study of the electronic ground state of iron(II) porphine. II. *J. Chem. Phys.* **1999**, *111*, 3837−3845.
(73) Liao, M.-S.; Scheiner, S. Electronic structure and bonding in metal porphyrins, metal = Fe, Co, Ni, Cu, Zn. *J. Chem. Phys.* **2002**, *117*, 205−219.
(74) Groenhof, A. R.; Swart, M.; Ehlers, A. W.; Lammertsma, K. Electronic ground states of iron porphyrin and of the first species in the catalytic reaction cycle of cytochrome P450s. *J. Phys. Chem. A* **2005**, *109*, 3411−3417.
(75) Radoń, M. Spin-State Energetics of Heme-Related Models from DFT and Coupled Cluster Calculations. *J. Chem. Theory Comput.* **2014**, *10*, 2306−2321.
(76) Lee, J.; Malone, F. D.; Morales, M. A. Utilizing Essential Symmetry Breaking in Auxiliary-Field Quantum Monte Carlo: Application to the Spin Gaps of the C36 Fullerene and an Iron Porphyrin Model Complex. *J. Chem. Theory Comput.* **2020**, *16*, 3019−3027.
(77) Li Manni, G.; Smart, S. D.; Alavi, A. Combining the Complete Active Space Self-Consistent Field method and the Full Configuration Interaction Quantum Monte Carlo within a Super-CI framework, with application to challenging metal-porphyrins. *J. Chem. Theory Comput.* **2016**, *12*, 1245−1258.
(78) Smith, J. E.; Mussard, B.; Holmes, A. A.; Sharma, S. Cheap and Near Exact CASSCF with Large Active Spaces. *J. Chem. Theory Comput.* **2017**, *13*, 5468−5478.
(79) Pierloot, K.; Phung, Q. M.; Domingo, A. Spin State Energetics in First-Row Transition Metal Complexes: Contribution of (3s3p)

Correlation and Its Description by Second-Order Perturbation Theory. *J. Chem. Theory Comput.* **2017**, *13*, 537−553.
(80) Zhou, C.; Gagliardi, L.; Truhlar, D. G. Multiconfiguration Pair-Density Functional Theory for Iron Porphyrin with CAS, RAS, and DMRG Active Spaces. *J. Phys. Chem. A* **2019**, *123*, 3389−3394.
(81) Weser, O.; Guther, K.; Ghanem, K.; Li Manni, G. Stochastic Generalized Active Space Self-Consistent Field: Theory and Application. *J. Chem. Theory Comput.* **2022**, *18*, 251−272.
(82) Antalík, A.; Nachtigallová, D.; Lo, R.; Matoušek, M.; Lang, J.; Legeza, Ö.; Pittner, J.; Hobza, P.; Veis, L. Ground state of the Fe(ii)-porphyrin model system corresponds to quintet: a DFT and DMRG-based tailored CC study. *Phys. Chem. Chem. Phys.* **2020**, *22*, 17033−17037.
(83) Beran, P.; Matoušek, M.; Hapka, M.; Pernal, K.; Veis, L. Density Matrix Renormalization Group with Dynamical Correlation via Adiabatic Connection. *J. Chem. Theory Comput.* **2021**, *17*, 7575−7585.
(84) Swart, M.; Groenhof, A. R.; Ehlers, A. W.; Lammertsma, K. Validation of exchange-correlation functionals for spin states of iron complexes. *J. Phys. Chem. A* **2004**, *108*, 5479−5483.
(85) Berryman, V. E. J.; Boyd, R. J.; Johnson, E. R. Balancing Exchange Mixing in Density-Functional Approximations for Iron Porphyrin. *J. Chem. Theory Comput.* **2015**, *11*, 3022−3028.
(86) Stroscio, G. D.; Zhou, C.; Truhlar, D. G.; Gagliardi, L. Multiconfiguration Pair-Density Functional Theory Calculations of Iron(II) Porphyrin: Effects of Hybrid Pair-Density Functionals and Expanded RAS and DMRG Active Spaces on Spin-State Orderings. *J. Phys. Chem. A* **2022**, *126*, 3957−3963.
(87) Tishchenko, O.; Zheng, J.; Truhlar, D. G. Multireference model chemistries for thermochemical kinetics. *J. Chem. Theory Comput.* **2008**, *4*, 1208−1219.
(88) Guo, Y.; Zhang, N.; Lei, Y.; Liu, W. iCISCF: An Iterative Configuration Interaction-Based Multiconfigurational Self-Consistent Field Theory for Large Active Spaces. *J. Chem. Theory Comput.* **2021**, *17*, 7545−7561.
(89) Dunning, T. H.; Dunning, T. H., Jr. Gaussian basis sets for use in correlated molecular calculations. I. The atoms boron through neon and hydrogen. *J. Chem. Phys.* **1989**, *90*, 1007−1023.
(90) Balabanov, N. B.; Peterson, K. A. Systematically convergent basis sets for transition metals. I. All-electron correlation consistent basis sets for the 3d elements Sc-Zn. *J. Chem. Phys.* **2005**, *123*, 064107−15.
(91) Lew-Yee, J. F. H.; Piris, M.; Del Campo, J. M. Resolution of the identity approximation applied to PNOF correlation calculations. *J. Chem. Phys.* **2021**, *154*, 064102.
(92) Weigend, F. A fully direct RI-HF algorithm: Implementation, optimized auxiliary basis sets, demonstration of accuracy and efficiency. *Phys. Chem. Chem. Phys.* **2002**, *4*, 4285−4291.
(93) Weigend, F. Hartree-Fock exchange fitting basis sets for H to Rn. *J. Comput. Chem.* **2008**, *29*, 167−175.
(94) Rovira, C.; Kunc, K.; Hutter, J.; Ballone, P.; Parrinello, M. Equilibrium Geometries and Electronic Structure of Iron-Porphyrin Complexes: A Density Functional Study. *J. Phys. Chem. A* **1997**, *101*, 8914−8925.
(95) Piris, M.; Matxain, J. M.; Lopez, X.; Ugalde, J. M. The one-electron picture in the Piris natural orbital functional 5 (PNOF5). *Theor. Chem. Acc.* **2013**, *132*, 1298.
(96) Manni, G. L.; Alavi, A. Understanding the Mechanism Stabilizing Intermediate Spin States in Fe(II)-Porphyrin. *J. Phys. Chem. A* **2018**, *122*, 4935−4947.
(97) Aroeira, G. J. R.; Davis, M. M.; Turney, J. M.; Schaefer, H. F. 3rd Fermi.jl: A Modern Design for Quantum Chemistry. *J. Chem. Theory Comput.* **2022**, *18*, 677−686.
(98) Abbott, M.; Aluthge, D.; N3N; Schaub, S.; Elrod, C.; Lucibello, C.; Chen, J.*mcabbott/Tullio.jl*, v0.3.5.2022; https://github.com/mcabbott/Tullio.jl.
(99) Jutho; getzdan; Lyon, S.; Protter, M.; Marcus, P. S.; Leo; Garrison, J.; Otto, F.; Saba, E.; Iouchtchenko, D.; Privett, A.; Morley, A.*TensorOperations.jl*, v1.1.0. 2019; https://github.com/Jutho/TensorOperations.jl.
(100) Piris, M.; Ugalde, J. M. Iterative Diagonalization for Orbital Optimization in Natural Orbital Functional Theory. *J. Comput. Chem.* **2009**, *30*, 2078−2086.

https://doi.org/10.1021/acs.jctc.2c01093
J. Chem. Theory Comput. 2023, 19, 211−220

Outstanding Improvement in Removing the Delocalization Error by Global Natural Orbital Functional

Juan Felipe Huan Lew-Yee,[1] Mario Piris,[2, a)] and Jorge M. del Campo[1, b)]

[1)] *Departamento de Física y Química Teórica, Facultad de Química, Universidad Nacional Autónoma de México, México City, C.P. 04510, México*

[2)] *Donostia International Physics Center (DIPC), 20018 Donostia, Euskadi, Spain; Euskal Herriko Unibertsitatea (UPV/EHU), PK 1072, 20080 Donostia, Euskadi, Spain; and Basque Foundation for Science (IKERBASQUE), 48009 Bilbao, Euskadi, Spain*

(Dated: 1 February 2023)

This work assesses the performance of the recently proposed global natural orbital functional (GNOF) against the charge delocalization error. GNOF provides a good balance between static and dynamic electronic correlation leading to accurate total energies while preserving spin, even for systems with a highly multi-configurational character. Several analyses were applied to the functional, namely i) how the charge is distributed in super-systems of two fragments, ii) the stability of ionization potentials while increasing the system size, and iii) potential energy curves of a neutral and charged diatomic system. GNOF was found to practically eliminate the charge delocalization error in many of the studied systems or greatly improves the results obtained previously with PNOF7.

I. INTRODUCTION

The delocalization error is one of the biggest pending challenges of current electronic structure methods.[1,2] It appears in many density functional approximations (DFAs),[3,4] as well as wavefunction-based methods, such as unrestricted Hartree-Fock and its second-order perturbative corrections.[5] It has been studied from many perspectives considering that the energy of a system with a fractional number of electrons should be linearly related to the energy of the closest systems with integer electron numbers. Consequently, the lack of discontinuity in the energy derivative at an integer number of particles correlates with the delocalization error.[6] The delocalization error has been explained as a self-interaction consequence,[7] and more recently as a multi-electron self-interaction error.[3] This problem causes an energetic overstabilization of fractional charges[8], and has important consequences in many chemical situations of interest as band gap predictions[9], dissociation curves[10] of neutral and charged molecules,[11] and ionization potentials.[12] Due to its relevance to chemical predictions, many attempts have been made to overcome the problem of the delocalization error in DFAs.[13] Some of these ideas include functional tuning,[12,14] the design of explicitly corrected functionals[8,15,16], and the use of machine learning approaches.[17,18] In fact, surpassing this error has become a desirable feature to be satisfied in the development of new methods.[19]

One-particle reduced density matrix (1RDM) functional theory emerged[20–22] in the 1970s as an alternative formalism to both density functional and wavefunction based methods. Advances in this area lead to approximate functionals of the 1RDM in its diagonal form, that is, the use of natural orbitals (NOs) and its occupation numbers (ONs), which define a natural orbital functional (NOF).[23,24] It is more appropriate to speak of a NOF rather than a 1RDM functional when dealing with approximations, since a dependency of the two-particle RDM (2RDM) persists[25] leading to the functional N-representability problem.[26,27] Comprehensive reviews of approximate NOFs can be found elsewhere.[28–30] Nowadays, the NOF theory has become an active field of research,[31–54] and several advances have been achieved regarding to its efficient implementation.[55–58] Special emphasis should be made on the open source program DoNOF[59] that has been made available to the community (github.com/DoNOF) to perform NOF-based calculations.

The design of NOFs has been highly motivated by their ability to recover static correlation through fractional ONs, offering an intermediate cost between multireference methods and common DFAs. In fact, approximate NOFs have demonstrated to be more accurate than their electron density-dependent counterparts and to have better scaling with respect to the number of basis functions than wavefunction-type methods for systems with large amount of strong non-dynamic correlation. Particularly successful in describing static electron correlation have been Piris NOFs (PNOFs) based on electron-pairing,[60] namely PNOF5,[61,62] PNOF6,[63] and PNOF7.[64,65] These NOFs are the only ones that have hitherto been able to achieve the correct number of electrons for the resulting fragments in homolytic dissociations,[66,67] therefore, no delocalization problems have been observed in these processes.

Although some reports have considered the delocalization error in NOFs,[68] this issue has not received much attention as in other electronic structure methods. In a previous report[69], it has been shown that PNOFs can simultaneously deal with static correlation and charge delocalization errors, becoming a promising option for studying charge-related problems. In particular, PNOF5 was shown to prefer localized solutions,

[a)] Electronic mail: mario.piris@ehu.eus
[b)] Electronic mail: jmdelc@unam.mx

whereas PNOF7 can suffer from charge delocalization error, although it far outperforms common DFAs. Two years after PNOF5 was proposed[61], it was realized[70] that an antisymmetrized product of strongly orthogonal geminals with the expansion coefficients explicitly expressed by the ONs leads to it, which confirms that PNOF5 is strictly N-representable, i.e., the functional can also be derived from a wavefunction that is antisymmetric in N-particles. This exceptional property of PNOF5 is responsible for the absence of delocalization error, as occurs with wavefunctions that do not violate inherent physical symmetries. Nevertheless, we must recall that PNOF5 is equivalent to an independent electron pair model, hence it only takes into account the intrapair electron correlation, whereas PNOF7 also includes essentially nondynamic interpair correlation which allows it to perform better on challenging strong correlation problems[38–40,71] where PNOF5 fails.

Like in the other PNOFs, PNOF7 satisfies several analytic (2,2)-positivity conditions[72] as a consequence of imposing them on the reconstructed 2RDM. It is well known that these conditions are necessary but not sufficient for the ensemble N-representability, so there might be situations where PNOF7 violates the N-representability and the delocalization error appears. This small but consistent charge delocalization error shown by PNOF7 was related[69] to spurious contributions of static correlation due to the absence of dynamic interpair correlation terms in the functional. We therefore hope that a better balance between dynamic and static electron correlation will improve or even make the delocalization error disappear.

Recently,[48] a new NOF has been proposed for electronic systems with any spin value regardless of the external potential, i.e. a global NOF (GNOF), to precisely achieve a better balance of static and dynamic electronic correlation even for those systems with multi-configurational character, preserving total spin. The agreement obtained[50] by GNOF with accurate wavefunction-based methods is good for relative energies and for absolute energies, a fact that points out that good results come out for good reasons. Therefore, it invites us to test its performance in the delocalization error, and the best correlation balance is expected to provide improved results. The objective of this work is to show that the dynamic correlation provided by GNOF allows to greatly improve the performance in the delocalization problem.

The work is organized as follows. First, Section II presents a brief review of GNOF. This is followed by the computational details of the tests used to characterize the charge delocalization error in Section III. Section IV presents an analysis of the performance of GNOF over the charge delocalization error in dimers, ionization potentials of chains and the fractional charge that arises in the dissociation of diatomic molecules. Finally, conclusions are given in Section V.

II. THEORY

In this section, we briefly describe GNOF, a more detailed description can be found in Ref.[48] The nonrelativistic Hamiltonian under consideration is spin coordinate free; therefore, a state with total spin S is a multiplet, i.e., a mixed quantum state that allows all possible S_z values. We consider $\mathrm{N_I}$ single electrons which determine the spin S of the system, and the rest of electrons ($\mathrm{N_{II}} = \mathrm{N} - \mathrm{N_I}$) are spin-paired, so that all spins corresponding to $\mathrm{N_{II}}$ electrons altogether provide a zero spin. In the absence of single electrons ($\mathrm{N_I} = 0$), the energy reduces to a NOF that describes singlet states, as expected.

We focus on the mixed state of highest multiplicity: $2S+1 = \mathrm{N_I}+1, S = \mathrm{N_I}/2$.[31] For an ensemble of pure states $\{|SM_s\rangle\}$, we note that the expected value of $\hat{S}_z$ for the whole ensemble is zero. Consequently, the spin-restricted theory can be adopted even if the total spin of the system is not zero. We use a single set of orbitals for α and β spins. All the spatial orbitals will then be doubly occupied in the ensemble, so that occupancies for particles with α and β spins are equal: $n_p^\alpha = n_p^\beta = n_p$.

The orbital space Ω is divided into two subspaces: $\Omega = \Omega_\mathrm{I} \oplus \Omega_\mathrm{II}$. Ω_II is composed of $\mathrm{N_{II}}/2$ mutually disjoint subspaces Ω_g. Each of which contains one orbital $|g\rangle$ with $g \leq \mathrm{N_{II}}/2$, and N_g orbitals $|p\rangle$ with $p > \mathrm{N_{II}}/2$, namely,

$$\Omega_g = \left\{ |g\rangle, |p_1\rangle, |p_2\rangle, ..., \left|p_{\mathrm{N}_g}\right\rangle \right\}. \tag{1}$$

Taking into account the spin, the total occupancy for a given subspace Ω_g is 2. In general, N_g can be different for each subspace as long as it describes the electron pair well. For convenience, in this work, we take it equal for all subspaces $\Omega_g \in \Omega_\mathrm{II}$ to the maximum possible value determined by the basis set used in calculations.

Similarly, Ω_I is composed of $\mathrm{N_I}$ mutually disjoint subspaces Ω_g. In contrast to Ω_II, each subspace $\Omega_g \in \Omega_\mathrm{I}$ contains only one orbital g with $2n_g = 1$. It is worth noting that each orbital is completely occupied individually, but we do not know whether the electron has α or β spin: $n_g^\alpha = n_g^\beta = n_g = 1/2$.

Reconstruction of 2RDM in terms of ONs leads to GNOF:

$$E = E^{intra} + E_{HF}^{inter} + E_{sta}^{inter} + E_{dyn}^{inter} \tag{2}$$

The intra-pair component is formed by the sum of the energies of the electron pairs with opposite spins and the single-electron energies of the unpaired electrons, namely

$$E^{intra} = \sum_{g=1}^{\mathrm{N_{II}}/2} E_g + \sum_{g=\mathrm{N_{II}}/2+1}^{\mathrm{N}_\Omega} H_{gg} \tag{3}$$

$$E_g = \sum_{p\in\Omega_g} n_p(2H_{pp} + J_{pp}) + \sum_{q,p\in\Omega_g, p\neq q} \Pi(n_q, n_p) L_{pq} \tag{4}$$

$$\Pi(n_q, n_p) = \sqrt{n_q n_p}\left(\delta_{q\Omega^a}\delta_{p\Omega^a} - \delta_{qg} - \delta_{pg}\right) \tag{5}$$

H_{pp} are the diagonal one-electron matrix elements of the kinetic energy and external potential operators, whereas $J_{pq} =$

$\langle pq|pq\rangle$ and $L_{pq} = \langle pp|qq\rangle$ are the Coulomb and exchange-time-inversion integrals, respectively. $N_\Omega = N_{II}/2 + N_I$ denotes the total number of suspaces in Ω, as Ω^a denotes the subspace composed of orbitals above the level N_Ω ($p > N_\Omega$).

The inter-subspace Hartree-Fock (HF) term is

$$E_{HF}^{inter} = \sum_{p,q=1}^{N_B}{}' n_q n_p (2J_{pq} - K_{pq}) \tag{6}$$

where $K_{pq} = \langle pq|qp\rangle$ are the exchange integrals. The prime in the summation indicates that only the inter-subspace terms are taken into account ($p \in \Omega_f, q \in \Omega_g, f \neq g$). N_B represents the number of basis functions considered. The inter-subspace static component is written as

$$\begin{aligned} E_{sta}^{inter} = &-\left(\sum_{p=1}^{N_\Omega} \sum_{q=N_\Omega+1}^{N_B} + \sum_{p=N_\Omega+1}^{N_B} \sum_{q=1}^{N_\Omega} + \sum_{p,q=N_\Omega+1}^{N_B} \right)' \\ &\Phi_q \Phi_p L_{pq} - \frac{1}{2} \left(\sum_{p=1}^{N_{II}/2} \sum_{q=N_{II}/2+1}^{N_\Omega} + \sum_{p=N_{II}/2+1}^{N_\Omega} \sum_{q=1}^{N_{II}/2} \right)' \\ &\Phi_q \Phi_p L_{pq} - \frac{1}{4} \sum_{p,q=N_{II}/2+1}^{N_\Omega} K_{pq} \end{aligned} \tag{7}$$

where $\Phi_p = \sqrt{n_p h_p}$ with the hole $h_p = 1 - n_p$. Note that Φ_p has significant values only when the n_p differs substantially from 1 and 0. Finally, the inter-subspace dynamic energy can be conveniently expressed as

$$E_{dyn}^{inter} = \sum_{p,q=1}^{N_B}{}' \left[n_q^d n_p^d + \Pi\left(n_q^d, n_p^d\right) \right] \left[1 - \delta_{q\Omega_{II}^b} \delta_{p\Omega_{II}^b} \right] L_{pq} \tag{8}$$

where Ω_{II}^b denotes the subspace composed of orbitals below the level $N_{II}/2$, so interactions between orbitals belonging to Ω_{II}^b are excluded from E_{dyn}^{inter}. The dynamic part of n_p is defined as

$$n_p^d = n_p \cdot e^{-\left(\frac{h_g}{h_c}\right)^2}, \quad p \in \Omega_g \tag{9}$$

with $h_c = 0.02\sqrt{2}$. The maximum value of n_p^d is around 0.012 in accordance with the Pulay's criterion that establishes an occupancy deviation of approximately 0.01 with respect to 1 or 0 for a NO to contribute to the dynamic correlation.

It is worth pointing out that GNOF preserves the total spin of a multiplet: $\left\langle \hat{S}^2 \right\rangle = S(S+1)$, and, Eq. (2) reduces to a PNOF7-like functional when the inter-pair dynamic term (E_{dyn}^{inter}) is neglected, and to PNOF5 if the inter-subspace static term (E_{sta}^{inter}) is also disregarded.

III. COMPUTATIONAL DETAILS

Several tests related to the charge delocalization error will be applied to the functionals, some related to ionized supersystems of repeated well-separated fragments. To analyze the calculations performed, let us recall the charge localization metric (CLM) proposed in previous work,[69] defined as the difference between the most charged fragment and the least charged fragment,

$$\mathrm{CLM} = \max\left\{ \begin{matrix} \text{Fragment} \\ \text{Charges} \end{matrix} \right\} - \min\left\{ \begin{matrix} \text{Fragment} \\ \text{Charges} \end{matrix} \right\}, \tag{10}$$

where the curly braces indicate the set of all fragment charges in a system. According to this metric, systems with the charge concentrated in a single fragment will present a value of 1. Conversely, systems with the charge fully delocalized will have a value of 0 since all fragments are equally charged. Values of CLM between these two limit cases indicate partial localization of the charge.

The CLM provides information on how the charge is distributed in a molecule but does not quantify whether the charge delocalization error is present. Because fragments in a given system will be well-separated, there should not be interactions between them. In the case of two fragments, the energy of the a supersystem should be the sum of the energy of the neutral fragment, E_0, and the energy of the positive charged fragment E_+. Consequently, the energy deviation of the supersystem from this expected value,

$$\Delta E = E_{system} - (E_0 + E_+), \tag{11}$$

together with the charge distribution, can be used to quantify the charge delocalization error in systems made up of two fragments, with a straightforward extension to more fragments when required.

On the other hand, the charge delocalization error makes the ionization potentials of such supersystems depend on the number of fragments; therefore, the deviation of the ionization potentials in relation to the number of fragments can also be used as a qualitative indicator of the charge delocalization error.

All NOF calculations were performed in an internal Julia version of the DoNOF code (https://github.com/DoNOF),[59] using the resolution of the identity implementation.[55] Since the purpose of this work is to compare PNOF5, PNOF7 and GNOF at its maximum capacity, the extended pairing approach has been used, that is, N_g is equal to the maximum possible value determined by the basis set used in the calculations, namely a cc-pVDZ/cc-pVDZ-jkfit basis set.[73] In addition, DFAs calculations were performed in ORCA software[74,75] and Full-CI calculations were performed on the Psi4 software when required for comparison.[76,77]

IV. RESULTS

Charge delocalization error in dimers

In a previous report,[69] PNOF5 and PNOF7 were shown to outperform common DFAs by exhibiting a much lower charge delocalization error. In fact, PNOF5 was shown to be free

of the delocalization error, while PNOF7 exhibited a small but consistent error in very strongly correlated systems. To this end, studies of the relationship between charge distribution and energy stabilization were carried out for chains of well-separated repeated fragments. The 17 molecules with multireference character of the set W4-17-MR[78] were used as basic units of the chains. In this work, we have adopted a similar approach, that is, we have built a supersystem consisting of two fragments separated by a distance of 10 Å using the same set of W4-17-MR molecules. Our intention is to directly compare the charge distribution and energy stabilization between two fragments obtained by GNOF with the results of PNOF7.

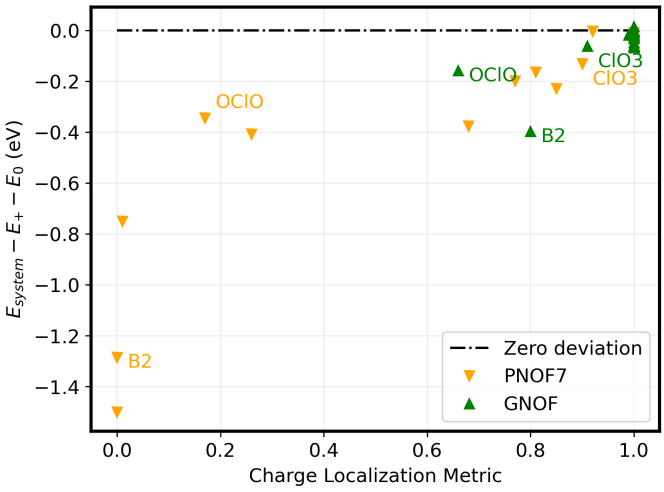

FIG. 1. Energy deviation of the supersystems with respect to the energy sum of the neutral and charged fragments, $\Delta E = E_{system} - (E_0 + E_+)$, as a function of the charge localization metric.

The results are presented in Fig. 1, where the vertical axis corresponds to the energy deviation of the supersystem with respect to the energy sum of the isolated charged and neutral fragments, while the horizontal axis corresponds to the CLM. The PNOF7 values are consistent with the previous report.[69] Recall that the orange downward triangles on the left (CLM=0) indicate that the charge is equally shared between the fragments, on the right (CLM=1) that the charge is on a single fragment, and those distributed along the horizontal axis indicate that the charge is delocalized between the fragments, increasing the energy deviation with this delocalization. In contrast, the green upward triangles of the GNOF values are located mostly to the right and above, indicating that the charge is located on a single fragment. Regrettably, there are still some systems in which the charge delocalization error has persisted, namely the supersystems OClO (CLM = 0.66), B_2 (CLM = 0.80) and ClO_3 (CLM = 0.91). Interestingly, in the case of OClO, another solution was also found with the charge located in a single fragment but with higher energy.

Ionization potentials of chains

A known effect of the charge delocalization error is the deviation of the ionization potentials as the number of fragments in the system increases.[12] Although it has been shown[69] that PNOF7 can provide stable results for helium atom chains and other weakly correlated systems, even with a multireference character, its performance deteriorates in cases of extreme static correlation. However, it should be noted that the observed error for PNOF7 is small compared to common DFA errors that can reach several electron volts.[12]

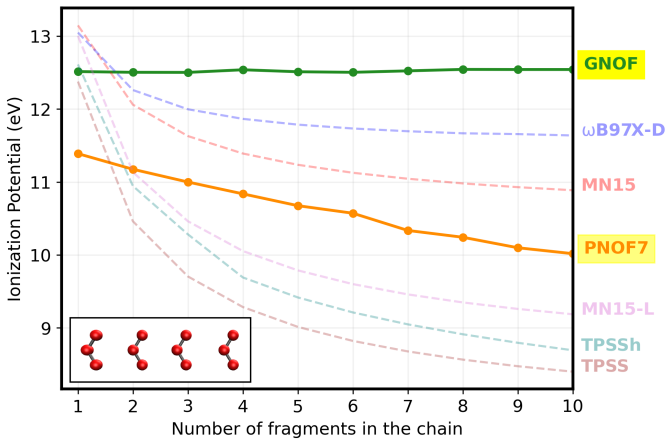

FIG. 2. Ionization potentials of chains of repeated and well-separated fragments of O_3. Each mark correspond to a chain with the number of fragments indicated by the value in the horizontal axis.

To illustrate this effect, the ionization potentials of chains formed by repetition of the O_3 molecule were calculated with GNOF, PNOF7, and some common DFAs, as presented in Fig. 2. For O_3 chains, it was found[69] that PNOF7 improves with respect to DFAs in reproducing the ionization potential as the chain size increases, but still fails due to the delocalization error. It can be seen that DFAs present large deviations in ionization potentials; for example, ωB97X-D predicts an ionization potential of 13.0 eV for a single O_3, but of 11.6 eV for the chain of ten fragments, $(O_3)_{10}$, that is, a difference of 1.3 eV. Similar differences can be found in other DFAs as a consequence of the charge delocalization error that affects the ionized system; namely, the aforementioned difference is 2.3 eV for MN15, 3.8 eV for MN15-L, 3.9 eV for TPSSh, and 4.0 eV for TPSS. Note that PNOF7 achieves a 1.3 eV difference between the single molecule and the ten-fragment chain, with an accuracy for a single molecule that is not as good as DFAs, but remains more stable, exceeding the accuracy of some DFAs just beyond the dimer $(O_3)_2$. By contrast, GNOF predicts stable ionization potentials for all chains. Furthermore, the ionization potential predicted by GNOF is in excellent agreement with the experimental value of 12.5 eV.[79]

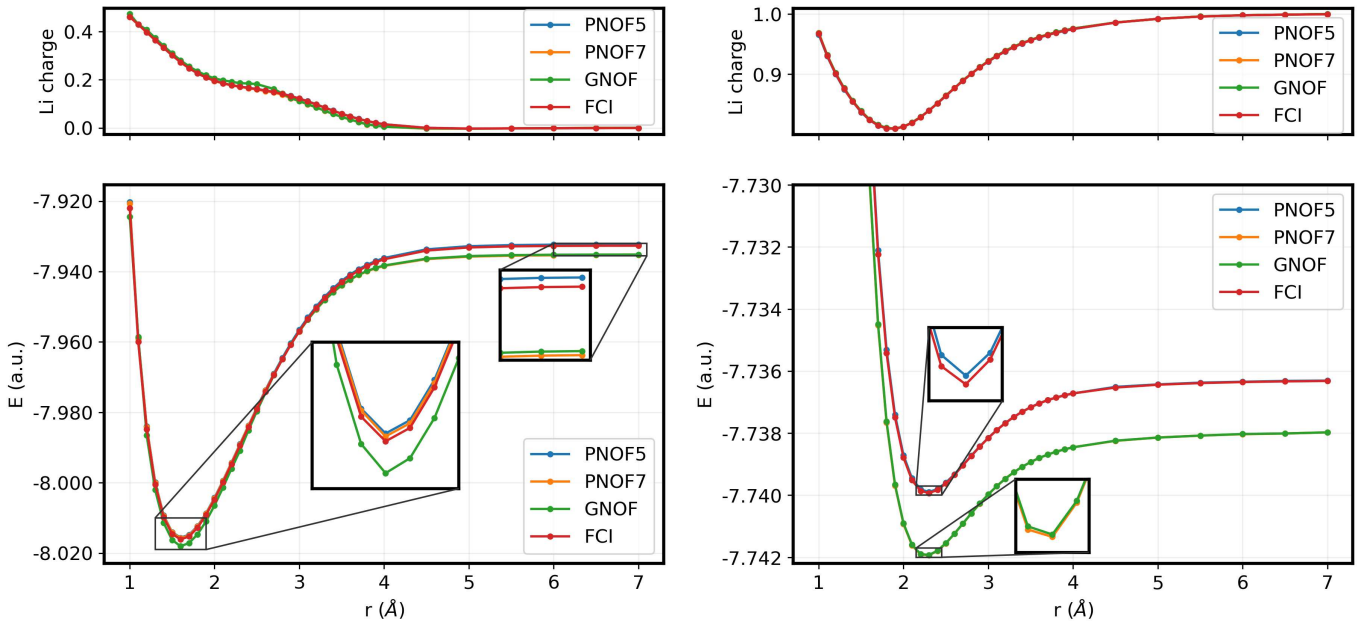

(a) LiH (b) LiH^+

FIG. 3. Dissociation curves of Lithium hydride, (a) neutral (LiH) and (b) charged (LiH^+). The bottom panels present the potential energy curve, while the top panels present the charge of the lithium atom through the dissociation computed by a Löwdin population. In Fig. 3b, the PNOF7 (orange) curve is under the curve of GNOF (green), and the PNOF5 (blue) curve is under the curve of FCI (red).

Potential Energy Curves

Another known problem associated with the charge delocalization error is the fractional charge that arises in the dissociation of diatomic molecules. Take the case of LiH as an example, for which it was reported[68] that the charge delocalization error may lead to an incorrect electron distribution in the dissociation limit. The corresponding potential energy curves for neutral and positively charged lithium hydrides are presented in Fig. 3 for PNOF5 (blue), PNOF7 (orange) and GNOF (green); also, the FCI curve (re) is presented for comparison.

The neutral LiH shown in Fig. 3a is formed by four electrons; therefore, the calculation consists of two electron pairs distributed in the double occupied orbitals of the Ω_{II} subspace. The bottom panel shows that PNOF5 remains above the FCI curve as a consequence of being exactly N-representable. In contrast, PNOF7 and GNOF may be below the FCI curve due to N-representability violations; nevertheless, GNOF achieves energies close to FCI, with a deviation of 1.6 kcal/mol in the dissociation region (7.0 Å), and of 1.2 kcal/mol at the bonding region (1.6 Å). Remarkably, all NOFs dissociate the system into a neutral lithium atom and a neutral hydrogen atom, and the charges along the disociation curve remain almost identical to those predicted by FCI, as can be seen in the top panel of Fig. 3a.

The charged LiH^+ is presented in Fig. 3b. This molecule is a three-electron system, then the calculation consists of only one electron pair distributed in the orbitals of the Ω_{II} subspace, and one single occupied orbital in the Ω_I subspace. Again, all NOFs correctly dissociate LiH^+ into a charged lithium atom and a neutral hydrogen atom, with a charge curve that almost perfectly coincides with the FCI curve. Furthermore, PNOF7 and GNOF provide very similar values (the orange curve of PNOF7 is under the green curve of GNOF) below the FCI curve due to N-representability violations, in this case the deviation at the bonding region is 1.3 kcal/mol (2.3 Å) and 1.0 kcal/mol at the dissociation region (7.0 Å).

V. CONCLUSIONS

The results provided in this work show that GNOF greatly improves the already promising performance of PNOF7 in the charge delocalization error. In particular, energetic predictions of quantities such as ionization potentials and potential energy curves benefit from an increase in stability. Therefore, the good performance in the charge delocalization error, together with an excellent balance of dynamic and static correlation, makes GNOF a valuable functional for electronic structure calculations of general interest.

ACKNOWLEDGMENTS

Support comes from Ministerio de Economía y Competitividad (Ref. PID2021-126714NB-I00). The authors thank for technical and human support provided by IZO-SGI SGIker of

UPV/EHU and European funding (ERDF and ESF). J. F. H. Lew-Yee with CVU Grant No. 867718 acknowledges CONACyT for the Ph.D. scholarship. J. M. del Campo acknowledges funding from projects Grant Nos. CB-2016-282791, PAPIIT-IN201822, and computing resources from the LANCAD-UNAM-DGTIC-270 project.

Data Availability

The data that support the findings of this study are available from the corresponding author upon reasonable request.

[1] K. R. Bryenton, A. A. Adeleke, S. G. Dale, and E. R. Johnson, WIREs Comput Mol Sci. **e1631** (2022).
[2] A. J. Cohen, P. Mori-Sánchez, and W. Yang, Science **321**, 792 (2008).
[3] P. Mori-Sánchez, A. J. Cohen, and W. Yang, J. Chem. Phys. **125**, 201102 (2006).
[4] D. Hait and M. Head-Gordon, J. Phys. Chem. Lett. **9**, 6280 (2018).
[5] A. J. Cohen, P. Mori-Sánchez, and W. Yang, J. Chem. Theory Comput. **5**, 786 (2009).
[6] J. P. Perdew, R. G. Parr, M. Levy, and J. L. Balduz, Phys. Rev. Lett. **49**, 1691 (1982).
[7] Y. Zhang and W. Yang, J. Chem. Phys. **109**, 2604 (1998).
[8] A. J. Cohen, P. Mori-Sánchez, and W. Yang, J. Chem. Phys. **126**, 191109 (2007).
[9] P. Mori-Sánchez, A. J. Cohen, and W. Yang, Phys. Rev. Lett. **100**, 146401 (2008).
[10] A. Ruzsinszky, J. P. Perdew, G. I. Csonka, O. A. Vydrov, and G. E. Scuseria, J. Chem. Phys. **125**, 194112 (2006).
[11] A. Ruzsinszky, J. P. Perdew, and G. I. Csonka, J. Phys. Chem. A **109**, 11006 (2005).
[12] S. R. Whittleton, X. A. Sosa Vazquez, C. M. Isborn, and E. R. Johnson, J. Chem. Phys. **142**, 184106 (2015).
[13] D. N. Komsa and V. N. Staroverov, J. Chem. Theory Comput. **12**, 5361 (2016).
[14] J. Autschbach and M. Srebro, Acc. Chem. Res. **47**, 2592 (2014).
[15] A. D. Becke, S. G. Dale, and E. R. Johnson, J. Chem. Phys. **148**, 211101 (2018).
[16] E. Proynov and J. Kong, J. Chem. Theory Comput. **17**, 4633 (2021).
[17] J. Kirkpatrick, B. McMorrow, D. H. P. Turban, A. L. Gaunt, J. S. Spencer, A. G. D. G. Matthews, A. Obika, L. Thiry, M. Fortunato, D. Pfau, L. R. Castellanos, S. Petersen, A. W. R. Nelson, P. Kohli, P. Mori-Sánchez, D. Hassabis, and A. J. Cohen, Science **374**, 1385 (2021).
[18] J. P. Perdew, Science **374**, 1322 (2021).
[19] J. L. Bao, Y. Wang, X. He, L. Gagliardi, and D. G. Truhlar, J. Phys. Chem. Lett. **8**, 5616 (2017).
[20] T. L. Gilbert, Phys. Rev. B **12**, 2111 (1975).
[21] M. Levy, Proc. Natl. Acad. Sci. USA **76**, 6062 (1979).
[22] S. M. Valone, J. Chem. Phys. **73**, 1344 (1980).
[23] S. Goedecker and C. J. Umrigar, in *Many-electron densities Reduc. density matrices*, edited by J. Cioslowski (Kluwer Academic/Plenum Publishers, New York, 2000) pp. 165–181.
[24] M. Piris, in *Reduced-Density-Matrix Mech. with Appl. to many-electron atoms Mol.* Vol. 134, edited by D. A. Mazziotti (John Wiley and Sons, Hoboken, New Jersey, USA, 2007) Chap. 14, pp. 387–427.
[25] R. A. Donnelly, J. Chem. Phys. **71**, 2874 (1979).
[26] E. V. Ludeña, F. J. Torres, and C. Costa, J. Mod. Phys. **04**, 391 (2013).
[27] M. Piris, in *Many-body approaches Differ. scales a Tribut. to N. H. March Occas. his 90th Birthd.*, edited by G. G. N. Angilella and C. Amovilli (Springer, New York, 2018) Chap. 22, pp. 261–278.
[28] K. Pernal and K. J. H. Giesbertz, Top Curr Chem **368**, 125 (2016).
[29] R. Schade, E. Kamil, and P. Blöchl, Eur. Phys. J. Spec. Top. **226**, 2677 (2017).
[30] I. Mitxelena, M. Piris, and J. M. Ugalde, in *State Art Mol. Electron. Struct. Comput. Correl. Methods, Basis Sets More*, Advances in Quantum Chemistry, Vol. 79, edited by P. Hoggan and U. Ancarani (Academic Press, 2019) Chap. 7, pp. 155–177.
[31] M. Piris, Phys. Rev. A **100**, 32508 (2019).
[32] C. L. Benavides-Riveros and M. A. Marques, J. Chem. Phys. **151**, 044112 (2019).
[33] J. Cioslowski, Z. E. Mihalka, and A. Szabados, J. Chem. Theory Comput. **15**, 4862 (2019).
[34] K. J. Giesbertz and M. Ruggenthaler, Phys. Rep. **806**, 1 (2019).
[35] O. V. Gritsenko and K. Pernal, Phys. Rev. A **100**, 012509 (2019).
[36] X. Lopez and M. Piris, Theor. Chem. Acc. **138**, 10.1007/s00214-019-2475-5 (2019).
[37] C. Schilling and R. Schilling, Phys. Rev. Lett. **122**, 013001 (2019).
[38] R. Quintero-Monsebaiz, I. Mitxelena, M. Rodríguez-Mayorga, A. Vela, and M. Piris, J. Phys. Condens. Matter **31**, 165501 (2019).
[39] I. Mitxelena and M. Piris, J. Phys. Condens. Matter **32**, 17LT01 (2020).
[40] I. Mitxelena and M. Piris, J. Chem. Phys. **152**, 064108 (2020).
[41] K. J. Giesbertz, Phys. Rev. A **102**, 052814 (2020).
[42] J. Cioslowski, J. Chem. Theory Comput. **16**, 1578 (2020).
[43] I. Mitxelena and M. Piris, J. Chem. Phys. **153**, 044101 (2020).
[44] J. M. Mercero, J. M. Ugalde, and M. Piris, Theor. Chem. Acc. **140**, 74 (2021).
[45] R. Quintero-Monsebaiz, L. Perea-Ramírez, M. Piris, and A. Vela, Phys. Chem. Chem. Phys. **19**, 10.1039/d0cp05430e (2021).
[46] M. Rodríguez-Mayorga, I. Mitxelena, F. Bruneval, and M. Piris, J. Chem. Theory Comput. **17**, 7562 (2021).
[47] C. Schilling and S. Pittalis, Phys. Rev. Lett. **127**, 023001 (2021).
[48] M. Piris, Phys. Rev. Lett. **127**, 233001 (2021).
[49] S. Di Sabatino, J. Koskelo, J. A. Berger, and P. Romaniello, Phys. Rev. B **105**, 235123 (2022).
[50] I. Mitxelena and M. Piris, J. Chem. Phys. **156**, 214102 (2022).
[51] J. Liebert, F. Castillo, J.-P. Labbé, and C. Schilling, J. Chem. Theory Comput. **18**, 124 (2022).
[52] J. Wang and E. J. Baerends, Phys. Rev. Lett. **128**, 013001 (2022).
[53] M. Rodríguez-Mayorga, K. J. H. Giesbertz, and L. Visscher, SciPost Chem. **1**, 004 (2022).
[54] B. Senjean, S. Yalouz, N. Nakatani, and E. Fromager, Phys. Rev. A **106**, 032203 (2022).
[55] J. F. H. Lew-Yee, M. Piris, and J. M. del Campo, J. Chem. Phys. **154**, 064102 (2021).
[56] Y.-F. Yao, W.-H. Fang, and N. Q. Su, J. Phys. Chem. Lett. **12**, 6788 (2021).
[57] Y.-F. Yao, Z. Zhang, W.-H. Fang, and N. Q. Su, J. Phys. Chem. A **126**, 5654 (2022).
[58] Y. Lemke, J. Kussmann, and C. Ochsenfeld, J. Chem. Theory Comput. **18**, 4229 (2022).
[59] M. Piris and I. Mitxelena, Comput. Phys. Commun. **259**, 107651 (2021).
[60] M. Piris, in *Quantum Chem. Daw. 21st Century. Ser. Innov. Comput. Chem.*, edited by R. Carbó-Dorca and T. Chakraborty (Apple Academic Press, 2018) Chap. 22, pp. 593–620.
[61] M. Piris, X. Lopez, F. Ruipérez, J. M. Matxain, and J. M. Ugalde, J. Chem. Phys. **134**, 164102 (2011).
[62] M. Piris, J. M. Matxain, and X. Lopez, J. Chem. Phys. **139**, 234109 (2013).
[63] M. Piris, J. Chem. Phys. **141**, 044107 (2014).
[64] M. Piris, Phys. Rev. Lett. **119**, 063002 (2017).
[65] I. Mitxelena, M. Rodríguez-Mayorga, M. Piris, M. Rodriguez-Mayorga, and M. Piris, Eur. Phys. J. B **91**, 109 (2018).
[66] J. M. Matxain, M. Piris, F. Ruipérez, X. Lopez, and J. M. Ugalde, Phys. Chem. Chem. Phys. **13**, 20129 (2011).
[67] F. Ruipérez, M. Piris, J. M. Ugalde, and J. M. Matxain, Phys. Chem. Chem. Phys. **15**, 2055 (2013).
[68] M. Hellgren and T. Gould, J. Chem. Theory Comput. **15**, 4907 (2019).
[69] J. F. H. Lew-Yee and J. M. del Campo, J. Chem. Phys. **157**, 104113 (2022).
[70] K. Pernal, Comp.Theor. Chem. **1003**, 127 (2013).
[71] I. Mitxelena, M. Piris, and M. Rodriguez-Mayorga, J. Phys. Condens. Matter **29**, 425602 (2017).
[72] D. a. Mazziotti, Phys. Rev. Lett. **108**, 263002 (2012).
[73] B. P. Pritchard, D. Altarawy, B. Didier, T. D. Gibson, and T. L. Windus, J. Chem. Inf. Model. **59**, 4814 (2019).
[74] F. Neese, Wiley Interdiscip. Rev. Comput. Mol. Sci. **2**, 73 (2012).
[75] F. Neese, Wiley Interdiscip. Rev. Comput. Mol. Sci. **12** (2022).
[76] D. G. A. Smith, L. A. Burns, A. C. Simmonett, R. M. Parrish, M. C. Schieber, R. Galvelis, P. Kraus, H. Kruse, R. Di Remigio, A. Alenaizan, A. M. James, S. Lehtola, J. P. Misiewicz, M. Scheurer, R. A. Shaw, J. B. Schriber, Y. Xie, Z. L. Glick, D. A. Sirianni, J. S. O'Brien, J. M. Waldrop,

A. Kumar, E. G. Hohenstein, B. P. Pritchard, B. R. Brooks, H. F. Schaefer, 3rd, A. Y. Sokolov, K. Patkowski, A. E. DePrince, 3rd, U. Bozkaya, R. A. King, F. A. Evangelista, J. M. Turney, T. D. Crawford, and C. D. Sherrill, J. Chem. Phys. **152**, 184108 (2020).

[77] C. David Sherrill and H. F. Schaefer, in *Advances in Quantum Chemistry*, Vol. 34, edited by P.-O. Löwdin, J. R. Sabin, M. C. Zerner, and E. Brändas (Academic Press, 1999) pp. 143–269.

[78] A. Karton, N. Sylvetsky, and J. M. L. Martin, J. Comput. Chem. **38**, 2063 (2017).

[79] M. Weiss, J. Berkowitz, and E. Appelman, J. Chem. Phys. **66**, 2049 (1977).

Accepted to J. Chem. Phys. 10.1063/5.0102310

Charge delocalization error in Piris Natural Orbital Functionals

Juan Felipe Huan Lew-Yee[1] and Jorge M. del Campo[1]

Departamento de Física y Química Teórica, Facultad de Química, Universidad Nacional Autónoma de México, Mexico City, C.P. 04510, México

(*Electronic mail: jmdelc@unam.mx)

(*Electronic mail: felipe.lew.yee@quimica.unam.mx)

(Dated: 11 August 2022)

Piris Natural Orbital Functionals (PNOF) have been recognized as a low-scaling alternative to study strong correlated systems. In this work, we address the performance of the fifth functional (PNOF5) and the seventh functional (PNOF7) to deal with another common problem, the charge delocalization error. The effects of this problem can be observed in charged systems of repeated well-separated fragments, where the energy should be the sum of the charged and neutral fragments, regardless of how the charge is distributed. In practice, an energetic overstabilization of fractional charged fragments leads to a preference for having the charge delocalized throughout the system. To establish the performance of PNOF functionals regarding charge delocalization error, charged chains of helium atoms and the W4-17-MR set molecules were used as base fragments and their energy, charge distribution and correlation regime were studied. It was found that PNOF5 prefers localized charge distributions, while PNOF7 improves the treatment of interpair static correlation and tends to the correct energetic limit for several cases, although a preference for delocalized charge distributions may arise in highly strong correlation regimes. Overall, it is concluded that PNOF functionals can simultaneously deal with static correlation and charge delocalization errors, resulting in a promising choice to study charge-related problems.

Accepted to J. Chem. Phys. 10.1063/5.0102310

I. INTRODUCTION

Static correlation and charge delocalization represent two major challenges to be addressed by current electronic structure methods.[1–5] The former characterize systems that cannot be described by a single determinant due to nearly degenerate occupied and unoccupied orbitals, namely, strongly correlated systems,[6–9] and is required to describe a wide variety of molecules including transition metal compounds,[10–13] polyacenes,[14–18] cyclacenes,[19] molecules out of the equilibrium, diradicals,[16,20] superconductors,[21] photochemical devices,[22–24] and molecular switches.[25,26] On the other hand, the charge delocalization problem, commonly related to a multielectron self-interaction error,[27] arises as an energetic overstabilization of fractional charged systems.[1,28–30] This error can also be observed in charged chains of repeated well-separated fragments when delocalization of the charge throughout the system lowers the energy relative to its localization in a single fragment.[31,32] The charge delocalization error appears in common density functional approximations (DFAs), and an opposite charge localization problem appears in Hartree-Fock, having impact in the study of potential energy surfaces,[33] band-gaps,[34] chemical reactivity of conjugated, highly branched systems,[35] and charge transfer processes.[36]

Dealing simultaneously with static correlation and charge distribution is a difficult task from a DFAs perspective. It has been found that increasing the Hartree-Fock exchange contribution improves the charge delocalization description, an idea that has guided the design of some hybrid and long-range separated functionals;[37–39] however, it has also been reported that increasing the amount of Hartree-Fock exchange badly recovers static correlation,[40] leading to a conflict in the correction. In this regard, some DFAs have been proposed to deal separately with these effects, specifically the B05,[41] B13,[42] and KP16/B13,[43] for static correlation, and rCAM-B3LYP and MCY3[37] for the charge delocalization problem. Furthermore, the mKP16/B13[44] functional and the multiconfigurational pair density functional theory (MC-PDFT)[45,46] have been shown to improve the results simultaneously.

Methods based on the Reduced Density Matrix (RDM) have attracted attention as a promising alternative to study strongly correlated systems, standing at the middle point between the accuracy of multireference methods and the efficiency of density functional theory (DFT).[12,15,47–57] In this framework, Piris Natural Orbital Functionals (PNOF)[58–67] provide a chemical description through the second-order reduced density matrix (2-RDM) reconstructed from the first-order reduced density matrix (1-RDM), in its representation of natural orbitals (ϕ_p) and occupation num-

bers (n_p). In particular, PNOF5 became a breakthrough in the context of RDM-based methods by being strictly N-representable as shown by its connection with an antisymmetrized product of strongly orthogonal geminals (APSG), size-extensive and multiconfigurational,[63,68] but it includes only intrapair correlation, however, this was corrected in PNOF7 with a term to include static interpair correlation.[65] PNOF functionals reach a low computational cost when combined with the resolution of the identity approximation,[69–72] and have been applied to study static correlation problems.[73–77] In this work, we explore the PNOF performance in the charge delocalization error. We focus on PNOF7 performance and compare it with PNOF5 due to its similar functional form.

The paper is organized as follows; the theoretical framework of the PNOF functionals, quantification of the correlation regime, and a proposed metric to quantify the charge distribution are described in Section 2, the computational details are described in Section 3, which is followed by the results of applying the PNOF functionals to charged systems composed by repeated well-separated fragments, chosen to be helium atoms and the molecules of the W4-17-MR set,[78] in Section 4. Finally, the conclusions are given in Section 5.

II. THEORY

A. Piris Natural Orbital Functionals

Since the Hamiltonian contains at most two-electron interactions, the 2-RDM contains all the information required to compute the energy of the system as expressed in equation (1),

$$E = \sum_{ij} H_{ij}\Gamma_{ji} + \sum_{ijkl} \langle ij|kl\rangle D_{kl,ij} \ , \tag{1}$$

where the indices i, j, k and l represent spin molecular orbitals (MO), $\mathbf{H}$ is the core Hamiltonian matrix, $\langle ij|kl\rangle$ corresponds to the tensor of molecular orbital electron repulsion integrals, $\mathbf{\Gamma}$ is the 1-RDM, and $\mathbf{D}$ is the 2-RDM. The 2-RDM must be constrained to N-representability conditions which ensure that it remains connected to the wave function of the system.[79–82] PNOF functionals intrinsically incorporate several of these conditions by using the 1-RDM and its connection with the 2-RDM via the Piris cummulant,[58,83] which depends on $\mathbf{\Delta}$ and $\mathbf{\Pi}$ matrices, and within the use of a spin-restricted formalism leads to the expression

$$E = 2\sum_{p} n_p H_{pp} + \sum_{qp} \Pi_{qp} L_{pq} + \sum_{qp} (n_q n_p - \Delta_{qp})(2J_{pq} - K_{pq}) \ , \tag{2}$$

where p and q represent the spatial natural orbitals that diagonalize the 1-RDM, with n_p and n_q being their corresponding occupation numbers; $\mathbf{J}$ represents Coulomb spatial NO integrals, $\mathbf{K}$ represents exchange spatial NO integrals, and $\mathbf{L}$ represents exchange and time-inversion spatial NO integrals that reduce to exchange integrals for real orbitals, as used in this work. The energy in equation (2) is optimized with respect to the natural orbitals and their corresponding occupation numbers, using an iterative diagonalization method[84] with an electron pairing approach.[62,63] In this process, the orbital space (Ω) is divided into contributions, Ω_I and Ω_{II}. The former is divided into N_I subspaces, each with a single orbital occupied by one electron, but with an occupation number of $1/2$ due to the spin-restricted formalism, while Ω_{II} is divided into $N_{II}/2$ subspaces Ω_g, each containing a strongly occupied orbital, labeled $\{n_g\}$, coupled with N_g weakly occupied orbitals, labeled $\{n_{p_i}\}$; overall giving $N_\Omega = N_{II}/2 + N_I$ subspaces.[85] Here, N_I corresponds to the number of unpaired electrons, and N_{II} represents the number of paired electrons such that

$$2S + 1 = N_I + 1 \tag{3}$$

$$N_I + N_{II} = N \ , \tag{4}$$

where S is the net spin of the system and N corresponds to the number of electrons. This partition scheme leads to an ensemble of states with zero spin projection, $\langle s_z \rangle = 0$.

Bounds to the $\mathbf{\Delta}$ and $\mathbf{\Pi}$ matrices are obtained by imposing sum rules and N-representability conditions, explicit forms of these matrices give rise to the available PNOF correlation functionals.[86] For PNOF5 this becomes[63]

$$E = \sum_{g=1}^{N_{II}/2} E_g + \sum_{g=N_{II}/2+1}^{N_\Omega} H_{gg} + \sum_{f,g,f\neq g}^{N_\Omega} E_{fg} \ , \tag{5}$$

where E_g is the intrapair contribution to the energy given by

$$E_g = 2 \sum_{p\in\Omega_g} n_p H_{pp} + \sum_{q,p\in\Omega_g} \Pi_{qp}^g K_{pq} \ , \tag{6}$$

with

$$\Pi_{qp}^g = \begin{cases} \sqrt{n_q n_p} & q = p \text{ or } q, p > N_{II}/2 \\ -\sqrt{n_q n_p} & q = g \text{ or } p = g \end{cases} \tag{7}$$

and E_{fg} is the Hartree-Fock like interpair contribution

$$E_{fg} = \sum_{p\in\Omega_f} \sum_{q\in\Omega_g} n_q n_p (2J_{pq} - K_{pq}) \ . \tag{8}$$

It has been proven that the PNOF5 functional can be related to an APSG theory,[63,68] hence inheriting several advantages such as size-extensitivty and N-representability, but also underestimating the interpair correlation. PNOF7 improves on this problem by adding a term to the interpair contribution of equation (8), leading to[65]

$$E_{fg} = \sum_{p\in\Omega_f}\sum_{q\in\Omega_g}\left[n_q n_p(2J_{pq} - K_{pq}) - \Phi_q\Phi_p K_{pq}\right] , \tag{9}$$

with

$$\Phi_p = \sqrt{n_p(1-n_p)} . \tag{10}$$

The Φ_p contribution of equation (10) and hence the last contribution of equation (9) has significant values when n_p is far from zero and one, hence PNOF7 recovers only the static part of the interpair correlation.[65]

B. M-diagnostic to measure static correlation

The M-diagnostic was proposed by Truhlar and coworkers[87] and considers the deviation of the occupation numbers as an indicator of the importance of static correlation. Here, we have adapted its definition to be valid in the context of spin-restricted natural orbital functional theory as

$$M = \frac{1}{2}\left([2-2n_{LSDONO}] + [\sum_{j\in SONO}|2n_j - 1|] + [2n_{MWDONO}]\right) , \tag{11}$$

where LSDONO stands for the Least Strongly Double Occupied Natural Orbital, that is, the strongly double occupied orbital with the largest deviation from one, SONO stands for Single Occupied Natural Orbitals, and MWDONO stands for the Most Weakly Double Occupied Natural Orbital, namely, the weakly double occupied orbital with the largest deviation from zero. M-diagnostic values equal to or greater than 0.1 indicate that static correlation effects are relevant. It is worth noticing that in PNOF, the SONOs correspond to natural orbitals in Ω_I with occupation numbers fixed to $1/2$, thus, the second term of equation (11) vanishes, on the other hand the LSDONO and MWDONO correspond to Ω_{II}, and the first and third term are non vanishing unless the occupation numbers become zero or one, that is, on the Hartree-Fock limit. Furthermore, in a PNOF perfect pairing approach, there is only one orbital coupled to each strongly double occupied orbital, hence, the MWDONO and the LSDONO are coupled in the same subspace, and the first and third terms of equation (11) become equal due to the N-representability restriction of the orbitals in a subspace Ω_g to add up to one. Taking everything into account, the M-diagnostic applied

to a perfect pairing PNOF functional becomes

$$M = 2 - 2min\{n_g\} = 2max\{n_{p_i}\};\ \{n_g, n_{p_i}\} \in \Omega_g\ , \tag{12}$$

where the first equality indicates to analyze the deviation from one for the smallest valued strongly double occupied orbital, and the second equality indicates to analyze the deviation from zero for the highest valued weakly double occupied orbital. The last condition of equation (12) emphasizes that within the PNOF perfect pairing approach, the orbitals selected in the first and second equality belong to the same orbital subspace, Ω_g.

C. Measure of the charge delocalization problem

The energy of a system with fractional electron number should be linearly connected to the energy of the systems with the closest integer numbers, however, in practice, approximate functionals may overestimate or underestimate this energy.[28,29,34,88,89] A common test for the charge delocalization error is the ionization of systems formed by several repeated well-separated fragments, as illustrated in Figure 1a, where each sphere represents a fragment and r represents their separation distance.[32,38,46,90] Because the fragments in the system are well-separated, there should not be interactions between them, and the energy of the system should be the sum of the energy of a positive charged fragment, $E_{charged}$, and several uncharged fragments, E_0,

$$E_{system} = E_{charged} - (w-1)E_0\ , \tag{13}$$

where w indicates the number of fragments in the system. Another possible solution corresponds to the equivalent delocalization of the charge throughout the fragments of the system. Both solutions are valid and should be energetically equivalent. In fact, if the linearity of the energy holds, any charge distribution leads to the same energy. However, equation (13) is no longer satisfied when the charge delocalization error manifests and its deviation can be taken as evidence of the energetic overestimation of having fractional charged fragments.

To describe the charge distribution over the fragments, we propose to take the difference between the most charged fragment and the least charged fragment as a charge localization metric,

$$\begin{matrix}\text{Charge}\\ \text{Localization}\\ \text{Metric}\end{matrix} = max\left\{\begin{matrix}\text{Charges}\\ \text{of}\\ \text{Fragments}\end{matrix}\right\} - min\left\{\begin{matrix}\text{Charges}\\ \text{of}\\ \text{Fragments}\end{matrix}\right\}\ , \tag{14}$$

Accepted to J. Chem. Phys. 10.1063/5.0102310

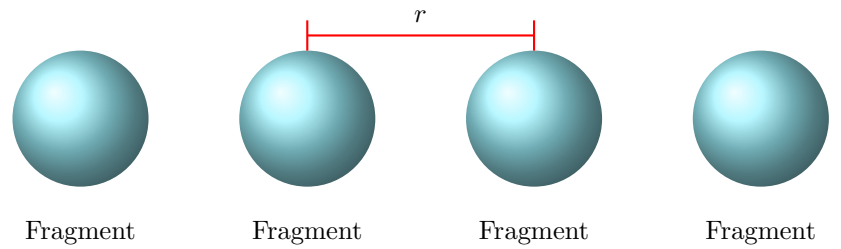

(a) Sketch of systems

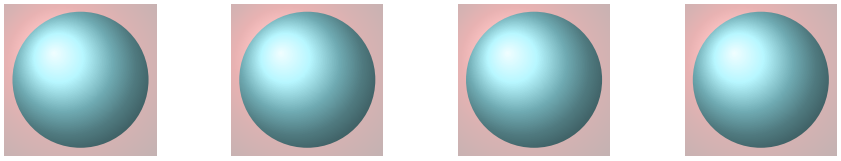

(b) Totally delocalized charge

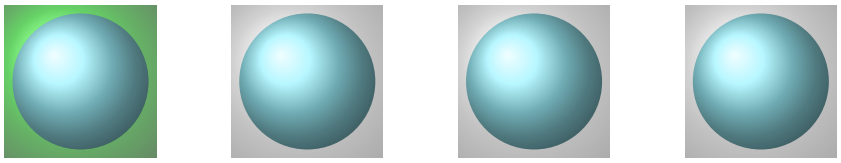

(c) Totally localized charge

FIG. 1. Representation of the studied systems, depicted as chains of repeated, well-separated fragments. Figure 1a presents a scheme where the fragments are symbolized by spheres separated by a distance r, in this work $r = 7$ Å was used. Once the system is ionized, there are two limit cases. Figure 1b depicts the case where the charge is fully delocalized throughout the fragments of the system, colored in red, hence all atoms are equally charged, leading to a charge localization metric value of zero in this case. Figure 1c illustrates the case where the charge is totally localized in a single fragment, colored in green, which leads to a charge localization metric value of one.

where the curly braces indicate the set of all fragment charges in a system.

According to this metric, systems with the charge fully delocalized will have a value of zero since all fragments are equally charged, as depicted in Figure 1b, conversely, systems with the charge concentrated in a single fragment will present a value of one, as illustrated in Figure 1c. The metric values between these two limit cases indicate partial localization of the charge. The

proposed charge localization metric provides information about how the charge is distributed in the molecule, but it does not quantify if the charge delocalization error is present. In practice, the energy deviation from equation (13) together with the charge distribution will indicate the presence of charge delocalization error. In addition, the charge delocalization error causes the ionization potentials of the systems to depend on the number of fragments; therefore, the deviation of the ionization potentials relative to the number of fragments can also be used as a qualitative indicator of the performance in the charge delocalization error.

III. METHODOLOGY AND COMPUTATIONAL DETAILS

Calculations were performed using a helium atom as base fragment for the systems (see Figure 1a). The built helium chains become of interest since they do not present static correlation, thus providing a clear picture of the charge delocalization problem. However, one of the main advantages of PNOF functionals is the capability of studying strongly correlated systems; therefore, we have taken the molecules from the W4-17-MR set as base fragments to build systems such as the one presented in Figure 1a. In all cases, a separation distance (r) of 7 Å was used.

PNOF calculations were performed using an in-house Python version of DoNOF[91] software (PyNOF code) based on Numba[92] for performance, NumPy[93] and SciPy[94] for numerical calculations and optimization problems, and with graphics processing unit (GPU) accelerators through CuPy for molecular integral transformation.[95] Electron repulsion integrals were calculated using the Psi4 interface,[96,97] and resolution of the identity approximation[70–72] was used for molecular orbital integral transformation[69] with cc-pVDZ / cc-pVDZ-jkfit bases sets.[98–101] A perfect pairing scheme was used for all PNOF calculations, that is, one weakly occupied orbital coupled to each strongly occupied orbital. The charges were computed according to a Löwdin population analysis. The DFAs calculations were performed using the ORCA Software[102–105] for comparison.

IV. RESULTS

The ionization potentials (IP) of the helium chains with up to 20 well-separated helium atoms were computed to analyze the variation with the number of fragments relative to the ionization potential of a single helium atom as an effect of the charge distribution, as presented in Figure 2 for the PNOF5 and PNOF7 functionals; additionally, five DFAs are included for comparison, namely,

Accepted to J. Chem. Phys. 10.1063/5.0102310

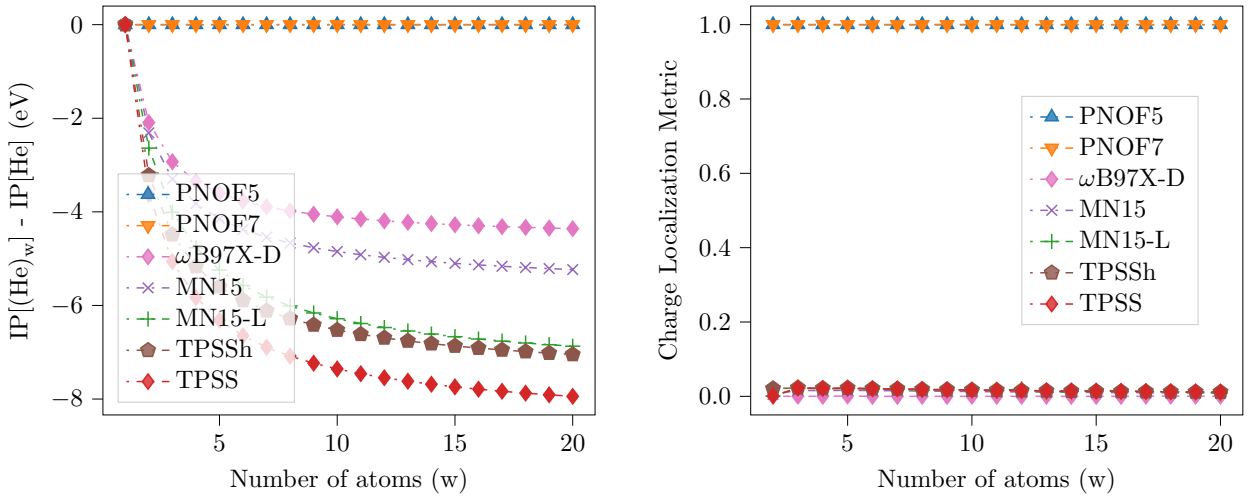

(a) Deviations of the Ionization Potential (IP) of helium chains $(He)_w$ relative to the IP of a single atom. Closeness to zero is better, and indicates less deviation.

(b) Charge Localization Metric for the helium chains $(He)_w$. Closeness to one indicates localization of the charge, while closeness to zero indicates delocalization of the charge.

FIG. 2. Charge localization in the ionization of helium chains for PNOF5, PNOF7, and several density functional approximations. PNOF functionals predicts stable ionization potentials with the charge localized in a single atom, while DFAs ionization potentials degrade with the number of atoms in the chains due to the delocalization of the charge through all the atoms.

the meta-GGA MN15-L[106] and TPSS[107,108] functionals, the hybrid MN15[109] and TPSSh[110] functionals, and the long range-separated ωB97X-D functional.[111] All tested DFAs provide a good prediction of the ionization potential of a single helium atom; however, their predictions quickly degrade to errors of several eV, while PNOF5 (blue triangle marks) and PNOF7 (orange inverted triangles marks) predictions remain stable independently of the number of helium atoms in the chain. This behavior can be understood in terms of the charge localization metric, as revealed in Figure 2b, where it can be seen that both the PNOF5 and PNOF7 functionals present charge localization metric values of 1.0, indicating that the resulting charge of the ionization process is completely localized in a single atom, as in the example case in Figure 1c. On the other hand, DFAs present values of the charge localization metric close to zero, indicating an almost entirely delocalized charge distribution corresponding to the example case in Figure 1b of the proposed charge localization metric. It is worth noticing that helium dimers have already been studied with PNOF functionals in Ref.[59,112] The M-diagnostic values of the helium chains are 0.009, which

confirms that the helium chains does not present significant static correlation, and the behavior can be completely attributed to the performance in the charge delocalization problem, as previously reported.[45]

Due to the results obtained for helium chains, we have expanded the analysis to study the charge localization behavior of PNOF functionals under various correlation regimes. To this effect, we have taken the seventeen molecules of the W4-17-MR strongly correlated set[78,113] as fragments to build chains of four units. First, the M-diagnostic was applied to the PNOF calculations for the neutral and charged molecules. Figure 3 compares the M-diagnostic values of PNOF5 in the second multicolumn and of PNOF7 in the third multicolumn, for the calculations of neutral, $M^{(0)}$, and charged, $M^{(1)}$, systems, with each row labeled with the base molecule of the chain. Recall that for the M-diagnostic, the higher the value, the stronger the correlation regime; and the lower the value, the weaker the correlation regime. Numerical values have been colored so that values higher than 0.1 are green-colored, that is, the systems diagnosed as strongly correlated, and lower values are yellow-colored. It can be seen that both PNOF functionals treat most systems as strongly correlated according to the multireference nature of the set; however, there are some exceptions for PNOF5, particularly for eight neutral molecules, namely, Cl_2O, ClF_3, ClF_5, ClO_3, ClOOCl, F_2O, OClO and OF, and five charged molecules, namely, Cl_2O, ClF_3, ClF_5, ClOOCl and OF. This is mostly corrected by PNOF7, which treats all charged molecules as strongly correlated, as well as all neutral molecules except ClF_5, ClO_3, and OClO. The tendency of PNOF7 to yield higher M-diagnostic values than PNOF5 can be interpreted in terms of the last term of equation (9), which indicates that PNOF7 incorporates static interpair correlation to the functional form of PNOF5, thus stabilizing strongly correlated systems.

The charge localization metric of equation (14) applied to the four fragments systems is presented in Figure 4, where the first column indicates the base fragment used to build the chain, and the rest of the columns indicate the value of the metric for the converged calculations of PNOF5, PNOF7, and DFAs. Values close to one represent the case of a totally localized charge and are green-colored, and values close to zero represent the case of a totally delocalized charge and are yellow-colored. The first thing to notice is that PNOF5 results, numerically, indicate that it completely localizes the charge in a single fragment without preference for fractional charges. However, PNOF7 presents a wider range of metric values, with six systems exhibiting complete charge localization with metric values of one, namely Cl_2O, ClF_3, ClF_5, ClOOCl, F_2O and OF, and the others presenting lower metric values indicating partial charge delocalization. The results

Accepted to J. Chem. Phys. 10.1063/5.0102310

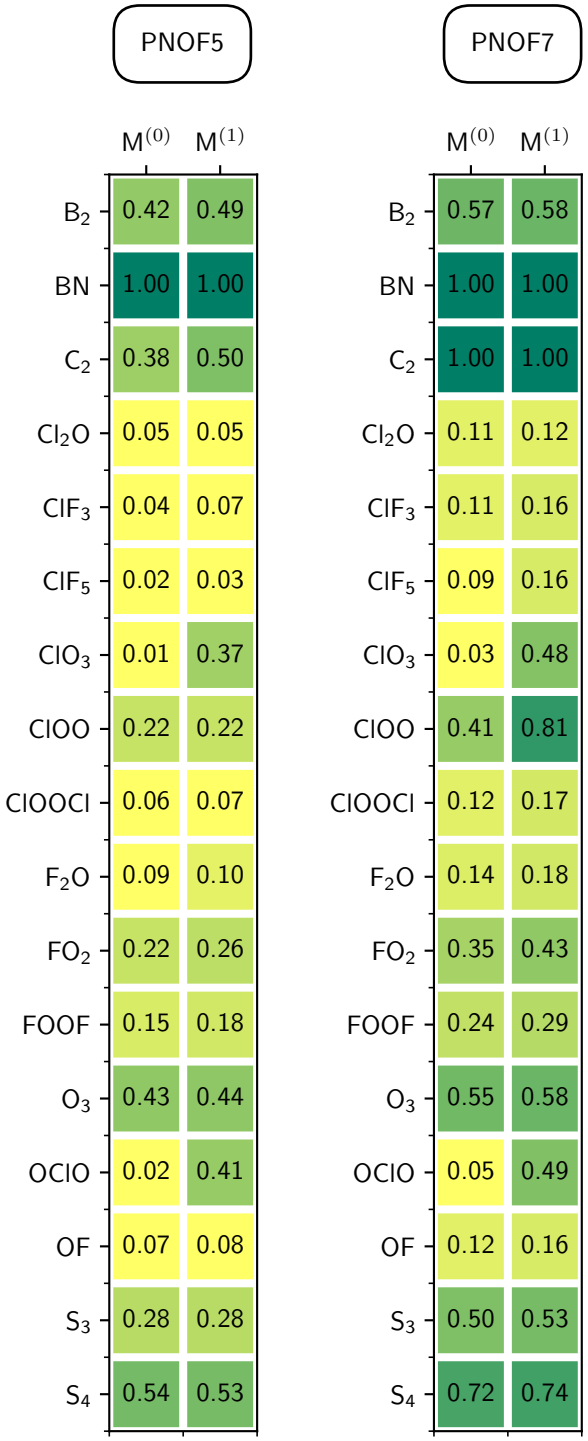

FIG. 3. M-diagnostic of static correlation applied to the neutral, $M^{(0)}$, and charged, $M^{(1)}$, chains of four units taken the molecules of the W4-17-MR set as base units. Molecules with M-diagnostic equal or higher than 0.10 are considered as strongly correlated. Systems with high M-diagnostic values are indicated by green-colored numbers and systems with low M-diagnostic values are indicated by yellow-colored numbers

Accepted to J. Chem. Phys. 10.1063/5.0102310

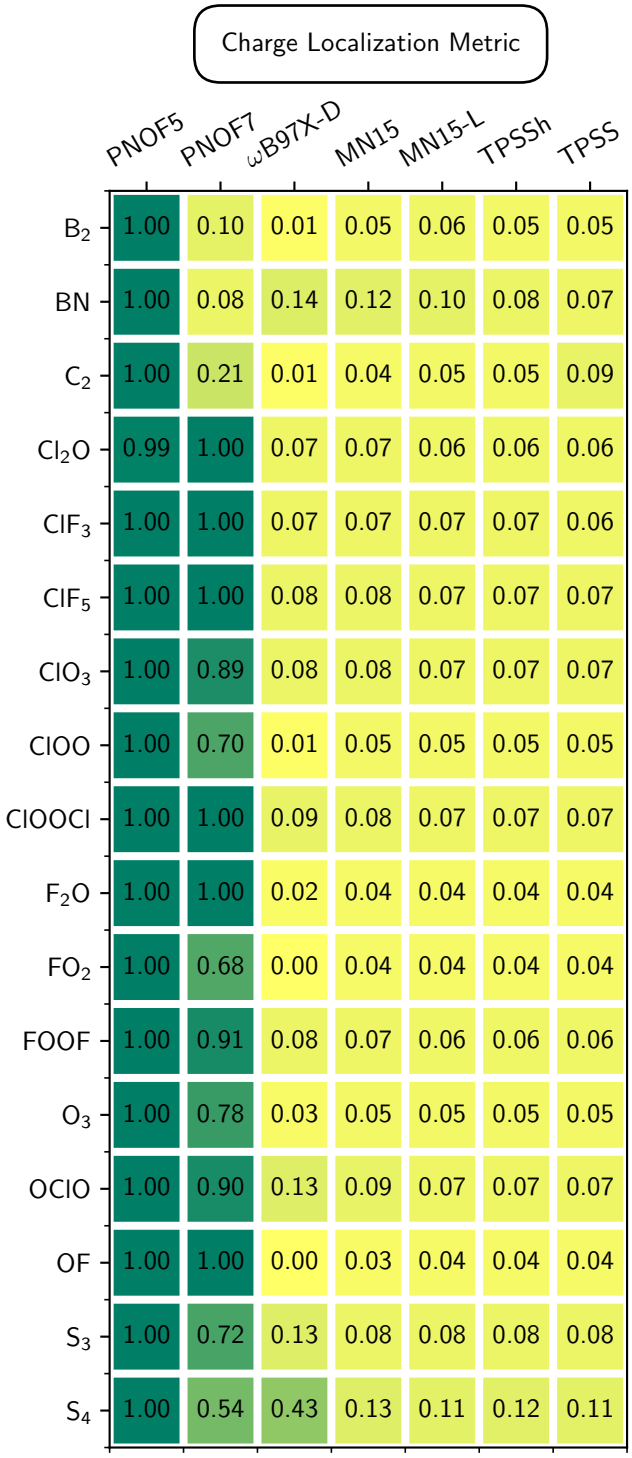

FIG. 4. Charge localization metric for the positively charged chains of four well-separated fragments with PNOF5, PNOF7, and several density functional approximations for comparison. Values of one indicate complete localization of the charge in a single fragment (green), while values of zero indicate complete delocalization of the charge (yellow), and intermediate values indicate partial localization of the charge

of common DFAs are presented for comparison, where it can be seen that they have localization metric values close to zero, that is, the charge is delocalized throughout the fragments.

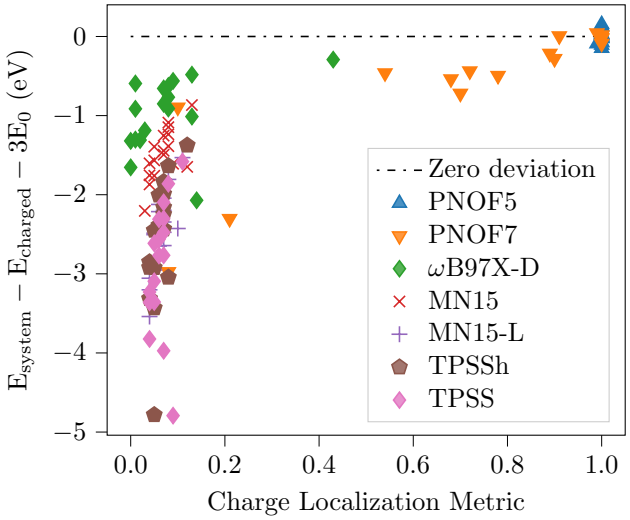

FIG. 5. Deviation of the energy of the W4-17-MR charged chains as a function of the charge localization metric for PNOF5, PNOF7, and common DFAs. Points at the left side indicate that the charge is delocalized throughout all the fragments, while points at the right size indicates that the charge is localized in a single fragment. Points close to zero in the vertical axes are desirable and indicates that the energy tends to be the equivalent to the sum of a charged fragment and three neutral fragments, while points far from zero at the bottom of vertical axes indicate overstabilization of the charge distributed solution due to charge delocalization error. All points correspond to converged calculations.

The preference of the methods for the charge distributions achieved in Figure 4 can be understood by means of the energy. The comparison is shown in Figure 5, where the charge localization metric is related to the energy deviation from the sum of the separated fragments, that is, a charged fragment and three neutral fragments as in equation (13) with $w = 4$ for systems with four fragments. As long as the charge delocalization error is not manifested, any charge distribution should have a zero energy deviation; hence, all points in a horizontal line at zero of the vertical axis are valid, and deviation from this line indicates charge delocalization error. In practice, the DFAs appear on the left side with large energy deviations as they overstabilize fractional charges, leading to delocalized charge distributions. On the other hand, PNOF5 appears in the upper right corner, preferring to localize the charge in a single fragment with no energy deviations; this behavior reminds the Hartree-Fock preference for localized charge distributions, but with PNOF5 presenting intrapair electron correlation. In contrast, PNOF7 shows a wide distribution of points in the upper

part of the plot. Several of these points present negative energy deviations, indicating that PNOF7 may suffer from charge delocalization error; however, these are generally closer to the horizontal line, and their lower energy deviations lead us to conclude that PNOF7 is able to outperform common DFAs.

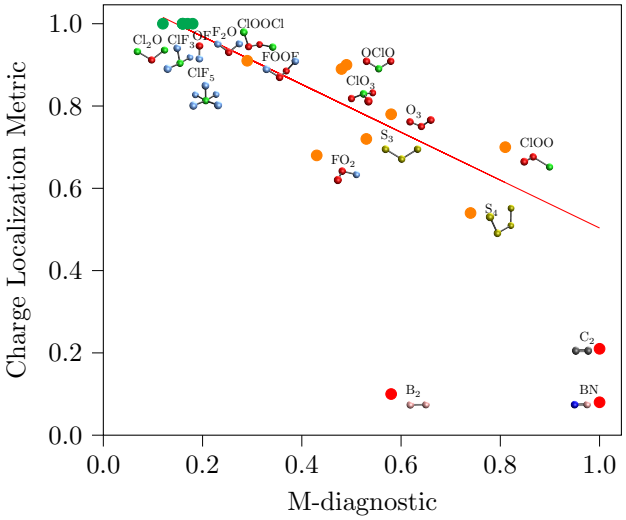

FIG. 6. Distribution of the W4-17-MR molecules according to the M-diagnostic and Charge Localization Metric of the charged system computed with PNOF7. Each point in the plot corresponds to a four unit chain and is labeled with the molecular formula of the base fragment. The green points correspond to completely localized systems, orange points to partially localized systems, and red points to completely delocalized systems.

Finally, the performance of PNOF7 in the charge delocalization problem can be related to the correlation regime with the M-diagnostic, as shown in Figure 6. Each point has been labeled with the molecular formula of the base fragment and colored according to the charge distribution achieved. Green points correspond to systems where the charge is completely localized in a single fragment of the system, that is, with charge localization metric values of one. These points include the six systems on the top left side of the plot and all present M-diagnostic values below 0.2. Orange points correspond to systems with charge localization metric below one, but still with partial localization of the charge, and include eight systems. Three systems are presented in red, corresponding to the systems with highly delocalized charge distributions. A line has been drowned to highlight the relation between charge distribution and correlation regime for PNOF7, as the charge is localized for systems with low values of the M-diagnostic, but a preference for fractional charges arises as the M-diagnostic values increase.

The observed relation between charge delocalization error and the M-diagnostic in PNOF7 can be attributed to an imbalance between static and dynamic correlation. In fact, PNOF7 does not has interpair dynamic correlation, which leads to an overestimation of the static correlation and contributes to the charge delocalization error, as shown in this work. PNOF5 treats accurately the intrapair correlation but do not include the interpair correlation, and shows a preference for localized charges with the correct dissociation limit. Although PNOF7 has charge delocalization error, its contribution is acceptable and small in most cases, and it becomes a promising method for studying charge-related problems. Recently, a Global Natural Orbital Functional has been proposed,[66,67] which preserves the accurately described intrapair correlation but leads to a better balance between static and dynamic interpair correlation, it is expected that this functional will improve over the already promising results of PNOF7 in the charge delocalization problem.

V. CONCLUSIONS

In summary, the results presented here for the systems of repeated well-separated fragments prove that PNOFs are capable of incorporating static correlation and achieve good performance in the charge delocalization error for the studied cases. In particular, stable ionization potentials have been obtained with PNOF5 and PNOF7 for helium atom chains of up to 20 atoms. A careful analysis under various correlation regimes, performed with the molecules in the W4-17-MR set used as base fragments, showed a preference of PNOF5 for localized charge distributions. PNOF7 allows for more diverse charge distributions, although they are overstabilized with the increase of the strong correlation, as quantified by the M-diagnostic. In these cases, the charge delocalization problem may appear due to an imbalance between the static and dynamic interpair correlation, but energy deviations are acceptable. Overall, satisfactory results have been achieved with respect to the charge delocalization error for PNOF7, making it a promising low-scale methodology capable of studying multireference systems and charge-related problems.

ACKNOWLEDGMENTS

J. F. H. Lew-Yee with CVU number 867718 gratefully thanks CONACyT for the Ph.D. scholarship. J. M. del Campo acknowledges funding from projects CB-2016-282791, PAPIIT-IN201822, and computing resources from the LANCAD-UNAM-DGTIC-270 project.

DATA AVAILABILITY STATEMENT

The data that support the findings of this study are available within the article.

REFERENCES

[1]A. J. Cohen, P. Mori-Sánchez, and W. Yang, Science **321**, 792 (2008).

[2]P. Mori-Sánchez, A. J. Cohen, and W. Yang, Phys. Rev. Lett. **102**, 066403 (2009).

[3]A. J. Cohen, P. Mori-Sánchez, and W. Yang, Chem. Rev. **112**, 289 (2012).

[4]H. S. Yu, S. L. Li, and D. G. Truhlar, J. Chem. Phys. **145**, 130901 (2016).

[5]M. Hellgren and T. Gould, J. Chem. Theory Comput. **15**, 4907 (2019).

[6]D. L. Crittenden, J. Phys. Chem. A **117**, 3852 (2013).

[7]E. Ramos-Cordoba, P. Salvador, and E. Matito, Physical Chemistry Chemical Physics **18**, 24015 (2016).

[8]C. L. Benavides-Riveros, N. N. Lathiotakis, and M. A. L. Marques, Physical Chemistry Chemical Physics **19**, 12655 (2017).

[9]J. W. Hollett and P. M. W. Gill, J. Chem. Phys. **134**, 114111 (2011).

[10]E. R. Johnson and A. D. Becke, J. Chem. Phys. **146**, 211105 (2017).

[11]W. Jiang, N. J. Deyonker, and A. K. Wilson, J. Chem. Theory Comput. **8**, 460 (2012).

[12]A. W. Schlimgen and D. A. Mazziotti, J. Phys. Chem. A **121**, 9377 (2017).

[13]K. A. Moltved and K. P. Kepp, J. Phys. Chem. A **123**, 2888 (2019).

[14]J. W. Mullinax, E. Epifanovsky, G. Gidofalvi, and A. Eugene Deprince, J. Chem. Theory Comput. **15**, 276 (2019).

[15]J. Fosso-Tande, T. S. Nguyen, G. Gidofalvi, and A. E. Deprince, J. Chem. Theory Comput. **12**, 2260 (2016).

[16]J. Shee, E. J. Arthur, S. Zhang, D. R. Reichman, and R. A. Friesner, J. Chem. Theory Comput. **15**, 4924 (2019).

[17]C. U. Ibeji and D. Ghosh, Phys. Chem. Chem. Phys. **17**, 9849 (2015).

[18]B. Hajgató, M. Huzak, and M. S. Deleuze, J. Phys. Chem. A **115**, 9282 (2011).

[19]C. S. Wu, P. Y. Lee, and J. D. Chai, Sci. Rep. **6**, 1 (2016).

[20]X. Lopez, F. Ruipérez, M. Piris, J. M. Matxain, and J. M. Ugalde, Chemphyschem **12**, 1061 (2011).

[21]J. K. Perry, J. Phys. Chem. A **104**, 2438 (2000).

[22]P. De Silva, J. Phys. Chem. Lett. **10**, 5674 (2019).

[23]Z. Shuai and Q. Peng, Natl Sci Rev **4**, 224 (2016).

[24]L. Brus, Acc. Chem. Res. **47**, 2951 (2014).

[25]M. Sajjan, S. Hemmatiyan, and D. A. Mazziotti, J. Phys. Chem. A **125**, 5448 (2021).

[26]N. Sylvetsky, A. Banerjee, M. Alonso, and J. M. L. Martin, J. Chem. Theory Comput. **16**, 3641 (2020).

[27]Y. Zhang and W. Yang, J. Chem. Phys. **109**, 2604 (1998).

[28]J. P. Perdew, R. G. Parr, M. Levy, and J. L. Balduz, Phys. Rev. Lett. **49**, 1691 (1982).

[29]W. Yang, Y. Zhang, and P. W. Ayers, Phys. Rev. Lett. **84**, 5172 (2000).

[30]P. Mori-Sánchez, A. J. Cohen, and W. Yang, J. Chem. Phys. **125**, 201102 (2006).

[31]A. Ruzsinszky, J. P. Perdew, G. I. Csonka, O. A. Vydrov, and G. E. Scuseria, J. Chem. Phys. **125**, 194112 (2006).

[32]S. R. Whittleton, X. A. Sosa Vazquez, C. M. Isborn, and E. R. Johnson, J. Chem. Phys. **142**, 184106 (2015).

[33]F. Liu and H. J. Kulik, J. Chem. Theory Comput. **16**, 264 (2020).

[34]P. Mori-Sánchez, A. J. Cohen, and W. Yang, Phys. Rev. Lett. **100**, 146401 (2008).

[35]E. R. Johnson, P. Mori-Sánchez, A. J. Cohen, and W. Yang, J. Chem. Phys. **129**, 204112 (2008).

[36]A. D. Becke, S. G. Dale, and E. R. Johnson, J. Chem. Phys. **148**, 211101 (2018).

[37]A. J. Cohen, P. Mori-Sánchez, and W. Yang, J. Chem. Phys. **126**, 191109 (2007).

[38]T. Körzdörfer and J. L. Brédas, Accounts of Chemical Research **47**, 3284 (2014).

[39]J. Autschbach and M. Srebro, Accounts of Chemical Research **47**, 2592 (2014).

[40]D. Zhang and D. G. Truhlar, Journal of Chemical Theory and Computation **16**, 5432 (2020).

[41]A. D. Becke, J. Chem. Phys. **122**, 064101 (2005).

[42]A. D. Becke, J. Chem. Phys. **138**, 074109 (2013).

[43]J. Kong and E. Proynov, J. Chem. Theory Comput. **12**, 133 (2016).

[44]E. Proynov and J. Kong, J. Chem. Theory Comput. **17**, 4633 (2021).

[45]L. Gagliardi, D. G. Truhlar, G. L. Manni, R. K. Carlson, C. E. Hoyer, and J. L. Bao, Acc. Chem. Res. **50**, 66 (2017).

[46]J. L. Bao, Y. Wang, X. He, L. Gagliardi, and D. G. Truhlar, J. Phys. Chem. Lett. **8**, 5616 (2017).

[47]J. W. Mullinax, A. Y. Sokolov, and H. F. Schaefer, Journal of Chemical Theory and Computation **11**, 2487 (2015).

[48]D. A. Mazziotti, Chemical Reviews **112**, 244 (2012).

[49]D. Gibney, J.-N. Boyn, and D. A. Mazziotti, J. Phys. Chem. Lett. **12**, 385 (2021).

[50]R. van Meer, O. V. Gritsenko, and E. J. Baerends, J. Chem. Phys. **148**, 104102 (2018).

[51]D. A. Mazziotti, Acc. Chem. Res. **39**, 207 (2006).

[52]E. Maradzike, G. Gidofalvi, J. M. Turney, H. F. Schaefer, and A. E. DePrince, J. Chem. Theory Comput. **13**, 4113 (2017).

[53]M. Mostafanejad and A. Eugene Deprince, J. Chem. Theory Comput. **15**, 290 (2019).

[54]M. Mostafanejad, M. D. Liebenthal, and A. E. DePrince, 3rd, J. Chem. Theory Comput. **16**, 2274 (2020).

[55]M. Piris, Phys. Rev. A **98**, 1 (2018).

[56]M. Rodríguez-Mayorga, I. Mitxelena, F. Bruneval, and M. Piris, J. Chem. Theory Comput. **17**, 7562 (2021).

[57]W. Ai, W.-H. Fang, and N. Q. Su, J. Phys. Chem. Lett. , 1744 (2022).

[58]P. Leiva and M. Piris, J. Chem. Phys. **123**, 214102 (2005).

[59]M. Piris, X. Lopez, and J. M. Ugalde, J. Chem. Phys. **126**, 214103 (2007).

[60]M. Piris, J. M. Matxain, X. Lopez, and J. M. Ugalde, J. Chem. Phys. **132**, 031103 (2010).

[61]M. Piris, J. M. Matxain, X. Lopez, and J. M. Ugalde, J. Chem. Phys. **133**, 111101 (2010).

[62]M. Piris, X. Lopez, F. Ruipérez, J. M. Matxain, and J. M. Ugalde, J. Chem. Phys. **134**, 164102 (2011).

[63]M. Piris, J. M. Matxain, and X. Lopez, J. Chem. Phys. **139**, 234109 (2013).

[64]M. Piris, J. Chem. Phys. **141**, 044107 (2014).

[65]M. Piris, Phys. Rev. Lett. **119**, 1 (2017).

[66]M. Piris, Phys. Rev. Lett. **127**, 233001 (2021).

[67]I. Mitxelena and M. Piris, J. Chem. Phys. **156**, 214102 (2022).

[68]K. Pernal, Computational and Theoretical Chemistry **1003**, 127 (2013).

[69]J. F. H. Lew-Yee, M. Piris, and J. M. del Campo, The Journal of Chemical Physics **154**, 064102 (2021).

[70]J. L. Whitten, J. Chem. Phys. **58**, 4496 (1973).

[71]B. I. Dunlap, J. W. D. Connolly, and J. R. Sabin, J. Chem. Phys. **71**, 3396 (1979).

[72]M. Feyereisen, G. Fitzgerald, and A. Komornicki, Chem. Phys. Lett. **208**, 359 (1993).

[73]I. Mitxelena and M. Piris, J. Phys. Condens. Matter **32**, 17LT01 (2020).

[74]I. Mitxelena and M. Piris, J. Chem. Phys. **152**, 064108 (2020).

[75]J. M. Mercero, J. M. Ugalde, and M. Piris, Theor. Chem. Acc. **140**, 74 (2021).

[76]R. Quintero-Monsebaiz, L. I. Perea-Ramírez, M. Piris, and A. Vela, Phys. Chem. Chem. Phys. **23**, 2953 (2021).

[77]X. Lopez, M. Piris, J. M. Matxain, F. Ruipérez, and J. M. Ugalde, Chemphyschem **12**, 1673 (2011).

[78]A. Karton, N. Sylvetsky, and J. M. Martin, Journal of Computational Chemistry **38**, 2063 (2017).

[79]A. J. Coleman, Rev. Mod. Phys. **35**, 668 (1963).

[80]D. A. Mazziotti, Phys. Rev. Lett. **108**, 263002 (2012).

[81]D. W. Smith, "N-Representability problem for fermion density matrices. II. the First-Order density matrix withNEven," (1966).

[82]C. Garrod and J. K. Percus, J. Math. Phys. **5**, 1756 (1964).

[83]M. Piris, Int. J. Quantum Chem. **106**, 1093 (2006).

[84]M. Piris and J. M. Ugalde, J. Comput. Chem. **30**, 2078 (2009).

[85]M. Piris, Phys. Rev. A **100**, 1 (2019).

[86]M. Piris, Int. J. Quantum Chem. **113**, 620 (2013).

[87]O. Tishchenko, J. Zheng, and D. G. Truhlar, J. Chem. Theory Comput. **4**, 1208 (2008).

[88]D. Hait and M. Head-Gordon, J. Phys. Chem. Lett. **9**, 6280 (2018).

[89]K. R. Bryenton, A. A. Adeleke, S. G. Dale, and E. R. Johnson, Wiley Interdiscip. Rev. Comput. Mol. Sci. (2022).

[90]X. Zheng, M. Liu, E. R. Johnson, J. Contreras-García, and W. Yang, J. Chem. Phys. **137**, 214106 (2012).

[91]M. Piris and I. Mitxelena, Computer Physics Communications **259**, 107651 (2021).

[92]S. K. Lam, A. Pitrou, and S. Seibert, in *Proceedings of the Second Workshop on the LLVM Compiler Infrastructure in HPC*, LLVM '15 (Association for Computing Machinery, New York, NY, USA, 2015).

[93]C. R. Harris, K. J. Millman, S. J. van der Walt, R. Gommers, P. Virtanen, D. Cournapeau, E. Wieser, J. Taylor, S. Berg, N. J. Smith, R. Kern, M. Picus, S. Hoyer, M. H. van Kerkwijk, M. Brett, A. Haldane, J. F. del Río, M. Wiebe, P. Peterson, P. Gérard-Marchant, K. Sheppard, T. Reddy, W. Weckesser, H. Abbasi, C. Gohlke, and T. E. Oliphant, Nature **585**, 357 (2020).

[94]P. Virtanen, R. Gommers, T. E. Oliphant, M. Haberland, T. Reddy, D. Cournapeau, E. Burovski, P. Peterson, W. Weckesser, J. Bright, S. J. van der Walt, M. Brett, J. Wilson, K. J. Millman,

N. Mayorov, A. R. J. Nelson, E. Jones, R. Kern, E. Larson, C. J. Carey, İ. Polat, Y. Feng, E. W. Moore, J. VanderPlas, D. Laxalde, J. Perktold, R. Cimrman, I. Henriksen, E. A. Quintero, C. R. Harris, A. M. Archibald, A. H. Ribeiro, F. Pedregosa, P. van Mulbregt, and SciPy 1.0 Contributors, Nature Methods **17**, 261 (2020).

[95]R. Okuta, Y. Unno, D. Nishino, S. Hido, and C. Loomis, in *Proceedings of Workshop on Machine Learning Systems (LearningSys) in The Thirty-first Annual Conference on Neural Information Processing Systems (NIPS)* (2017).

[96]D. G. A. Smith, L. A. Burns, D. A. Sirianni, D. R. Nascimento, A. Kumar, A. M. James, J. B. Schriber, T. Zhang, B. Zhang, A. S. Abbott, E. J. Berquist, M. H. Lechner, L. A. Cunha, A. G. Heide, J. M. Waldrop, T. Y. Takeshita, A. Alenaizan, D. Neuhauser, R. A. King, A. C. Simmonett, J. M. Turney, H. F. Schaefer, F. A. Evangelista, A. E. DePrince, T. D. Crawford, K. Patkowski, and C. D. Sherrill, Journal of Chemical Theory and Computation **14**, 3504 (2018).

[97]D. G. A. Smith, L. A. Burns, A. C. Simmonett, R. M. Parrish, M. C. Schieber, R. Galvelis, P. Kraus, H. Kruse, R. Di Remigio, A. Alenaizan, A. M. James, S. Lehtola, J. P. Misiewicz, M. Scheurer, R. A. Shaw, J. B. Schriber, Y. Xie, Z. L. Glick, D. A. Sirianni, J. S. O'Brien, J. M. Waldrop, A. Kumar, E. G. Hohenstein, B. P. Pritchard, B. R. Brooks, H. F. Schaefer, A. Y. Sokolov, K. Patkowski, A. E. DePrince, U. Bozkaya, R. A. King, F. A. Evangelista, J. M. Turney, T. D. Crawford, and C. D. Sherrill, The Journal of Chemical Physics **152**, 184108 (2020).

[98]T. H. Dunning, J. Chem. Phys. **90**, 1007 (1989).

[99]R. A. Kendall, T. H. Dunning, and R. J. Harrison, J. Chem. Phys. **96**, 6796 (1992).

[100]D. E. Woon and T. H. Dunning, J. Chem. Phys. **98**, 1358 (1993).

[101]F. Weigend, Phys. Chem. Chem. Phys. **4**, 4285 (2002).

[102]F. Neese, Wiley Interdiscip. Rev. Comput. Mol. Sci. **2**, 73 (2012).

[103]F. Neese, Wiley Interdiscip. Rev. Comput. Mol. Sci. **8**, e1327 (2018).

[104]S. Lehtola, C. Steigemann, M. J. T. Oliveira, and M. A. L. Marques, SoftwareX **7**, 1 (2018).

[105]B. Helmich-Paris, J. Chem. Phys. **154**, 164104 (2021).

[106]H. S. Yu, X. He, and D. G. Truhlar, J. Chem. Theory Comput. **12**, 1280 (2016).

[107]J. P. Perdew, J. Tao, V. N. Staroverov, and G. E. Scuseria, J. Chem. Phys. **120**, 6898 (2004).

[108]J. Tao, J. P. Perdew, V. N. Staroverov, and G. E. Scuseria, Phys. Rev. Lett. **91**, 146401 (2003).

[109]H. S. Yu, X. He, S. L. Li, and D. G. Truhlar, Chem. Sci. **7**, 5032 (2016).

[110]V. N. Staroverov, G. E. Scuseria, J. Tao, and J. P. Perdew, J. Chem. Phys. **119**, 12129 (2003).

[111]J.-D. Chai and M. Head-Gordon, Phys. Chem. Chem. Phys. **10**, 6615 (2008).

[112]M. Piris, J. M. Matxain, and J. M. Ugalde, J. Chem. Phys. **129**, 014108 (2008).

[113]"W4-17 database," `https://www.chemtheorist.com/w4-17-database.html`, accessed: 2021-11-29.

Resolution of the identity approximation applied to PNOF correlation calculations

Juan Felipe Huan Lew-Yee[1], Mario Piris[2,3,*], Jorge M. del Campo[1,*]

[1] *Departamento de Física y Química Teórica, Facultad de Química, Universidad Nacional Autónoma de México, Mexico City, C.P. 04510, México*
[2] *Kimika Fakultatea, Euskal Herriko Unibertsitatea (UPV/EHU) and Donostia International Physics Center (DIPC), 20018 Donostia, Euskadi, Spain.*
[3] *Basque Foundation for Science (IKERBASQUE), 48013 Bilbao, Euskadi, Spain.*

In this work, the required algebra to employ the resolution of the identity approximation within Piris Natural Orbital Functional (PNOF) is developed, leading to an implementation named DoNOF-RI. The arithmetic scaling is reduced from fifth-order to fourth-order, and the memory scaling is reduced from fourth-order to third-order, allowing significant computational time savings. After the DoNOF-RI calculation has fully converged, a restart with four-center electron repulsion integrals can be performed to remove the effect of the auxiliary basis set incompleteness, quickly converging to the exact result. The proposed approach has been tested on cycloalkanes and other molecules of general interest to study the numerical results as well as the speed-ups achieved by PNOF7-RI when compared with PNOF7.

Keywords: Resolution of the Identity, Density Fitting, 1RDM, PNOF, DoNOF

I. INTRODUCTION

Recently [1], an open-source implementation of natural orbital functional (NOF) based methods has been made available to the scientific community. The associated computer program DoNOF is designed to solve the energy minimization problem of an approximate NOF which describes the ground-state of an N-electron system in terms of the natural orbitals (NOs) and their occupation numbers (ONs). Approximate NOFs have demonstrated [2] to be more accurate than density functionals for highly multi-configurational systems, and scale better with the number of basis functions than correlated wavefunction methods. A detailed account of the state of the art of the NOF-based methods can be found elsewhere [3–7].

A route [8] for the construction of an approximate NOF involves the employment of necessary N-representability conditions [9] for the two-particle reduced density matrix (2RDM) reconstructed in terms of the one-particle reduced density matrix (1RDM). Appropriate 2RDM reconstructions have led to different implementations known in the literature as PNOFi (i=1-7) [10–17]. This family of functionals provide an efficient way of including dynamic and static correlation with chemical accuracy in many cases [18, 19]. It has recently been shown [20, 21] that PNOF7 is an efficient method for strongly correlated electrons in one and two dimensions. In addition, the use of perturbative corrections allow to improve the dynamic correlation in order to achieve a complete method to describe electron correlated systems [22, 23].

*Electronic address: mario.piris@ehu.eus, jmdelc@unam.mx

In the current implementation, DoNOF computer code needs to transform the atomic orbital (AO) electron repulsion integrals (AO-ERIs) into molecular orbital (MO) electron repulsion integrals (MO-ERIs) in order to evaluate the Coulomb and exchange integrals required in PNOF. The optimization process involves searching for ONs, which requires the computation of Coulomb and exchange matrices in MO representation, and for NOs, which requires computing Coulomb and exchange matrices in AO representation for each MO. These procedures have overall fifth-order arithmetic scaling factor. While this scaling factor is lower compared to other procedures such as those based on configuration interaction and coupled cluster approaches, there is still room for improvement.

Resolution of the identity (RI), also known as density fitting [24–26], approximates the product of basis functions as a linear combination of an auxiliary basis set [27]. It usually reduces the arithmetic and memory scaling factors, and produces intermediate easy-to-handle arrays, as has been reported in other methodologies [28–39] such as RI-MP2 [34, 40–44], DF-MP2 [45, 45], DF-MP2.5 [46, 47], DF-MP3 [46, 47], DF-LCCD [48],DF-CCSD [33, 49, 50], and DF-CCSD(T) [50, 51]. In particular, the use of the RI approximation in v2RDM-CASSCF calculations [52, 53] has been shown, leading to energy expressions and handling of the MO-ERIs in the optimization procedure different from those necessary in the PNOF family of functionals. Applying the RI approximation in PNOF correlation calculations allows faster calculations, decreasing the arithmetic scale factor of the integral transformation of AO-ERIs to MO-ERIs from fifth order to fourth order, as shown in this work.

The text is structured as follows. In the second section, the elemental theory of PNOF formulation is shown and

the use of the RI approximation in the ONs and NOs optimization process is analyzed. In the third section, the details about the implementation are given. In the fourth section, the time savings due to the use of the RI approximation as well as the energy results in standard cycloalkanes test set up to nine carbon atoms are presented, another relevant molecules such as oxazole, borazine, coumarin, cyanuryc chloride, benzene, thiepine, and thieno[2,3-b]thiophene are also presented. Finally, conclusions are given in the fifth section.

II. THEORY

The ground-state electronic energy of an approximate NOF is given by the expression

$$E = 2\sum_p n_p H_{pp} + \sum_{pqrs} D[n_p, n_q, n_r, n_s](pq|rs) \qquad (1)$$

where H_{pp} denotes the one-electron matrix elements of the kinetic energy and outer potential operators, $(pq|rs)$ are the MO-ERIs in chemists' notation, and $D[n_p, n_q, n_r, n_s]$ represents the reconstructed 2RDM from the ONs $\{n_p\}$. Restrictions on the ONs to the range $0 \leq n_p \leq 1$ represent the necessary and sufficient conditions for ensemble N-representability of the 1RDM under the normalization condition, $2\sum_p n_p = \mathrm{N}$.

It is worth noting that any explicit dependence of D on the NOs $\{\phi_p\}$ themselves is neglected. Accordingly, NOs are the MOs that diagonalize the 1RDM of an approximate ground-state energy, so it is more appropriate to speak of a NOF rather than a functional of 1RDM due to the explicit dependence on the 2RDM [54].

It is clear that the construction of an N-representable functional given by Eq. (1) is related to the N-representability problem of D. Using its ensemble N-representability conditions to generate a reconstruction functional leads to PNOF [8]. This particular reconstruction is based on the introduction of two auxiliary matrices $\mathbf{\Delta}$ and $\mathbf{\Pi}$ expressed in terms of the ONs to reconstruct the cumulant part of the 2RDM [55]. For the sake of simplicity, let us address only singlet states in this work. The generalization of our results to spin-multiplet states [23] is straightforward. Consequently, energy expression of Eq. (1) becomes

$$\begin{aligned} E = & 2\sum_p n_p H_{pp} + \sum_{qp} \Pi_{qp} L_{pq} \\ & + \sum_{qp} (n_q n_p - \Delta_{qp})\,(2J_{pq} - K_{pq}) \end{aligned} \qquad (2)$$

where J_{pq}, K_{pq}, and L_{pq} are Coulomb, exchange, and exchange-time-inversion integrals [56]. Note that $L_{pq} = K_{pq}$ for real MOs as developed in this work. Therefore, only two-index J_{pq} and K_{pq} integrals are necessary due to our approximation for the 2RDM. Appropriate forms of matrices $\mathbf{\Delta}$ and $\mathbf{\Pi}$ lead to different implementations known as PNOFi (i=1-7). Remarkable is the case of PNOF5 which turned out to be strictly pure N-representable [57].

In the current implementation, minimization of the energy $E[\{n_p\}, \{\phi_p\}]$ is performed under orthonormality requirement for real NOs, whereas ONs conform to the ensemble N-representability conditions. The solution is established by optimizing the functional of Eq. (2) with respect to the ONs and to the NOs, separately [58].

In DoNOF [1], the Coulomb integrals are built according to the equation

$$\begin{aligned} J_{pq} &= \sum_{\mu\nu} P^p_{\mu\nu} J^q_{\mu\nu} \\ &= \sum_\mu C_{\mu p} \sum_\nu C_{\nu p} \sum_\sigma C_{\sigma q} \sum_\lambda C_{\lambda q} (\mu\nu|\sigma\lambda) \end{aligned} \qquad (3)$$

where the indices μ, ν, σ, λ label AOs of dimension N_b, and $(\mu\nu|\sigma\lambda)$ is an AO-ERI. Hence, $\boldsymbol{J}^q$ is the Coulomb matrix in AO basis for the MO ϕ_q, and $\boldsymbol{P}^p$ is computed by means of the MO coefficient matrix, $\boldsymbol{C}$, as

$$P^p_{\mu\nu} = C_{\mu p} C_{\nu p} \ . \qquad (4)$$

Similarly, the integrals are defined as

$$\begin{aligned} K_{pq} &= \sum_{\mu\sigma} P^p_{\mu\sigma} K^q_{\mu\sigma} \\ &= \sum_\mu C_{\mu p} \sum_\sigma C_{\sigma p} \sum_\nu C_{\nu q} \sum_\lambda C_{\lambda q} (\mu\nu|\sigma\lambda) \end{aligned} \qquad (5)$$

where $\boldsymbol{K}^q$ is the exchange matrix in AO basis for the MO ϕ_q.

From Eqs. (3) - (5), we observe that the four-index transformation of the ERIs generally scales as N_b^5. In the occupancy optimization, this operation is carried out once for fixed orbitals, however, in the orbital optimization it is necessary to perform this transformation every time orbitals change, which is a time-consuming process.

It is worth noting that the last members of the PNOF family, namely PNOF5-PNOF7, use electron-pairing constraints [7]. Until now, only these NOFs can provide the correct number of electrons in the fragments after a homolytic dissociation [19, 59]. Moreover, the constrained nonlinear programming problem for the ONs can be transformed into an unconstrained optimization with the corresponding saving of computational time. In the case of electron-pairing approaches, we can additionally reduce the number of orbitals in calculations, and use just orbitals in the pairing scheme, which we will represent as N_Ω ($N_\Omega \leq N_b$). From now on we will focus on the electron-pairing-based PNOFs.

In Table I, we show the conventional algorithm used to compute the Coulomb ($\boldsymbol{J}$) and exchange ($\boldsymbol{K}$) integrals in MO representation, and the Coulomb ($\boldsymbol{J}^q$) and exchange ($\boldsymbol{K}^q$) matrices in AO representation for each orbital ϕ_q. In the last columns, the memory and arithmetic scaling of the steps are reported. We see that the evaluation of

Table I: Algorithm used to compute $\boldsymbol{J}$ and $\boldsymbol{K}$ in the occupancy optimization, and $\boldsymbol{J}^q$ and $\boldsymbol{K}^q$ in the orbital optimization.

	Step	Operation	Scaling	
			Memory	Arithmetic
Common	0	Evaluation of $(\mu\nu\|\sigma\lambda)$	N_b^4	N_b^4
	1	$P^p_{\mu\nu} = C_{\mu p}C_{\nu p}$	$N_b^2 N_\Omega$	$N_b^2 N_\Omega$
J_{pq}	2	$J^q_{\mu\nu} = \sum_{\sigma\lambda} P^q_{\sigma\lambda}(\mu\nu\|\sigma\lambda)$	$N_b^2 N_\Omega$	$N_b^4 N_\Omega$
	3	$J_{pq} = \sum_{\mu\nu} P^p_{\mu\nu} J^q_{\mu\nu}$	N_Ω^2	$N_b^2 N_\Omega^2$
K_{pq}	2	$K^q_{\mu\sigma} = \sum_{\nu\lambda} P^q_{\nu\lambda}(\mu\nu\|\sigma\lambda)$	$N_b^2 N_\Omega$	$N_b^4 N_\Omega$
	3	$K_{pq} = \sum_{\mu\sigma} P^p_{\mu\sigma} K^q_{\mu\sigma}$	N_Ω^2	$N_b^2 N_\Omega^2$

the AO-ERIs $(\mu\nu|\sigma\lambda)$, labeled as step zero, has an arithmetic scaling of N_b^4. In the current implementation, they are evaluated and stored at the beginning, consequently, this step does not contribute significantly to the computational time. However, its storage represents the highest memory demand with a memory scaling of N_b^4.

The first step corresponds to the evaluation of $\boldsymbol{P}$ matrix, as shown in Eq. (4), which has low arithmetic and memory scaling factors of $N_b^2 N_\Omega$. The second step corresponds to the evaluation of $\boldsymbol{J}^q$ and $\boldsymbol{K}^q$ matrices for each MO in AO basis. This is the bottleneck of the current implementation with an arithmetic scaling factor of $N_b^4 N_\Omega$ and memory scaling of $N_b^2 N_\Omega$. Finally, in the third step, $\boldsymbol{J}$ and $\boldsymbol{K}$ integrals in MO representation are computed with an arithmetic scaling factor of $N_b^2 N_\Omega^2$. The memory scaling of this step is N_Ω^2, which is not significant compared to the other steps.

As mentioned above, energy minimization is made up of two independent optimization procedures, an outer one that involves the optimization of the ONs for fixed orbitals, and an inner one that involves the optimization of the NOs for fixed occupancies, as shown in Fig. 1. Both optimizations are iterative procedures in which many inner iterations are performed per each outer iteration until convergence. In the next subsections, the introduction of the RI approximation in each optimization procedure applied to PNOFi (i=5-7) is analyzed. For further reference, to emphasize the specific functional used, the calculations within this approach will be labeled as PNOFi-RI (i=5-7), while the global implementation will be named DoNOF-RI.

Occupancy Optimization with RI

In DoNOF [1], bounds on $\{n_p\}$ are imposed automatically by expressing the ONs through new auxiliary variables $\{\gamma_p\}$. In this way, the constrained minimization problem with respect to ONs for a fixed set of NOs is transformed into an unconstrained minimization problem with respect to auxiliary γ-variables.

Figure 1: General scheme of the energy optimization. A guess for ONs and NOs is considered, then an iterative procedure composed of two independent optimizations, with respect to ONs and NOs respectively, is performed. For a more detailed description, see the reference [1].

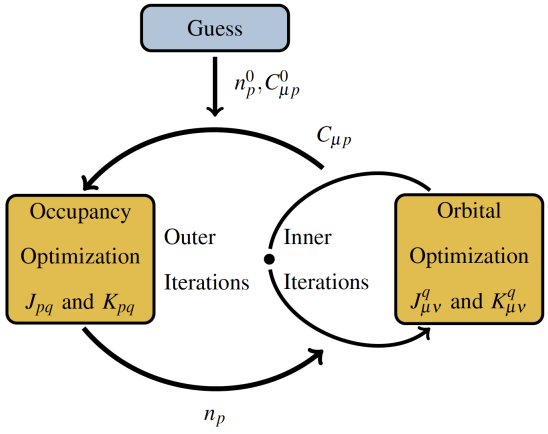

Since the orbitals do not change, $\boldsymbol{J}$ and $\boldsymbol{K}$ can be computed once and stored along the occupancy optimization process of an outer iteration. The RI approximation can be used to reduce the arithmetic scaling factors of $\boldsymbol{J}$ and $\boldsymbol{K}$ integrals. In this approximation, the four-center AO-ERI, $(\mu\nu|\sigma\lambda)$, is expressed using three-center ERIs, $(\mu\nu|k)$, and two-center ERIs, $(k|l)$, according to the equation

$$(\mu\nu|\sigma\lambda) = \sum_k (\mu\nu|k) \sum_l \boldsymbol{G}^{-1}_{kl} (l|\sigma\lambda) \ , \tag{6}$$

where k, l represent functions of the auxiliary basis of dimension N_{aux}, and $\boldsymbol{G}$ is a metric matrix defined as $G_{kl} = (k|l)$. In a symmetric approach, $\mathbf{G}^{-1/2}$ would be computed through eigenvalue decomposition or singular value decomposition, and multiplied by the three-center AO-ERIs, however, the metric matrix may be numerically ill conditioned [38], having small or even negative eigenvalues. Although this problem might be surpassed truncating eigenvalues below a certain tolerance, the overall process is slow and may affect the numerical stability. Recently, a modified Cholesky decomposition has been applied to factorize the metric matrix and correct the numerical problems if required [38, 60]. In this approach, the metric matrix is expressed as [61]

$$\boldsymbol{G} = \mathbf{PLDL}^T\mathbf{P}^T \ , \tag{7}$$

where $\mathbf{P}$ is a permutation matrix, $\mathbf{L}$ is a lower triangular matrix, and $\mathbf{D}$ is a block diagonal matrix with blocks of dimension 1×1 and 2×2 [62]. The eigenvalue spectrum

of the $\mathbf{D}$ matrix is analyzed block by block to correct negative and very small eigenvalues, giving a corrected matrix, $\tilde{\mathbf{D}}$ [63]. In PNOF correlation calculations a symmetric approach results convenient, thus the $\mathbf{G}$ matrix is expressed as

$$\mathbf{G} = \mathbf{P}\mathbf{L}\tilde{\mathbf{D}}^{1/2}\tilde{\mathbf{D}}^{1/2}\mathbf{L}^T\mathbf{P}^T \ , \tag{8}$$

the process of decomposing the $\mathbf{D}$ matrix in its eigenvectors and eigenvalues is fast due to the small dimension of its blocks. Once the eigenvalues have been corrected, its square root can be evaluated directly. Then, a $\mathbf{b}$ tensor is found by solving the following linear equation system

$$\mathbf{P}\mathbf{L}\tilde{\mathbf{D}}^{1/2}\mathbf{b}^T = (\mu\nu|k) \ . \tag{9}$$

Using RI, the Coulomb and exchange integrals can be expressed as

$$J_{pq} = \sum_l b^l_{pp} b^l_{qq} \ , \tag{10}$$

$$K_{pq} = \sum_l b^l_{pq} b^l_{pq} \ , \tag{11}$$

where the change of indices in $\boldsymbol{b}$ denotes contractions from AOs (μ, ν) to MOs (p, q) according to

$$b^l_{p\nu} = \sum_\mu C_{\mu p} b^l_{\mu\nu} \ , \tag{12}$$

$$b^l_{pq} = \sum_\nu C_{\nu q} b^l_{p\nu} \ . \tag{13}$$

An equivalent $\mathbf{b}$ tensor is employed in RI implementations that use $\mathbf{G}^{-1/2}$, particularly, the equations are similar to those used in RI-MP2 [34, 40–44] to build other MO-ERIs.

The memory and arithmetic scaling factors of the Eqs. (6)-(13) with the RI approximation are shown in Table II. The zero step corresponds to the evaluation of the $(\mu\nu|k)$ AO-ERIs, and the first step corresponds to solve the linear equation system for the $\boldsymbol{b}$ tensor with a memory scaling factor of $N_b^2 N_{aux}$ and arithmetic scaling factor of $N_b^2 N_{aux}^2$. Assuming that enough memory is available to store the $\boldsymbol{b}$ tensor in AO representation, this step can be performed only once at the beginning of the calculation; hence, although the first step has the largest memory scaling, it does not pose a problem through the iterative process. The second step is the contraction of an index of the $\mathbf{b}$ tensor from AO to MO with memory scaling of $N_b N_{aux} N_\Omega$ and arithmetic scaling of $N_b^2 N_{aux} N_\Omega$, being the most demanding step per outer iteration; in the third step the remaining atomic orbital is contracted with arithmetic scaling of $N_b N_{aux} N_\Omega^2$ and memory scaling of $N_{aux} N_\Omega^2$ respectively. Finally, in step four, the $\mathbf{b}$ tensor is used to build the Coulomb and exchange integrals with arithmetic scaling of $N_{aux} N_\Omega^2$ and memory scaling of N_Ω. The overall procedure has a fourth-order arithmetic scaling of $N_b^2 N_{aux} N_\Omega$.

Table II: Algorithm used to compute $\boldsymbol{J}$ and $\boldsymbol{K}$ in the occupancy optimization with RI. Formal memory scaling is shown. However, to optimize memory usage, the contraction of $\boldsymbol{b}$ tensor for $\boldsymbol{J}$ and $\boldsymbol{K}$ (steps 2, 3, and 4) are carried out simultaneously for each l, such that the dimension of the auxiliary basis does not affect the memory scaling.

	Step	Operation	Scaling	
			Memory	Arithmetic
Common	0	Evaluation of $(\mu\nu\|k)$	$N_b^2 N_{aux}$	$N_b^2 N_{aux}$
	1	Solve $\mathbf{P}\mathbf{L}\tilde{\mathbf{D}}^{1/2}\mathbf{b}^T$	$N_b^2 N_{aux}$	$N_b^2 N_{aux}^2$
	2	$b^l_{p\nu} = \sum_\mu C_{\mu p} b^l_{\mu\nu}$	$N_b N_{aux} N_\Omega$	$N_b^2 N_{aux} N_\Omega$
	3	$b^l_{pq} = \sum_\nu C_{\nu q} b^l_{p\nu}$	$N_{aux} N_\Omega^2$	$N_b N_{aux} N_\Omega^2$
J_{pq}	4	$J_{pq} = \sum_l b^l_{pp} b^l_{qq}$	N_Ω^2	$N_{aux} N_\Omega^2$
K_{pq}	4	$K_{pq} = \sum_l b^l_{pq} b^l_{pq}$	N_Ω^2	$N_{aux} N_\Omega^2$

Orbital Optimization with RI

In the inner optimization procedure of the current implementation (see Fig. 1), the energy minimization is performed with respect to real MOs under the requirement of orthonormality, and considering a fixed set of ONs. In general, an approximate NOF is not invariant with respect to an orthogonal transformation of the orbitals. Consequently, orbital optimization cannot be reduced to a pseudo-eigenvalue problem like in the Hartree-Fock approximation.

In DoNOF [1], the optimal NOs are obtained by iterative diagonalizations of a symmetric matrix $\boldsymbol{F}^\lambda$ determined by the Lagrange multipliers $\{\lambda_{pq}\}$ associated to the orthonormality conditions. A remarkable advantage of this procedure is that the orthonormality constraints are automatically satisfied. Unfortunately, the diagonal elements cannot be determined from the symmetry property of $\boldsymbol{\lambda}$, so this procedure does not provide a generalized Fockian in the conventional sense. Nevertheless, $\{F^\lambda_{pp}\}$ may be determined with the help of an aufbau principle [58].

Thus, the orbital optimization requires to calculate $\{\lambda_{pq}\}$ in each step of the inner iterations in order to determine the symmetric matrix $\boldsymbol{F}^\lambda$. Since orbitals change in each step, $\boldsymbol{J}^q$ and $\boldsymbol{K}^q$ must be recomputed in each inner iteration. Many inner iterations are performed per outer iteration, so the computation of these matrices in the orbital optimization is the most important contribution to the computational time of the present algorithm.

The RI approximation can also be applied in this case, using the procedure shown in Table III. The zero and first steps evaluate the $(\mu\nu|k)$ AO-ERIs and the $\boldsymbol{b}$ tensor in AO basis, both are common steps shared with the oc-

Table III: Algorithm used to compute $\boldsymbol{J}^q$ and $\boldsymbol{K}^q$ in the orbital optimization with RI. Formal memory scaling is shown. However, to optimize memory usage, the contraction of $\boldsymbol{b}$ tensor for $\boldsymbol{J}^q$ (steps 2, 3, and 4) and $\boldsymbol{K}^q$ (steps 2 and 3) are carried out simultaneously for each l, such that the dimension of the auxiliary basis does not affect the memory scaling.

	Step	Operation	Scaling	
			Memory	Arithmetic
Common	0	Evaluation of $(\mu\nu\|k)$	$N_b^2 N_{aux}$	$N_b^2 N_{aux}$
	1	Solve $\mathbf{PL\tilde{D}}^{1/2}\mathbf{b}^T$	$N_b^2 N_{aux}$	$N_b^2 N_{aux}^2$
	2	$b_{q\nu}^l = \sum_\mu C_{\mu q} b_{\mu\nu}^l$	$N_b N_{aux} N_\Omega$	$N_b^2 N_{aux} N_\Omega$
$J_{\mu\nu}^q$	3	$b_{qq}^l = \sum_\nu C_{\nu q} b_{q\nu}^l$	$N_{aux} N_\Omega$	$N_b N_{aux} N_\Omega$
	4	$J_{\mu\nu}^q = \sum_l b_{qq}^l b_{\mu\nu}^l$	$N_b^2 N_\Omega$	$N_b^2 N_{aux} N_\Omega$
$K_{\mu\nu}^q$	3	$K_{\mu\nu}^q = \sum_l b_{q\mu}^l b_{q\nu}^l$	$N_b^2 N_\Omega$	$N_b^2 N_{aux} N_\Omega$

cupancy optimization and performed at the beginning of the calculation. In the second step, an index of the $\mathbf{b}$ tensor is contracted from AO to MO with arithmetic scaling of $N_b^2 N_{aux} N_\Omega$. In the third step of the Coulomb procedure, an additional contraction is performed for the $\mathbf{b}$ tensor. Finally, in the last steps of both the Coulomb and exchange procedures, the intermediate tensors are multiplied to compute $\boldsymbol{J}^q$ and $\boldsymbol{K}^q$. The algorithm reduces the arithmetic scaling factor of orbital optimization to the fourth-order ($N_b^2 N_{aux} N_\Omega$), as in the previous case. Hence, an overall reduction of the arithmetic scaling factor from fifth-order to the fourth-order, and of the memory scaling factor from fourth-order to the third-order is achieved due to the RI approximation.

Table IV: Comparison of the energies (Hartrees) obtained with PNOF7, PNOF7-RI using aug-cc-pVDZ/GEN-A2* for the cycloalkanes test. Mean diff: 2.2×10^{-4}

Molecule	E_{PNOF7}	$\Delta E_{PNOF7-RI}$ [a]
Cyclopropane (C_3H_6)	-117.228991	1.5×10^{-4}
Cyclobutane (C_4H_8)	-156.328758	1.9×10^{-4}
Cyclopentane (C_5H_{10})	-195.449913	2.5×10^{-4}
Cyclohexane (C_6H_{12})	-234.549938	2.2×10^{-4}
Cycloheptane (C_7H_{14})	-273.630436	2.3×10^{-4}
Cyclooctane (C_8H_{16})	-312.714209	2.4×10^{-4}
Cyclononane (C_9H_{18})	-351.799073	2.9×10^{-4}

[a] Positive differences mean that PNOF7-RI energy is above than the PNOF7 energy.

III. COMPUTATIONAL DETAILS

The proposed PNOFi-RI (i=5-7) algorithm was implemented in a modified version of the DoNOF software [1] using Cartesian Gaussian basis functions and MPI parallelization, leading to a new implementation labeled as DoNOF-RI.

We assume that there is enough memory available to compute at the beginning all the required AO-ERIs as well as the $\mathbf{b}$ tensor on the atomic basis, and store them for use along the calculation. Operations of optimization procedures correspond only to arithmetic manipulations and not to AO-ERI evaluations. Four-center AO-ERIs, $(\mu\nu|\sigma\lambda)$, have been screened to discard those lower than 10^{-9}. This approach has been taken to reduce the arithmetic scaling when four center ERIs are used [24, 64–66]. All results shown in this article were calculated using 24 threads of an Intel Xeon Gold 5118 CPU. Basis sets were taken from the basis set exchange [67–69] www.basissetexchange.org website.

IV. RESULTS

Single point energy calculations were performed to study the numerical stability and speed-up achieved with the DoNOF-RI implementation. The structures were optimized with Psi4 software [70] using M06-2X [71] and aug-cc-pVDZ/aug-cc-pVDZ-jkfit [72] basis set. Initial auxiliary variables $\{\gamma_p^0\}$ corresponding to a Fermi–Dirac distribution of $\{n_p^0\}$ were employed. For NOs, the guess MOs were taken from a Hartree-Fock calculation.

Figure 2 presents the computational times of an outer iteration for occupancy optimization (top panel) as well as for orbital optimization (bottom panel) from cyclopropane to cyclononane employing aug-cc-pVDZ basis set [73, 74] and GEN-A2* auxiliary basis set [75–77], which generates auxiliary basis functions according to the basis set. In both plots, blue bars represent the elapsed time obtained with PNOF7 and yellow bars correspond to computed time with PNOF7-RI, the speed-up achieved by PNOF7-RI with respect to PNOF7 is presented over each pair of bars. The different sizes of the blue bars compared to the yellow bars makes evident the different arithmetic scaling factors between PNOF7 and PNOF7-RI. For the smallest cycloalkane tested, C_3H_6, an outer iteration of PNOF7-RI is 12 times faster than the equivalent iteration in PNOF7, in the other hand, for the largest cycloalkane tested, C_9H_{18}, PNOF7-RI is 83 and 37 times faster for occupancy and orbital optimization respectively. Speed-ups for occupancy and orbital optimization behave accordingly to the described arithmetic scaling factors, since the final steps of the integral evaluation for the orbital optimization shown in Table III have slightly higher arithmetic scaling factors than the final steps of the integral evaluation in the occupancy optimization described in Table II.

Table V: Comparison of the energies (Hartrees) obtained with PNOF7, PNOF7-RI using cc-pVTZ/GEN-A2* for molecules of general interest. Mean diff: 3.1×10^{-3}

Molecule		E_{PNOF7}	$\Delta E_{PNOF7-RI}$ [a]	Speed-up[b]
Oxazole	(C_3H_3NO)	-244.980370	8.8×10^{-4}	23
Borazine	($B_3H_3N_3$)	-241.487944	7.0×10^{-4}	19
Coumarin	($C_9H_6O_2$)	-494.724761	1.7×10^{-3}	19
Cyanuric Chloride	($C_3Cl_3N_3$)	-1655.966373	8.0×10^{-3}	23
Benzene	(C_6H_6)	-231.058747	6.7×10^{-4}	28
Thiepine	(C_6H_6S)	-628.585882	2.4×10^{-3}	37
Thieno[2,3-b]thiophene	($C_6H_4S_2$)	-1239.953451	7.1×10^{-3}	27

[a]Positive differences mean that the PNOF7-RI energy is above than the PNOF7 energy.
[b]Global speed-up per outer iteration

Figure 2: Analysis of occupancy (top panel) and orbital optimizations (bottom panel) for PNOF7 and PNOF7-RI computing time using aug-cc-pVDZ/GEN-A2*. Achieved speed-up is presented over each pair of bars.

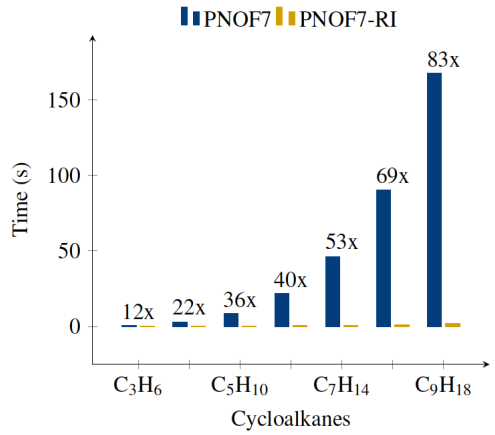

(a) Outer occupancy optimization cycle.

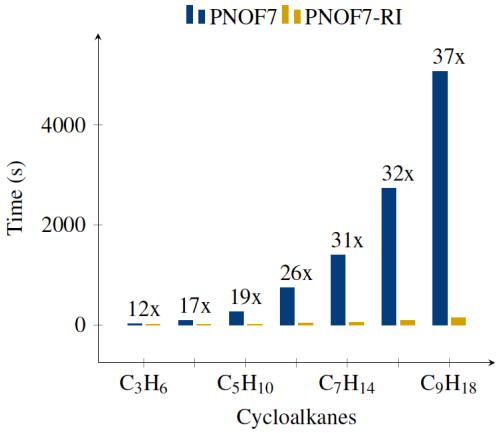

(b) Outer orbital optimization cycle.

Although a significant reduction of computational time has been achieved, it is important to analyze the numerical impact of the RI approximation applied to PNOF7 on the final energy values. For this purpose, the NO's and ON's of the converged PNOF7-RI calculation have been used to restart the calculation using four center ERIs, namely, a PNOF7 calculation. The results are presented in Table IV, where the PNOF7 energy and PNOF7-RI energy difference for each cycloalkane is tabulated. It can be seen that PNOF7-RI allows achieving a general accuracy between three and four decimal places, with a mean difference of 2.2×10^{-4} Hartrees. In all cases a restart of the PNOF7-RI calculation converged to the PNOF7 energy in at most two outer iterations, allowing for a PNOF7 result in a reduced amount of time.

The described restarting procedure using cc-pVTZ/GEN-A2* basis sets for molecules of general interest has been performed. The results are shown in Table V, where the PNOF7 energy is shown with the corresponding deviation of the PNOF7-RI result. The minimum error of 6.7×10^{-4} corresponds to the benzene molecule, and the maximum error of 1.7×10^{-3} corresponds to the coumarin molecule. The global times of an outer iteration of PNOF7-RI and PNOF7 were compared and the result can be seen in the column labeled as speed-up, where it is shown that PNOF7-RI is 37 times faster than PNOF7 for the case of the thiepine, as well as important speed-ups for the other cases. Overall, the results prove that DoNOF-RI allows to compute medium size molecules of general interest.

V. CONCLUSIONS

The resolution of the identity approximation has proved to be significant to decrease the arithmetic and memory scaling factors of the PNOFi (i=5-7) functionals, leading to the DoNOF-RI implementation. The generality of the algorithm proposed here makes it applicable to

all approximate natural orbital functionals known so far. While having an acceptable deviation of the final energy value, the solution for the natural orbitals and occupation numbers can be used as a start guess for a regular PNOF calculation with convergence in few iterations. Consequently, DoNOF-RI provides a way of reaching accurate results in a reduced amount of time, allowing PNOFi (i=5-7) functionals to be used to study systems of general interest.

Acknowledgments

J. F. H. Lew-Yee with CVU number 867718 gratefully thanks CONACyT for PhD scholarship. J. M. del Campo acknowledges funding from CONACyT project CB-2016-282791, PAPIIT-IN114418 and computing resources from LANCAD-UNAM-DGTIC-270 project. M.P. acknowledges the financial support of MCIU/AEI/FEDER, UE (PGC2018-097529-B-100) and Eusko Jaurlaritza (Ref. IT1254-19).

[1] M. Piris and I. Mitxelena, Comp. Phys. Comm. **259**, 107651 (2021).
[2] I. Mitxelena, M. Piris, and J. M. Ugalde, in *State Art Mol. Electron. Struct. Comput. Correl. Methods, Basis Sets More*, edited by P. Hoggan and U. Ancarani (Academic Press, 2019), Advances in Quantum Chemistry, chap. 7, pp. 155–177.
[3] S. Goedecker and C. J. Umrigar, *Natural Orbital Functional Theory* (Springer US, Boston, MA, 2000), pp. 165–181, ISBN 978-1-4615-4211-7.
[4] M. Piris, *Natural Orbital Functional Theory* (John Wiley & Sons, Ltd, 2007), chap. 14, pp. 385–427, ISBN 9780470106600.
[5] M. Piris and J. M. Ugalde, Int. J. Quantum Chem. **114**, 1169 (2014).
[6] K. Pernal and K. J. H. Giesbertz, in *Density-Functional Methods for Excited States* (Springer International Publishing, 2015), vol. 368, pp. 125–183.
[7] M. Piris, in *Theoretical and Quantum Chemistry at the Dawn of the 21st Century*, edited by T. Chakraborty and R. Carbó-Dorca (Apple Academic Press, 2018), chap. 22, pp. 593–620.
[8] M. Piris, Int. J. Quantum Chem. **106**, 1093 (2006).
[9] D. A. Mazziotti, Phys. Rev. Lett. **108**, 263002 (2012).
[10] P. Leiva and M. Piris, Journal of Chemical Physics **123**, 214102 (2005).
[11] M. Piris, X. Lopez, and J. M. Ugalde, Journal of Chemical Physics **126**, 214103 (2007).
[12] M. Piris, J. M. Matxain, X. Lopez, and J. M. Ugalde, Journal of Chemical Physics **132**, 031103 (2010).
[13] M. Piris, J. M. Matxain, X. Lopez, and J. M. Ugalde, Journal of Chemical Physics **133**, 111101 (2010).
[14] M. Piris, X. Lopez, F. Ruipérez, J. M. Matxain, and J. M. Ugalde, Journal of Chemical Physics **134**, 164102 (2011).
[15] M. Piris, Int. J. Quantum Chem. **113**, 620 (2013).
[16] M. Piris, Journal of Chemical Physics **141**, 044107 (2014).
[17] M. Piris, Physical Review Letters **119**, 063002 (2017).
[18] X. Lopez, M. Piris, J. M. Matxain, and J. M. Ugalde, Physical Chemistry Chemical Physics **12**, 12931 (2010).
[19] M. Piris, X. Lopez, and J. M. Ugalde, Chemistry - A European Journal **22**, 4109 (2016).
[20] I. Mitxelena and M. Piris, Journal of Physics Condensed Matter **32**, 17LT01 (2020).
[21] I. Mitxelena and M. Piris, Journal of Chemical Physics **152**, 064108 (2020).
[22] M. Piris, Physical Review A **98**, 022504 (2018).
[23] M. Piris, Physical Review A **100**, 032508 (2019).
[24] J. L. Whitten, The Journal of Chemical Physics **4496**, 4496 (1973).
[25] B. I. Dunlap, J. W. D. Connolly, and J. R. Sabin, J. Chem. Phys. **71**, 3396 (1979).
[26] M. Feyereisen, G. Fitzgerald, and A. Komornicki, Chem. Phys. Lett. **208**, 359 (1993).
[27] O. Vahtras, J. Almlöf, and M. W. Feyereisen, Chem. Phys. Lett. **213**, 514 (1993).
[28] P. Calaminici, A. Alvarez-Ibarra, D. Cruz-Olvera, V. D. Domínguez-Soria, R. Flores-Moreno, G. U. Gamboa, G. Geudtner, A. Goursot, D. Mejía-Rodríguez, D. R. Salahub, et al., in *Handbook of Computational Chemistry* (Springer Netherlands, Dordrecht, 2017), pp. 795–860, ISBN 9783319272825.
[29] R. A. Kendall and H. A. Früchtl, Theoretical Chemistry Accounts **97**, 158 (1997).
[30] A. Sodt, G. J. O. Beran, Y. Jung, B. Austin, and M. Head-Gordon, Journal of Chemical Theory and Computation **2**, 300 (2006).
[31] A. Sodt and M. Head-Gordon, The Journal of Chemical Physics **128**, 104106 (2008).
[32] C. Hattig and F. Weigend, The Journal of Chemical Physics **113**, 5154 (2000).
[33] A. E. DePrince and C. D. Sherrill, Journal of Chemical Theory and Computation **9**, 2687 (2013).
[34] U. Bozkaya, Journal of Chemical Theory and Computation **10**, 2371 (2014).
[35] B. Q. Pham and M. S. Gordon, Journal of Chemical Theory and Computation **15**, 2254 (2019).
[36] T. Shen, Z. Zhu, I. Y. Zhang, and M. Scheffler, Journal of Chemical Theory and Computation **15**, 4721 (2019).
[37] A. Forster, M. Franchini, E. van Lenthe, and L. Visscher, Journal of Chemical Theory and Computation **16**, 875 (2020).
[38] J. F. H. Lew-Yee, R. Flores-Moreno, J. L. Morales, and J. M. del Campo, Journal of Chemical Theory and Computation **16**, 1597 (2020).
[39] J. N. Pedroza-Montero, F. A. Delesma, J. L. Morales, P. Calaminici, and A. M. Koster, The Journal of Chemical Physics **153**, 134112 (2020).
[40] F. Weigend and M. Haser, Theoretical Chemistry Accounts: Theory, Computation, and Modeling (Theoretica Chimica Acta) **97**, 331 (1997).
[41] F. Weigend, M. Haser, H. Patzelt, and R. Ahlrichs, Chemical Physics Letters **294**, 143 (1998).
[42] T. Ishikawa and K. Kuwata, The Journal of Physical

Chemistry Letters **3**, 375 (2012).
[43] M. Katouda, A. Naruse, Y. Hirano, and T. Nakajima, Journal of Computational Chemistry **37**, 2623 (2016).
[44] L. Vogt, R. Olivares-Amaya, S. Kermes, Y. Shao, C. Amador-Bedolla, and A. Aspuru-Guzik, The Journal of Physical Chemistry A **112**, 2049 (2008).
[45] U. Bozkaya, Journal of Chemical Physics **141** (2014).
[46] U. Bozkaya, Journal of Chemical Theory and Computation **12**, 1179 (2016).
[47] U. Bozkaya, Journal of Computational Chemistry **39**, 351 (2018).
[48] U. Bozkaya, Phys. Chem. Chem. Phys. **18**, 11362 (2016).
[49] U. Bozkaya and C. D. Sherrill, The Journal of Chemical Physics **144**, 174103 (2016).
[50] U. Bozkaya, E. Soydas, and B. Filiz, Journal of Computational Chemistry **41**, 769 (2020).
[51] C. Peng, J. A. Calvin, and E. F. Valeev, International Journal of Quantum Chemistry **119**, e25894 (2019).
[52] J. Fosso-Tande, T.-S. Nguyen, G. Gidofalvi, and A. E. DePrince, Journal of Chemical Theory and Computation **12**, 2260 (2016).
[53] J. W. Mullinax, E. Epifanovsky, G. Gidofalvi, and A. Eugene Deprince, J. Chem. Theory Comput. **15**, 276 (2019).
[54] M. Piris, in *Many-body approaches at different scales: a tribute to N. H. March on the occasion of his 90th birthday*, edited by G. G. N. Angilella and C. Amovilli (Springer, New York, 2018), chap. 22, pp. 283–300.
[55] D. A. Mazziotti, Chem. Phys. Lett. **289**, 419 (1998).
[56] M. Piris, J. Math. Chem. **25**, 47 (1999).
[57] M. Piris, J. M. Matxain, and X. Lopez, J. Chem. Phys. **139**, 234109 (2013).
[58] M. Piris and J. M. Ugalde, J. Comput. Chem. **30**, 2078 (2009).
[59] J. M. Matxain, M. Piris, F. Ruipérez, X. Lopez, and J. M. Ugalde, Phys. Chem. Chem. Phys. **13**, 20129 (2011).
[60] J. N. Pedroza-Montero, F. A. Delesma, J. L. Morales, P. Calaminici, and A. M. Köster, The Journal of Chemical Physics **153**, 134112 (2020).
[61] This is the bounded Bunch-Kaufman (rook) diagonal pivoting method available in lapack. E. Anderson, Z. Bai, C. Bischof, S. Blackford, J. Demmel, J. Dongarra, J. Du Croz, A. Greenbaum, S. Hammarling, A. McKenney, et al., *LAPACK Users' Guide* (Society for Industrial and Applied Mathematics, Philadelphia, PA, 1999), 3rd ed., ISBN 0-89871-447-8.
[62] J. R. Bunch and L. Kaufman, Mathematics of Computation (1977).
[63] S. H. Cheng and N. J. Higham, SIAM Journal on Matrix Analysis and Applications **19**, 1097 (1998).
[64] J. Almlöf, K. Faegri, and K. Korsell, Journal of Computational Chemistry **3**, 385 (1982).
[65] M. Häser and R. Ahlrichs, Journal of Computational Chemistry **10**, 104 (1989).
[66] S. A. Maurer, D. S. Lambrecht, D. Flaig, and C. Ochsenfeld, Journal of Chemical Physics **136** (2012).
[67] K. L. Schuchardt, B. T. Didier, T. Elsethagen, L. Sun, V. Gurumoorthi, J. Chase, J. Li, and T. L. Windus, J. Chem. Inf. Model. **47**, 1045 (2007).
[68] D. Feller, J. Comput. Chem. **17**, 1571 (1996).
[69] B. P. Pritchard, D. Altarawy, B. Didier, T. D. Gibson, and T. L. Windus, J. Chem. Inf. Model. **59**, 4814 (2019).
[70] R. M. Parrish, L. A. Burns, D. G. A. Smith, A. C. Simmonett, A. E. DePrince, E. G. Hohenstein, U. Bozkaya, A. Y. Sokolov, R. Di Remigio, R. M. Richard, et al., J. Chem. Theory Comput. **13**, 3185 (2017), ISSN 1549-9618.
[71] Y. Zhao and D. G. Truhlar, Theoretical Chemistry Accounts **120**, 215 (2008).
[72] F. Weigend, Physical Chemistry Chemical Physics **4**, 4285 (2002).
[73] R. A. Kendall, T. H. Dunning, and R. J. Harrison, J. Chem. Phys. **96**, 6796 (1992), ISSN 0021-9606.
[74] T. H. Dunning, J. Chem. Phys. **90**, 1007 (1989), ISSN 00219606.
[75] J. Andzelm, E. Radzio, and D. R. Salahub, J. Comput. Chem. **6**, 520 (1985).
[76] J. Andzelm, N. Russo, and D. R. Salahub, J. Chem. Phys. **87**, 6562 (1987).
[77] P. Calaminici, F. Janetzko, A. M. Köster, R. Mejia-Olvera, and B. Zuniga-Gutierrez, J. Chem. Phys. **126**, 044108 (2007).

RESEARCH ARTICLE | JUNE 07 2023

Correlation balance for describing carbenes: An NOF study

Lizeth Franco ; Juan Felipe Huan Lew-Yee ; Jorge M. del Campo

AIP Advances 13, 065213 (2023)
https://doi.org/10.1063/5.0146543

Correlation balance for describing carbenes: An NOF study

Cite as: AIP Advances 13, 065213 (2023); doi: 10.1063/5.0146543
Submitted: 17 March 2023 • Accepted: 19 May 2023 •
Published Online: 7 June 2023

Lizeth Franco,[a] Juan Felipe Huan Lew-Yee,[b] and Jorge M. del Campo[c]

AFFILIATIONS

Departamento de Física y Química Teórica, Facultad de Química, Universidad Nacional Autónoma de México, Mexico City C.P. 04510, Mexico

[a]Electronic mail: francolizeth@hotmail.com
[b]Electronic mail: felipe.lew.yee@quimica.unam.mx
[c]Author to whom correspondence should be addressed: jmdelc@unam.mx

ABSTRACT

Carbenes are a remarkable type of molecules because of the two electrons that might be paired or unpaired, providing a singlet or a triplet state, respectively. The preference for one of these states can be measured by the singlet-triplet energy gap; however, theoretical prediction is challenging when static correlation arises, and an adequate balance with dynamic correlation is required to achieve correct predictions. Piris Natural Orbital Functionals (PNOFs) have been used before to deal with other static correlation problems, but they have suffered from lack of dynamic correlation, which has been solved by coupling PNOF7 with many-body perturbation theory. Recently, the development of a Global Natural Orbital Functional (GNOF) has been proposed with the aim of including dynamic correlation without the need to couple with perturbation theory, thus becoming a promising alternative to study challenging chemical problems. In this work, we applied the PNOF family of functionals to compute the adiabatic singlet-triplet energy gaps of a set of simple carbenes and compared them with those computed with coupled-cluster methods and experimental values when available. We have found that the GNOF achieves promising results due to an intrinsic balance of static and dynamic correlation. In this regard, the GNOF presents errors that are lower than those of PNOF7, comparable to those of NOF-c-MP2, and is capable of predicting the tendency of substituent effects, proving to be suitable for further application to predict general singlet-triplet energy gaps.

I. INTRODUCTION

Carbenes are a fascinating type of molecule. Its existence was predicted by Hermann in 1855[1] and then by Nef in 1897.[2] The first carbene was detected in 1912,[3] and a stable carbene was isolated by Igau *et al.* in 1988.[4] Since then, several carbenes have been isolated, mainly in their singlet state,[5–7] but more recently, they have also been isolated in their triplet state.[8–11] Carbenes are known to appear as electrophilic intermediates in several organic reactions.[12] Particularly, they can be bonded with transition metals to perform organometallic reactions; this is the case of Fischer's electrophilic carbene complexes with large singlet-triplet (ST) gaps and Schrock's nucleophilic carbene complexes with short singlet-triplet gaps.[13] N-heterocyclic carbenes have also attracted interest in recent years due to their application in catalysis.[14–18]

Carbenes are molecules with two non-bonding electrons in the carbon atom that allow them to be in a singlet state when these electrons have opposite spins or in a triplet state when they have parallel spins. The properties and structure of these molecules are determined by their ground state, with singlet state carbenes showing angles slightly below than 120° corresponding to having a lone pair of electrons in an sp^2-hybridized orbital and triplet state carbenes showing angles over 120° corresponding to having unpaired electrons in either sp- or sp^2-hybrid orbitals. The preference for one or the other state is influenced by the substituent, with highly electronegative and π-electron-donating substituents favoring the singlet state and bulky steric groups favoring the triplet state when electronic effects are negligible.[19–21] The first two phenomena can be explained through degeneracy breaking of the carbene σ and p orbitals: when σ-electron-withdrawing substituents are present,

the σ orbital is stabilized by an inductive effect that decreases its energy, leaving the p orbital unchanged, and if there are π-electron-donating substituents, the orbital energy of p increases and the σ orbital remains the same.[22] On the other hand, bulky groups induce linear geometry due to steric effects, which lead to orbital degeneracy and thus favor the triplet state.[23] The multiplicity of the ground state is usually determined by the presence of π-electron-donating substituents due to mesomeric effects followed by the electronegativity of substituents through inductive effects and finally influenced by steric effects.[9,24–26]

Calculating the singlet-triplet carbene energy gap (ST gap) is of interest because it reflects the spin nature of the ground state and the possibility of an excitation that may lead to a different chemical reactivity.[27,28] The computational prediction of carbene ST gaps depends on the correlation nature of the systems. Some singlet carbenes are well described by a single reference wavefunction, and density functional approximations lead to good prediction of these molecules;[29] however, a significant amount of carbenes may be of multireference nature, as has been shown recently in the analysis of the QMSpin database,[30] thus requiring the inclusion of static electron correlation and becoming a challenge for single reference electronic structure methods. Interestingly, multiconfigurational methods such as the complete active space self-consistent field (CASSCF) might not necessarily lead to accurate results as dynamic correlation is important for these molecules and highly demanding multireference methods such as CASPT2 and MRCI are required to properly describe these situations.[31,32] Alternatively, wavefunction methods such as coupled-cluster calculations with single and double excitations and perturbative treatment of triple excitations [CCSD(T)][33] and composite methods[34] have been found to provide an acceptable compromise between accuracy and arithmetic scaling in several cases, although the use of methods that provide better results in a less demanding way is required. Moreover, studies of this kind have become a test for recently developed theoretical methods.[35–40]

Reduced density matrix (RDM) based methods have been tested as an affordable way to study multireference problems,[41,42] and recently, a Global Natural Orbital Functional (GNOF) has been proposed in the context of Piris Natural Orbital Functionals (PNOF).[43] In contrast to previous versions of these functionals,[44–46] the GNOF aims to provide a good balance between static and dynamic electron correlation,[47] successfully describing, for example, the stability order of the states of iron(II) porphyrin, as has been demonstrated by some of the authors of this contribution.[48] In this regard, the GNOF presents a promising method for studying the singlet-triplet gap of carbenes.

II. THEORY

PNOFs are based on reconstruction of the second-order reduced density matrix (2-RDM) from the first-order reduced density matrix (1-RDM) throughout a cumulant expansion on the basis of natural orbitals that diagonalize the 1-RDM, giving the occupation numbers (ONs), n_p.[49] Since PNOF5, the functionals use an electron pairing approach, an illustrative representation is presented in Fig. 1, and it can also be found in Refs. 50 and 51. The electron pairing approach consists of dividing the orbital space, Ω, into N_Ω subspaces Ω_g; these can be classified as Ω_{II} if double occupied and Ω_I if single occupied such that $\Omega = \Omega_{II} + \Omega_I$. In a system of N electrons, there are $N_{II}/2$ subspaces in Ω_{II} and N_I subspaces in Ω_I such that $N = N_{II} + N_I$. Finally, each subspace in Ω_{II} is formed by a strongly double occupied natural orbital (ON ≥ 0.5) that can be coupled with a weakly occupied natural orbital (ON ≤ 0.5) in the perfect pairing approach ($N_g = 1$) or many weakly occupied natural orbitals in the extended pairing approach ($N_g > 1$). In the case of Ω_I, there is only one orbital in each subspace. From the perspective of electronic correlation, this means that it can be split into intrapair and interpair contributions, with PNOF5 only including complete intrapair correlation.[44,45] The path forward to recover the interpair contribution passes through PNOF6[52] and leads to PNOF7,[46] PNOF7s,[46] NOF-MP2,[46,53] NOF coupled with many-body perturbation theory (NOF-MBPT)[54] and GNOF.[43] In the following, we briefly review the energy expressions for real orbitals of the most recently proposed GNOF, and a more detailed description can be found in Refs. 43 and 47.

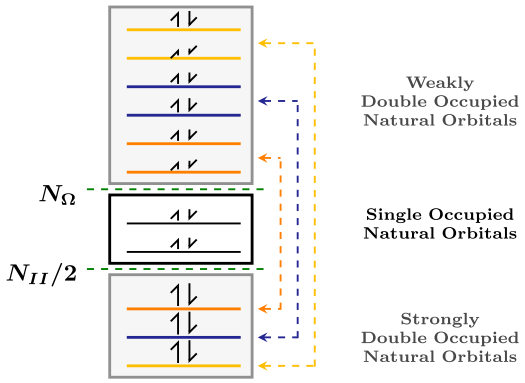

FIG. 1. Electron pairing scheme for a system with $N = 8$ and $S = 1$; hence, $N_I = 2$ and $N_{II} = 6$ (recall that $N = N_I + N_{II}$). In this example, the maximum possible number of weakly occupied orbitals coupled with each strongly occupied orbital allowed by the basis set is $N_g = 2$. The single occupied orbitals in Ω_I are inside the white rectangle, while double occupied subspaces in Ω_{II} are inside the gray rectangles. There are $N_{II}/2 = 3$ subspaces that belong to Ω_{II}, namely, Ω_1, Ω_2 and Ω_3, which are represented by the yellow, blue, and orange horizontal lines, respectively.

The energy of the GNOF can be expressed as an intrapair contribution E^{intra}, and Hartree–Fock-like E^{inter}_{HF} static E^{inter}_{sta}, and dynamic E^{inter}_{dyn} interpair contributions,

$$E = E^{intra} + E^{inter}_{HF} + E^{inter}_{sta} + E^{inter}_{dyn}. \tag{1}$$

The intrapair contribution is calculated from the PNOF5 formulation as

$$E^{intra} = \sum_{g=1}^{\frac{N_{II}}{2}} E_g + \sum_{g=N_{II}/2+1}^{N_\Omega} \mathcal{H}_{gg}, \tag{2}$$

where $\mathcal{H}_{gg}$ corresponds to the diagonal elements of the core Hamiltonian matrix and E_g is the energy contribution of a double occupied subspace, given by

$$E_g = \sum_{p\in\Omega_g} n_p(2\mathcal{H}_{pp} + \mathcal{J}_{pp}) + \sum_{q,p\in\Omega_g} \Pi(n_q, n_p)\mathcal{K}_{pq}, \tag{3}$$

where J_{pq} and K_{pq} are the elements of Coulomb and exchange integrals in the natural orbital basis and

$$\Pi(n_q, n_p) = \sqrt{n_q n_p}(\delta_{q\Omega^a}\delta_{p\Omega^a} - \delta_{qg} - \delta_{pg}), \tag{4}$$

with Ω^a denoting the orbitals above N_Ω, where $N_\Omega = N_{II}/2 + N_I$. It is worth noting that the Π defined in Eq. (4) is applicable to a given subspace Ω_g that belongs to Ω_{II}, as indicated in the last sum of Eq. (3). Let us choose the subspace given by the right orange arrow in Fig. 1; in this case, the Kronecker deltas, $\delta_{q\Omega^a}$ and $\delta_{p\Omega^a}$, assess whether p or q corresponds to an orange colored weakly occupied natural orbital, and the meaning of δ_{qg} and δ_{pg} is to check whether p or q corresponds to the orange colored strongly occupied natural orbital.

The Hartree–Fock like interpair contribution is given by

$$E_{HF}^{inter} = \sum_{p,q=1}^{N_{bf}}{}' \quad n_q n_p (2J_{pq} - K_{pq}), \tag{5}$$

where N_{bf} is the number of basis functions and the prime in the summation indicates that contributions of natural orbitals in the same subspace are excluded. The static interspace contribution is given by

$$\begin{aligned} E_{sta}^{inter} = &-\left(\sum_{p=1}^{N_\Omega}\sum_{q=N_\Omega+1}^{N_{bf}} + \sum_{p=N_\Omega+1}^{N_{bf}}\sum_{q=1}^{N_\Omega} + \sum_{p,q=N_\Omega+1}^{N_{bf}}\right)' \\ &\times \Phi_q\Phi_p\mathcal{K}_{pq} - \frac{1}{2}\left(\sum_{p=1}^{N_{II}/2}\sum_{q=N_{II}/2+1}^{N_\Omega} + \sum_{N_{II}/2+1}^{N_\Omega}\sum_{q=1}^{N_{II}/2}\right)' \\ &\times \Phi_q\Phi_p\mathcal{K}_{pq} - \frac{1}{4}\sum_{p,q=N_{II}/2+1}^{N_\Omega}\mathcal{K}_{pq}, \end{aligned} \tag{6}$$

where $\Phi_p = \sqrt{n_p(1-n_p)}$. It is worth mentioning that for singlets, the contributions described until this point lead to PNOF7, and if $\Phi_p = 2n_p(1-n_p)$ is taken, the equations lead to PNOF7s, from which NOF-MP2 can be computed as described in Refs. 53 and 54.

Finally, the dynamic interpair contribution is

$$E_{dyn}^{inter} = \sum_{p,q=1}^{N_{bf}}{}' \quad \left[n_q^d n_p^d + \Pi(n_q^d, n_p^d)\right](1 - \delta_{q\Omega_{II}^b}\delta_{p\Omega_{II}^b})K_{pq}, \tag{7}$$

with Ω_{II}^b denoting the orbitals below the level $N_{II}/2$ and the dynamic ONs given by n_p^d are

$$n_p^d = n_p e^{-\left(\frac{h_g}{h_c}\right)^2}, \tag{8}$$

with $h_g = 1 - n_p$ and $h_c = 0.02\sqrt{2}$.

III. METHODS

PNOF7, NOF-MP2 and GNOF adiabatic singlet-triplet calculations have been performed in PyNOF software[55] (an *in-house code* based on DoNOF software[51]) using the spin-restricted formalism, that is, the same set of natural orbitals and ONs were used for α and β orbitals. The extended pairing approach was used, with the maximum possible number of weakly occupied orbitals coupling with each strongly occupied orbital allowed by the basis set. NOF-MP2 calculations were performed as indicated by the NOF-MBPT equations;[54] therefore, it will be labeled NOF-c-MP2 from now on. The resolution of the identity approximation (RI)[56–58] in the context of the PNOF was used for efficiency.[59] Additional CCSD and CCSD(T) calculations based on the restricted-open Hartree–Fock method have been performed in the Psi4 software for comparison.[60]

The def2-TZVPD/def2-universal-JKFIT basis sets have been used in all cases,[61–66] with the geometries reported in Refs. 42 and 67–69. At this point, it is worth noticing that the chosen basis set has two effects on the NOF calculations: the completeness of the basis, and the number of weakly occupied orbitals that appear in each double occupied subspace. Regarding the latter effect, the observed ONs allow us to conclude that the number of weakly occupied natural orbitals is adequate.

IV. RESULTS

A. General performance of PNOFs

We have studied the singlet and triplet states of a set of carbenes connected to up to two substituents having the formula HCX or XCX (X = F, Cl, Br, CN, Li, CH_3, or SiH_3) to test the ability of the GNOF to predict singlet-triplet gaps. To verify the importance of static and dynamic correlation in these species, we present some diagnostics computed using the CCSD method in Table I; in particular, the green and orange cells correspond to values where the T1[70] and D1[65] diagnostics suggest that the species are of multireference nature. Interestingly, there are both single reference (e.g., CH_2 and CH_3CH) and multireference species in the set, and the importance of the static correlation may arise in both the singlet and triplet

TABLE I. Diagnostics T1 and D1 for molecules in the carbene set in its singlet and triplet states, computed by CCSD. Green cells correspond to values of T1 greater than or equal to 0.02, and orange cells correspond to values of D1 greater than or equal to 0.05, indicating multireference nature.

Carbene	Singlet		Triplet	
	T1	D1	T1	D1
CLi_2	0.023	0.059	0.025	0.082
$C(SiH_3)_2$	0.013	0.062	0.011	0.026
SiH_3CH	0.012	0.045	0.011	0.021
LiCH	0.008	0.016	0.007	0.014
NCCCN	0.020	0.054	0.024	0.054
HCCN	0.019	0.056	0.026	0.047
CH_2	0.008	0.019	0.010	0.014
CH_3CH	0.011	0.035	0.013	0.021
CBr_2	0.013	0.095	0.013	0.056
ClCH	0.015	0.066	0.018	0.044
BrCH	0.014	0.083	0.015	0.050
FCH	0.016	0.055	0.018	0.036
CCl_2	0.014	0.073	0.016	0.048
CF_2	0.016	0.061	0.017	0.038

TABLE II. Singlet-triplet gaps in kcal/mol for carbenes computed with members of the PNOF family of functionals and coupled cluster methods with the def2-TZVPD/def2-universal-JKFIT basis set. The singlet-triplet gaps used as a reference are presented on the column label as ΔE_{ST}^{ref}, where positive values indicate a triplet ground state and negative values indicate a singlet ground state; the signed errors of the predictions may be found at the bottom of the table.

		ST gaps				
		PNOF			Coupled-cluster	
Carbene	ΔE_{st}^{ref}	PNOF7	NOF-c-MP2	GNOF	CCSD	CCSD(T)
CLi_2	23[84]	18.5	34.7	21.3	22.9	21.4
$C(SiH_3)_2$	22.1[67]	37.8	24.9	18.7	25.4	23.5
SiH_3CH	18.1[67]	34.2	24.1	14.5	20.9	19.4
LiCH	15.8[42]	25.4	36.8	26.3	29.8	28.2
NCCCN	12.2[67]	10.1	−17.6	−8.1	15.7	12.7
HCCN	11.9 (exp.)[71]	23.4	4.4	2.2	13.0	10.5
CH_2	9 (exp.)[72,73]	23.6	18.6	5.9	11.3	10.4
CH_3CH	3 (exp.)[74]	25.8	7.8	−0.8	5.7	4.3
CBr_2	−1.912 (exp.)[75]	12.4	−23.1	−25.2	−11.2	−14.9
ClCH	−6.1852 (exp.)[76,77]	17.4	−7.5	−13.3	−3.1	−5.1
BrCH	−5.64 (exp.)[78–81]	14.3	−5.3	−15.2	−2.0	−4.3
FCH	−14.9 (exp.)[78,79]	8.4	−16.3	−14.0	−12.4	−13.9
CCl_2	−20.8 (exp.)[82]	11.2	−30.3	−29.6	−15.9	−19.0
CF_2	−54 (exp.)[75,83]	−23.9	−67.3	−64.8	−53.6	−55.8
		Errors				
		PNOF			Coupled-cluster	
Carbene		PNOF7	NOF-c-MP2	GNOF	CCSD	CCSD(T)
CLi_2		−4.5	11.7	−1.7	−0.1	−1.6
$C(SiH_3)_2$		15.7	2.8	−3.4	3.3	1.4
SiH_3CH		16.1	6.0	−3.6	2.8	1.3
LiCH		9.6	21.0	10.5	14.0	12.4
NCCCN		−2.1	−29.8	−20.3	3.5	0.5
HCCN		11.5	−7.5	−9.7	1.1	−1.4
CH_2		14.6	9.6	−3.1	2.3	1.4
CH_3CH		22.8	4.8	−3.8	2.7	1.3
CBr_2		14.3	−21.2	−23.3	−9.3	−13.0
ClCH		23.6	−1.3	−7.1	3.1	1.1
BrCH		19.9	0.3	−9.6	3.6	1.3
FCH		23.3	−1.4	0.9	2.5	1.0
CCl_2		32.0	−9.5	−8.8	4.9	1.8
CF_2		30.1	−13.3	−10.8	0.4	−1.8
	ME-all[a]	16.2	−2.0	−6.7	2.5	0.4
	ME-exp[b]	22.2	−2.3	−6.5	2.6	0.6
	MAE-all[a]	17.2	10.0	8.3	3.8	2.9
	MAE-exp[b]	22.2	6.0	6.7	2.6	1.4
	STD-all[a]	10.1	12.9	8.1	4.6	4.9
	STD-exp[b]	6.5	7.1	3.8	1.3	1.3
	RMSE-all[a]	19.1	13.1	10.5	5.2	5.0
	RMSE-exp[b]	23.2	7.4	7.5	2.9	1.4

[a]Root mean signed errors calculated with all data.
[b]Root mean signed errors calculated without CBr_2, CLi_2, NCCCN, LiCH, $C(SiH_3)_2$, and SiH_3CH.

states or in only one of them. In particular, the static correlation may critically result in the case of CLi_2 and NCCCN, where both diagnostics point toward the multireference nature of these systems.

The results of the ST gap for the set of carbenes are shown in Table II, where the first column labels the molecule and the second column indicates the ST reference gap computed as $\Delta E_{ST} = E_S - E_T$, that is, a positive sign indicates a triplet ground state and a negative sign indicates a singlet ground state; experimental values have been used when available,[71–83] indicated by the label "(exp)" next to the reference value, and the theoretical value was used in the other cases;[42,67,71,84] the systems have been ordered from positive to negative ST gaps. The following columns indicate the predictions provided by PNOF7, NOF-c-MP2, and the GNOF. In addition, coupled cluster calculations are presented for comparison, particularly CCSD and CCSD(T), since accurate results have been demonstrated for carbenes with the last method.[67] Signed errors relative to the reference can be found at the bottom of the table, and statistical data, namely, mean errors (MEs), mean absolute error (MAE), standard deviation (STD), and the root mean square error (RMSE) have been included in the last rows of Table II; in particular, the rows labeled "-all" are based on all the studied molecules, and the rows labeled "-exp" are presented by omitting molecules without experimental data and the CBr_2 molecule as it significantly increases all statistical values.[85,86] Furthermore, we present the violin plots of all molecule errors by each method shown in Fig. 2 and the violin plots for molecules with experimental data in Fig. 3, with the purpose of comparing the error distribution of the PNOFs and coupled cluster methods because statistical data such as ME and STD are insufficient to collate the data and MAE and RMSE do not provide information about outliers.

Regarding the PNOF results, PNOF7 generally presents the largest deviations from the reference values, as expected due to the lack of dynamic correlation in its functional form. It presents positive signed errors in almost all cases as reflected in the ME, indicating a preference for triplet states; in fact, it incorrectly predicts that most of the singlet ground-state molecules are triplets. This behavior can be fixed by NOF-c-MP2, which adds a dynamic correlation

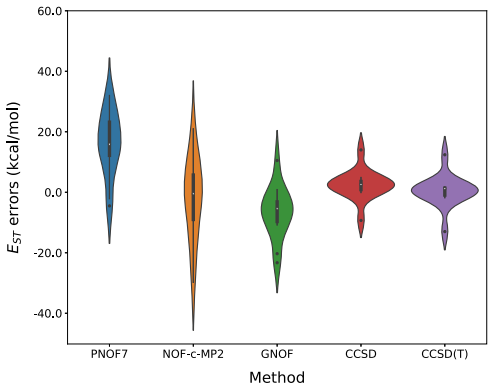

FIG. 2. Violin plots of all errors calculated by the PNOF family of functionals and coupled-cluster methods, with the white points showing the corresponding median, the thick gray bar representing each interquartile range, and the thin line bar representing the rest of the data of each method except for outliers, which are marked with black points.

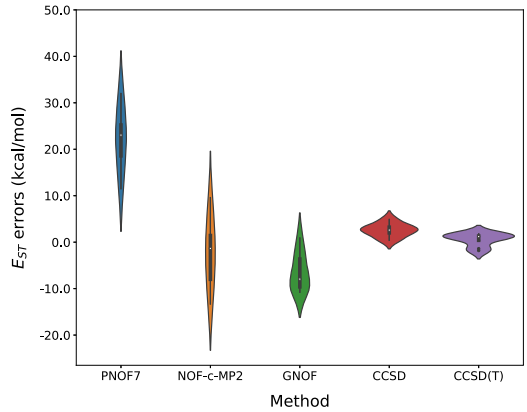

FIG. 3. Violin plots of exp errors calculated by the PNOF family of functionals and coupled-cluster methods, with the white points showing the corresponding median, the thick gray bar representing each interquartile range, and the thin line bar representing the rest of the data of each method except for outliers, which are marked with black points.

to a modified form of PNOF7, and it can be seen that, except for the dicyanocarbene, most of the predicted ST gaps now present the same sign as the reference values, which means that the correct ground state is being predicted. Interestingly, the same effect is achieved by the GNOF, which is relevant since it was designed to intrinsically balance the correlation regimes in a pure NOF.[43] In particular, NOF-c-MP2 and the GNOF present negative MEs, which reflects that methods make more negative ST gaps and provide an MAE-exp and RSME-exp with at least 60% of improvement relative to the value of PNOF7; all these results are in line with the previous discussion; however, as can be seen in Table II and Fig. 3, the GNOF has a lower STD value and a more concentrated error distribution than PNOF7 and NOF-c-MP2, and it also maintains the scalability of the method in N^4 order when coupled with RI, which makes it an amenable theory to be applied to medium size molecules of interest. As already discussed, coupled cluster calculations can be used to compare the results of PNOF calculations. In this regard, CCSD presents an RMSE-exp of 2.9 kcal/mol, and CCSD(T) presents an RMSE-exp of 1.4 kcal/mol, where it can be seen that the MAE-exp and RMSE-exp error obtained by CCSD(T) shows 50% of improvement with respect to CCSD, which confirms the importance of handling static and dynamic correlations simultaneously. In order to provide a more in-depth analysis, let us now focus on violin plots. We observe a decrease in outliers by switching from analysis of all data to analysis of experimental data except for CBr, which questions the quality of the theoretical values, and it allows us to see that the last data are appropriate to compare the computational methods. It is clear to see that coupled cluster methods, namely, CCSD and CCSD(T), have their medians closest to 0 kcal/mol, followed by NOF-c-MP2, the GNOF, and finally PNOF7. In this context, we would conclude that NOF-c-MP2 gives the best description for these systems compared to other PNOF methods; however, the error distribution shows that it has a larger prediction error since the shape is flatter than in the other methods, where the GNOF has a bias to the left (toward negative values) but has a more concentrated distribution and a smaller thin line bar, as expected

due to STD values. Despite the fact that coupled cluster calculations present lower MAE and RMSE values than PNOF calculations and more central shapes of the error distributions, some specific remarks must be made for specific carbenes, as will be done in Sec. IV B.

B. Analysis of specific carbenes

In this section, we give special comments for some of the studied carbenes; experimental data will be used for comparison when available, and theoretical data will be used when experimental values are not reported.

1. Methylene

Let us start with the most elemental carbene, CH_2, which is known to present a triplet ground state with sp^2 hybridization. All PNOFs correctly predict a triplet ground state. An advantage of PNOFs is that they can provide a direct chemical picture of the systems through the natural orbitals,[87] as can be seen in Figs. 4 and 5 for the singlet and triplet states of methylene. In particular, two bonding σ-like orbitals can be observed, as well as a non-bonding σ-like orbital and a p-like orbital perpendicular to the plane of the molecule. In the context of the PNOF's orbital pairing scheme, note

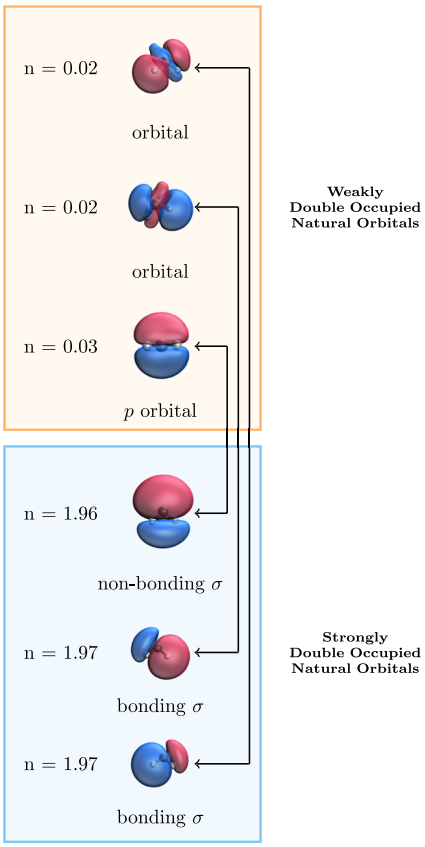

FIG. 4. Natural orbitals for the singlet state of the CH_2 computed with the GNOF. For simplicity, only the main weakly occupied orbital coupled with each strongly occupied orbital is shown.

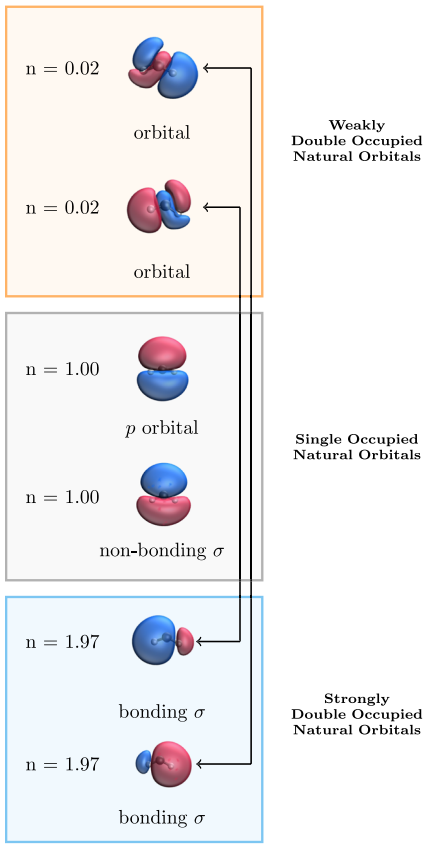

FIG. 5. Natural orbitals for the triplet state of the CH_2 computed with the GNOF. For simplicity, only the main weakly occupied orbital coupled with each strongly occupied orbital is shown.

that for singlets, the two σ orbitals appear as strongly double occupied natural orbitals and the non-bonding σ orbital appears as a strongly double occupied orbital natural coupled to the p orbital, as illustrated in Fig. 4. A similar picture is obtained in the case of triplets, but in this case, the non-bonding σ orbital and the p orbital appeared in the single occupied natural orbital subspace, as shown in Fig. 5. Similar orbitals and pairing schemes have been observed in most of the studied carbenes in both PNOF7 and GNOF calculations, except when otherwise stated; these orbital couplings were not enforced in any way but appeared naturally as a chemical consequence of the systems.

2. LiCH and CLi_2

Lithium carbenes present special characteristics due to the electropositive lithium atom, which favors the triplet as the ground state, and constitute an exception to the common orbital picture seen for methylene, as depicted in Fig. 6. In fact, the triplet state of CLi_2 and both the singlet and triplet states of LiCH present a linear geometry. In the case of LiCH, two delocalized orbitals are observed as single occupied orbitals (SONOs) in the triplet; on the other hand, these are coupled as double occupied orbitals in the singlet state; similar orbitals are observed in the triplet state of CLi_2. The LiCH molecule

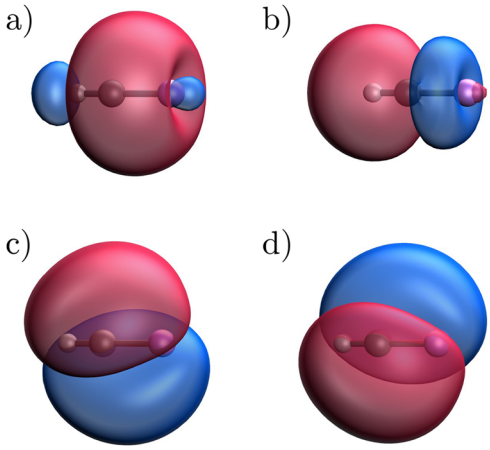

FIG. 6. Natural orbitals that appear in the triplet state of LiCH. (a) HONO-1, (b) HONO, (c) SONO(I), and (d) SONO(II).

has also recently been studied by Montgomery with the variational 2-RDM (v2RDM) that predicts a 15.8 kcal/mol singlet-triplet gap,[42] which is significantly lower than that predicted by PNOF7, the GNOF, CCSD, and CCSD(T), where all are in good agreement with values around 30 kcal/mol. In the case of singlet LiCH, its highest occupied natural orbital (HONO) has an ON of 1.063 when studied with PNOF7, which is in good agreement with the diradical character reported for the molecule. Regarding CLi_2, PNOF7, the GNOF, CCSD, and CCSD(T), ST gaps are in good agreement.

3. Cyanocarbenes

A negative singlet-triplet gap has been predicted for dicyanocarbene, NCCCN, using NOF-c-MP2 and the GNOF, and this is in disagreement with the positive singlet triplet gap predicted using the G3MP2 level of theory.[67,71] On the contrary, the coupled cluster calculations achieve positive values of ST gaps for cyanocarbenes; however, it can be seen that including more correlation by going from CCSD to CCSD(T) increases the stability of the singlet, which is also observed by going from PNOF7 to the GNOF; hence, it remains unclear whether the marked overstabilization of the singlet state in cyanocarbenes is an artifact of the PNOF calculations or an improved prediction achieved by the GNOF due to a balanced inclusion of static and dynamic correlation.

4. Methylcarbene

The singlet-triplet gap for CH_3CH has recently been experimentally studied by photofragment translational energy spectroscopy by Datta and Davis,[74] and it was concluded that the results are consistent with the ~3 kcal/mol value, which is in agreement with the low values obtained by the GNOF, NOF-c-MP2, CCSD, and CCSD(T).

5. SiH_3C and $C(SiH_3)_2$

Regarding $C(SiH_3)_2$ and SiH_3C carbenes, they have a positive prediction of the singlet-triplet gap,[21] in accordance with PNOFs and coupled cluster calculations. Furthermore, all PNOF calculations show an sp^2 hybridization for the singlet and an sp hybridization for the carbon in the linear triplet state. The GNOF presents errors comparable to those of CCSD(T).

6. Halocarbenes

It has previously been reported that the presence of electronegative atoms bonded to the carbon atom tends to stabilize the singlet state[24,88,89] while substituents that are less electronegative than carbon tend to stabilize the triplet state.[9,90] Furthermore, dihalocarbenes suffer from multiple bond characters due to the donation of the lone pairs of substituents, thus generating a π-system that stabilizes the singlet state.[24] Despite the fact that the singlet-triplet gap decreases as the ability of the π-electron donor substituents increases, PNOF7 incorrectly predicts a triplet ground state for almost all halocarbenes, contradicting all reported experimental data.[22,75,91] These results are improved by NOF-c-MP2 and the GNOF, which predict a singlet ground state for all halocarbenes.

V. CONCLUSION

We have studied the ST gap of several simple carbenes using a GNOF. The performance of the GNOF method was evaluated by comparing with the experimental and theoretical values, including CCSD(T) and CCSD. Furthermore, the GNOF method has been compared with previous functionals of the PNOF family, namely, PNOF7 and NOF-c-MP2.

Interestingly, despite presenting static correlation, PNOF7 fails to describe the carbenes' ground state preference for singlets and triplets due to the lack of dynamic correlation, which is corrected by NOF-c-MP2 and the GNOF. In general, the effect of substituents can be well described by the GNOF and NOF-c-MP2 methods not only by the signed singlet-triplet gap but also by agreeing with the tendency to decrease its magnitude as the ability of the π-electron-donor substituents increases.

The RDM- and wavefunction-based methods investigated here indicate that a proper balance between static and dynamic correlation is required since the GNOF, NOF-c-MP2, and CCSD(T) methods obtain small RMSE errors compared to their counterparts that predominantly include one type of correlation.

Finally, we have shown that the GNOF method is capable of describing carbenes with acceptable scaling compared with multireference methods, which is a promising result, since the study of the spin nature of their ground state greatly benefits from the theoretical methods when experimental difficulties arise in these systems.

ACKNOWLEDGMENTS

L. Franco acknowledges the funding through project Grant No. PAPIITIN201822 from "Programa de Apoyo a Proyectos de Investigación e Innovación Tecnológica (PAPIIT)," and J. F. H. Lew-Yee acknowledges the funding through CVU Grant No. 867718 from "Consejo Nacional de Ciencia y Tecnología (CONACyT)" for the Ph.D. scholarship. J. M. del Campo acknowledges the funding through project Grant No. CB-2016-282791 from CONACyT and through project Grant No. PAPIITIN201822 from PAPIIT and

thanks "Laboratorio Nacional de Cómputo de Alto Desempeño (LANCAD)" for providing the computing resources through project Grant No. LANCAD-UNAMDGTIC-270.

AUTHOR DECLARATIONS

Conflict of Interest

The authors have no conflicts to disclose.

Author Contributions

Lizeth Franco: Data curation (equal); Formal analysis (equal); Investigation (equal); Methodology (equal); Validation (equal); Visualization (equal); Writing – original draft (equal). **Juan Felipe Huan Lew-Yee**: Conceptualization (equal); Investigation (equal); Methodology (equal); Software (equal); Supervision (equal); Validation (equal); Writing – original draft (equal); Writing – review & editing (equal). **Jorge M. del Campo**: Conceptualization (equal); Funding acquisition (equal); Investigation (equal); Methodology (equal); Project administration (equal); Resources (equal); Supervision (equal); Validation (equal); Visualization (equal); Writing – original draft (equal); Writing – review & editing (equal).

DATA AVAILABILITY

The data that support the findings of this study are available from the corresponding author upon reasonable request.

REFERENCES

[1] M. Hermann, "Ueber die bei der technischen gewinnung des broms beobachtete flüchtige bromverbindung," Justus Liebigs Ann. Chem., **95**, 211–225 (1855).
[2] J. U. Nef, "Ueber das zweiwerthige kohlenstoffatom. (Vierte Abhandlung.) Die chemie des methylens," Justus Liebigs Ann. Chem. **298**, 202–374 (1897).
[3] H. Staudinger and O. Kupfer, "Über reaktionen des methylens. III. Diazomethan," Ber. Dtsch. Chem. Ges. **45**, 501–509 (1912).
[4] A. Igau, H. Grutzmacher, A. Baceiredo, and G. Bertrand, "Analogous *α, α'*-bis-carbenoid, triply bonded species: Synthesis of a stable *λ*3-phosphino carbene-*λ*5-phosphaacetylene," J. Am. Chem. Soc. **110**, 6463–6466 (1988).
[5] S. C. Lapin and G. B. Schuster, "Chemical and physical properties of 9-xanthylidene: A ground-state singlet aromatic carbene," J. Am. Chem. Soc. **107**, 4243–4248 (1985).
[6] A. J. Arduengo, R. L. Harlow, and M. Kline, "A stable crystalline carbene," J. Am. Chem. Soc. **113**, 361–363 (1991).
[7] G. Bertrand and R. Reed, "λ^3-phosphinocarbenes λ^5-phosphaacetylenes," Coord. Chem. Rev. **137**, 323–355 (1994).
[8] H. Tomioka, T. Watanabe, K. Hirai, K. Furukawa, T. Takui, and K. Itoh, "2,2',4,4',6,6'-hexabromodiphenylcarbene. The first stable triplet carbene in fluid solution at low temperature and in the crystal state at room temperature," J. Am. Chem. Soc. **117**, 6376–6377 (1995).
[9] K. Hirai, T. Itoh, and H. Tomioka, "Persistent triplet carbenes," Chem. Rev. **109**, 3275–3332 (2009).
[10] K. Hirai, K. Hatanaka, T. Yamaguchi, A. Miyajima, T. Kitagawa, and H. Tomioka, "Generation and reactivities of triplet diphenylcarbenes protected by bulky groups as *para* substituents," J. Phys. Org. Chem. **24**, 909–920 (2011).
[11] T. Nakajo, J. Kumagai, S. Kusaka, A. Hori, Y. Hijikata, J. Pirillo, Y. Ma, and R. Matsuda, "Triplet carbene with highly enhanced thermal stability in the nanospace of a metal-organic framework," J. Am. Chem. Soc. **143**, 8129–8136 (2021).
[12] K. A. Savin, "Chapter 4—Reactions involving acids and other electrophiles," in *Writing Reaction Mechanisms in Organic Chemistry*, 3rd ed., edited by K. A. Savin (Academic Press, Boston, 2014), pp. 161–235.
[13] P. de Frémont, N. Marion, and S. P. Nolan, "Carbenes: Synthesis, properties, and organometallic chemistry," Coord. Chem. Rev. **253**, 862–892 (2009).
[14] Y. Narayana, N. C. Sandhya, H. E. Dinesh, S. B. Thimmaiah, K. S. Rangappa, and K. Mantelingu, "N-heterocyclic carbene mediated organocatalysis reactions," in *Carbene*, edited by S. Saha and A. Manna (IntechOpen, Rijeka, 2022), pp. 137–155.
[15] O. Hollóczki, "The mechanism of N-heterocyclic carbene organocatalysis through a magnifying glass," Chem. - Eur. J. **26**, 4885 (2020).
[16] Z. Hu, C. Wei, Q. Shi, X. Hong, J. Liu, X. Zhou, J. Han, W. Cao, A. K. Gupta, X. Zhang, D. Wei, Z. Fu, and W. Huang, "Desymmetrization of N-Cbz glutarimides through N-heterocyclic carbene organocatalysis," Nat. Commun. **13**, 4042 (2022).
[17] P. Bellotti, M. Koy, M. N. Hopkinson, and F. Glorius, "Recent advances in the chemistry and applications of N-heterocyclic carbenes," Nat. Rev. Chem. **5**, 711–725 (2021).
[18] Y. Matsuki, N. Ohnishi, Y. Kakeno, S. Takemoto, T. Ishii, K. Nagao, and H. Ohmiya, "Aryl radical-mediated N-heterocyclic carbene catalysis," Nat. Commun. **12**, 3848 (2021).
[19] C. M. Geise and C. M. Hadad, "Computational study of the electronic structure of substituted phenylcarbene in the gas phase," J. Org. Chem. **65**, 8348–8356 (2000).
[20] H. L. Woodcock, D. Moran, B. R. Brooks, P. v. R. Schleyer, and H. F. Schaefer, "Carbene stabilization by aryl substituents. Is bigger better?," J. Am. Chem. Soc. **129**, 3763–3770 (2007).
[21] S. Gronert, J. R. Keeffe, and R. A. More O'Ferrall, "Correlations between carbene and carbenium stability: Ab initio calculations on substituted phenylcarbenes, nonbenzenoid arylcarbenes, heteroatom-substituted carbenes, and the corresponding carbocations and hydrogenation products," J. Org. Chem. **74**, 5250–5259 (2009).
[22] K. K. Irikura, W. A. Goddard, and J. L. Beauchamp, "Singlet-triplet gaps in substituted carbenes CXY (X, Y = H, fluoro, chloro, bromo, iodo, silyl)," J. Am. Chem. Soc. **114**, 48–51 (1992).
[23] B. C. Gilbert, D. Griller, and A. S. Nazran, "Structures of diarylcarbenes and their effect on the energy separation between singlet and triplet states," J. Org. Chem. **50**, 4738–4742 (1985).
[24] D. Bourissou, O. Guerret, F. P. Gabbaï, and G. Bertrand, "Stable carbenes," Chem. Rev. **100**, 39–92 (2000).
[25] R. Hoffmann, G. D. Zeiss, and G. W. Van Dine, "The electronic structure of methylenes," J. Am. Chem. Soc. **90**, 1485–1499 (1968).
[26] N. C. Baird and K. F. Taylor, "Multiplicity of the ground state and magnitude of the T1-S0 gap in substituted carbenes," J. Am. Chem. Soc. **100**, 1333–1338 (1978).
[27] D. Bethell, G. Stevens, and P. Tickle, "The reaction of diphenylmethylene with isopropyl alcohol and oxygen: The question of reversibility of singlet–triplet interconversion of carbenes," J. Chem. Soc. D **1970**, 792b–794b.
[28] P. Costa and W. Sander, "Hydrogen bonding switches the spin state of diphenylcarbene from triplet to singlet," Angew. Chem., Int. Ed. **53**, 5122–5125 (2014).
[29] J. Gräfenstein and D. Cremer, "Can density functional theory describe multireference systems? Investigation of carbenes and organic biradicals," Phys. Chem. Chem. Phys. **2**, 2091–2103 (2000).
[30] M. Schwilk, D. N. Tahchieva, and O. A. von Lilienfeld, "Large yet bounded: Spin gap ranges in carbenes," arXiv:2004.10600v1 [physics.chem-ph] (2020).
[31] P. Rivero, C. A. Jiménez-Hoyos, and G. E. Scuseria, "Predicting singlet-triplet energy splittings with projected Hartree-Fock methods," J. Phys. Chem. A **117**, 8073–8080 (2013).
[32] E. Sun, T. Ren, S. Shan, Q. Liu, H. Xu, and B. Yan, "Multireference configuration interaction study of dichlorocarbene," Chem. Phys. **459**, 54–58 (2015).
[33] D. Gerbig and D. Ley, "Computational methods for contemporary carbene chemistry," Wiley Interdiscip. Rev.: Comput. Mol. Sci. **3**, 242–272 (2013).
[34] I. Alkorta and J. Elguero, "A LFER analysis of the singlet-triplet gap in a series of sixty-six carbenes," Chem. Phys. Lett. **691**, 33–36 (2018).

[35]Z. Qu and Y. Ma, "Variational multistate density functional theory for a balanced treatment of static and dynamic correlations," J. Chem. Theory Comput. **16**, 4912–4922 (2020).
[36]R. G. Shirazi, D. A. Pantazis, and F. Neese, "Performance of density functional theory and orbital-optimised second-order perturbation theory methods for geometries and singlet–triplet state splittings of aryl-carbenes," Mol. Phys. **118**, e1764644 (2020).
[37]R. Ghafarian Shirazi, F. Neese, D. A. Pantazis, and G. Bistoni, "Physical nature of differential spin-state stabilization of carbenes by hydrogen and halogen bonding: A domain-based pair natural orbital coupled cluster study," J. Phys. Chem. A **123**, 5081–5090 (2019).
[38]A. Altun, M. Saitow, F. Neese, and G. Bistoni, "Local energy decomposition of open-shell molecular systems in the domain-based local pair natural orbital coupled cluster framework," J. Chem. Theory Comput. **15**, 1616–1632 (2019).
[39]P. B. Szabó, J. Csóka, M. Kállay, and P. R. Nagy, "Linear-scaling open-shell MP2 approach: Algorithm, benchmarks, and large-scale applications," J. Chem. Theory Comput. **17**, 2886–2905 (2021).
[40]D. J. Coughtrie, R. Giereth, D. Kats, H.-J. Werner, and A. Köhn, "Embedded multireference coupled cluster theory," J. Chem. Theory Comput. **14**, 693–709 (2018).
[41]L. Greenman and D. A. Mazziotti, "Energy barriers of vinylidene carbene reactions from the anti-hermitian contracted Schrödinger equation," J. Phys. Chem. A **114**, 583–588 (2010).
[42]J. M. Montgomery, E. Alexander, and D. A. Mazziotti, "Prediction of the existence of LiCH: A carbene-like organometallic molecule," J. Phys. Chem. A **124**, 9562–9566 (2020).
[43]M. Piris, "Global natural orbital functional: Towards the complete description of the electron correlation," Phys. Rev. Lett. **127**, 233001 (2021).
[44]M. Piris, X. Lopez, F. Ruipérez, J. M. Matxain, and J. M. Ugalde, "A natural orbital functional for multiconfigurational states," J. Chem. Phys. **134**, 164102 (2011).
[45]M. Piris, J. M. Matxain, and X. Lopez, "The intrapair electron correlation in natural orbital functional theory," J. Chem. Phys. **139**, 234109 (2013).
[46]M. Piris, "Global method for electron correlation," Phys. Rev. Lett. **119**, 063002 (2017).
[47]I. Mitxelena and M. Piris, "Benchmarking GNOF against FCI in challenging systems in one, two, and three dimensions," J. Chem. Phys. **156**, 214102 (2022).
[48]J. F. H. Lew-Yee, J. M. del Campo, and M. Piris, "Electron correlation in the iron(II) porphyrin by natural orbital functional approximations," J. Chem. Theory Comput. **19**, 211–220 (2023).
[49]M. Piris, "A new approach for the two-electron cumulant in natural orbital functional theory," Int. J. Quantum Chem. **106**, 1093–1104 (2006).
[50]M. Piris, "Natural orbital functional for multiplets," Phys. Rev. A **100**, 032508 (2019).
[51]M. Piris and I. Mitxelena, "DoNOF: An open-source implementation of natural-orbital-functional-based methods for quantum chemistry," Comput. Phys. Commun. **259**, 107651 (2021).
[52]M. Piris, "Interacting pairs in natural orbital functional theory," J. Chem. Phys. **141**, 044107 (2014).
[53]M. Piris, "Dynamic electron-correlation energy in the natural-orbital-functional second-order-Möller-Plesset method from the orbital-invariant perturbation theory," Phys. Rev. A **98**, 022504 (2018).
[54]M. Rodríguez-Mayorga, I. Mitxelena, F. Bruneval, and M. Piris, "Coupling natural orbital functional theory and many-body perturbation theory by using nondynamically correlated canonical orbitals," J. Chem. Theory Comput. **17**, 7562–7574 (2021).
[55]J. F. H. Lew-Yee and J. M. del Campo, Pynof, 2022.
[56]J. L. Whitten, "Coulombic potential energy integrals and approximations," J. Chem. Phys. **58**, 4496–4501 (1973).
[57]B. I. Dunlap, J. W. D. Connolly, and J. R. Sabin, "On some approximations in applications of Xα theory," J. Chem. Phys. **71**, 3396–3402 (1979).
[58]M. Feyereisen, G. Fitzgerald, and A. Komornicki, "Use of approximate integrals in ab initio theory. An application in MP2 energy calculations," Chem. Phys. Lett. **208**, 359–363 (1993).
[59]J. F. H. Lew-Yee, M. Piris, and J. M. del Campo, "Resolution of the identity approximation applied to PNOF correlation calculations," J. Chem. Phys. **154**, 064102 (2021).
[60]D. G. A. Smith, L. A. Burns, A. C. Simmonett, R. M. Parrish, M. C. Schieber, R. Galvelis, P. Kraus, H. Kruse, R. Di Remigio, A. Alenaizan, A. M. James, S. Lehtola, J. P. Misiewicz, M. Scheurer, R. A. Shaw, J. B. Schriber, Y. Xie, Z. L. Glick, D. A. Sirianni, J. S. O'Brien, J. M. Waldrop, A. Kumar, E. G. Hohenstein, B. P. Pritchard, B. R. Brooks, H. F. Schaefer, A. Y. Sokolov, K. Patkowski, A. E. DePrince, U. Bozkaya, R. A. King, F. A. Evangelista, J. M. Turney, T. D. Crawford, and C. D. Sherrill, "Psi4 1.4: Open-source software for high-throughput quantum chemistry," J. Chem. Phys. **152**, 184108 (2020).
[61]B. P. Pritchard, D. Altarawy, B. Didier, T. D. Gibson, and T. L. Windus, "New basis set exchange: An open, up-to-date resource for the molecular sciences community," J. Chem. Inf. Model. **59**, 4814–4820 (2019).
[62]D. Feller, "The role of databases in support of computational chemistry calculations," J. Comput. Chem. **17**, 1571–1586 (1996).
[63]K. L. Schuchardt, B. T. Didier, T. Elsethagen, L. Sun, V. Gurumoorthi, J. Chase, J. Li, and T. L. Windus, "Basis set exchange: A community database for computational sciences," J. Chem. Inf. Model. **47**, 1045–1052 (2007).
[64]F. Weigend and R. Ahlrichs, "Balanced basis sets of split valence, triple zeta valence and quadruple zeta valence quality for H to Rn: Design and assessment of accuracy," Phys. Chem. Chem. Phys. **7**, 3297–3305 (2005).
[65]D. Rappoport and F. Furche, "Property-optimized Gaussian basis sets for molecular response calculations," J. Chem. Phys. **133**, 134105 (2010).
[66]F. Weigend, "Hartree-Fock exchange fitting basis sets for H to Rn," J. Comput. Chem. **29**, 167–175 (2008).
[67]S. Gronert, J. R. Keeffe, and R. A. More O'Ferrall, "Stabilities of carbenes: Independent measures for singlets and triplets," J. Am. Chem. Soc. **133**, 3381–3389 (2011).
[68]D. Y. Kim, D. C. Yang, J. M. L. Madridejos, A. Hajibabaei, C. Baig, and K. S. Kim, "Anisotropic and amphoteric characteristics of diverse carbenes," Phys. Chem. Chem. Phys. **20**, 13722–13733 (2018).
[69]G. B. Bacskay, "Quantum chemical characterization of the $\tilde{X}(^1A')$, $\tilde{a}(^3A'')$ and $\tilde{A}(^1A'')$ states of CHBr and CHI and computed heats of formation for CHI and CI," J. Phys. Chem. A **114**, 8625–8630 (2010).
[70]T. J. Lee and P. R. Taylor, "A diagnostic for determining the quality of single-reference electron correlation methods," Int. J. Quantum Chem. **36**, 199–207 (1989).
[71]M. R. Nimlos, G. Davico, C. M. Geise, P. G. Wenthold, W. C. Lineberger, S. J. Blanksby, C. M. Hadad, G. A. Petersson, and G. B. Ellison, "Photoelectron spectroscopy of $HCCN^-$ and $HCNC^-$ reveals the quasilinear triplet carbenes, HCCN and HCNC," J. Chem. Phys. **117**, 4323–4339 (2002).
[72]A. R. W. McKellar, P. R. Bunker, T. J. Sears, K. M. Evenson, R. J. Saykally, and S. R. Langhoff, "Far infrared laser magnetic resonance of singlet methylene: Singlet–triplet perturbations, singlet–triplet transitions, and the singlet–triplet splitting," J. Chem. Phys. **79**, 5251–5264 (1983).
[73]D. G. Leopold, K. K. Murray, and W. C. Lineberger, "Laser photoelectron spectroscopy of vibrationally relaxed CH_2^-: A reinvestigation of the singlet–triplet splitting in methylene," J. Chem. Phys. **81**, 1048–1050 (1984).
[74]S. Datta and H. F. Davis, "Direct observation of ethylidene (CH_3CH), the elusive high-energy isomer of ethylene," J. Phys. Chem. Lett. **11**, 10476–10481 (2020).
[75]R. L. Schwartz, G. E. Davico, T. M. Ramond, and W. Carl Lineberger, "Singlet-triplet splittings in CX_2 (X = F, Cl, Br, I) dihalocarbenes via negative ion photoelectron spectroscopy," J. Phys. Chem. A **103**, 8213–8221 (1999).
[76]C.-S. Lin, Y.-E. Chen, and B.-C. Chang, "New electronic spectra of the HCCl and DCCl $\tilde{A} - \tilde{X}$ vibronic bands," J. Chem. Phys. **121**, 4164–4170 (2004).
[77]C. Tao, C. Mukarakate, Z. Terranova, C. Ebben, R. H. Judge, and S. A. Reid, "High resolution study of spin-orbit mixing and the singlet-triplet gap in chlorocarbene: Stimulated emission pumping spectroscopy of $CH^{35}Cl$ and $CD^{35}Cl$," J. Chem. Phys. **129**, 104309 (2008).
[78]K. K. Murray, D. G. Leopold, T. M. Miller, and W. C. Lineberger, "Photoelectron spectroscopy of the halocarbene anions HCF^-, $HCCl^-$, $HCBr^-$, HCI^-, CF_2^-, and CCl_2^-," J. Chem. Phys. **89**, 5442–5453 (1988).
[79]M. K. Gilles, K. M. Ervin, J. Ho, and W. C. Lineberger, "Negative ion photoelectron spectroscopy of halocarbene anions (HCF^-, $HCCl^-$, $HCBr^-$, and HCI^-);

photoelectron angular distributions and neutral triplet excitation energies," J. Phys. Chem. **96**, 1130–1141 (1992).
[80]W.-Z. Chang, H.-J. Hsu, and B.-C. Chang, "New dispersed fluorescence spectra of HCBr and DCBr," Chem. Phys. Lett. **413**, 25–30 (2005).
[81]T.-C. Tsai, C.-W. Chen, and B.-C. Chang, "Laser excitation and dispersed fluorescence spectra of the HCBr $\tilde{A} - \tilde{X}$ vibronic transition," J. Chem. Phys. **115**, 766–770 (2001).
[82]S. W. Wren, K. M. Vogelhuber, K. M. Ervin, and W. C. Lineberger, "The photoelectron spectrum of CCl_2^-: The convergence of theory and experiment after a decade of debate," Phys. Chem. Chem. Phys. **11**, 4745 (2009).
[83]S. Koda, "Emission and energy transfer of triplet difluoromethylene produced in the reaction of oxygen atoms with tetrafluoroethylene," Chem. Phys. Lett. **55**, 353–357 (1978).
[84]J. F. Harrison, R. C. Liedtke, and J. F. Liebman, "The multiplicity of substituted acyclic carbenes and related molecules," J. Am. Chem. Soc. **101**, 7162–7168 (1979).
[85]H.-j. Hsu, W.-Z. Chang, and B.-C. Chang, "Dispersed fluorescence spectroscopy of the CBr2 $\tilde{A}^1B_1\tilde{X}^1A_1$ transition," Phys. Chem. Chem. Phys. **7**, 2468 (2005).
[86]C. Tao, C. Mukarakate, and S. A. Reid, "Single vibronic level emission spectroscopy of the CBr2 $\tilde{A}^1B_1\tilde{X}^1A_1$ system of dibromocarbene," J. Mol. Spectrosc. **241**, 136–142 (2007).
[87]M. Piris, J. M. Matxain, X. Lopez, and J. M. Ugalde, "The one-electron picture in the Piris natural orbital functional 5 (PNOF5)," Theor. Chem. Acc. **132**, 1298 (2013).
[88]N. Harrison, A. L. Cornelius, H. Harima, K. Takegahara, J. A. Detwiler, G. M. Schmiedeshoff, J. C. Cooley, and J. L. Smith, "Electronic structure of $ThBe_{13}$," Phys. Rev. B **61**, 1779–1785 (1971).
[89]D. Feller, W. Thatcher Borden, and E. R. Davidson, "Dependence of the singlet-triplet splitting in heterosubstituted carbenes on the heteroatom electronegativity and conformation," Chem. Phys. Lett. **71**, 22–26 (1980).
[90]A. Nemirowski and P. R. Schreiner, "Electronic stabilization of ground state triplet carbenes," J. Org. Chem. **72**, 9533–9540 (2007).
[91]B. Ruscic, M. Litorja, and R. L. Asher, "Ionization energy of methylene revisited: Improved values for the enthalpy of formation of CH_2 and the bond dissociation energy of CH_3 via simultaneous solution of the local thermochemical network," J. Phys. Chem. A **103**, 8625–8633 (1999).